Susceptibility calculations for strongly correlated materials

Von der Fakultät für Mathematik, Informatik und Naturwissenschaften der RWTH Aachen University zur Erlangung des akademischen Grades eines Doktors der Naturwissenschaften genehmigte Dissertation

vorgelegt von

Julian Mußhoff, M.Sc.

aus Wickede (Ruhr)

Berichter: Univ.-Prof. Eva Pavarini, Ph.D.

Univ.-Prof. Stefan Wessel, Ph.D.

Tag der mündlichen Prüfung: 16. März 2021

Diese Dissertation ist auf den Internetseiten der Universitätsbibliothek online verfügbar.

Abstract

The task of understanding and correctly describing strongly correlated materials has posed a challenge to physicists since the discovery of quantum mechanics. The state-of-the-art approach to strongly correlated materials is the combination of density functional theory (DFT) with dynamical mean-field theory (DMFT). We use the DFT to build material-specific Hubbard models for real materials. Within DMFT the Hubbard model is mapped to an impurity model, which is solved with a hybridization expansion continuous-time quantum Monte Carlo (CT-QMC) solver. DMFT is formulated in the language of single-particle Green functions. To connect the theory to experiments we additionally need susceptibilities (linear response functions), whose calculation is significantly more challenging.

In this thesis we present our implementation of the calculation of dynamical lattice susceptibilities. For this, we extend our massively-parallel general implementation of the CT-QMC to obtain dynamical local susceptibilities. The implementation scales almost ideally with the number of processors of the used supercomputers and is further improved by the use of symmetries of the susceptibilities. Besides this, it is essential to store and process them in an efficient compact basis. Therefore, our implementation makes use of Legendre polynomials and an even more compact numerical basis (intermediate representation). The calculation of lattice susceptibilities is done via the Bethe-Salpeter equation using the local vertex approximation, also implemented in either of the compact basis.

We present two representative applications. In the first we obtain magnetic and orbital susceptibilities of the layered perovskite K_2CuF_4. We show that this system is qualitatively different from the infinite layered $KCuF_3$ due to the tetragonal crystal field and an additional orbital Zeeman interaction. In K_2CuF_4 we find that the Zeeman interaction is small and superexchange alone cannot explain orbital ordering found at high temperatures in experiments. To explain this the crystal-field due to, e.g., Jahn-Teller distortions is essential. The Zeeman term is likely to play a role in more covalent materials.

In the second application we explore magnetism in the Hubbard model on a square lattice representing high-temperature superconducting cuprates. Their superconducting phase is still an open problem; it is however believed that magnetic properties play an important role. We calculate static and dynamical susceptibilities and explain their dependence on the screened Coulomb interaction U, the doping x and the next-nearest neighbor hopping t' representing different cuprates. At half-filling and for $t/U \ll 1$ the results are close to those for the equivalent Heisenberg model. We find that the inverse susceptibility scales almost linearly with the temperature in the paramagnetic phase. Below the Néel temperature we find antiferromagnetic (AFM) order. In that phase we obtain the spin-wave dispersion, which is found in experiments, within DMFT. For small dopings the results resemble the half-filling ones, but for large dopings they change significantly. With increasing x and t' we find a trend from the AFM phase to a ferromagnetic phase, going through regions with possible incommensurate-order phases.

Zusammenfassung

Seit der Entdeckung der Quantenmechanik stellt das Verständnis von Materialien mit stark korrelierten Elektronen eine Herausforderung für Physiker dar. Die etablierten Methoden um mit dieser Herausforderung umzugehen sind die Dichtefunktionaltheorie (DFT) in Kombination mit der dynamischen Molekularfeldtheorie (DMFT). Wir nutzen die DFT um materialspezifische Hubbard-Modelle zu konstruieren. Die DMFT beschreibt die Abbildung eines Hubbard-Modells auf ein effektives Störstellenproblem, das wir mit Hilfe von einem Quanten Monte Carlo Algorithmus (CT-QMC) lösen. Die DMFT ist formuliert in der Sprache der Ein-Teilchen Greenschen Funktionen. Um die Verbindung der Theorie mit Experimenten herstellen zu können benötigen wir Suszeptibilitäten (lineare Antwortfunktionen), deren Berechnung signifikant schwieriger ist.
In dieser Arbeit präsentieren wir unsere Implementierung der Berechnung von dynamischen Gitter-Suszeptibilitäten. Hierfür erweitern wir unsere existierende hochparallelisierte Implementierung des CT-QMC Algorithmus um die Möglichkeit der Berechnung von dynamischen lokalen Suszeptibilitäten. Unsere Implementierung skaliert nahezu perfekt mit der Anzahl der Prozessoren der verwendeten Supercomputer und wird beschleunigt durch die Verwendung von Symmetrien der Suszeptibilitäten. Für eine effiziente Berechnung der Suszeptibilitäten ist die Wahl einer kompakten Basis entscheidend, weshalb wir Legendre Polynome und eine noch kompaktere numerische Basis (intermediate representation) verwenden. Die Gitter-Suszeptibilitäten erhalten wir letztendlich durch die Lösung der Bethe-Salpeter Gleichung, ebenfalls implementiert in den kompakten Basen, mit der lokalen Vertex Näherung.
Wir präsentieren zwei repräsentative Anwendungen. In einer Ersten berechnen wir magnetische und orbitale Suszeptibilitäten für K_2CuF_4, welches eine geschichtete Perowskit-Struktur aufweist. Wir zeigen, dass dieses System sich durch ein tetragonales Kristallfeld und eine zusätzliche orbitale Zeeman Wechselwirkung qualitativ von $KCuF_3$ mit unendlich vielen Schichten unterscheidet. Im Fall von K_2CuF_4 ist die Zeeman Wechselwirkung klein und Superaustausch liefert allein keine hinreichende Erklärung für orbitale Ordnung. Zusätzlich muss auch das Kristallfeld, das z.B. aus Jahn-Teller Deformationen resultiert, beachtet werden. In mehr kovalenten Materialien spielt die von uns identifizierte Zeeman Wechselwirkung wahrscheinlich ebenfalls eine Rolle.
In einer weiteren Anwendung untersuchen wir Magnetismus für ein Hubbard-Modell definiert auf einem Quadratgitter, welches ein Modell für verschiedene Hochtemperatursupraleiter mit Kupferoxid ist. Deren supraleitende Phase ist ein ungelöstes Problem. Es wird vermutet, dass magnetische Eigenschaften entscheidend sind. Wir untersuchen den Einfluss der abgeschirmten Coulomb Abstoßung U, der Dotierung x und der kinetischen Energie t' auf die magnetische Suszeptibilität. Bei halber Füllung und $t/U \ll 1$ ähneln unsere Ergebnisse denen eines entsprechenden Heisenberg-Modells. Wir finden, dass die inverse Suszeptibilität in der paramagnetischen Phase nahezu linear von der Temperatur abhängt. Unterhalb der Néel Temperatur finden wir antiferromagnetische (AFM) Ordnung. In dieser Phase zeigen sich experimentell bekannte Spinwellen im bosonischen Spin-Anregungsspektrum. Sind die Ergebnisse bei kleiner Dotierung noch ähnlich, verändert die Erhöhung der Dotierung x und des Parameters t' diese drastisch. Die magnetische Ordnung ändert sich von AFM über möglicherweise inkommensurabel hin zu ferromagnetisch.

Contents

Summary of notation **VIII**

1 Introduction **1**

2 Solution of realistic models for correlated materials **3**
2.1 Building realistic ab-initio models . . . 3
2.1.1 Density-functional theory . . . 3
2.1.2 Material-specific Hubbard models . . . 5
2.2 Solution of realistic models . . . 6
2.2.1 Dynamical mean-field theory . . . 6
2.2.2 Susceptibility calculations in DMFT . . . 9
2.2.3 Practical implementation of LDA+DMFT . . . 10

3 Continuous-time quantum Monte Carlo impurity solver **12**
3.1 Quantum Monte Carlo solvers . . . 13
3.2 Hybridization expansion of partition function . . . 14
3.3 Segment solver . . . 17
3.3.1 Evaluation of local trace . . . 18
3.3.2 Monte Carlo moves . . . 19
3.4 Krylov solver . . . 21
3.4.1 Time evolution in Krylov subspace . . . 21
3.4.2 Evaluation of local trace . . . 23
3.4.3 Monte Carlo moves . . . 24
3.5 Measurements . . . 25
3.5.1 Measurement of diagonal operators . . . 26
3.5.2 Measurement of Green functions . . . 27
3.6 Parallelization and scaling . . . 31

4 Response functions **33**
4.1 One and two-particle Green function . . . 33
4.2 Linear response theory . . . 34
4.3 Experimental techniques . . . 37
4.3.1 Photoemission spectroscopy . . . 37
4.3.2 Scanning tunneling microscopy and spectroscopy . . . 38
4.3.3 Scattering experiments . . . 39
4.3.4 Nuclear magnetic resonance . . . 40

4.4 Generalized susceptibility 41
4.4.1 Lattice susceptibility from Bethe-Salpeter equation 41
4.4.2 Magnetic susceptibility 44
4.4.3 Orbital susceptibility 46
4.5 Basis choice for the susceptibility 46
4.5.1 Imaginary time formalism 46
4.5.2 Matsubara frequency representation 52
4.5.3 Compact basis function representation 57
4.5.4 Real frequency representation 68

5 Orbital ordering in the layered perovskite K_2CuF_4 72
5.1 Model 72
5.2 Orbital and magnetic ordering mechanism 74
5.2.1 Electron-phonon mechanism 74
5.2.2 Superexchange mechanism 76
5.2.3 Susceptibility from static mean-field theory 80
5.3 Method 82
5.4 Results 84
5.4.1 Results for the experimental structure 84
5.4.2 Results for the structure with removed crystal-field 86
5.4.3 The role of the orbital Zeeman interaction 87
5.5 Conclusions 90

6 Magnetic properties of high temperature superconducting cuprates 91
6.1 Model and method 91
6.2 Static and dynamical susceptibility at half-filling 94
6.2.1 Paramagnetic phase 95
6.2.2 Antiferromagnetic phase 97
6.3 Static and dynamical susceptibility in the hole doped regime 99
6.3.1 Static susceptibility 99
6.3.2 Dynamical susceptibility 105
6.4 Conclusions 106

7 Summary 107

A Appendix 109
A.1 Determinant ratios and matrix updates for hybridization function 109
A.1.1 Insertion and removal of a single row and column 109
A.1.2 Insertion and removal of two rows and columns 111
A.1.3 Change of a single row or column 111
A.2 Imaginary time evolution operator 113
A.3 Bethe-Salpeter equation in paramagnetic systems 114
A.4 Basis functions 115
A.4.1 Matsubara frequency representation 115
A.4.2 Legendre polynomials 115
A.4.3 Unitary transformation from Legendre to Matsubara representation 116
A.4.4 Improvement of Green function tail 117

A.4.5 Intermediate representation 118
A.5 Maximum entropy method 121
A.6 Analytic calculations for magnetic susceptibilities in cuprates 123
A.6.1 Bare dynamical lattice susceptibility for an antiferromagnetic Mott insulator 123
A.6.2 Dynamical lattice susceptibility for an antiferromagnetic Mott insulator 125
A.6.3 Static lattice susceptibility close to half-filling 127
A.6.4 Stoner susceptibility 129
A.7 Notes on the implementation of DMFT with a CT-QMC solver and the Bethe-Salpeter equation 133

Bibliography **133**

Summary of notation

τ	Imaginary time
t	Real time
ω_m	Bosonic Matsubara frequency
ν_n	Fermionic Matsubara frequency
ω	Real frequency
l	Legendre or intermediate representation index
$\mathbf{r}$	Space vector
$\mathbf{k}$, $\mathbf{q}$	Momentum vector
m	Band/orbital index or bosonic frequency index
s	Index for site inside supercell
σ	Spin index
α, γ	Combined indices: (σ,s,m) for lattice and (σ,m) for local susceptibility
i	Site index of lattice
$\mathcal{Z}$	Partition function
$\mathcal{T}$	Time-ordering operator
$f_l(x(\tau))$	Polynomial in general
$P_l(x(\tau))$	Legendre polynomial
$u_l(x(\tau))$	Intermediate representation polynomial
$G(\tau)$	Imaginary time Green function
$G(i\nu_n)$	Matsubara frequency representation of Green function
G_l	Polynomial representation of Green function
$A(\mathbf{k},\omega)$	Spectral function
$\rho(\omega)$	Density of states
$\chi_{P_\nu O_{\nu'}}$	Physical susceptibility
$\chi_{\alpha\alpha'\gamma\gamma'}$	Generalized susceptibility
χ^0	Bare susceptibility
$\chi_{nn'}(i\omega_m)$	Matsubara frequency representation of susceptibility
$\chi_{ll'}(i\omega_m)$	Polynomial representation of susceptibility
$\mathcal{S}$	Correlation function / structure factor
$\mathcal{C}$	Two-particle Green function
χ^{zz}, χ^{xx}	Magnetic susceptibility in z- and x-direction
$\chi^{\parallel}$	Magnetic susceptibility parallel to aligned spins
$\chi^{\perp}$	Magnetic susceptibility perpendicular to aligned spins
χ^{zz}_{oo}, χ^{xx}_{oo}	Orbital susceptibility in z- and x-direction
U^m_{nl}	Transformation matrix between Matsubara frequencies and polynomials

1 Introduction

Strongly correlated electron systems are in the focus of attention of condensed matter physicists since the discovery of quantum mechanics. Among these systems, materials with open d- and f-shells pose many open questions. Although the Schrödinger equation, which describes these problems, is known almost for one century, the general solution of the many-body problem is unknown.

For small numbers of electrons a computer can nowadays solve such problems by diagonalization of the Hamiltonian, but already for a single atom, like copper, the number of electrons is too large to be solved in this way. The reason is the exponential growth of the Hilbert space dimension. If we discretize every space dimension of N electrons into L intervals, we need to store L^{3N} variables only for the wavefunction, i.e., the eigenvector. This number soon exceeds the number of atoms in the universe. Aside from that, the knowledge of all eigenvectors and eigenenergies, would help little to understand the mechanisms behind observable phenomena like magnetic and orbital ordering, or high temperature superconductivity.

In chapter 2 we introduce a state-of-the-art approach for strongly correlated materials, the density-functional theory (DFT) with dynamical mean-field theory (DMFT). The DFT is based on knowing the universal exchange-correlation functional. In general, this functional is unknown and has to be approximated, e.g., by the local density approximation (LDA). For large classes of materials LDA gives accurate results. In strongly correlated materials, however, it can produce results which are even qualitatively wrong. We use the DFT to construct material specific Hubbard models, which are solved within DMFT. Despite their reduced complexity, such Hubbard models are only exactly solvable in certain limits like the non-interacting or atomic limit. With DMFT we solve the Hubbard model by a self-consistent mapping of the model to an impurity model, which is solved instead. The theory is formulated in terms of Green functions and self-energies, and it is the frequency dependence of the self-energy which gives the dynamical nature of the mean-field theory.

For the solution of impurity models various approaches have been developed. We employ the continuous-time quantum Monte Carlo (CT-QMC) solver of Refs. [1, 2]; this is described in chapter 3. Being the central part of DMFT, the CT-QMC solver is also the part of the program where most of the computation time is spend. The advantages of our CT-QMC implementation are that it can solve multi-orbital models with general on-site interaction matrices and that it is highly parallelized. After an overview over the CT-QMC method, we present our extension of the method, which is the calculation of two-particle Green functions.

The calculation of two-particle Green functions is significantly more difficult than the calculation of single-particle Green functions. We use the two-particle Green functions from

LDA+DMFT to construct response functions or susceptibilities. These susceptibilities give valuable insights into materials and can be used to determine the type of ordering, ordering temperature and bosonic excitation spectra. They bridge the gap between theory and experiments like nuclear magnetic resonance (NMR) or scattering experiments. Susceptibilities are the topic of chapter 4, where we construct lattice susceptibilities using the Bethe-Salpeter (BS) equation, and compare different basis to store and process susceptibilities effectively. Among different basis functions, the Legendre and a numerical basis prove to be very compact opposed to, e.g., Matsubara frequencies. In chapter 4 we describe also the use of these basis in the BS equation, which was implemented for supercomputers in the course of this work.
In chapter 5 and chapter 6 we make use of our implementation to investigate magnetism and orbital ordering in the layered perovskite K_2CuF_4 and study magnetism in high temperature superconducting cuprates, respectively.
Central for our investigations in chapter 5 are the static magnetic and orbital susceptibility, which are calculated for a two band Hubbard model. We compare the superexchange mechanism to orbital ordering because of Jahn-Teller distortions and find that superexchange alone cannot explain orbital ordering in K_2CuF_4. Furthermore, we identify a Zeeman-like term, which is absent in previously studied cubic perovskites like $KCuF_3$.
In chapter 6 we study static and dynamical susceptibilities for a Hubbard model representing high-temperature superconducting cuprates. We explore the role of different parameters in that model, including doping. At zero doping we investigate the Mott insulating regime, in the para- and antiferromagnetic (AFM) phase. For the latter the dynamical susceptibility shows spin-waves, which resemble experimental findings. For small doping close to the AFM phase we find similar results, which however change drastically when doping is increased. In the overdoped regime AFM order changes to ferromagnetic order. We end that chapter by showing bosonic excitation spectra for finite doping comparable to spin-waves at half-filling.

2 Solution of realistic models for correlated materials

In this chapter we describe methods to solve realistic models for strongly correlated systems. For this, we first construct a material-specific generalized Hubbard model using ab-initio methods, and later solve the model using the dynamical mean-field theory (DMFT) method.
The starting point is the general many-body Hamiltonian describing interactions between electrons and nuclei. In atomic units[1] and in the non-relativistic limit it is given by

$$\begin{aligned} H &= -\sum_j \frac{1}{2M_j}\nabla^2_{\mathbf{R}_j} - \frac{1}{2}\sum_i \nabla^2_{\mathbf{r}_i} + \frac{1}{2}\sum_{j\neq j'} \frac{Z_j Z_{j'}}{|\mathbf{R}_j - \mathbf{R}_{j'}|} - \sum_{ij} \frac{Z_j}{|\mathbf{R}_j - \mathbf{r}_i|} + \frac{1}{2}\sum_{i\neq i'} \frac{1}{|\mathbf{r}_i - \mathbf{r}_{i'}|} \\ &= T_n + T_e + V_{nn} + V_{ne} + V_{ee} \end{aligned}$$

with the kinetic energy of the nuclei T_n and electrons T_e and the Coulomb interactions V_{nn}, V_{ne} and V_{ee}. The vectors $\mathbf{R}_j$ give the positions of the N_n nuclei with masses M_j and atomic numbers Z_j; $\mathbf{r}_i$ are the positions of the N_e electrons. Because the mass of the electrons is much smaller than those of the nuclei, the movement of electrons and nuclei can be approximately separated. This is done in the Born-Oppenheimer approximation, in which the wave function is written as a product $\Psi(\{\mathbf{R}_j\},\{\mathbf{r}_i\}) = \psi(\{\mathbf{R}_j\},\{\mathbf{r}_i\})\phi(\{\mathbf{R}_j\})$. This leads to the electron Hamiltonian

$$H_e = T_e + V_{nn} + V_{ne} + V_{ee}, \tag{2.1}$$

where $\{\mathbf{R}_j\}$ are parameters, and the associated eigenvalue equation, $H_e\psi = E\psi$, for $\psi(\{\mathbf{R}_j\},\{\mathbf{r}_i\})$ only. Due to the Coulomb interaction term V_{ee}, this problem cannot be solved exactly in the general case. In this chapter we will introduce the state-of-the-art approximate solution schemes.

2.1 Building realistic ab-initio models

2.1.1 Density-functional theory

The density-functional theory is the state-of-the-art approach used to find the ground-state energy of (2.1). It relies on the Hohenberg-Kohn theorem [3], that says that the ground-state energy is a functional of the density $n(\mathbf{r})$. More specifically, it is the minimum of a

[1] In atomic units the electron mass m_e, electron charge e, Bohr radius a_B and $1/4\pi\epsilon_0$ are equal to 1.

functional

$$E[n(\mathbf{r})] = F[n(\mathbf{r})] + \int \mathrm{d}^3 r\, n(\mathbf{r}) v(\mathbf{r}). \tag{2.2}$$

Here, the potential $v(\mathbf{r})$ originates from $V_{nn} + V_{ne}$ and $F[n(\mathbf{r})] = T_e[n(\mathbf{r})] + V_{ee}[n(\mathbf{r})]$ is a functional of the kinetic and electron-electron interaction, independent of $v(\mathbf{r})$. The exact functional $F[n(\mathbf{r})]$ is universal but it is unknown.
Kohn and Sham showed that the problem can be rewritten in terms of a fictitious one-particle problem [4]. To this end, we rewrite the functional

$$F[n(\mathbf{r})] = T_0[n(\mathbf{r})] + \frac{1}{2} \int \mathrm{d}^3 r \int \mathrm{d}^3 r' \, \frac{n(\mathbf{r}) n(\mathbf{r}')}{|\mathbf{r} - \mathbf{r}'|} + E_{xc}[n(\mathbf{r})] \tag{2.3}$$

in terms of the kinetic energy of non-interacting electrons $T_0[n(\mathbf{r})]$, the Hartree term and the exchange-correlation energy functional $E_{xc}[n(\mathbf{r})]$. Minimizing (2.2) results in the condition

$$\begin{aligned} &\frac{\delta}{\delta n(\mathbf{r})} \left(E[n(\mathbf{r})] + \epsilon \left(N_e - \int \mathrm{d}^3 r\, n(\mathbf{r}) \right) \right) \\ &= \frac{\delta T_0[n(\mathbf{r})]}{\delta n(\mathbf{r})} + v(\mathbf{r}) + \int \mathrm{d}^3 r' \, \frac{n(\mathbf{r}')}{|\mathbf{r} - \mathbf{r}'|} + \frac{\delta E_{xc}[n(\mathbf{r})]}{\delta n(\mathbf{r})} - \epsilon \\ &= \frac{\delta T_0[n(\mathbf{r})]}{\delta n(\mathbf{r})} + v_{KS}(\mathbf{r}) - \epsilon = 0, \end{aligned} \tag{2.4}$$

where we used the constraint $N_e = \int \mathrm{d}^3 r\, n(\mathbf{r})$ and Lagrange multiplier ϵ. Equation (2.4) is the same one obtained for a non-interacting electron system with the potential

$$v_{KS}(\mathbf{r}) = v(\mathbf{r}) + \int \mathrm{d}^3 r' \, \frac{n(\mathbf{r}')}{|\mathbf{r} - \mathbf{r}'|} + v_{xc}(\mathbf{r}). \tag{2.5}$$

Here, $v_{xc}(\mathbf{r}) = \frac{\delta E_{xc}[n(\mathbf{r})]}{\delta n(\mathbf{r})}$. The Schrödinger equation of the non-interacting auxiliary problem

$$\left[-\frac{1}{2} \nabla^2 + v_{KS}(\mathbf{r}) \right] \varphi_i(\mathbf{r}) = \varepsilon_i \varphi_i(\mathbf{r}) \tag{2.6}$$

is the Kohn-Sham equation. The ground-state density of this auxiliary problem

$$n(\mathbf{r}) = \sum_{i=1}^{N_e} |\varphi_i(\mathbf{r})|^2 \tag{2.7}$$

is identical to the density of the original interacting problem.
The here presented steps are exact, but the exchange-correlation potential $v_{xc}(\mathbf{r})$ is in general not known. The simplest known approximation is the LDA (local-density approximation). In the LDA we approximate $v_{xc}(\mathbf{r})$ with its expression for the homogeneous electron gas, obtained numerically via QMC simulations. Then

$$E_{xc}^{\mathrm{LDA}}[n(\mathbf{r})] = \int \mathrm{d}^3 r\, n(\mathbf{r}) \epsilon_{xc}^{\mathrm{LDA}}(n(\mathbf{r})).$$

This approximation works well in many cases. For systems with strong local interaction, however, like the materials at the center of this thesis, the LDA gives even qualitatively wrong results. In this cases, we use the LDA only as a starting point to build material-specific many-body models.
In practical implementations, DFT calculations start with, e.g., an initial $n(\mathbf{r})$. This yields $v_{KS}(\mathbf{r})$, and defines the Kohn-Sham equation (2.6), whose solutions are the eigenenergies ε_i and eigenstates $\varphi_i(\mathbf{r})$. The eigenstates $\varphi_i(\mathbf{r})$ lead to a new density by (2.7), which is used to start a new iteration. The procedure is repeated until $n(\mathbf{r})$ converges.

2.1.2 Material-specific Hubbard models

To build a minimal material-specific many-body model, which contains correlation effects beyond the LDA approximation, we start with the LDA eigenfunctions $\varphi_i(\mathbf{r})$. For lattice periodic potentials $v_{KS}(\mathbf{r}) = v_{KS}(\mathbf{r}+\mathbf{T})$, where $\mathbf{T}$ is a lattice vector, the wave functions $\varphi_i(\mathbf{r})$ can be written as Bloch wave functions

$$\psi_{\mathbf{k}\alpha}(\mathbf{r}) = e^{i\mathbf{k}\mathbf{r}} u_{\alpha\mathbf{k}}(\mathbf{r})$$

with a lattice periodic $u_{\alpha\mathbf{k}}(\mathbf{r}) = u_{\alpha\mathbf{k}}(\mathbf{r}+\mathbf{T})$. The index $\alpha = (\sigma,s,m)$ represents spin index σ, site index s inside the unit cell and band index m; $\mathbf{k}$ is a momentum vector. From the Bloch wave functions we construct Wannier functions

$$\psi_{i\alpha}(\mathbf{r}) = \frac{1}{\sqrt{N_\mathbf{k}}} \sum_{\mathbf{k}} e^{-i\mathbf{k}\mathbf{T}_i} \psi_{\mathbf{k}\alpha}(\mathbf{r}),$$

which are localized at the lattice sites i. In this localized basis, the electron Hamiltonian (2.1) in second quantization is given by

$$H_e = H^{\mathrm{LDA}} + H^{\mathrm{U}} - H^{\mathrm{DC}} \tag{2.8}$$

$$H^{\mathrm{LDA}} = -\sum_{ii'} \sum_{\alpha\alpha'} t^{ii'}_{\alpha\alpha'} c^\dagger_{i,\alpha} c_{i',\alpha'} \tag{2.9}$$

$$H^{\mathrm{U}} = \frac{1}{2} \sum_{\substack{ii'\\ \tilde{i}\tilde{i}'}} \sum_{\substack{\alpha\alpha'\\ \tilde{\alpha}\tilde{\alpha}'}} U^{ii'\tilde{i}\tilde{i}'}_{\alpha\alpha'\tilde{\alpha}\tilde{\alpha}'} c^\dagger_{i,\alpha} c^\dagger_{i',\alpha'} c_{\tilde{i}',\tilde{\alpha}'} c_{\tilde{i},\tilde{\alpha}}. \tag{2.10}$$

This is a general multi-band Hubbard model. The LDA part (2.9) contains the crystal-field ($i = i'$) and the hopping ($i \neq i'$) parts with matrix elements

$$t^{ii'}_{\alpha\alpha'} = -\int \mathrm{d}^3 r\, \psi^*_{i\alpha}(\mathbf{r}) \left[-\frac{1}{2}\nabla^2 + v_{KS}(\mathbf{r})\right] \psi_{i'\alpha'}(\mathbf{r}).$$

The Coulomb interaction (2.10) contains the tensor

$$U^{ii'\tilde{i}\tilde{i}'}_{\alpha\alpha'\tilde{\alpha}\tilde{\alpha}'} = \int \mathrm{d}^3 r \int \mathrm{d}^3 r'\, \psi^*_{i\alpha}(\mathbf{r}) \psi^*_{i'\alpha'}(\mathbf{r}') \frac{1}{|\mathbf{r}-\mathbf{r}'|} \psi_{\tilde{i}'\tilde{\alpha}'}(\mathbf{r}') \psi_{\tilde{i}\tilde{\alpha}}(\mathbf{r}).$$

Finally, H^{DC} in (2.8) is the double-counting correction, which subtracts the parts of the Coulomb interaction (2.10) contained already in the LDA term (2.9).

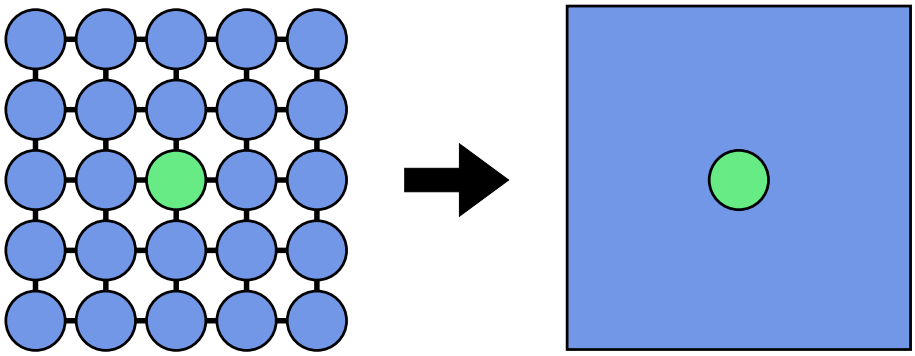

Figure 2.1: In DMFT, the lattice model is mapped onto an impurity model. The impurity is coupled to a self-consistent determined bath, which describes the other sites as mean-field.

The Hamiltonian in second quantization is identical to (2.1), and therefore impossible to solve in the general case. However, to study low-energy properties of given materials it is often sufficient to consider only the states close to the Fermi level. Therefore, we downfold the LDA Hamiltonian to an effective Hamiltonian with states in an energy window around the Fermi level. Information on the downfolding and various localized basis are given in Ref. [5] and [6].
Finally, the difference $H^{\mathrm{U}} - H^{\mathrm{DC}}$ is almost local and is replaced by

$$H^{\mathrm{U}}_{\mathrm{loc}} - H^{\mathrm{DC}}_{\mathrm{loc}} = \frac{1}{2} \sum_i \sum_{\substack{\alpha\alpha' \\ \tilde{\alpha}\tilde{\alpha}'}} \tilde{U}^i_{\alpha\alpha'\tilde{\alpha}\tilde{\alpha}'} c^\dagger_{i,\alpha} c^\dagger_{i,\alpha'} c_{i,\tilde{\alpha}'} c_{i,\tilde{\alpha}} - H^{\mathrm{DC}}_{\mathrm{loc}}.$$

This is due to the fact that the average effect of the long-range Hartree interaction and of the mean-field exchange-correlation potential are included in the LDA. The screened Coulomb interaction tensor $\tilde{U}^i_{\alpha\alpha'\tilde{\alpha}\tilde{\alpha}'}$ is strongly reduced with respect to $U^{ii'\tilde{i}\tilde{i}'}_{\alpha\alpha'\tilde{\alpha}\tilde{\alpha}'}$.[2]

2.2 Solution of realistic models

2.2.1 Dynamical mean-field theory

The dynamical mean-field theory (DMFT) is a powerful approach for the solution of Hubbard-like models. It is based on the works of Metzner, Vollhardt [7], Müller-Hartmann [8], Georges, Kotliar [9,10] and Jarrell [11,12]. The core idea consists in the mapping of the lattice problem onto an effective impurity model, which is solved self-consistently. While local interactions on one lattice site are fully taken into account, the other sites are treated as an effective bath, the dynamical mean-field.

[2] We give details on $\tilde{U}^i_{\alpha\alpha'\tilde{\alpha}\tilde{\alpha}'}$ for a specific material class in chapter 5.

In the last section we defined a general Hubbard model

$$H_{\mathrm{Hub}} = -\sum_{ii'}\sum_{\alpha\alpha'} t^{ii'}_{\alpha\alpha'} c^\dagger_{i,\alpha} c_{i',\alpha'} + \frac{1}{2}\sum_i \sum_{\substack{\alpha\alpha'\\ \tilde\alpha\tilde\alpha'}} \tilde U^i_{\alpha\alpha'\tilde\alpha\tilde\alpha'} c^\dagger_{i,\alpha} c^\dagger_{i,\alpha'} c_{i,\tilde\alpha'} c_{i,\tilde\alpha} - H^{\mathrm{DC}}_{\mathrm{loc}} - \mu \sum_i \sum_\alpha c^\dagger_{i,\alpha} c_{i,\alpha}. \tag{2.11}$$

The indices i name lattice sites. The indices $\alpha = (\sigma,s,m)$ are compounds of the spin index σ, the band index m and the site s inside the unit cell. It is convenient to include the chemical potential μ and the total number of particles $\sum_{i\alpha} c^\dagger_{i,\alpha} c_{i,\alpha}$ in the Hamiltonian.

Metzner, Vollhardt [7] and Müller-Hartmann [8] described the simplification of perturbation theory in infinite dimensions $d \to \infty$ or more precisely the limit of infinite coordination number $z \to \infty$. Since the hopping parameter $t^{ii'}_{\alpha\alpha'}$ is scaled by the coordination number the diagrams in perturbation theory become local in the infinite coordination number limit. In particular, the self-energy is purely local

$$\lim_{z\to\infty} \Sigma^{\alpha\alpha'}_{ii'}(i\nu_n) = \delta_{i,i'} \Sigma^{\alpha\alpha'}_{ii}(i\nu_n),$$

which means it is constant in momentum space

$$\lim_{z\to\infty} \Sigma^{\alpha\alpha'}_{\mathbf{k}}(i\nu_n) = \Sigma_{\alpha\alpha'}(i\nu_n).$$

However, it is a dynamic quantity depending on the frequency $i\nu_n$. The self-energy is the term in the lattice Green function[3]

$$G^{\alpha\alpha'}_{\mathbf{k}}(i\nu_n) = \left[i\nu_n \mathbb{1} - \epsilon_{\mathbf{k}} - H^{\mathrm{DC}}_{\mathrm{loc}} - \Sigma(i\nu_n)\right]^{-1}_{\alpha\alpha'}, \tag{2.12}$$

which accounts for Coulomb interaction effects.[4] In addition, the lattice Green function depends on $\epsilon^{\alpha\alpha'}_{\mathbf{k}}$, which is the Fourier transform of $t^{ii'}_{\alpha\alpha'}$. The chemical potential μ is included for convenience in the self-energy. The local Green function $G_{\alpha\alpha'}(i\nu_n) = G^{\alpha\alpha'}_{ii}(i\nu_n)$ is given by the momentum sum

$$G_{\alpha\alpha'}(i\nu_n) = \frac{1}{N_{\mathbf{k}}} \sum_{\mathbf{k}} G^{\alpha\alpha'}_{\mathbf{k}}(i\nu_n). \tag{2.13}$$

This is the Green function for one site i of the lattice. Because of the local nature of the self-energy there exists an impurity model

$$H_{\mathrm{imp}} = H_{\mathrm{loc}} + H_{\mathrm{bath}} + H_{\mathrm{mix}},$$

[3] Details on Green functions are given in chapter 4.

[4] Here $\epsilon_{\mathbf{k}}$, $H^{\mathrm{DC}}_{\mathrm{loc}}$ and $\Sigma(i\nu_n)$ are matrices in the indices α and α'. The subscripts α and α' at the braces $[\cdots]^{-1}$ mean that we first invert the matrix and afterwards choose the entries from the result according to the subscripts.

for which the impurity Green function $G^{\mathrm{imp}}_{\alpha\alpha'}(i\nu_n)$ is equal to the local Green function (2.13). The individual contributions of the impurity model are given by

$$\begin{aligned} H_{\mathrm{loc}} &= \sum_{\alpha\alpha'} \epsilon_{\alpha\alpha'} c^\dagger_\alpha c_{\alpha'} + \frac{1}{2} \sum_{\substack{\alpha\alpha' \\ \tilde{\alpha}\tilde{\alpha}'}} U_{\alpha\alpha'\tilde{\alpha}\tilde{\alpha}'} c^\dagger_\alpha c^\dagger_{\alpha'} c_{\tilde{\alpha}'} c_{\tilde{\alpha}} - \mu \sum_\alpha c^\dagger_\alpha c_\alpha \\ H_{\mathrm{bath}} &= \sum_{\mathbf{k}} \sum_{\gamma\gamma'} \epsilon^d_{\mathbf{k}\gamma\gamma'} d^\dagger_{\mathbf{k}\gamma} d_{\mathbf{k}\gamma'} \\ H_{\mathrm{mix}} &= \sum_{\mathbf{k}} \sum_{\alpha\gamma} \left(V_{\mathbf{k}\alpha\gamma} c^\dagger_\alpha d_{\mathbf{k}\gamma} + V^*_{\mathbf{k}\alpha\gamma} d^\dagger_{\mathbf{k}\gamma} c_\alpha \right). \end{aligned}$$

Here, the tensor $U_{\alpha\alpha'\tilde{\alpha}\tilde{\alpha}'}$ is the same as in (2.11), and $\epsilon_{\alpha\alpha'}$ is the crystal-field $t^{ii'}_{\alpha\alpha'}$ with $i = i'$. The operator $c^\dagger_\alpha$ (c_α) creates (annihilates) an electron on the impurity with flavor α. The operator $d^\dagger_{\mathbf{k}\gamma}$ ($d_{\mathbf{k}\gamma}$) creates (annihilates) a bath electron with flavor γ and momentum $\mathbf{k}$. The parameters $\epsilon^d_{\mathbf{k}\gamma\gamma'}$ and $V_{\mathbf{k}\alpha\gamma}$ have to be chosen such that $G^{\mathrm{imp}}_{\alpha\alpha'}(i\nu_n) = G_{\alpha\alpha'}(i\nu_n)$ from (2.13). This mapping from the lattice to the impurity model is at the center of DMFT. However, if we solve the impurity problem with CT-QMC, instead of determining the parameters $\epsilon^d_{\mathbf{k}\gamma\gamma'}$ and $V_{\mathbf{k}\alpha\gamma}$ directly, we work with Green functions. The impurity Green function is given by

$$G^{\mathrm{imp}}_{\alpha\alpha'}(i\nu_n) = \left[i\nu_n \mathbb{1} - \epsilon - F(i\nu_n) - \Sigma(i\nu_n) \right]^{-1}_{\alpha\alpha'},$$

where $F(i\nu_n)$ is the hybridization function matrix

$$F_{\alpha\alpha'}(i\nu_n) = \frac{1}{N_{\mathbf{k}}} \sum_{\mathbf{k}} \sum_{\gamma\gamma'} \frac{V_{\mathbf{k}\alpha\gamma} V^*_{\mathbf{k}\alpha'\gamma'}}{i\nu_n - \epsilon^d_{\mathbf{k}\gamma\gamma'}}. \tag{2.14}$$

The parameters $\epsilon^d_{\mathbf{k}\gamma\gamma'}$ and $V_{\mathbf{k}\alpha\gamma}$ enter only through the hybridization function. The non-interacting part of the impurity Green function is the bath Green function

$$G^0_{\alpha\alpha'}(i\nu_n) = \left[i\nu_n \mathbb{1} - \epsilon - F(i\nu_n) \right]^{-1}_{\alpha\alpha'}. \tag{2.15}$$

The impurity and bath Green function matrix as well as the self-energy matrix are related by the local Dyson equation

$$G(i\nu_n) = G^0(i\nu_n) + G^0(i\nu_n)\Sigma(i\nu_n)G(i\nu_n). \tag{2.16}$$

In the limit of infinite coordination number DMFT is exact. For finite coordination number it is an approximation.

In practice, we use the following algorithm:

1. Initialize the self-energy $\Sigma_{\alpha\alpha'}(i\nu_n)$.
2. Construct the local Green function $G(i\nu_n)$ using (2.13), where the lattice Green function $G_k(i\nu_n)$ is given by (2.12).
3. Use the Dyson equation to calculate the bath Green function

$$G^0(i\nu_n) = \left[G(i\nu_n)^{-1} + \Sigma(i\nu_n) \right]^{-1}.$$

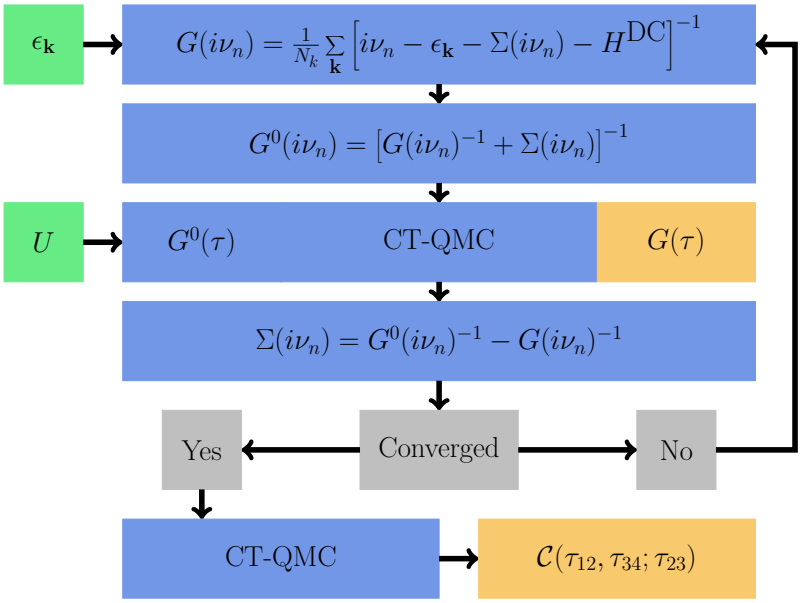

Figure 2.2: Calculation of the single-particle Green function using DMFT. The two-particle Green function is calculated from the impurity model after the self-energy is converged.

4. Solve the impurity problem using a solver with the bath Green function $G^0(i\nu_n)$ and the Coulomb matrix $U_{\alpha\alpha'\tilde{\alpha}\tilde{\alpha}'}$ as input and the local Green function $G(i\nu_n)$ as output.

5. Use the Dyson equation to obtain the self-energy

$$\Sigma(i\nu_n) = G^0(i\nu_n)^{-1} - G(i\nu_n)^{-1}.$$

6. If $\Sigma(i\nu_n)$ is not converged, repeat all steps starting from 2. with the new $\Sigma(i\nu_n)$.

2.2.2 Susceptibility calculations in DMFT

Within the DMFT approach the calculation of lattice susceptibilities $\chi(\mathbf{q},i\omega_m)$ can be reduced to calculations of two-particle impurity Green functions.[5]
The perturbation expansion of the susceptibility $\chi(\mathbf{q},i\omega_m)$ in terms of the bare susceptibility $\chi^0(\mathbf{q},i\omega_m)$ and the vertex function $\Gamma(\mathbf{q},i\omega_m)$ is the Bethe-Salpeter equation

$$\chi_{\bar{k}\bar{k}'}(\bar{q}) = \chi^0_{\bar{k}\bar{k}'}(\bar{q}) + \frac{1}{(\beta N_{\mathbf{k}})^2}\sum_{\bar{\kappa}\bar{\kappa}'}\chi^0_{\bar{k}\bar{\kappa}'}(\bar{q})\Gamma_{\bar{\kappa}\bar{\kappa}'}(\bar{q})\chi_{\bar{\kappa}\bar{k}'}(\bar{q})$$

with the indices $\bar{q} = (\mathbf{q},i\omega_m)$, $\bar{k} = (\mathbf{k},i\nu_n,\alpha,\alpha')$ and $\bar{k}' = (\mathbf{k}',i\nu_{n'},\gamma,\gamma')$, and the summation indices $\bar{\kappa}$ and $\bar{\kappa}'$. Here, ν_n is a fermionic and ω_m a bosonic Matsubara frequency. The Bethe-Salpeter equation (BSEQ) is the two-particle function equivalent of the Dyson equation (2.16).

[5]Details of the procedure are given in section 4.4.1.

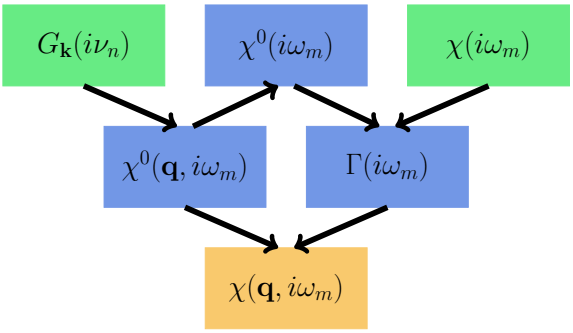

Figure 2.3: Calculation of the lattice susceptibility using the Bethe-Salpeter equation and local results from DMFT.

The bare susceptibility $\chi^0(\mathbf{q},i\omega_m)$ is determined by the lattice Green function $G^{\alpha\alpha'}_{\mathbf{k}}(i\nu_n)$. In the local vertex approximation $\Gamma(\mathbf{q},i\omega_m)$ is replaced by its local form $\Gamma(i\omega_m)$. By summation over all momenta we obtain the local BSEQ

$$\chi_{\bar{n}\bar{n}'}(i\omega_m) = \chi^0_{\bar{n}\bar{n}'}(i\omega_m) + \frac{1}{\beta^2}\sum_{\bar{\eta}\bar{\eta}'} \chi^0_{\bar{n}\bar{\eta}'}(i\omega_m)\Gamma_{\bar{\eta}\bar{\eta}'}(i\omega_m)\chi_{\bar{\eta}\bar{n}'}(i\omega_m)$$

with the indices $\bar{n} = (i\nu_n,\alpha,\alpha')$ and $\bar{n}' = (i\nu_{n'},\gamma,\gamma')$. Here, we retain only the frequency and flavor dependency.
The bare local susceptibility $\chi^0(i\omega_m)$ is the momentum summed $\chi^0(\mathbf{q},i\omega_m)$. If we know the local susceptibility $\chi(i\omega_m)$, the local $\Gamma(i\omega_m)$ can then be obtained by inversion of the local BSEQ. In the limit $z \to \infty$ the local susceptibility $\chi(i\omega_m)$ equals the impurity susceptibility, which depends on the single- and two-particle Green function of the impurity model. These Green functions are obtained by the impurity solver.[6]

2.2.3 Practical implementation of LDA+DMFT

The input of DMFT calculations are the matrix $\epsilon^{\alpha\alpha'}_{\mathbf{k}}$, the tensor $\tilde{U}^i_{\alpha\alpha'\tilde{\alpha}\tilde{\alpha}'}$ and the matrix $H^{\mathrm{DC}}_{\mathrm{loc}}$. The dispersion of the non-interacting electrons $\epsilon^{\alpha\alpha'}_{\mathbf{k}}$ is obtained via material-specific DFT-based calculations. The theoretical determination of the screened Coulomb interaction $\tilde{U}^i_{\alpha\alpha'\tilde{\alpha}\tilde{\alpha}'}$ from first principles is in general difficult. Depending on the material, the tensor can be reduced to a few parameters, which can often be chosen guided by experiments or calculated, e.g., in the constrained random-phase approximation (cRPA) [13]. The double-counting correction is often approximated to the mean-field value of $\tilde{U}^i_{\alpha\alpha'\tilde{\alpha}\tilde{\alpha}'}$. For the problems considered in this thesis it is merely a shift of the chemical potential, since we include only correlated electrons in the models.

A central component of DMFT is the impurity solver. In this work we use the continuous-time quantum Monte Carlo (CT-QMC) solver described in the next chapter. Besides the parameters $\epsilon_{\alpha\alpha'}$ and $\tilde{U}^i_{\alpha\alpha'\tilde{\alpha}\tilde{\alpha}'}$, it requires the hybridization function $F_{\alpha\alpha'}(\tau)$ as input. For this, we calculate the inverse Fourier transformation of $F_{\alpha\alpha'}(i\nu_n)$ (2.14), which is obtained

[6] Details of the measurement Green functions in the CT-QMC are given in the next chapter.

from the bath Green function $G^0_{\alpha\alpha'}(i\nu_n)$ as

$$F_{\alpha\alpha'}(i\nu_n) = i\nu_n - \epsilon_{\alpha\alpha'} - \left[G^0(i\nu_n)\right]^{-1}_{\alpha\alpha'}. \tag{2.17}$$

So far we considered for simplicity lattice models with one site per unit cell. In realistic cases, we however solve models with multiple equivalent sites per unit cell with index s in the Hamiltonian (2.11). The lattice Green function (2.12) is calculated with

$$G^{\sigma sm,\sigma' s' m'}_{\mathbf{k}}(i\nu_n) = \left[i\nu_n \mathbb{1} - \epsilon_{\mathbf{k}} - H^{\mathrm{DC}}_{\mathrm{loc}} - \Sigma(i\nu_n)\right]^{-1}_{\sigma sm,\sigma' s' m'} \tag{2.18}$$

and the local Green function is the on-site term

$$G_{\sigma m,\sigma' m'}(i\nu_n) = \frac{1}{N_{\mathbf{k}}} \sum_{\mathbf{k}} G^{\sigma sm,\sigma' sm'}_{\mathbf{k}}(i\nu_n).$$

The last two equations are used in the second step of the DMFT algorithm. The other steps in the DMFT self-consistency loop do not change when increasing the number of sites per unit cell. In the paramagnetic phase, or if the spins of multiple sites align in parallel, the self-energy matrix for (2.18) is

$$\Sigma_{s\sigma m,s'\sigma' m'}(i\nu_n) = \delta_{s,s'} \Sigma_{\sigma m,\sigma' m'}(i\nu_n). \tag{2.19}$$

For antiferromagnetism, neighboring sites have spins aligning antiparallel, however. Thus

$$\Sigma_{s\sigma m,s'\sigma' m'}(i\nu_n) = (-1)^{\sigma+\sigma'} \delta_{s,s'} \Sigma_{-\sigma m,-\sigma' m'}(i\nu_n).$$

Here, $\sigma \in \{\uparrow = 0, \downarrow = 1\}$, $-\uparrow = \downarrow$ and $-\downarrow = \uparrow$.

Once the DMFT iteration converged, we solve the impurity model one more time to calculate the local two-particle Green function. We then obtain the lattice susceptibility via the Bethe-Salpeter equation in the local vertex approximation.

3 Continuous-time quantum Monte Carlo impurity solver

The numerically most challenging step in the DMFT method described in the previous chapter is to solve the quantum impurity model. In this chapter, we introduce the continuous-time quantum Monte Carlo (CT-QMC) solver for this task.
Following the notation and derivation of Refs. [1, 2], we split the Hamiltonian of the impurity model into a bath part, a local part and a term mixing both

$$H_{\text{imp}} = H_{\text{loc}} + H_{\text{bath}} + H_{\text{mix}}, \tag{3.1}$$

where the different parts are given by

$$H_{\text{loc}} = \sum_{\alpha\alpha'} \epsilon_{\alpha\alpha'} c^\dagger_\alpha c_{\alpha'} + \frac{1}{2} \sum_{\substack{\alpha\alpha' \\ \tilde{\alpha}\tilde{\alpha}'}} U_{\alpha\alpha'\tilde{\alpha}\tilde{\alpha}'} c^\dagger_\alpha c^\dagger_{\alpha'} c_{\tilde{\alpha}'} c_{\tilde{\alpha}} - \mu \sum_\alpha c^\dagger_\alpha c_\alpha \tag{3.2}$$

$$H_{\text{bath}} = \sum_\gamma H^\gamma_{\text{bath}} = \sum_p \sum_\gamma \epsilon_{p\gamma} d^\dagger_{p\gamma} d_{p\gamma} \tag{3.3}$$

$$H_{\text{mix}} = \sum_p \sum_{\alpha\gamma} \left(V_{p\alpha\gamma} c^\dagger_\alpha d_{p\gamma} + V^*_{p\alpha\gamma} d^\dagger_{p\gamma} c_\alpha \right). \tag{3.4}$$

The bath Hamiltonian describes non-interacting fermionic particles. For the moment, for simplicity, we assume that H_{bath} is diagonal in the flavors γ. Later we will show that the results do not depend on this assumption. The operators $d^\dagger_{p\gamma}$ ($d_{p\gamma}$) create (annihilate) bath electrons with momentum p and flavor γ; the latter is a shortcut for band index and spin σ.
The local Hamiltonian describes a multi-orbital impurity. The operators $c^\dagger_\alpha$ (c_α) create (annihilate) particles at the impurity site with flavor α, shortcut for orbital m and spin σ. Impurity electrons interact with each other via the on-site Coulomb tensor $U_{\alpha\alpha'\tilde{\alpha}\tilde{\alpha}'}$. We include the chemical potential μ term into H_{loc} for convenience.
The term H_{mix} describes the hybridization between bath and impurity. In the absence of the coupling, H_{loc} and H_{bath} can both be solved exactly, in the case of H_{loc} at least for a small number of orbitals. In the presence of H_{mix} the problem can still be solved, but we need advanced numerical techniques.
This chapter presents the continuous-time quantum Monte Carlo (CT-QMC) solver in its hybridization expansion form [14–16] for multi-orbital models with general local interactions [1, 2], and explains how we use it to calculate expectation values and Green functions.

3.1 Quantum Monte Carlo solvers

Our aim is to calculate an expectation value in the grand canonical ensemble

$$\langle O \rangle = \mathrm{Tr}\left[\rho O\right] = \frac{1}{\mathcal{Z}} \mathrm{Tr}\left[e^{-\beta H} O\right]$$

for an operator O, for example a Green function G, where we included in the Hamiltonian H the term μN, with the chemical potential μ and the particle number operator $N = \sum_\alpha c_\alpha^\dagger c_\alpha$. The factor $\beta = 1/k_B T$, with $k_B \approx 8.6173 \times 10^{-5}\,\mathrm{eV\,K^{-1}}$ being the Boltzmann constant, is the inverse temperature. Finally, $\mathcal{Z}$ is the partition function

$$\mathcal{Z} = \mathrm{Tr}\left[e^{-\beta H}\right]. \tag{3.5}$$

The trace $\mathrm{Tr}[\cdots] = \sum_x \langle x| \cdots |x\rangle$ is a sum over all basis states $|x\rangle$ in Fock space.
In general, the partition function has the form $\mathcal{Z} = \sum_x p(x)$ and the expectation value $\langle O \rangle$ is a weighted average

$$\langle O \rangle = \sum_x \frac{p(x)}{\mathcal{Z}} O(x) = \frac{\sum_x p(x) O(x)}{\sum_x p(x)}.$$

In this form, one can see that $p(x)/\mathcal{Z}$ can be viewed as a probability. The idea of the Monte Carlo (MC) method is to approximate the full sum over x by a sum over a finite set of sample configurations x_c. If we choose N_c samples x_c randomly with the probability $p(x_c)$, we can approximate the average by

$$\langle O \rangle \approx \frac{1}{N_c} \sum_{c=1}^{N_c} O(x_c). \tag{3.6}$$

In quantum Monte Carlo (QMC) the probability $p(x)$ is replaced by a weight $w(x)$, which can, however, be negative. To still use the MC method, we take the absolute value of the weights as probabilities $p(x) = |w(x)|$ and include the sign of the weights into the operator O. The partition function is then given by

$$\mathcal{Z} = \sum_x \mathrm{sign}(w(x)) |w(x)| \tag{3.7}$$

and the average of an operator O is

$$\langle O \rangle = \frac{\sum_x |w(x)| \mathrm{sign}(w(x)) O(x)}{\sum_x |w(x)| \mathrm{sign}(w(x))} = \frac{\langle \mathrm{sign}(w(x)) O(x) \rangle}{\langle \mathrm{sign}(w(x)) \rangle}.$$

This is approximated by

$$\langle O \rangle \approx \frac{\sum_c \mathrm{sign}(w(x_c)) O(x_c)}{\sum_c \mathrm{sign}(w(x_c))}. \tag{3.8}$$

The so called "sign problem" occurs when the denominator of equation (3.8) becomes very small. Fortunately, the sign problem for impurity problems with few orbitals is typically not severe; however, it becomes worse for many orbital models and at low temperature.

The choice of the sample configurations x_c according to the probability $p(x)$, without prior knowledge of $p(x)$, is done by the Metropolis-Hastings algorithm [17,18]. The configuration space is sampled by a Markov chain process. A Markov chain is constructed step by step proposing new configurations x, where the probability for the next configuration x' depends only on the actual configuration x. A proper Markov chain process needs to be ergodic and have a stationary state. This can be achieved for example by the detailed balance condition

$$p(x)p(x \to x') = p(x')p(x' \to x).$$

Here, $p(x \to x')$ is the transition probability to go from configuration x to x', and $p(x)$ the probability to sample. Splitting the transition probability

$$p(x \to x') = p_{\text{prop}}(x \to x')p_{\text{acc}}(x \to x')$$

into proposal and acceptance probability, the detailed balance condition is fulfilled by the Metropolis-Hastings condition

$$p_{\text{acc}}(x \to x') = \min\left(\frac{p(x')}{p(x)}\frac{p_{\text{prop}}(x' \to x)}{p_{\text{prop}}(x \to x')}, 1\right). \tag{3.9}$$

In the QMC $p(x) = |w(x)|$. In practice, the procedure is the following. We pick a new configuration x' randomly with the known probabilities $p_{\text{prop}}(x' \to x)$ and $p_{\text{prop}}(x \to x')$. Then, we calculate $|w(x')|/|w(x)|$ and $p_{\text{acc}}(x \to x')$. We choose a random number $r \in [0,1[$ and accept the new configuration x' if $r < p_{\text{acc}}(x \to x')$. If x' is accepted, we set $x = x'$, otherwise x does not change. This process is repeated N_c times. The statistical error σ of the result $\langle O \rangle$ decreases by $1/\sqrt{N_c}$ for all MC algorithms.
The remaining task is to derive $w(x)$, which we do in the next section.

3.2 Hybridization expansion of partition function

To identify the weights $w(x)$ in (3.7) we expand the partition function (3.5) in a perturbation series. We start by inserting the time-evolution operator of the interaction picture $U^I(\beta)$ into the partition function (3.5)

$$\begin{aligned}\mathcal{Z} &= \text{Tr}\left[U^I(\beta)e^{-\beta H_0}\right] \\ &= \sum_{n=0}^{\infty}\frac{(-1)^n}{n!}\int_0^\beta \mathrm{d}\tau_1 \int_0^\beta \mathrm{d}\tau_2 \cdots \int_0^\beta \mathrm{d}\tau_n \,\text{Tr}\left[\mathcal{T}e^{-H_0\beta}H_1^I(\tau_1)H_1^I(\tau_2)\cdots H_1^I(\tau_n)\right].\end{aligned} \tag{3.10}$$

The expansion here is done in the hybridization, i.e.,

$$H_1 = H_{\text{mix}}.$$

Operators evolve in time via

$$H_0 = H_{\text{loc}} + H_{\text{bath}}.$$

We split the perturbation $H_{\mathrm{mix}} = H_1^{c^\dagger} + H_1^c$ into a part containing only local annihilation operators c_α

$$H_1^c = \sum_{p\alpha\gamma} V^*_{p\alpha\gamma} d^\dagger_{p\gamma} c_\alpha$$

and a part $H_1^{c^\dagger} = [H_1^c]^\dagger$ containing only local creation operators $c^\dagger_\alpha$. The terms inside the trace can then be written as

$$\mathrm{Tr}\left[\mathcal{T} e^{-\beta H_0} (H_1^{c^\dagger}(\tau_1) + H_1^c(\tau_1)) \cdots (H_1^{c^\dagger}(\tau_n) + H_1^c(\tau_n))\right].$$

Performing the multiplication yields a sum of different products of $H_1^{c^\dagger}$ and H_1^c. Because H_0 does not change particle numbers, only products with equal numbers of c_α and $c^\dagger_\alpha$ contribute to the trace. We will indicate the imaginary times of terms of type $H_1^{c^\dagger}$ with τ'_n and of terms of type H_1^c with τ_n. Due to the time-ordering operator, we can also change the order and integration boundaries. These steps allow us to obtain a simpler expression

$$\begin{aligned}\mathcal{Z} = \sum_{n=0}^{\infty} \int_0^\beta \mathrm{d}\tau_1 \cdots \int_{\tau_{n-1}}^\beta \mathrm{d}\tau_n \int_0^\beta \mathrm{d}\tau'_1 \cdots \int_{\tau'_{n-1}}^\beta \mathrm{d}\tau'_n \times \\ \times \mathrm{Tr}\left[\mathcal{T} e^{-\beta H_0} H_1^{c^\dagger}(\tau'_1) H_1^c(\tau_1) \cdots H_1^{c^\dagger}(\tau'_n) H_1^c(\tau_n)\right].\end{aligned}$$

At this point, we insert H_0 and H_1 explicitly. Because the two Hamiltonians H_{loc} and H_{bath} commute, $e^{-\beta H_0} = e^{-\beta H_{\mathrm{loc}}} e^{-\beta H_{\mathrm{bath}}}$, and we separate the local and bath operators in the trace. This gives the partition function expansion

$$\begin{aligned}\mathcal{Z} = \sum_{n=0}^{\infty} \int_0^\beta \mathrm{d}\tau_1 \cdots \int_{\tau_{n-1}}^\beta \mathrm{d}\tau_n \int_0^\beta \mathrm{d}\tau'_1 \cdots \int_{\tau'_{n-1}}^\beta \mathrm{d}\tau'_n \sum_{\substack{p_1\cdots p_n \\ p'_1\cdots p'_n}} \sum_{\substack{\alpha_1\cdots\alpha_n \\ \alpha'_1\cdots\alpha'_n}} \sum_{\substack{\gamma_1\cdots\gamma_n \\ \gamma'_1\cdots\gamma'_n}} \times \\ \times \prod_{i=1}^n V_{p'_i\alpha'_i\gamma'_i} V^*_{p_i\alpha_i\gamma_i} \mathrm{Tr}\left[\mathcal{T} e^{-\beta H_{\mathrm{bath}}} \prod_{i=1}^n d^\dagger_{p_i\gamma_i}(\tau_i) d_{p'_i\gamma'_i}(\tau'_i)\right] \times \\ \times \mathrm{Tr}\left[\mathcal{T} e^{-\beta H_{\mathrm{loc}}} \prod_{i=1}^n c_{\alpha_i}(\tau_i) c^\dagger_{\alpha'_i}(\tau'_i)\right].\end{aligned}$$

The calculation of the local trace is the topic of the next two sections. Here, we focus on the trace over the bath operators and use the notation $\langle O\rangle_{\mathrm{bath}} = \mathrm{Tr}\left[e^{-\beta H_{\mathrm{bath}}}/\mathcal{Z}_{\mathrm{bath}} O\right]$ for the expectation value of bath operators O. We can calculate this expectation value analytically because the bath Hamiltonian is non-interacting. Wick's theorem allows us to write the expectation value of a product of operators as product of expectation values

$$\langle \prod_{i=1}^n d^\dagger_i d_i \rangle_{\mathrm{bath}} = \prod_{i=1}^n \sum_{\pi\in S_n} \mathrm{sign}(\pi) \langle d^\dagger_i d_{\pi(i)} \rangle_{\mathrm{bath}},$$

where π is an element of the permutation group of n elements S_n. If π is equivalent to an even (odd) number of pairwise permutations, its sign is positive (negative). Each of the resulting expectation values is a single-particle Green function

$$G_{p'_{\pi(i)}\gamma'_{\pi(i)} p_i\gamma_i}(\tau'_{\pi(i)}, \tau_i) = \langle \mathcal{T} d^\dagger_{p_i\gamma_i}(\tau_i) d_{p'_{\pi(i)}\gamma'_{\pi(i)}}(\tau'_{\pi(i)}) \rangle_{\mathrm{bath}}.$$

However, here we are interested in the hybridization function. This is given by

$$\begin{aligned} F_{\alpha'\alpha}(\tau'-\tau) &= \sum_{pp'}\sum_{\gamma\gamma'} V_{p'\alpha'\gamma'}V^*_{p\alpha\gamma}G_{p'\gamma'p\gamma}(\tau',\tau) \\ &= \sum_{p}\sum_{\gamma} \frac{V_{p\alpha'\gamma}V^*_{p\alpha\gamma}}{1+e^{-\beta\epsilon_{p\gamma}}} \begin{cases} e^{-\epsilon_{p\gamma}(\beta-(\tau-\tau'))} & \text{if } \tau > \tau' \\ -e^{-\epsilon_{p\gamma}(\tau'-\tau)} & \text{if } \tau < \tau' \end{cases}. \end{aligned}$$

It is convenient to use the inverse hybridization function matrix

$$M^{-1}_{ij} = F_{\alpha'_i\alpha_j}(\tau'_i - \tau_j).$$

In appendix A.1 we show that it is more efficient to store M instead of M^{-1} in actual calculations. This allows us to write the sum over different permutations as determinant of M^{-1} in the partition function

$$\begin{aligned} \mathcal{Z} = \mathcal{Z}_{\text{bath}} \sum_{n=0}^{\infty} \int_0^\beta \mathrm{d}\tau_1 \cdots \int_{\tau_{n-1}}^\beta \mathrm{d}\tau_n \int_0^\beta \mathrm{d}\tau'_1 \cdots \int_{\tau'_{n-1}}^\beta \mathrm{d}\tau'_n \sum_{\substack{\alpha_1\cdots\alpha_n \\ \alpha'_1\cdots\alpha'_n}} \times \\ \times \det M^{-1} \operatorname{Tr}\left[\mathcal{T} e^{-\beta H_{\text{loc}}} \prod_{i=1}^{n} c_{\alpha_i}(\tau_i) c^\dagger_{\alpha'_i}(\tau'_i)\right]. \end{aligned}$$

Although in the derivation above we assumed that the hybridization function $F_{\alpha'_i\alpha_j}(\tau'_i-\tau_j)$ is diagonal in the bath flavors, this is not necessary. If the bath Hamiltonian is not diagonal, it can always be rotated to a diagonal form with a unitary transformation. For a non-diagonal bath with energies $\tilde{\epsilon}_{p\tilde{\gamma}\tilde{\gamma}'}$ and a coupling strength $\tilde{V}_{p\alpha\tilde{\gamma}}$ the hybridization function then becomes[1]

$$F_{\alpha'\alpha}(\tau'-\tau) = \sum_{p}\sum_{\tilde{\gamma}\tilde{\gamma}'} \tilde{V}_{p\alpha'\tilde{\gamma}'}\tilde{V}^*_{p\alpha\tilde{\gamma}} \begin{cases} \left(\frac{e^{-\tilde{\epsilon}_p(\beta-(\tau-\tau'))}}{1+e^{-\beta\tilde{\epsilon}_p}}\right)_{\tilde{\gamma}'\tilde{\gamma}} & \text{if } \tau > \tau' \\ \left(\frac{-e^{-\tilde{\epsilon}_p(\tau'-\tau)}}{1+e^{-\beta\tilde{\epsilon}_p}}\right)_{\tilde{\gamma}'\tilde{\gamma}} & \text{if } \tau < \tau' \end{cases}. \tag{3.11}$$

The matrix M^{-1} has a size of $n \times n$, where each entry M^{-1}_{ij} depends on the flavors α_i and α_j, as well as the corresponding times τ_i and τ_j. If the matrix M^{-1} has block diagonal form, due to some symmetry property, the determinant can be written as a product of determinants of the blocks. This is the case if the hybridization function is diagonal in a flavor, for example the spin, because of a symmetry of the bath Hamiltonian. The matrix

$$M^{-1} = \begin{pmatrix} M_1^{-1} & 0 & \cdots & \cdots \\ 0 & M_2^{-1} & 0 & \cdots \\ \vdots & 0 & \ddots & 0 \\ \vdots & \vdots & 0 & M_{N_B}^{-1} \end{pmatrix}$$

consists of N_B smaller matrices M_b^{-1} on the diagonal, where b labels the block. Each matrix M_b^{-1} has $n_b \times n_b$ entries. To bring the matrix in this block diagonal form, the rows

[1] $\tilde{\epsilon}_p$ is a matrix in the indices $\tilde{\gamma}$ and $\tilde{\gamma}'$. When using the CT-QMC as DMFT impurity solver $F_{\alpha'\alpha}(\tau)$ is obtained from (2.17).

and columns of M^{-1} are sometimes permuted. This does not change the sign, because the operators in the local trace are permuted correspondingly. The flavors α as well as the times τ get the block index b and we use $\tilde{\alpha}$ ($\tilde{\tau}$) instead of α' (τ'). The sum over the flavor indices has to be performed only inside a block, because all block off-diagonal elements in M^{-1} are zero. The total expansion order n can be written as $n = \sum_{b=1}^{N_B} n_b$, where n_b denotes the block expansion order, the number of operator pairs in the trace in block b. The sub matrices M_b^{-1} are given by

$$(M_b^{-1})_{ij} = F_{\tilde{\alpha}_i^b \alpha_j^b}(\tilde{\tau}_i^b - \tau_j^b). \tag{3.12}$$

After renaming and reordering of the local operators as described above, the partition function finally becomes

$$\begin{aligned}\mathcal{Z} = \mathcal{Z}_{\text{bath}} \left(\prod_{b=1}^{N_B} \sum_{n_b=0}^{\infty} \int_0^\beta \mathrm{d}\tau_1^b \cdots \int_{\tau_{n_b-1}^b}^\beta \mathrm{d}\tau_{n_b}^b \int_0^\beta \mathrm{d}\tilde{\tau}_1^b \cdots \int_{\tilde{\tau}_{n_b-1}^b}^\beta \mathrm{d}\tilde{\tau}_{n_b}^b \sum_{\alpha_1^b \cdots \alpha_{n_b}^b} \sum_{\tilde{\alpha}_1^b \cdots \tilde{\alpha}_{n_b}^b} \right) \times \\ \times \left(\prod_{b=1}^{N_B} \det M_b^{-1} \right) \mathrm{Tr} \left[\mathcal{T} e^{-\beta H_{\text{loc}}} \prod_{b=1}^{N_B} c_{b,\alpha_{n_b}^b}(\tau_{n_b}^b) c_{b,\tilde{\alpha}_{n_b}^b}^\dagger(\tilde{\tau}_{n_b}^b) \cdots c_{b,\alpha_1^b}(\tau_1^b) c_{b,\tilde{\alpha}_1^b}^\dagger(\tilde{\tau}_1^b) \right].\end{aligned} \tag{3.13}$$

To make the connection to section 3.1 we formally express the latter as

$$\mathcal{Z} = \sum_x w(x)$$

by putting all sums and integrals into $\sum_x$ and the rest into $w(x)$

$$\begin{aligned}\sum_x &= \prod_{b=1}^{N_B} \sum_{n_b=0}^{\infty} \int_0^\beta \cdots \int_{\tau_{n_b-1}^b}^\beta \int_0^\beta \cdots \int_{\tilde{\tau}_{n_b-1}^b}^\beta \sum_{\alpha_1^b \cdots \alpha_{n_b}^b} \sum_{\tilde{\alpha}_1^b \cdots \tilde{\alpha}_{n_b}^b} \\ w(x) &= (\mathrm{d}\tau)^{2\sum_b n_b} w_{\text{bath}}(x) w_{\text{loc}}(x).\end{aligned}$$

Here, we split the weights into

$$w_{\text{bath}}(x) = \mathcal{Z}_{\text{bath}} \prod_{b=1}^{N_B} \det M_b^{-1} \tag{3.14}$$

$$w_{\text{loc}}(x) = \mathrm{Tr} \left[\mathcal{T} e^{-\beta H_{\text{loc}}} \prod_{b=1}^{N_B} c_{b,\alpha_{n_b}^b}(\tau_{n_b}^b) c_{b,\tilde{\alpha}_{n_b}^b}^\dagger(\tilde{\tau}_{n_b}^b) \cdots c_{b,\alpha_1^b}(\tau_1^b) c_{b,\tilde{\alpha}_1^b}^\dagger(\tilde{\tau}_1^b) \right]. \tag{3.15}$$

The next two sections focus on the calculation of $w_{\text{loc}}(x)$, and also give the acceptance probabilities (3.9) for various MC updates.

3.3 Segment solver

The segment solver is designed for the case in which the Hamiltonian conserves the number of particles in each flavor. This happens if it depends on density operators $\hat{n}_\alpha = c_\alpha^\dagger c_\alpha$ only

$$H_{\text{loc}} = \sum_\alpha \epsilon_\alpha \hat{n}_\alpha + \sum_{\alpha<\alpha'} U_{\alpha\alpha'} \hat{n}_\alpha \hat{n}_{\alpha'} - \mu \sum_\alpha \hat{n}_\alpha. \tag{3.16}$$

We use the segment solver [14] in the implementation [1, 2].

3.3.1 Evaluation of local trace

Because of the special form of the Hamiltonian (3.16), a creation operator has to be followed by an annihilation operator or vice versa for each flavor α. Therefore, we can represent the operators for one flavor with the segment picture of the imaginary time-line spanning from $\tau = 0$ to $\tau = \beta$.
Let n_α be the expansion order of flavor α. A state with flavor α can be either occupied $|1\rangle_\alpha$ or unoccupied $|0\rangle_\alpha$, which is represented here by a thick or a thin line. For example, the zeroth order ($n_\alpha = 0$) term of the partition function expansion is just one of these states at all times, and is thus represented by a full thick ((b) in figure 3.1) or a thin line ((a) in figure 3.1).

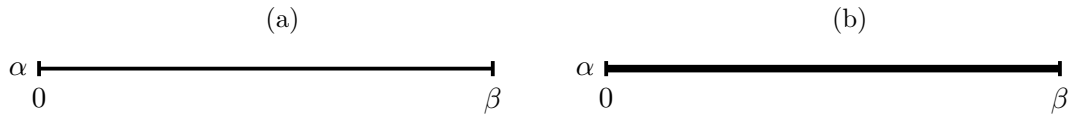

Figure 3.1: Representation of zeroth expansion order $n_\alpha = 0$ of flavor α. An empty line (a) represents the state $|0\rangle_\alpha$ and a full line (b) represents $|1\rangle_\alpha$.

The number of creation and annihilation operator pairs is equal to the expansion order n_α. We represent the creation operators with filled dots and the annihilation operators with circles. A segment is a creation operator followed by an annihilation operator. An anti-segment is an annihilation operator followed by a creation operator. Because, in the trace, the left bra state and the right ket state are the same, segments going beyond $\tau = \beta$ continue at $\tau = 0$. The same is true for anti-segments.

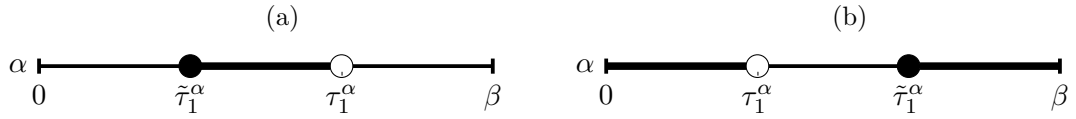

Figure 3.2: Representation of expansion order $n_\alpha = 1$. A particle is created at time $\tilde{\tau}_1^\alpha$ and removed at time τ_1^α. The filled dot represents the creation operator, while the circle represents the annihilation operator.

To calculate the local trace (3.15) we need to measure the length of a segment, which is given by the times τ_{start} and τ_{end} as

$$l = \begin{cases} \tau_{\text{end}} - \tau_{\text{start}} & \text{if} \quad \tau_{\text{end}} > \tau_{\text{start}} \\ \beta - \tau_{\text{end}} + \tau_{\text{start}} & \text{if} \quad \tau_{\text{end}} < \tau_{\text{start}} \end{cases}. \tag{3.17}$$

The total length of all segments for one flavor α is $L_\alpha = \sum_i l_i$. Furthermore, we need to calculate the overlap o of two segments with different flavors α and α'. The overlap o is the length of time, where there is a segment in both the α and α' channel. The total overlap of all segments in two flavors is called $O_{\alpha\alpha'} = \sum_i o_i$. An example is shown in figure 3.3.
Once we calculated the length L_α and the overlap $O_{\alpha\alpha'}$ the local trace for one configuration

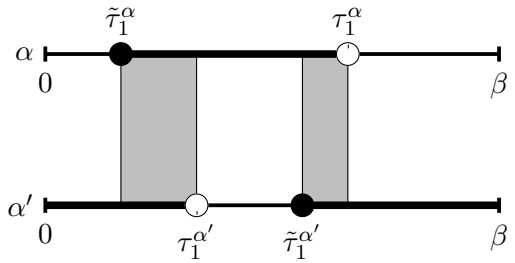

Figure 3.3: Total overlap $O_{\alpha\alpha'}$ (horizontal length of gray areas) of two segments with different flavors α and α'.

is obtained as

$$w_{\text{loc}}(x) = e^{-\sum_\alpha(\epsilon_\alpha-\mu)L_\alpha-\sum_{\alpha<\alpha'}U_{\alpha\alpha'}O_{\alpha\alpha'}}\prod_\alpha(s_\alpha)^{n_\alpha}. \tag{3.18}$$

The sign $s_\alpha \in \{-1,1\}$ is due to time-ordering. It is determined by the order of the first creation (time $\tilde{\tau}_1^\alpha$) and annihilation operator (time τ_1^α)

$$s_\alpha = \text{sgn}(\tau_1^\alpha - \tilde{\tau}_1^\alpha).$$

For MC moves from configuration x to a different configuration x', which change the segment of one specific α, the ratio of the old $w_{\text{loc}}(x)$ and the new $w_{\text{loc}}(x')$ is given by

$$\frac{w_{\text{loc}}(x')}{w_{\text{loc}}(x)} = e^{-(\epsilon_\alpha-\mu)\Delta L_\alpha}\prod_{\alpha'\neq\alpha}e^{-U_{\alpha\alpha'}\Delta O_{\alpha\alpha'}}\frac{(s'_\alpha)^{n_{\alpha'}}}{(s_\alpha)^{n_\alpha}}, \tag{3.19}$$

where ΔL_α stands for the change of the segment length of flavor α and $\Delta O_{\alpha\alpha'}$ for the change of the overlap of the segment for flavor α with a segment with flavor α'.

3.3.2 Monte Carlo moves

We use different Monte Carlo (MC) moves to sample the full configuration space. We perform basic moves for a fixed flavor α, i.e., the insertion or removal of one or two segments or anti-segments and shift moves, as well as global moves which exchange full time-lines. Insertion and removal of one or two segments are in principle enough to guarantee ergodicity. Additional moves speed up the sampling.
Let us consider in more detail the two basic moves, insertion and removal. In the MC simulation, we first randomly pick one of them with probability of 1/2. When inserting a segment into a time-line of a certain α, we choose τ_{start} randomly from $[0,\beta)$ and reject the move if it falls on an existing segment. Then, we draw the length l randomly from the interval $[0,l_{\max})$ with $l_{\max}$ determined as

$$l_{\max} = \begin{cases} \beta & \text{if} \quad n_\alpha = 0 \\ \tilde{\tau}_i^\alpha - \tau_{\text{start}} & \text{if a segment start time } \tilde{\tau}_i^\alpha > \tau_{\text{start}} \text{ exists} \\ \beta - \tau_{\text{start}} + \tilde{\tau}_1^\alpha & \text{if a segment start time } \tilde{\tau}_i^\alpha > \tau_{\text{start}} \text{ is absent} \end{cases}.$$

The probability for this proposal is

$$p_{\text{prop}}(x \to x') = \frac{(\mathrm{d}\tau)^2}{2\beta l_{\max}}.$$

The inverse removal of a segment is performed by choosing one randomly from $n_\alpha + 1$ segments. Consequently, the proposal probability for a removal of a segment is

$$p_{\text{prop}}(x' \to x) = \frac{1}{2(n_\alpha + 1)}.$$

With these proposal probabilities the acceptance probability (3.9) for a segment insertion becomes[2]

$$p_{\text{acc}}(x \to x') = \min\left(\frac{|\det \tilde{M}_b^{-1}|}{|\det M_b^{-1}|}\frac{\beta l_{\max}}{(n_\alpha+1)} e^{-(\epsilon_\alpha-\mu)l} \prod_{\alpha'\neq\alpha} e^{-U_{\alpha\alpha'}o_{\alpha'}}, 1\right), \tag{3.20}$$

where $o_{\alpha'}$ is the overlap of the new segment with the segment of flavor α'. The matrix $\tilde{M}_b^{-1}$ is obtained from M_b^{-1} by inserting one row and column as described in section A.1.1, and their determinant ratio is given by (A.1).
If we remove a segment, the new matrix $\tilde{M}_b^{-1}$ is obtained from M_b^{-1} by removing one row and one column. The removal of one of n_α segments has the acceptance probability

$$p_{\text{acc}}(x \to x') = \min\left(\frac{|\det \tilde{M}_b^{-1}|}{|\det M_b^{-1}|}\frac{n_\alpha}{\beta l_{\max}} e^{(\epsilon_\alpha-\mu)l} \prod_{\alpha'\neq\alpha} e^{U_{\alpha\alpha'}o_{\alpha'}}, 1\right) \tag{3.21}$$

with the determinant ratio (A.3).
The insertion and removal of an anti-segment are similar to the insertion or removal of a segment. A time τ_{start} is drawn randomly and rejected if it falls on an existing anti-segment. The length l and the acceptance probability are the same as in the segment case except for the exponents in (3.20) and (3.21), which are multiplied by -1.
At expansion order $n_\alpha = 0$ we additionally try to add or remove a full time-line depicted in figure 3.1.
A straightforward extension to single-segment moves are moves which insert or remove a pair of segments. The acceptance probability can be derived similarly to the single-segment moves. If the two segments are in the same block, the determinant ratio for insertion is given by (A.5) and for removal by (A.6).
The shift move is an additional move, which consists of shifting the time τ_{end} to a new time. After choosing a segment randomly, a new l is drawn from [0,$l_{\max}$). The expression of the new matrix $\tilde{M}_b^{-1}$ follows from the expression M_b^{-1} by changing one column, and the acceptance probability of the move, which is its own inverse, is given by

$$p_{\text{acc}}(x \to x') = \min\left(\frac{|\det \tilde{M}_b^{-1}|}{|\det M_b^{-1}|} e^{-(\epsilon_\alpha-\mu)\Delta l} \prod_{\alpha'\neq\alpha} e^{-U_{\alpha\alpha'}\Delta o_{\alpha'}}, 1\right),$$

[2]Note that $(\mathrm{d}\tau)^2$ of the insertion proposal probability cancels out, because $w(x')$ contains one more term $(\mathrm{d}\tau)^2$ compared to $w(x)$.

where Δl and $\Delta o_{\alpha'}$ are the change of the quantities $o_{\alpha'}$ and l. The determinant ratio is calculated by (A.8) and the new matrix $\tilde{M}_b^{-1}$ is obtained from (A.11).

In addition to the local moves presented so far, we use global moves to change complete time-lines. Global moves prevent the MC sampling from being trapped in parts of the configuration space. We interchange two time-lines of different flavors α and α' in the same block b with the acceptance probability

$$p_{\text{acc}}(x \to x') = \min\left(\frac{|\det\tilde{M}_b^{-1}|}{|\det M_b^{-1}|} e^{\tilde{L}_{\alpha'}-\tilde{L}_\alpha} \prod_{\gamma\neq\alpha,\alpha'} e^{(U_{\gamma\alpha}-U_{\gamma\alpha'})(\tilde{O}_{\gamma\alpha'}-O_{\gamma\alpha})}, 1\right). \tag{3.22}$$

For this global move the matrix $\tilde{M}_b^{-1}$ and its determinant have to be calculated from scratch. The second global move exchanges all operators of a block b_1 with the operators in a block b_2. Its acceptance probability is given by

$$p_{\text{acc}}(x \to x') = \min\left(\frac{|\det\tilde{M}_{b_1}^{-1}\det\tilde{M}_{b_2}^{-1}|}{|\det M_{b_1}^{-1}\det M_{b_2}^{-1}|} \frac{|w_{\text{loc}}(x')|}{|w_{\text{loc}}(x)|}, 1\right) \tag{3.23}$$

where $\tilde{M}_{b_1}^{-1}$ and $\tilde{M}_{b_2}^{-1}$ have to be calculated from scratch and $w_{\text{loc}}(x')$ is given by (3.18). Both global moves are their own inverse.

3.4 Krylov solver

The application of the segment solver is restricted to a Hamiltonian of form (3.16). To solve the generalized impurity model (3.1) we use the Krylov solver [19] in the generalized form presented in Refs. [1, 2]. The Krylov solver differs from the segment solver mainly by the evaluation of the local trace. To evaluate the local trace of arbitrarily ordered general local operators we need to perform computationally demanding matrix multiplications arising from two different operations. The first is the time evolution by a matrix exponential function, which is the topic of the next section. The second is the application of creation and annihilation operators.
The main idea of the Krylov solver is to express the time-evolution in a low dimensional Krylov subspace and use sparse matrices for the creation and annihilation operators.

3.4.1 Time evolution in Krylov subspace

The imaginary time-evolution of a state $|\psi\rangle$ in quantum mechanics is given by the exponential

$$\begin{aligned} |\psi(\tau)\rangle &= e^{-\tau H}|\psi\rangle \\ &= \sum_{n=0}^{\infty} \frac{(-1)^n\tau^n}{n!} H^n|\psi\rangle. \end{aligned} \tag{3.24}$$

The idea here is to use the Krylov subspace $\mathcal{K}_r(|\psi\rangle)$ to calculate the time evolution. The $r+1$ dimensional Krylov subspace is given by

$$\mathcal{K}_r(|\psi\rangle) = \text{span}\{H^r|\psi\rangle\}_r.$$

The motivation for using the Krylov subspace is the following. For $\tau = 0$ the state $|\psi\rangle$ is not changed. This solution of the time-evolution is included in the one-dimensional Krylov space $\mathcal{K}_0(|\psi\rangle)$. For small times the Krylov subspace $\mathcal{K}_r(|\psi\rangle)$ includes the dominant first $r+1$ terms of the expansion (3.24). For large times the time-evolution is dominated by the lowest eigenenergy of H with finite overlap with $|\psi\rangle$.
An orthonormal basis of $\mathcal{K}_r(|\psi\rangle)$ is constructed using the Lanczos algorithm [20,21]. Starting from a normalized $|\psi\rangle \in \mathbb{R}^{N_{\mathrm{dim}}}$ given by

$$|\psi_1\rangle = \frac{|\psi\rangle}{\||\psi\rangle\|}$$

we construct orthonormal basis vectors $|\psi_{i+1}\rangle$ by

$$\beta_i|\psi_{i+1}\rangle = H|\psi_i\rangle - \alpha_i|\psi_i\rangle - \beta_{i-1}|\psi_{i-1}\rangle.$$

The coefficient α_i is just the diagonal element of H in the new basis

$$\alpha_i = \langle\psi_i|H|\psi_i\rangle$$

and β_i is the normalization constant for $|\psi_{i+1}\rangle$, starting with $\beta_0|\psi_0\rangle = 0$.
After r steps of the Lanczos algorithm, the Hamiltonian, in the basis spanned by $|\psi_i\rangle$, is given by the tridiagonal matrix

$$H_T = \begin{pmatrix} \alpha_1 & \beta_1 & 0 & 0 \\ \beta_1 & \alpha_2 & \ddots & 0 \\ 0 & \ddots & \ddots & \beta_r \\ 0 & 0 & \beta_r & \alpha_{r+1} \end{pmatrix}.$$

The original Hamiltonian H can be reconstructed by

$$H = V H_T V^T$$

where $V = (|\psi_1\rangle \cdots |\psi_{r+1}\rangle)$. Diagonalizing the tridiagonal H_T we get the eigenenergies ϵ_l and eigenvectors $\mathbf{a}_l$ used to construct eigenvectors

$$|a_l\rangle = (\mathbf{a}_l)_1|\psi_1\rangle + \cdots + (\mathbf{a}_l)_{r+1}|\psi_{r+1}\rangle,$$

which are in $\mathbb{R}^{N_{\mathrm{dim}}}$. Now, we approximate the time evolution by expanding the exponential in the Krylov space basis vectors

$$\begin{aligned} |\psi(\tau)\rangle \approx |\psi(\tau)\rangle_r &= \sum_{i,j=1}^{r+1} |\psi_i\rangle\langle\psi_i|e^{-H\tau}|\psi_j\rangle\langle\psi_j|\psi\rangle \\ &= \|\psi\| \sum_{i=1}^{r+1} |\psi_i\rangle\langle\psi_i|e^{-H\tau}|\psi_1\rangle \\ &= \sum_{i,l=1}^{r+1} |\psi_i\rangle\langle\psi_i|a_l\rangle e^{-\epsilon_l\tau}\langle a_l|\psi\rangle \\ &= \sum_{l=1}^{r+1} e^{-\epsilon_l\tau}|a_l\rangle\langle a_l|\psi\rangle. \end{aligned} \tag{3.25}$$

The computational time consuming part here are the scalar products $\langle a_l|\psi\rangle$ scaling like $\mathcal{O}(r \cdot N_{\mathrm{dim}})$. It turns out that we need only a small r, which makes the approach very efficient [1, 2].

3.4.2 Evaluation of local trace

To calculate the local weights (3.15) we evaluate the trace in the occupation number basis. We start by time-ordering the creation and annihilation operators in (3.15). Permutations of operators in this process give the sign s. Using the indices $\alpha_i = (b,\alpha_i^b)$ for the operators the time ordered local trace is

$$w_{\mathrm{loc}}(x) = s\mathrm{Tr}\left[e^{-\beta H_{\mathrm{loc}}} c^{(\dagger)}_{\alpha_{2n}}(\tau_{2n}) c^{(\dagger)}_{\alpha_{2n-1}}(\tau_{2n-1}) \cdots c^{(\dagger)}_{\alpha_1}(\tau_1)\right]$$

with the expansion order n. The trace will be calculated by summing over the eigenstates $|m\rangle$ of the local Hamiltonian. For this purpose, the local Hamiltonian is diagonalized once at the beginning of the whole MC process. We factor out the lowest energy E_0 to ensure a proper time-evolution by the exponentials. We have therefore as a result

$$\begin{aligned} w_{\mathrm{loc}}(x) &= se^{-\beta E_0} \sum_m \langle m| e^{-(\beta-\tau_{2n})(H_{\mathrm{loc}}-E_0)} c^{(\dagger)}_{\alpha_{2n}} e^{-(\tau_{2n}-\tau_{2n-1})(H_{\mathrm{loc}}-E_0)} c^{(\dagger)}_{\alpha_{2n-1}} \times \\ &\quad \times \cdots c^{(\dagger)}_{\alpha_1} e^{-\tau_1(H_{\mathrm{loc}}-E_0)}|m\rangle \\ &= se^{-\beta E_0} \sum_m w_m(x). \end{aligned}$$

To calculate $w_m(x)$ we split the operators into operators for times $\tau > \beta/2$, which we apply to $\langle m|$ and operators for times $\tau < \beta/2$ which we apply to the $|m\rangle$ state.[3] For a fixed m we apply the operators step by step. The first operator can be applied directly

$$e^{-\tau_1(H_{\mathrm{loc}}-E_0)}|m\rangle = e^{-\tau_1(E_m-E_0)}|m\rangle, \tag{3.26}$$

because $|m\rangle$ is an eigenstate of H_{loc}. The next creation or annihilation operator $c^{(\dagger)}_{\alpha_1}$ has to be applied by matrix-vector multiplication. Because $c^{(\dagger)}_{\alpha_1}$ is sparse in the occupation number basis, we store only its non-zero matrix elements, together with their indices. For sparse matrices the matrix-vector product scales like $\mathcal{O}(N_{\mathrm{dim}})$. The next time-evolution is done in the Krylov subspace, as described in the previous section 3.4.1. This is necessary, because the propagated state is not an eigenstate of H_{loc} anymore. The steps of applying a $c^{(\dagger)}_{\alpha}$ and time-evolution are repeated up to the largest time $\tau_{i_0} < \beta/2$. Finally, we get the state

$$|\psi_0\rangle = c^{(\dagger)}_{\alpha_{i_0}} e^{-(\tau_{i_0}-\tau_{i_0-1})(H_{\mathrm{loc}}-E_0)} \cdots c^{(\dagger)}_{\alpha_1} e^{-\tau_1(H_{\mathrm{loc}}-E_0)}|m\rangle$$

from $|m\rangle$. Doing the same procedure to the $\langle m|$ state and times $\tau_{i_0+1} > \beta/2$ we get

$$|\psi_\beta\rangle = c^{(\dagger)}_{\alpha_{i_0+1}} e^{-(\tau_{i_0+2}-\tau_{i_0+1})(H_{\mathrm{loc}}-E_0)} \cdots c^{(\dagger)}_{\alpha_{2n}} e^{-(\beta-\tau_{2n})(H_{\mathrm{loc}}-E_0)}|m\rangle.$$

The associated contribution to the trace is then

$$w_m(x) = \langle\psi_\beta| e^{-(\tau_{i_0+1}-\tau_{i_0})(H_{\mathrm{loc}}-E_0)}|\psi_0\rangle.$$

[3] This simplifies the expressions for local observables in section 3.5.1.

Summing over m gives the local trace $w_{\mathrm{loc}}(x)$. When possible, calculations can be made faster by tracing just over N_{tr} states with energies in a selected low energy range.
With the average dimension of the Krylov subspaces $\bar{r}$ the scaling of the Krylov solver is then $\mathcal{O}(\bar{r} \cdot 2n \cdot N_{\mathrm{dim}} \cdot N_{\mathrm{tr}})$.
Additionally, symmetries are used to speed-up the trace calculation further. This is done exploiting the block structure of the Hamiltonian, i.e., the block indices b in (3.15). The method then scales with the largest dimension of blocks instead of N_{dim}.

3.4.3 Monte Carlo moves

For the Krylov QMC solver [1,2] we use basic one- and two-particle insertion and removal moves, a shift move, and two types of global moves, which work inside a block or between two blocks. The calculation of determinant ratios and the updates of the hybridization function matrices M_b^{-1} are the same as in the segment solver and explained in appendix A.1. The local traces are calculated with the Krylov approach described in the previous chapter.
The insertion and removal of a creation and annihilation operator pair are the most basic moves. These moves are the inverse of each other. For the insertion move we start by picking two flavors α^b and $\tilde{\alpha}^b$ randomly from the same block b. The probability for picking one of N_b flavors in b is $p = 1/N_b$. Furthermore, we pick two times τ and $\tilde{\tau}$ from the interval $[0,\beta)$ with the probability $\mathrm{d}\tau\,/\beta$.
When removing an operator pair we choose between n_b operators with the probability $p = 1/n_b^2$.
The acceptance probability in the Metropolis algorithm for inserting a pair is then

$$p_{\mathrm{acc}}(x \to x') = \min\left(\left(\frac{\beta N_b}{n_b+1}\right)^2 \frac{|\mathrm{det}\tilde{M}_b^{-1}|}{|\mathrm{det}M_b^{-1}|}\frac{|w_{\mathrm{loc}}(x')|}{|w_{\mathrm{loc}}(x)|}, 1\right) \tag{3.27}$$

and the probability for a removal is

$$p_{\mathrm{acc}}(x \to x') = \min\left(\left(\frac{n_b}{\beta N_b}\right)^2 \frac{|\mathrm{det}\tilde{M}_b^{-1}|}{|\mathrm{det}M_b^{-1}|}\frac{|w_{\mathrm{loc}}(x')|}{|w_{\mathrm{loc}}(x)|}, 1\right). \tag{3.28}$$

In case of an insertion, the new matrix $\tilde{M}_b^{-1}$ can be obtained from M_b^{-1} by inserting a row and a column, and the determinant ratio is given by (A.2). The sign of the new configuration x' can be obtained from the sign of the old configuration x as

$$s(x') = s_t(-1)^{i+j}s(x). \tag{3.29}$$

Here, s_t is the sign from time-ordering the local trace when inserting the operators from the right, at $\tau = 0$, and i and j are the final indices of the times $\tilde{\tau}_i$ and $\tilde{\tau}_j$ of the inserted operators.
In case of a removal, the expression of $\tilde{M}_b^{-1}$ follows from the expression of M_b^{-1} by removing one row and one column. The determinant ratio is proportional to (A.3).[4] The expression for the sign is (3.29). The indices of the times τ_i and $\tilde{\tau}_j$ are from the old

[4] For removal at an arbitrary position the determinant ratio (A.3) is multiplied by sign as explained in A.1.1.

configuration x. The time-ordering sign s_t is obtained by inserting the operators to the new configuration x' and time-ordering them to get x.

Additionally, we insert two creation and two annihilation operators into one block b. The acceptance probability of this move is

$$p_{\text{acc}}(x \to x') = \min\left(\frac{(\beta N_b)^4}{(n_b+1)^2(n_b+2)^2}\frac{|\det\tilde{M}_b^{-1}|}{|\det M_b^{-1}|}\frac{|w_{\text{loc}}(x')|}{|w_{\text{loc}}(x)|}, 1\right) \tag{3.30}$$

with the determinant ratio (A.5), and the sign is given by

$$s(x') = s_t\ (-1)^{i+j+k+l} s(x). \tag{3.31}$$

The probability for the inverse move, which is the removal of two creation and two annihilation operators, is

$$p_{\text{acc}}(x \to x') = \min\left(\frac{n_b^2(n_b-1)^2}{(\beta N_b)^4}\frac{|\det\tilde{M}_b^{-1}|}{|\det M_b^{-1}|}\frac{|w_{\text{loc}}(x')|}{|w_{\text{loc}}(x)|}, 1\right). \tag{3.32}$$

Here, the determinant ratio is given by (A.6).
Another basic move shifts the time of one randomly chosen operator. The acceptance probability for this shift move is

$$p_{\text{acc}}(x \to x') = \min\left(\frac{|\det\tilde{M}_b^{-1}|}{|\det M_b^{-1}|}\frac{|w_{\text{loc}}(x')|}{|w_{\text{loc}}(x)|}, 1\right). \tag{3.33}$$

The matrix $\tilde{M}_b^{-1}$ is obtained from M_b^{-1} by exchanging a row or column with a new row or column. The sign

$$s(x') = s_t\ (-1)^{i+i'} s(x) \tag{3.34}$$

is due to time-ordering the replaced operator (s_t) and from the indices of the times of that operator in the old (i) and new (i') configuration. The determinant ratio and update of the matrix M_b^{-1} is described in appendix A.1.3.

In addition to these basic moves, we also exchange operators in global moves. One possibility is to exchange two flavors α and $\tilde{\alpha}$ in the same block b. This is done with the same acceptance probability as in (3.33). There, the determinant has to be calculated from scratch as well as the traces $w_{\text{loc}}(x')$.
The second global move is to exchange all operators of a block b_1 with the operators of a block b_2. The acceptance probability of this move is the same as for the segment solver (3.23), with the local trace calculated by the Krylov approach. The global moves as well as the shift move are their own inverse moves.

3.5 Measurements

To derive the QMC procedure we started with the expansion of the partition function. The rules for the measurement of operators, while sampling the phase space, are derived from similar expansions. The next section describes the measurement of diagonal operators and the following section the measurement of Green functions.

3.5.1 Measurement of diagonal operators

We start with the expansion of the expectation value of the occupation number operator n_α. The expansion is similar to the partition function

$$\langle n_\alpha \rangle = \frac{1}{\mathcal{Z}} \sum_x w^{n_\alpha}(x)$$

but with weights $w^{n_\alpha}(x)$ including the occupation number operator n_α. Since the operator n_α is local, $w^{n_\alpha}(x)$ differs from the weights in the partition function $w(x)$ only by its local part. Let us insert n_α in the middle of the time-line at $\beta/2$ to get

$$\begin{aligned}
\langle n_\alpha \rangle &= \frac{1}{\mathcal{Z}} \sum_x w(x) \frac{w^{n\alpha}(x)}{w(x)} \\
&= \frac{1}{\mathcal{Z}} \sum_x w(x) \frac{w^{n_\alpha}_{\mathrm{loc}}(x)}{w_{\mathrm{loc}}(x)} \\
&= \frac{1}{\mathcal{Z}} \sum_x w(x) \frac{\mathrm{Tr}\left[\mathcal{T} e^{-\beta H_{\mathrm{loc}}} n_\alpha(\frac{\beta}{2}) \prod_{b=1}^{N_B} c_{b,\alpha^b_{n_b}}(\tau^b_{n_b}) c^\dagger_{b,\tilde{\alpha}^b_{n_b}}(\tilde{\tau}^b_{n_b}) \cdots c_{b,\alpha^b_1}(\tau^b_1) c^\dagger_{b,\tilde{\alpha}^b_1}(\tilde{\tau}^b_1)\right]}{\mathrm{Tr}\left[\mathcal{T} e^{-\beta H_{\mathrm{loc}}} \prod_{b=1}^{N_B} c_{b,\alpha^b_{n_b}}(\tau^b_{n_b}) c^\dagger_{b,\tilde{\alpha}^b_{n_b}}(\tilde{\tau}^b_{n_b}) \cdots c_{b,\alpha^b_1}(\tau^b_1) c^\dagger_{b,\tilde{\alpha}^b_1}(\tilde{\tau}^b_1)\right]}.
\end{aligned}$$

In the Krylov solver the fraction is evaluated for each configuration x in the following way. The denominator is the local trace w_{loc}, which is the sum over scalar products $\langle \psi_\beta | \psi_0 \rangle$ for each eigenenergy E_m as described in section 3.4.2. With the same states $|\psi_\beta\rangle$ and $|\psi_0\rangle$ the numerator is then given by

$$w^{n_\alpha}_{\mathrm{loc}}(x) = \sum_m \langle \psi_\beta | e^{-(\tau_{i_0+1} - \beta/2)(H_{\mathrm{loc}} - E_0)} c^\dagger_\alpha c_\alpha e^{-(\beta/2 - \tau_{i_0})(H_{\mathrm{loc}} - E_0)} | \psi_0 \rangle.$$

In general, the operator n_α can be inserted at any time. If the trace is truncated, however, it is important to insert n_α at $\beta/2$ [15]. All observables which consist of density terms can be calculated in this way. For off-diagonal operators like $c^\dagger_\alpha c_{\alpha'}$ with $\alpha \neq \alpha'$, this approach does not work because the measurement of off-diagonal operators by insertion at $\beta/2$ is not ergodic [19].

In the segment solver the expectation value $\langle n_\alpha \rangle$ is simply given by the total length L_α of all segments with flavor α [14]

$$\begin{aligned}
\langle n_\alpha \rangle &= \frac{1}{\beta} \int_0^\beta \mathrm{d}\tau \, \langle n_\alpha(\tau) \rangle \\
&= \frac{1}{\beta} \frac{1}{\mathcal{Z}} \sum_x w(x) L_\alpha.
\end{aligned}$$

The density-density correlation function is given by the total overlap element $O_{\alpha\alpha'}$ [15]

$$\langle n_\alpha n_{\alpha'} \rangle = \frac{1}{\beta} \int_0^\beta \mathrm{d}\tau \, \langle n_\alpha(\tau) n_{\alpha'}(\tau) \rangle = \frac{1}{\beta} \frac{1}{\mathcal{Z}} \sum_x w(x) O_{\alpha\alpha'}.$$

Hence, while evaluating the trace, we only need to save the segment length L_α and the overlap $O_{\alpha\alpha'}$ to obtain automatically $\langle n_\alpha \rangle$ and $\langle n_\alpha n_{\alpha'} \rangle$.

3.5.2 Measurement of Green functions

Green functions can also be expressed in terms of sums over weights.
The imaginary time single-particle Green function

$$G_{\alpha\alpha'}(\tau,\tau') = -\frac{1}{\mathcal{Z}}\mathrm{Tr}\left[\mathcal{T}e^{-\beta H}c_\alpha(\tau)c^\dagger_{\alpha'}(\tau')\right]$$

can be written as sum

$$G_{\alpha\alpha'}(\tau,\tau') = -\frac{1}{\mathcal{Z}}\sum_{x'} w^G(x')$$

over weights $w^G(x')$ of the QMC configurations x'. Thanks to symmetries of the Hamiltonian, we could expand the trace in separate blocks (3.13), which we indicated with b. Likewise, the expansion of the Green function is done in separate blocks. For a certain configuration x' we then get

$$w^G(x') = \mathcal{Z}_{\mathrm{bath}}\mathrm{d}\tau^{\,2\sum_b n_b}\left(\prod_{b=1}^{N_B}\det\tilde{M}_b^{-1}\right)w^G_{\mathrm{loc}}(x'),$$

where the local trace $w^G_{\mathrm{loc}}(x')$ is given by

$$\begin{aligned} w^G_{\mathrm{loc}}(x') = \mathrm{Tr}\Big[&\mathcal{T}e^{-\beta H_{\mathrm{loc}}}c_\alpha(\tau)c^\dagger_{\alpha'}(\tau')\times \\ &\times\prod_{b=1}^{N_B}c_{b,\alpha^b_{n_b}}(\tau^b_{n_b})c^\dagger_{b,\tilde{\alpha}^b_{n_b}}(\tilde{\tau}^b_{n_b})\cdots c_{b,\alpha^b_1}(\tau^b_1)c^\dagger_{b,\tilde{\alpha}^b_1}(\tilde{\tau}^b_1)\Big]. \end{aligned} \tag{3.35}$$

Each block needs to contain an equal number of creation and annihilation operators in the trace (3.35). Therefore, the flavors α and α' of the Green function $G_{\alpha\alpha'}(\tau,\tau')$ have to be in the same block for $G_{\alpha\alpha'}(\tau,\tau')$.
To calculate the Green function, we express $w^G_{\mathrm{loc}}(x')$ in terms of the weights of the partition function $w(x)$. The configuration x is obtained from x' by ordering the two operators $c_\alpha(\tau)$ and $c^\dagger_{\alpha'}(\tau')$ inside the trace and also adding a row and column in $\tilde{M}_b^{-1}$ to get M_b^{-1}. The number of operators in the local parts $w^G_{\mathrm{loc}}(x')$ and $w_{\mathrm{loc}}(x)$ are the same then. After ordering the operators $c_\alpha(\tau)$ and $c^\dagger_{\alpha'}(\tau')$ with all other operators, their times are τ_j and $\tilde{\tau}_i$. Thus, the local trace for configuration x' and configuration x differ only by the sign of this ordering

$$\frac{w^G_{\mathrm{loc}}(x')}{w_{\mathrm{loc}}(x)} = (-1)^{i+j}.$$

Because the matrices $\tilde{M}_b^{-1}$ and M_b^{-1} of the two configurations x' and x differ by one row and one column, we express their determinants via the formula for removal of a row (A.3), obtaining[5]

$$\frac{\det\tilde{M}^{-1}_{b_0}}{\det M^{-1}_{b_0}} = (M_{b_0})_{ji}(-1)^{i+j}.$$

[5]Note that the row and column index are exchanged with respect to $M^{-1}_{b_0}$.

Because the minus sign cancels out, we obtain

$$w^G(x') = w(x)\frac{(M_{b_0})_{ji}}{\mathrm{d}\tau^{\,2}}.$$

The sum $\sum_x$ contains, with respect to $\sum_{x'}$, two additional sums over flavors and two additional integrals. We take this into account by including two Kronecker deltas and two Dirac delta distributions in the summand, when we change $\sum_{x'}$ to $\sum_x$. This gives the expression

$$G_{\alpha\alpha'}(\tau,\tau') = -\frac{1}{\mathcal{Z}}\sum_x w(x)\sum_{b=1}^{N_B}\sum_{ij=1}^{n_b}(M_b)_{ji}\delta_{b,b_0}\delta_{\alpha_j^b,\alpha^b}\delta_{\tilde{\alpha}_i^b,\tilde{\alpha}^b}\delta^-(\tau-\tau_j^b)\delta^-(\tau'-\tilde{\tau}_i^b)$$

for the Green function for the configurations x. In chapter 4 we will show that this function is β-antiperiodic in both arguments. This is taken into account via the (anti)periodic Dirac distribution

$$\delta^{\pm}(\tau) = \sum_{n\in\mathbb{Z}}(\pm 1)^n\delta(\tau-n\beta) \tag{3.36}$$

with the sign $+(-)$ for (anti)periodicity.
Another property of the Green function is that both time arguments can be shifted by the same time s, because the function is translation invariant in time. This means the Green function depends only on the time difference $\tau-\tau'$. Using this property we simplify the expression to

$$\begin{aligned}
G_{\alpha\alpha'}(\tau-\tau') &= -\frac{1}{\mathcal{Z}}\sum_x w(x)\sum_{b=1}^{N_B}\sum_{ij=1}^{n_b}(M_b)_{ji}\delta_{b,b_0}\delta_{\alpha_j^b,\alpha^b}\delta_{\tilde{\alpha}_i^b,\tilde{\alpha}^b}\times \\
&\quad\times\frac{1}{\beta}\int_0^\beta \mathrm{d}s\,\delta^-(\tau-\tau_j^b+s)\delta^-(\tau'-\tilde{\tau}_i^b+s) \\
&= -\frac{1}{\beta}\frac{1}{\mathcal{Z}}\sum_x w(x)\sum_{b=1}^{N_B}\sum_{ij=1}^{n_b}(M_b)_{ji}\delta_{b,b_0}\delta_{\alpha_j^b,\alpha^b}\delta_{\tilde{\alpha}_i^b,\tilde{\alpha}^b}\delta^-(\tau-\tau'-(\tau_j^b-\tilde{\tau}_i^b)).
\end{aligned} \tag{3.37}$$

To measure the Green function directly on a discrete time grid one can approximate the Dirac distribution as

$$\delta(\tau) \approx \frac{1}{\Delta\tau}\begin{cases}1 & \text{if} \quad \left|\frac{\tau}{\Delta\tau}\right| < \frac{1}{2} \\ 0 & \text{else}\end{cases}.$$

However, in actual calculations we use a polynomial representation. Before introducing it we give the expression analogous to (3.37) for the two-particle Green function in imaginary time.

To derive the two-particle Green function measurement formula we do the same steps as for the single-particle Green function. However, let us first ignore the block structure. We

expand the two-particle Green function as

$$\begin{aligned}\mathcal{C}_{\alpha\alpha'\gamma\gamma'}(\tau_1,\tau_2,\tau_3,\tau_4) &= \frac{1}{\mathcal{Z}}\mathrm{Tr}\left[\mathcal{T}e^{-\beta H}c_\alpha(\tau_1)c^\dagger_{\alpha'}(\tau_2)c_\gamma(\tau_3)c^\dagger_{\gamma'}(\tau_4)\right]\\ &= \frac{1}{\mathcal{Z}}\sum_{x'} w^{\mathcal{C}}(x').\end{aligned}$$

The difference of the local traces $w_{\mathrm{loc}}(x)$ and $w^{\mathcal{C}}_{\mathrm{loc}}(x')$ is again just a sign, which cancels with the sign from the hybridization function matrix M^{-1}. The remaining difference in the weights is from the determinant ratio of M^{-1} and $\tilde{M}^{-1}$, which is given by (A.6)

$$w^{\mathcal{C}}(x') = w(x)\frac{1}{\mathrm{d}\tau^{\,4}}\left(M_{ji}M_{lk} - M_{li}M_{jk}\right). \tag{3.38}$$

Introducing the Kronecker deltas and antiperiodic Dirac distributions to change the sum from x' to x we end up with

$$\begin{aligned}\mathcal{C}_{\alpha\alpha'\gamma\gamma'}(\tau_1,\tau_2,\tau_3,\tau_4) = \frac{1}{\mathcal{Z}}\sum_x w(x)\sum_{ijkl=1}^{n}&(M_{ji}M_{lk} - M_{li}M_{jk})\delta_{\alpha',\tilde{\alpha}_i}\delta_{\alpha,\alpha_j}\delta_{\gamma',\tilde{\alpha}_k}\delta_{\gamma,\alpha_l}\times\\ &\times\delta^-(\tau_1-\tau_j)\delta^-(\tau_2-\tilde{\tau}_i)\delta^-(\tau_3-\tau_l)\delta^-(\tau_4-\tilde{\tau}_k).\end{aligned} \tag{3.39}$$

In chapter 4 we will express the two-particle Green function in times τ_{12}, τ_{34}, and τ_{23}, where $\tau_{ij} = \tau_i - \tau_j$. Using the fact that a time $s + \tau_4$ can be subtracted in all time arguments, that $\tau_{14} = \tau_{12} + \tau_{24}$ and $\tau_{24} = \tau_{23} + \tau_{34}$, the two-particle Green function of the three time arguments τ_{12}, τ_{34} and τ_{23} is

$$\begin{aligned}\mathcal{C}_{\alpha\alpha'\gamma\gamma'}(\tau_{12},\tau_{34};\tau_{23}) &= \mathcal{C}_{\alpha\alpha'\gamma\gamma'}(\tau_{12}+\tau_{23}+\tau_{34},\tau_{23}+\tau_{34},\tau_{34},0)\\ &= \frac{1}{\beta}\int_0^\beta \mathrm{d}s\,\mathcal{C}_{\alpha\alpha'\gamma\gamma'}(\tau_{14}-s,\tau_{24}-s,\tau_{34}-s,s)\\ &= \frac{1}{\beta}\frac{1}{\mathcal{Z}}\sum_x w(x)\sum_{ijkl=1}^{n}(M_{ji}M_{lk} - M_{li}M_{jk})\delta_{\alpha',\tilde{\alpha}_i}\delta_{\alpha,\alpha_j}\delta_{\gamma',\tilde{\alpha}_k}\delta_{\gamma,\alpha_l}\times\\ &\quad\times\delta^-(\tau_{14}-\tau_j+\tilde{\tau}_k)\delta^-(\tau_{24}-\tilde{\tau}_i+\tilde{\tau}_k)\delta^-(\tau_{34}-\tau_l+\tilde{\tau}_k)\\ &= \frac{1}{\beta}\frac{1}{\mathcal{Z}}\sum_x w(x)\sum_{ijkl=1}^{n}(M_{ji}M_{lk} - M_{li}M_{jk})\delta_{\alpha',\tilde{\alpha}_i}\delta_{\alpha,\alpha_j}\delta_{\gamma',\tilde{\alpha}_k}\delta_{\gamma,\alpha_l}\times\\ &\quad\times\delta^-(\tau_{12}-(\tau_j-\tilde{\tau}_i))\delta^+(\tau_{23}-(\tilde{\tau}_i-\tau_l))\delta^-(\tau_{34}-(\tau_l-\tilde{\tau}_k)).\end{aligned} \tag{3.40}$$

This function is β-periodic in τ_{23} and β-antiperiodic in τ_{12} and τ_{34}.
We now consider the block structure due to symmetries, which enters through the hybridization function matrix M_b^{-1}. The hybridization function matrix is diagonal in the blocks $(M^{-1})_{bi,b'i'} = (M_b^{-1})_{ii'}\delta_{b,b'}$. By setting $\alpha = (b_1,\alpha^{b_1})$, $\alpha' = (b_2,\alpha'^{b_2})$, $\gamma = (b_3,\gamma^{b_3})$ and $\gamma' = (b_4,\gamma'^{b_4})$ we find that

$$M_{b_1j,b_2i}M_{b_3l,b_4k} - M_{b_3l,b_2i}M_{b_1j,b_4k} = \delta_{b_1,b_2}\delta_{b_3,b_4}(M_{b_1})_{ji}(M_{b_3})_{lk} - \delta_{b_1,b_4}\delta_{b_2,b_3}(M_{b_1})_{li}(M_{b_2})_{jk}.$$

The non vanishing parts of the two-particle Green function are the block longitudinal

$$\begin{aligned}\mathcal{C}^{b_1 b_2}_{\alpha\alpha'\gamma\gamma'}(\tau_{12},\tau_{34};\tau_{23}) = \frac{1}{\beta}\frac{1}{\mathcal{Z}}\sum_x w(x)\sum_{bb'=1}^{N_B}\sum_{ij=1}^{n_b}\sum_{kl=1}^{n_{b'}}\delta_{\alpha',\tilde{\alpha}_i^b}\delta_{\alpha,\alpha_j^b}\delta_{\gamma',\tilde{\alpha}_k^{b'}}\delta_{\gamma,\alpha_l^{b'}}\times \\ \times\,\delta_{b_1,b}\delta_{b_2,b'}((M_b)_{ji}(M_{b'})_{lk}-\delta_{b,b'}(M_b)_{li}(M_b)_{jk})\times \\ \times\,\delta^-(\tau_{12}-(\tau_j^b-\tilde{\tau}_i^b))\delta^-(\tau_{34}-(\tau_l^{b'}-\tilde{\tau}_k^{b'}))\delta^+(\tau_{23}-(\tilde{\tau}_i^b-\tau_l^{b'})),\end{aligned}$$

and the block transversal part

$$\begin{aligned}\mathcal{C}^{\bar{b}_1\bar{b}_2}_{\alpha\alpha'\gamma\gamma'}(\tau_{12},\tau_{34};\tau_{23}) = -\frac{1}{\beta}\frac{1}{\mathcal{Z}}\sum_x w(x)\sum_{bb'=1}^{N_B}\sum_{il=1}^{n_b}\sum_{kj=1}^{n_{b'}}\delta_{\alpha',\tilde{\alpha}_i^b}\delta_{\alpha,\alpha_j^{b'}}\delta_{\gamma',\tilde{\alpha}_k^{b'}}\delta_{\gamma,\alpha_l^b}\times \\ \times\,(1-\delta_{b,b'})\delta_{\bar{b}_1,b}\delta_{\bar{b}_2,b'}(M_b)_{li}(M_{b'})_{jk}\times \\ \times\,\delta^-(\tau_{12}-(\tau_j^{b'}-\tilde{\tau}_i^b))\delta^-(\tau_{34}-(\tau_l^b-\tilde{\tau}_k^{b'}))\delta^+(\tau_{23}-(\tilde{\tau}_i^b-\tau_l^b)).\end{aligned}$$

Let us now rewrite the single- and two-particle Green functions using a polynomial basis $f_l^m(x(\tau))$. The single-particle Green function is given by

$$\begin{aligned}G_l^{\alpha\alpha'} &= \int_0^\beta \mathrm{d}\tau\, f_l^0(\tau)G_{\alpha\alpha'}(\tau) \\ &= -\frac{1}{\mathcal{Z}}\frac{1}{\beta}\sum_x w(x)\sum_{b=1}^{N_B}\sum_{ij=1}^{n_b}(M_b)_{ji}\delta_{b,b_0}\delta_{\alpha_j^b,\alpha^b}\delta_{\tilde{\alpha}_i^b,\tilde{\alpha}^b}\hat{f}_l^0(x(\tau_j^b-\tilde{\tau}_i^b)).\end{aligned} \tag{3.41}$$

Here, we introduced the antiperiodic functions

$$\hat{f}_l^m(x(\tau)) = e^{-i\frac{\omega_m}{2}\tau}\begin{cases} f_l(x(\tau)) & \text{if} \quad \tau>0 \\ (-1)^{m+1}f_l(x(\tau+\beta)) & \text{if} \quad \tau<0\end{cases}.$$

In practice we use either Legendre polynomials for $f_l(x(\tau))$ or a numerical basis called intermediate representation. The details of this basis functions are the topic of section 4.5.3.

For the two-particle Green function it is convenient to use a mixed polynomial-Matsubara basis via the formula

$$\begin{aligned}\mathcal{C}^{\alpha\alpha'\gamma\gamma'}_{ll'}(i\omega_m) = (-1)^{l'+m+1}\int_0^\beta \mathrm{d}\tau_{12}\int_0^\beta \mathrm{d}\tau_{34}\int_0^\beta \mathrm{d}\tau_{23}\, f_l^m(\tau_{12})f_{l'}^m(\tau_{34})e^{-i\omega_m\tau_{23}}\times \\ \times\,\mathcal{C}_{\alpha\alpha'\gamma\gamma'}(\tau_{12},\tau_{34};\tau_{23}).\end{aligned}$$

This gives the block longitudinal part

$$\begin{aligned}\mathcal{C}^{\alpha\alpha'\gamma\gamma'}_{ll',b_1b_2}(i\omega_m) = \frac{1}{\beta}\frac{1}{\mathcal{Z}}(-1)^{l'+m+1}\sum_x w(x)\sum_{bb'=1}^{N_B}\sum_{ij=1}^{n_b}\sum_{kh=1}^{n_{b'}}\times \\ \times\,\delta_{\alpha',\tilde{\alpha}_i^b}\delta_{\alpha,\alpha_j^b}\delta_{\gamma',\tilde{\alpha}_k^{b'}}\delta_{\gamma,\alpha_h^{b'}}\delta_{b_1,b}\delta_{b_2,b'}((M_b)_{ji}(M_{b'})_{hk}-\delta_{b,b'}(M_b)_{hi}(M_b)_{jk})\times \\ \times\,\hat{f}_l^m(x(\tau_j^b-\tilde{\tau}_i^b))\hat{f}_{l'}^m(x(\tau_h^{b'}-\tilde{\tau}_k^{b'}))e^{-i\omega_m(\tilde{\tau}_i^b-\tau_h^{b'})}\end{aligned} \tag{3.42}$$

and the block transversal part

$$\mathcal{C}^{\alpha\alpha'\gamma\gamma'}_{ll',\bar{b}_1\bar{b}_2}(i\omega_m) = \frac{1}{\beta}\frac{1}{\mathcal{Z}}(-1)^{l'+m}\sum_x w(x)\sum_{bb'=1}^{N_B}\sum_{ih=1}^{n_b}\sum_{kj=1}^{n_{b'}}\times$$
$$\times\,\delta_{\alpha',\tilde{\alpha}^b_i}\delta_{\alpha,\alpha^{b'}_j}\delta_{\gamma',\tilde{\alpha}^{b'}_k}\delta_{\gamma,\alpha^b_h}(1-\delta_{b,b'})\delta_{\bar{b}_1,b}\delta_{\bar{b}_2,b'}(M_b)_{hi}(M_{b'})_{jk}\times$$
$$\times\,\hat{f}^m_l(x(\tau^{b'}_j-\tilde{\tau}^b_i))\hat{f}^m_{l'}(x(\tau^b_h-\tilde{\tau}^{b'}_k))e^{-i\omega_m(\tilde{\tau}^b_i-\tau^b_h)}. \tag{3.43}$$

The calculation of the two-particle Green function scales like $\mathcal{O}(N_B^2\cdot\bar{n}_b^4\cdot l^2_{\max}\cdot n_\omega)$, where $\bar{n}_b$ is the average expansion order of block b, $l_{\max}$ is the number of polynomials and n_ω the number of frequencies ω_m. For low temperatures T the expansion order $\bar{n}_b$ increases [1] and, depending on the basis, $l_{\max}$ increases, too. In addition, the distance between Matsubara frequencies $\omega_m \sim Tm$ becomes smaller, so that the number of frequencies n_ω in a certain frequency range increases. Considering all combination of flavors and polynomials, the time required to measure the two-particle Green function can be longer than the time for QMC sampling itself. To speed up the calculations the polynomials are calculated only once for l and l'. Furthermore, the required number of entries is reduced by the use of symmetries given in chapter 4.

3.6 Parallelization and scaling

As described in Refs. [1, 2], the complete DMFT procedure with a CT-QMC impurity solver can be well parallelized with MPI. Compared to all other steps in DMFT, solving the impurity model is most time-consuming. Therefore, it is less important that the other steps can be only partially parallelized, for example by performing sums with multiple MPI processes.
To parallelize the CT-QMC algorithm we run independent Markov chains for each parallel MPI process. A scaling limitation is the warm-up period at the beginning of the Markov chains, which cannot be parallelized. However, because in DMFT we solve impurity models self-consistently, we can reduce the warm-up period by starting from the QMC configuration of the previous DMFT iteration.
The measurement of the two-particle Green function is done for each Markov chain individually and is therefore well parallelized. Also, more QMC sweeps are typically needed for two-particle Green function measurements. Thus, the runtime increase of a run including two-particle Green function measurements, compared to DMFT with single-particle Green function measurements only, is due to parallelized parts of the algorithm. Therefore, the speed-up due to parallelization further increases, when measuring two-particle Green functions.
In Ref. [1] the speed-up is shown for the single-particle run. We give a similar scaling plot in figure 3.4 for the two-particle Green function measurement and find an almost ideal speed-up.

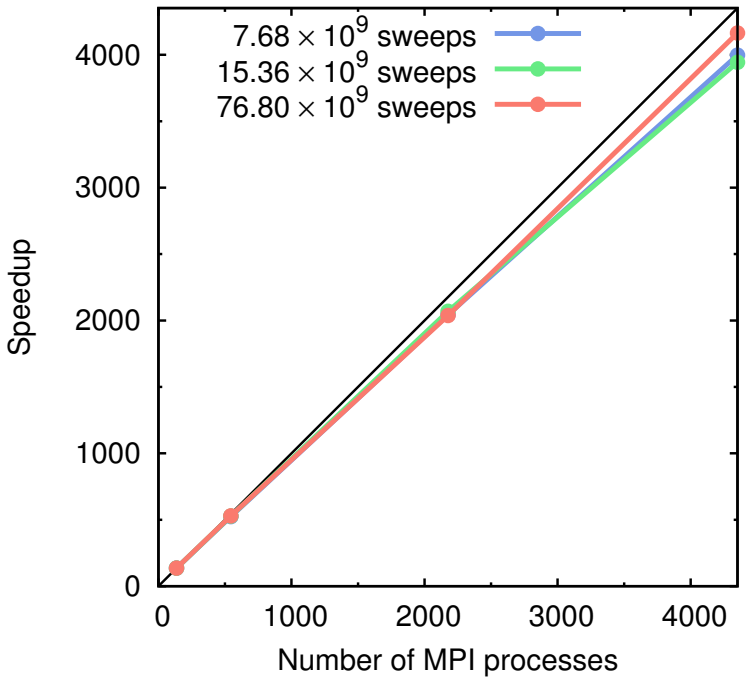

Figure 3.4: Speed-up by parallelization for the Krylov solver including measurement of the two-particle Green function on the supercomputer JURECA Booster. Different lines show different number of sweeps for representative calculations. The black line represents the ideal speed-up.

4 Response functions

4.1 One and two-particle Green function

Green functions are at the heart of DMFT and, together with response functions, are tools to explain experiments. The general form of the single-particle Green function in imaginary time is

$$G_{\alpha\alpha'}(\tau_1,\tau_2) = -\langle \mathcal{T} c_\alpha(\tau_1) c^\dagger_{\alpha'}(\tau_2)\rangle. \tag{4.1}$$

The generalized two-particle Green function is instead defined as[1]

$$\mathcal{C}_{\alpha\alpha'\gamma\gamma'}(\tau_1,\tau_2,\tau_3,\tau_4) = \langle \mathcal{T} c_\alpha(\tau_1) c^\dagger_{\alpha'}(\tau_2) c_\gamma(\tau_3) c^\dagger_{\gamma'}(\tau_4)\rangle. \tag{4.2}$$

The indices α, α', γ and γ' are flavors. They can represent spin $\sigma \in \{\uparrow, \downarrow\}$, orbital or band index $m \in \mathbb{N}$, site index $s \in \mathbb{N}$ inside the unit cell, and lattice site index $i \in \mathbb{N}$ or momenta $\mathbf{k}$,$\mathbf{q} \in \mathbb{R}^3$. One and two-particle Green functions build susceptibilities. The most general form of the susceptibility is

$$\chi_{\alpha\alpha'\gamma\gamma'}(\tau_1,\tau_2,\tau_3,\tau_4) = \mathcal{C}_{\alpha\alpha'\gamma\gamma'}(\tau_1,\tau_2,\tau_3,\tau_4) - G_{\alpha\alpha'}(\tau_1,\tau_2) G_{\gamma\gamma'}(\tau_3,\tau_4). \tag{4.3}$$

In strongly correlated materials the two-particle Green function can differ significantly from the bare susceptibility[2]

$$\chi^0_{\alpha\alpha'\gamma\gamma'}(\tau_1,\tau_2,\tau_3,\tau_4) = -G_{\alpha\gamma'}(\tau_1,\tau_4) G_{\gamma\alpha'}(\tau_3,\tau_2), \tag{4.4}$$

which consists of the product of single-particle Green functions.
Experiments measure the physical susceptibility

$$\chi_{P_\nu O_{\nu'}}(\mathbf{r},\mathbf{r}',\tau,\tau') = -\sum_{\substack{\alpha\alpha'\\ \gamma\gamma'}} [P_\nu]_{\alpha\alpha'} [O_{\nu'}]_{\gamma\gamma'} \left(\langle \mathcal{T} c_\alpha(\tau) c^\dagger_{\alpha'}(\tau) c_\gamma(\tau') c^\dagger_{\gamma'}(\tau')\rangle - \langle c_\alpha c^\dagger_{\alpha'}\rangle \langle c_\gamma c^\dagger_{\gamma'}\rangle \right). \tag{4.5}$$

Here, $[P_\nu]_{\alpha\alpha'}$ and $[O_{\nu'}]_{\gamma\gamma'}$ are elements of matrices of single-particle operators describing observables

$$\Delta P_\nu(\mathbf{r},\tau) = \sum_{\alpha\alpha'} [P_\nu]_{\alpha\alpha'} \left(c^\dagger_{\alpha'}(\tau) c_\alpha(\tau) - \langle c^\dagger_{\alpha'} c_\alpha\rangle \right)$$
$$\Delta O_{\nu'}(\mathbf{r}',\tau') = \sum_{\gamma\gamma'} [O_{\nu'}]_{\gamma\gamma'} \left(c^\dagger_{\gamma'}(\tau') c_\gamma(\tau') - \langle c^\dagger_{\gamma'} c_\gamma\rangle \right).$$

For example, $\mathbf{P}$ and $\mathbf{O}$ could represent the magnetization $\mathbf{M}$.

[1] We adopt the definitions of Ref. [22].

[2] This is due to the Wick's theorem, which for the two-particle Green function gives $\langle c_\alpha c^\dagger_{\alpha'} c_\gamma c^\dagger_{\gamma'}\rangle = \langle c_\alpha c^\dagger_{\alpha'}\rangle\langle c_\gamma c^\dagger_{\gamma'}\rangle - \langle c_\alpha c^\dagger_{\gamma'}\rangle\langle c_\gamma c^\dagger_{\alpha'}\rangle$.

4.2 Linear response theory

In this section we describe the linear change of the expectation value $\langle \mathbf{P}(\mathbf{r},t)\rangle$ of an observable due to a weak external perturbation $H_1(\mathbf{r},t)$ of the equilibrium Hamiltonian H_0. The total Hamiltonian in this case is

$$H = H_0 + H_1(t).$$

In many relevant cases we can split the perturbation into a vector operator $\mathbf{O}(\mathbf{r})$ and a vector function $\mathbf{h}(\mathbf{r},t)$

$$\begin{aligned} H_1(t) &= \int \mathrm{d}^3 r\, \mathbf{O}(\mathbf{r}) \cdot \mathbf{h}(\mathbf{r},t) \\ &= \sum_{\nu\in\{x,y,z\}} \int \mathrm{d}^3 r\, O_\nu(\mathbf{r}) h_\nu(\mathbf{r},t). \end{aligned}$$

The vector operator describes an observable of the system and the function $\mathbf{h}(\mathbf{r},t)$ the external field influencing that observable. An example of $\mathbf{O}(\mathbf{r})$ is the magnetization $\mathbf{M}(\mathbf{r})$ and correspondingly $\mathbf{h}(\mathbf{r},t)$ is an external magnetic field. Let us introduce the unitary time evolution operator $U^I(t,t_0)$ in the interaction picture and its first order approximation

$$\begin{aligned} U^I(t,t_0) &= \mathcal{T}\left(e^{-i\int_{t_0}^{t} \mathrm{d}t'\, H_1^I(t')}\right) \\ &\approx \mathbb{1} - i\int_{t_0}^{t} \mathrm{d}t'\, H_1^I(t'). \end{aligned}$$

Here, $\mathcal{T}$ is the time-ordering operator. We adopt the interaction picture (superscript I) so that

$$O^I(t) = e^{iH_0 t} O e^{-iH_0 t}.$$

The time evolution of an observable $\langle \mathbf{P}(\mathbf{r},t)\rangle$ can be expressed as

$$\begin{aligned} \langle \mathbf{P}(\mathbf{r},t)\rangle &= \mathrm{Tr}\left[e^{-iHt}\rho_0 e^{iHt}\mathbf{P}(\mathbf{r})\right] \\ &= \mathrm{Tr}\left[U_I^\dagger(t,-\infty)\rho_0 U_I(t,-\infty)\mathbf{P}^I(\mathbf{r},t)\right], \end{aligned}$$

where $\rho_0 = \exp(-\beta H_0)/\mathcal{Z}_0$ and $\mathcal{Z}_0 = \mathrm{Tr}\rho_0$. The system is in equilibrium, described by H_0, for $t_0 = -\infty$. Using the first order approximation of $U^I(t,t_0)$, we obtain

$$\begin{aligned} \langle \mathbf{P}(\mathbf{r},t)\rangle &= \mathrm{Tr}\left[\rho_0 \mathbf{P}(\mathbf{r})\right] - i\int_{-\infty}^{t} \mathrm{d}t'\, \mathrm{Tr}\left[H_1^I(t')\rho_0 \mathbf{P}^I(\mathbf{r},t) - \rho_0 H_1^I(t')\mathbf{P}^I(\mathbf{r},t)\right] + \mathcal{O}(H_1^2) \\ &\approx \langle \mathbf{P}(\mathbf{r})\rangle_0 - i\sum_{\nu\in\{x,y,z\}} \int_{-\infty}^{t} \mathrm{d}t' \int \mathrm{d}^3 r'\, \langle\left[\mathbf{P}^I(\mathbf{r},t), O_\nu^I(\mathbf{r}',t')\right]\rangle_0 h_\nu(\mathbf{r}',t'). \end{aligned}$$

In this way we need to calculate only equilibrium expectation values $\langle\cdots\rangle_0$ with ρ_0. The change of the operator $\mathbf{P}(\mathbf{r},t)$ from its equilibrium value at linear order of the perturbation $h_{\nu'}(\mathbf{r}',t')$ is thus

$$\begin{aligned} \langle \delta P_\nu(\mathbf{r},t)\rangle &= \langle P_\nu(\mathbf{r},t)\rangle - \langle P_\nu(\mathbf{r})\rangle_0 \\ &= \sum_{\nu'\in\{x,y,z\}} \int_{-\infty}^{\infty} \mathrm{d}t' \int \mathrm{d}^3 r'\, \chi_{P_\nu O_{\nu'}}(\mathbf{r},\mathbf{r}',t,t') h_{\nu'}(\mathbf{r}',t'). \end{aligned} \tag{4.6}$$

The susceptibility or linear response function $\chi_{P_\nu O_{\nu'}}(\mathbf{r},\mathbf{r}',t,t')$ is given by the Kubo formula

$$\chi_{P_\nu O_{\nu'}}(\mathbf{r},\mathbf{r}',t,t') = -i\langle\left[P_\nu^I(\mathbf{r},t),O_{\nu'}^I(\mathbf{r}',t')\right]\rangle_0\Theta(t-t'). \tag{4.7}$$

The function $\Theta(t-t')$ ensures that $\delta P_\nu(\mathbf{r},t)$ is only influenced by times $t' < t$ making the response function causal. The susceptibility is the derivative of the observable $\langle P_\nu(\mathbf{r},t)\rangle$ with respect to an infinitesimal external perturbation $h_{\nu'}$:

$$\chi_{P_\nu O_{\nu'}}(\mathbf{r},\mathbf{r}',t,t') = \lim_{h_{\nu'}\to 0}\frac{\partial\langle P_\nu(\mathbf{r},t)\rangle}{\partial h_{\nu'}(\mathbf{r}',t')}.$$

The Kubo formula becomes even simpler when we Fourier transform the times to frequencies. The Hamiltonian H_0 is time independent and therefore the susceptibility depends only on time differences

$$\chi_{P_\nu O_{\nu'}}(\mathbf{r},\mathbf{r}',t,t') = \chi_{P_\nu O_{\nu'}}(\mathbf{r},\mathbf{r}',t-t').$$

With the following definitions of the Fourier transformation in time and its inverse

$$f(\omega) = \int_{-\infty}^{\infty}\mathrm{d}t\, f(t)e^{i\omega t}$$
$$f(t) = \frac{1}{2\pi}\int_{-\infty}^{\infty}\mathrm{d}\omega\, f(\omega)e^{-i\omega t}$$

we get the frequency dependent susceptibility

$$\chi_{P_\nu O_{\nu'}}(\mathbf{r},\mathbf{r}',\omega) = \int_{-\infty}^{\infty}\mathrm{d}t\, e^{i\omega t}\chi_{P_\nu O_{\nu'}}(\mathbf{r},\mathbf{r}',t).$$

For a translational invariant system a similar transformation can be done from real to momentum space by using

$$f(\mathbf{q}) = \int \mathrm{d}^3r\, f(\mathbf{r})e^{i\mathbf{q}\cdot\mathbf{r}} \tag{4.8}$$
$$f(\mathbf{r}) = \frac{1}{(2\pi)^3}\int \mathrm{d}^3q\, f(\mathbf{q})e^{-i\mathbf{q}\cdot\mathbf{r}}. \tag{4.9}$$

Transforming both time and space we find

$$\langle\delta P_\nu(\mathbf{k},\omega)\rangle = \sum_{\nu'\in\{x,y,z\}}\chi_{P_\nu O_{\nu'}}(\mathbf{k},\omega)h_{\nu'}(\mathbf{k},\omega). \tag{4.10}$$

These result describes experiments as depicted in figure 4.1.
It is useful to express $\chi_{P_\nu O_{\nu'}}$ in imaginary time. Indeed, continuous-time quantum Monte Carlo (CT-QMC), the method we use to calculate it, is formulated in imaginary time. The perturbation expressed in imaginary time is

$$H_1(\tau) = \int \mathrm{d}^3r\, \mathbf{O}(\mathbf{r})\cdot\mathbf{h}(\mathbf{r},\tau).$$

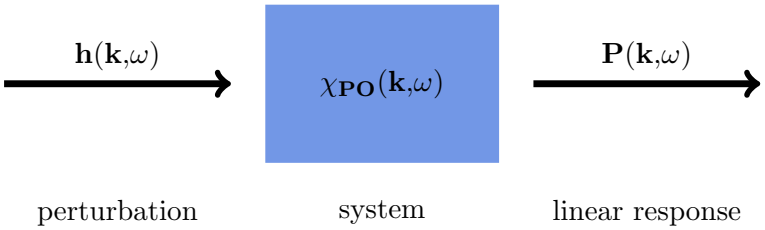

Figure 4.1: Schematic of an experiment described by the linear response theory (4.10).

The first order approximation of the time evolution operator $U^I(\beta)$ defined in (A.15) is

$$U^I(\beta) \approx \mathbb{1} - \int_0^\beta \mathrm{d}\tau\, H_1^I(\tau),$$

and the time dependence of H_1 follows from (A.12). Equation (3.10) gives the partition function $\mathcal{Z}$ in terms of $U^I(\beta)$. Similarly, the expectation value of an operator $\mathbf{P}(\mathbf{r},\tau)$ is given by

$$\begin{aligned}\langle \mathbf{P}(\mathbf{r},\tau)\rangle &= \frac{\mathrm{Tr}[e^{-H_0\beta}\mathbf{P}^I(\mathbf{r},\tau)U^I(\beta)]}{\mathrm{Tr}[e^{-H_0\beta}U^I(\beta)]} \\ &= \langle \mathbf{P}(\mathbf{r},\tau)U^I(\beta)\rangle_0 \langle [U^I(\beta)]^{-1}\rangle_0 \\ &\approx \left(\langle \mathbf{P}(\mathbf{r})\rangle_0 - \int_0^\beta \mathrm{d}\tau' \,\langle \mathcal{T}\mathbf{P}^I(\mathbf{r},\tau)H_1^I(\tau')\rangle_0\right) \times \\ &\quad \times \left(\mathbb{1} + \int_0^\beta \mathrm{d}\tau' \,\langle H_1^I(\tau')\rangle_0\right).\end{aligned} \tag{4.11}$$

The linear change of the observable due to an external perturbation is calculated by

$$\langle \delta P_\nu(\mathbf{r},\tau)\rangle = \sum_{\nu'\in\{x,y,z\}} \int_0^\beta \mathrm{d}\tau' \int \mathrm{d}^3 r'\, \chi_{P_\nu O_{\nu'}}(\mathbf{r},\mathbf{r}',\tau,\tau') h_{\nu'}(\mathbf{r}',\tau')$$

in which we used the definition of the susceptibility

$$\begin{aligned}\chi_{P_\nu O_{\nu'}}(\mathbf{r},\mathbf{r}',\tau,\tau') &= -\langle \mathcal{T} P_\nu^I(\mathbf{r},\tau) O_{\nu'}^I(\mathbf{r}',\tau')\rangle_0 + \langle P_\nu(\mathbf{r})\rangle_0 \langle O_{\nu'}(\mathbf{r}')\rangle_0 \\ &= -\langle \mathcal{T}\Delta P_\nu^I(\mathbf{r},\tau)\Delta O_{\nu'}^I(\mathbf{r}',\tau')\rangle_0\end{aligned} \tag{4.12}$$

with

$$\begin{aligned}\Delta P_\nu^I(\mathbf{r},\tau) &= P_\nu^I(\mathbf{r},\tau) - \langle P_\nu(\mathbf{r})\rangle_0 \\ \Delta O_{\nu'}^I(\mathbf{r}',\tau') &= O_{\nu'}^I(\mathbf{r}',\tau') - \langle O_{\nu'}(\mathbf{r}')\rangle_0.\end{aligned}$$

We transform the susceptibility to bosonic Matsubara frequencies ($\omega_m = 2\pi m/\beta$) by

$$f(i\omega_m) = \int_0^\beta \mathrm{d}\tau\, f(\tau) e^{i\omega_m\tau} \tag{4.13}$$

$$f(\tau) = \frac{1}{\beta}\sum_{m=-\infty}^{\infty} f(i\omega_m) e^{-i\omega_m\tau} \tag{4.14}$$

and transform the real space variables $\mathbf{r}$, $\mathbf{r}'$ to momentum space using (4.8).

$$\chi_{P_\nu O_{\nu'}}(\mathbf{q},i\omega_m) = \int_0^\beta \mathrm{d}\tau \int \mathrm{d}^3 r\, e^{i\omega_m(\tau-\tau')} e^{i\mathbf{q}\cdot(\mathbf{r}-\mathbf{r}')} \chi_{P_\nu O_{\nu'}}(\mathbf{r},\mathbf{r}',\tau,\tau')$$

From now on we will omit the subscript 0 at the expectation values and the superscript I. The time dependence of all operators follows always from (A.12) and all expectation values are calculated in equilibrium with ρ_0.
A crystal is only invariant under lattice translations, while here we assumed full translational invariance. Therefore, in a crystal the susceptibility $\chi_{P_\nu O_{\nu'}}$ has to be expressed in terms of crystal momenta and reciprocal lattice vectors [22]. However, the essence stays the same.

4.3 Experimental techniques

In the following we will give examples of common experimental techniques to measure single-particle Green functions and susceptibilities.
We start with methods measuring the spectral function, the imaginary part of the single-particle Green function. These techniques include photoemission spectroscopy (PES), scanning tunneling microscopy (STM) and scanning tunneling spectroscopy (STS). Then, we describe experiments which give access to susceptibilities. Among these are inelastic neutron scattering (INS), resonant inelastic X-ray scattering (RIXS) or nuclear magnetic resonance (NMR). Throughout this thesis, including this section, we use atomic units in all equations. For values given in different units, we state them explicitly.

measured function	symbol	operator	experimental technique
spectral function	$A_{\alpha\alpha'}(\mathbf{k},\omega)$	$\sim \langle c^\dagger_{\mathbf{k}\alpha'}(0) c_{\mathbf{k}\alpha}(t)\rangle$	ARPES, STS
magnetic susceptibility	$\chi^{\nu\nu'}(\mathbf{k},\omega)$	$\sim \langle M^\nu(\mathbf{k},t) M^{\nu'}(-\mathbf{k},0)\rangle$	NMR, INS, RIXS
optical conductivity	$\sigma^{\nu\nu'}(\mathbf{k},\omega)$	$\sim \langle j^\nu(\mathbf{k},t), j^{\nu'}(-\mathbf{k},0)\rangle$	optical spectroscopy

4.3.1 Photoemission spectroscopy

The spectral function $A(\mathbf{k},\omega)$, which is related to the single-particle Green function by

$$G(\mathbf{k},\tau) = -\int_{-\infty}^{\infty} \frac{\mathrm{d}\omega}{2\pi} \frac{e^{-\tau\omega}}{1+e^{-\beta\omega}} A(\mathbf{k},\omega),$$

and the density of states

$$\rho(\omega) = \frac{1}{N_\mathbf{k}} \sum_\mathbf{k} A(\mathbf{k},\omega)$$

are accessible by photoemission spectroscopy (PES) [23, 24] and scanning tunneling microscopy [25]. In PES, a monochromatic light source shines on a sample, which emits electrons because of the photoelectric effect. The energy ω and momentum $\mathbf{k}$ of the emitted electrons are detected.

Since electrons travel only a finite length in a solid, to access bulk states high energy photons are typically used.
If additionally the reflection angle is measured, the method becomes angular resolved photoemission spectroscopy (ARPES).
The PES measures the transition probability from a state $|n\rangle$, with N electrons, to a state $|m\rangle$, with $N-1$ electrons. Using Fermi's golden rule, this is given by

$$\begin{aligned} \mathrm{I}(\mathbf{k},\omega) &= \frac{2\pi}{\mathcal{Z}} \sum_{nm} e^{-\beta E_n} |\langle m|c_{\mathbf{k}}|n\rangle|^2 \delta(\omega - E_m + E_n) \\ &= n_F(-\omega) A(\mathbf{k}, -\omega). \end{aligned}$$

The spectral function is $A(\mathbf{k},\omega) = \sum_{\alpha\alpha'} A_{\alpha\alpha'}(\mathbf{k},\omega)$ and can be expressed as

$$A_{\alpha\alpha'}(\mathbf{k},\omega) = \left(1 + e^{-\beta\omega}\right) \frac{2\pi}{\mathcal{Z}} \sum_{nm} e^{-\beta E_n} \langle m|c^\dagger_{\mathbf{k}\alpha'}|n\rangle\langle n|c_{\mathbf{k}\alpha}|m\rangle \delta(\omega - E_m + E_n) \tag{4.15}$$

where $n_F(\omega)$ is the Fermi-Dirac distribution, $n_F(\omega) = (1 + e^{\beta\omega})^{-1}$.
If we replace the transition operator $c_{\mathbf{k}}$ with the creation operator $c^\dagger_{\mathbf{k}}$, we get the intensity $\mathrm{I}(\mathbf{k},\omega) = n_F(\omega) A(\mathbf{k},\omega)$ of the opposite process: Electrons shot on a material causing emission of photons. These experimental technique, called inverse photoemission spectroscopy (IPES), is used to measure $A(\mathbf{k},\omega)$ for unoccupied states.

4.3.2 Scanning tunneling microscopy and spectroscopy

The density of states $\rho(\omega)$ and, with limitations, its momentum dependence $A(\mathbf{k},\omega)$ are also accessible by scanning tunneling microscopy (STM) and spectroscopy (STS). In both methods [25] a metallic tip scans the surface of a material in a plane (x-y-direction). The experiment measures the tunneling current through the tip

$$I \sim \int_{-\infty}^{\infty} \mathrm{d}\omega\, \rho(\omega) \left[n_F(\omega) - n_F(\omega - V_{\mathrm{bias}})\right], \tag{4.16}$$

which results from a bias voltage V_{bias} applied between tip and surface. In the STM, the tip moves in x-y-direction and the z-direction is adjusted by a feedback loop, which keeps the tunneling current I constant. By recording the z-displacement, a topographical map of the surface is drawn. This is related to the integrated density of states via (4.16).
The STS measures the derivative of (4.16), the differential conductance

$$\left.\frac{\mathrm{d}I}{\mathrm{d}V}\right|_{V=V_{\mathrm{bias}}} \sim \int_{-\infty}^{\infty} \mathrm{d}\omega\, \rho(\omega) \left.\frac{\partial n_F(\omega - V)}{\partial V}\right|_{V=V_{\mathrm{bias}}}.$$

For low temperatures the derivative $\partial n_F/\partial V$ is a sharp peak at V_{bias}. This allows direct measurement of the density of states. A disadvantage of STM and STS is that they are restricted to two dimensions, because they work at the surface.

The methods introduced so far measure excitations between states with different numbers of electrons. In the following we discuss how to measure magnetic excitations described by two-particle Green functions.

4.3.3 Scattering experiments

In scattering experiments, like inelastic neutron scattering (INS) [26] and resonant inelastic X-ray scattering (RIXS) [27], a particle beam is directed to a target material. After scattering at the target, the particles are detected. In INS the particles are neutrons, in RIXS they are X-ray photons. The particles start with a momentum $\mathbf{k}$ and energy E; after they scattered at the target they reach the detector with a momentum $\mathbf{k}'$ and energy E'. Because of momentum and energy conservation, the difference of momentum $\mathbf{q} = \mathbf{k}' - \mathbf{k}$ and energy gain $\omega = E' - E$ results from the scattering process inside the target.

We first focus on the INS [26]. Because a neutron carries no electrical charge, it can penetrate deep into the sample. The neutrons carry a magnetic moment, which can interact with magnetic moments in the sample, especially with the spin of the electrons. INS is therefore used to study magnetic properties like the magnetic order and spin waves. We calculate the measured intensity after magnetic scattering events by

$$\begin{aligned} \mathrm{I}^{\nu\nu}(\mathbf{k},\omega) &= \frac{2\pi}{\mathcal{Z}} \sum_{nm} e^{-\beta E_n} |\langle m|\Delta M^{\nu}(\mathbf{q})|n\rangle|^2 \delta(\omega - E_m + E_n) \\ &= S^{\nu\nu}(\mathbf{q},\omega). \end{aligned}$$

This resembles the intensity formula of the PES, but with the correlation function $S^{\nu\nu}(\mathbf{q},\omega)$ instead of $A(\mathbf{k},\omega)$. The spin correlation function or dynamical spin structure factor $S^{\nu\nu'}(\mathbf{q},\omega)$ follows from its general form

$$S_{P_\nu O_{\nu'}}(\mathbf{q},\omega) = \frac{2\pi}{\mathcal{Z}} \sum_{nm} e^{-\beta E_n} P_\nu^{nm}(\mathbf{q}) O_{\nu'}^{mn}(-\mathbf{q}) \delta(\omega - E_m + E_n) \tag{4.17}$$

with the matrix elements $P_\nu^{nm}(\mathbf{q}) = \langle n|\Delta P_\nu(\mathbf{q})|m\rangle$ and $O_\nu^{nm}(\mathbf{q}) = \langle n|\Delta O_\nu(\mathbf{q})|m\rangle$, by setting $P_\nu = O_\nu = M_\nu$ with $\mathbf{M}$ being the magnetization operator.

Because of the steady improvement of X-ray sources and photon detectors, RIXS [27] is nowadays used to investigate a broad range of excitations like phonons, magnons and orbital excitations.
A simplified description of the microscopic process is the following: The incoming X-ray photons resonate with absorption edges high above the Fermi level. For example, for Cu^{2+} ions the copper K ($\sim 9\,\mathrm{keV}$), $L_{2,3}$ ($\sim 900\,\mathrm{eV}$) or $M_{2,3}$ ($\sim 80\,\mathrm{eV}$) edge can be excited. The incoming photon, with momentum $\mathbf{k}$ and energy E, excites an electron from a core level to an empty state. A different electron with high energy decays into the core hole, emitting a photon with momentum $\mathbf{k}'$ and energy E', which is detected. The momentum $\mathbf{q}$ and energy ω is transferred to the system. In addition to this direct process, indirect and thermalization processes are also possible.
Although the interactions are different than in the INS, the scattering phenomena is similar. For magnetic excitations the RIXS also gives access to the correlation function $S^{\nu\nu}(\mathbf{q},\omega)$. In Ref. [28], e.g., the magnon dispersion for La_2CuO_4 was measured with RIXS and compared to an INS measurement from [29].

INS and RIXS are only two types of known scattering experiments. RIXS belongs to the

large group of spectroscopy using electromagnetic waves.[3] Other types of experiments measure transmission, absorption, or reflection. Using visible light optical spectroscopy measures for example the optical conductivity $\sigma^{\nu\nu'}(\mathbf{k},\omega)$ and the dielectric function $\epsilon^{\nu\nu'}(\mathbf{k},\omega)$.

4.3.4 Nuclear magnetic resonance

In addition to INS and RIXS, magnetic properties are measured with nuclear magnetic resonance (NMR) [31]. The idea of the NMR technique is to probe the magnetic properties of the electrons by employing the magnetic moments of the nuclei.
In the experiment, a sample is placed inside a static magnetic field B_0, which aligns the nuclear spins, and an oscillating weaker field B_t, which perturbs the aligned spins. The total nuclear spin $\mathbf{I}$ couples to the electrons by dipole and contact interaction, and also to the orbital angular momentum of the electrons. The interaction Hamiltonian of all three interactions, called hyperfine interactions, has the form

$$H_{NMR} = -\gamma_n \mathbf{I} \cdot \mathbf{B}_{\text{eff}}$$

with γ_n being the nuclear gyromagnetic moment, defined by the nucleus, and $\mathbf{B}_{\text{eff}}$ the effective magnetic field at the nucleus induced by the electrons. For a spin in a magnetic field B the resonant frequency is the Larmor frequency

$$\omega_L = -\gamma_n B.$$

Depending on the material class the Larmor frequency is shifted by different mechanisms. In simple metals, the shift is typically dominated by the contact interaction

$$H_c = A_0 \mathbf{I} \cdot \mathbf{S}\delta(\mathbf{r})$$

and it is named Knight shift. Let the field B_0 align the spins in z-direction. The Knight shift [32] is then given by

$$K_s = \frac{A_0 \gamma_e}{\gamma_n} \operatorname{Re} \chi^{zz}(\mathbf{0},0), \tag{4.18}$$

where A_0 is the hyperfine coupling, and γ_e is the gyromagnetic moment of the electron.
When the oscillating external field B_t is switched off, the spins return to their initial orientation. The spin-lattice relaxation time T_1 is the time it takes the spins to return to their equilibrium state, and is given by [33]

$$\frac{1}{T_1} = \lim_{\omega \to 0} \frac{1}{\beta} \frac{\gamma_n^2}{2N_{\mathbf{q}}} \sum_{\mathbf{q}} F_\perp(\mathbf{q}) F_\perp(-\mathbf{q}) \frac{\operatorname{Im} \chi^\perp(\mathbf{q},\omega)}{\omega}. \tag{4.19}$$

The susceptibility $\chi^\perp = \chi^{\downarrow\uparrow\uparrow\downarrow}$ is the transverse susceptibility and $F_\perp(\mathbf{q})$ the form factor for a transverse magnetic field.

[3] A very short introduction and examples are given in [30].

4.4 Generalized susceptibility

4.4.1 Lattice susceptibility from Bethe-Salpeter equation

In this section we introduce the lattice susceptibility in real and reciprocal (momentum) space. Here, we write the indices i for lattice sites and $\mathbf{k}$, $\mathbf{q}$ for momenta explicitly and represent spin σ, orbital m and site s by the combined indices α, α', γ and γ'. To define the momentum dependent susceptibility, we start with the two-particle lattice Green function in real space and Matsubara frequencies

$$\mathcal{C}^{\alpha\alpha'\gamma\gamma'}_{nn'}(\mathbf{T}_{i_1},\mathbf{T}_{i_2},\mathbf{T}_{i_3},\mathbf{T}_{i_4},i\omega_m) = \langle c_{i_1,\alpha}(i\nu_n)c^\dagger_{i_2,\alpha'}(i\nu_n+i\omega_m)c_{i_3,\gamma}(i\nu_{n'}+i\omega_m)c^\dagger_{i_4,\gamma'}(i\nu_{n'})\rangle.$$

The Fourier transform from imaginary time to the bosonic Matsubara frequency $\omega_m = 2m\pi/\beta$ and the fermionic Matsubara frequencies $\nu_n = (2n+1)\pi/\beta$ was obtained by (4.14). The vectors

$$\mathbf{T}_i = n_1\mathbf{a}_1 + n_2\mathbf{a}_2 + n_3\mathbf{a}_3$$

are lattice vectors, and $\mathbf{a}_j$ unit cell vectors, while $n_j \in \mathbb{Z}$. The creation $c^\dagger_{i,\alpha}$ and annihilation operators $c_{i,\alpha}$ act on the lattice site i. For unit cells with more than one equivalent atom the atoms inside the cell are identified by a vector $\mathbf{r}_s$. Because only the lattice is transformed to momentum space, we first leave the site index s implicit in the α, α', γ and γ'. Using the momentum space representation of the operators

$$c_{i,\alpha} = \frac{1}{N_\mathbf{k}}\sum_\mathbf{k} e^{-i\mathbf{T}_i\mathbf{k}}c_{\mathbf{k},\alpha} \quad , \quad c^\dagger_{i,\alpha} = \frac{1}{N_\mathbf{k}}\sum_\mathbf{k} e^{i\mathbf{T}_i\mathbf{k}}c^\dagger_{\mathbf{k},\alpha}$$

with the number of $\mathbf{k}$-points $N_\mathbf{k}$, we get the lattice susceptibility in terms of momenta

$$\begin{aligned}\mathcal{C}^{\alpha\alpha'\gamma\gamma'}_{nn'}(\mathbf{T}_{i_1},\mathbf{T}_{i_2},\mathbf{T}_{i_3},\mathbf{T}_{i_4}) = \frac{1}{N^4_\mathbf{k}}\sum_{\substack{\mathbf{k}_1\mathbf{k}_2\\ \mathbf{k}_3\mathbf{k}_4}} e^{-i\mathbf{T}_{i_1}\mathbf{k}_1+i\mathbf{T}_{i_2}\mathbf{k}_2-i\mathbf{T}_{i_3}\mathbf{k}_3+i\mathbf{T}_{i_4}\mathbf{k}_4}\times \\ \times\langle c_{\mathbf{k}_1,\alpha}(i\nu_n)c^\dagger_{\mathbf{k}_2,\alpha'}(i\nu_n+i\omega_m)c_{\mathbf{k}_3,\gamma}(i\nu_{n'}+i\omega_m)c^\dagger_{\mathbf{k}_4,\gamma'}(i\nu_{n'})\rangle.\end{aligned}$$

Because of momentum conservation, we can eliminate one momentum by replacing the four momenta $\mathbf{k}_i$ with the three momenta $\mathbf{q}$, $\mathbf{k}$ and $\mathbf{k}'$, mapping $(\mathbf{k}_1,\mathbf{k}_2,\mathbf{k}_3,\mathbf{k}_4)$ to $(\mathbf{k},\mathbf{k}+\mathbf{q},\mathbf{k}'+\mathbf{q},\mathbf{k}')$. This yields

$$\begin{aligned}\chi^{\alpha\alpha'\gamma\gamma'}_{\mathbf{k}n\mathbf{k}'n'}(\mathbf{q},i\omega_m) &= \langle c_{\mathbf{k},\alpha}(i\nu_n)c^\dagger_{\mathbf{k}+\mathbf{q},\alpha'}(i\nu_n+i\omega_m)c_{\mathbf{k}'+\mathbf{q},\gamma}(i\nu_{n'}+i\omega_m)c^\dagger_{\mathbf{k}',\gamma'}(i\nu_{n'})\rangle \\ &\quad - \langle c_{\mathbf{k},\alpha}(i\nu_n)c^\dagger_{\mathbf{k}+\mathbf{q},\alpha'}(i\nu_n+i\omega_m)\rangle\langle c_{\mathbf{k}'+\mathbf{q},\gamma}(i\nu_{n'}+i\omega_m)c^\dagger_{\mathbf{k}',\gamma'}(i\nu_{n'})\rangle \\ &= \mathcal{C}^{\alpha\alpha'\gamma\gamma'}_{\mathbf{k}n\mathbf{k}'n'}(\mathbf{q},i\omega_m) - N_\mathbf{q}\beta\delta_{\mathbf{q},\mathbf{G}}\delta_{0,m}G^{\alpha\alpha'}_\mathbf{k}(i\nu_n)G^{\gamma\gamma'}_{\mathbf{k}'}(i\nu_{n'}).\end{aligned} \tag{4.20}$$

Here we used $\sum_i e^{i\mathbf{T}_i\cdot\mathbf{q}} = N_\mathbf{q}\delta_{\mathbf{q},\mathbf{G}}$ with the number of $\mathbf{q}$-points $N_\mathbf{q}$ and $\mathbf{G}$ being a reciprocal lattice vector. The same transformations can also be applied to the bare lattice susceptibility, obtaining

$$\begin{aligned}\chi^{0,\alpha\alpha'\gamma\gamma'}_{\mathbf{k}n\mathbf{k}'n'}(\mathbf{q},i\omega_m) &= -N_\mathbf{k}\beta\delta_{n,n'}\delta_{\mathbf{k},\mathbf{k}'}\times \\ &\quad\times\langle c_{\mathbf{k},\alpha}(i\nu_n)c^\dagger_{\mathbf{k},\gamma'}(i\nu_n)\rangle\langle c_{\mathbf{k}+\mathbf{q},\gamma}(i\nu_n+i\omega_m)c^\dagger_{\mathbf{k}+\mathbf{q},\alpha'}(i\nu_n+i\omega_m)\rangle \\ &= -N_\mathbf{k}\beta\delta_{\mathbf{k},\mathbf{k}'}\delta_{n,n'}G^{\alpha\gamma'}_\mathbf{k}(i\nu_n)G^{\gamma\alpha'}_{\mathbf{k}+\mathbf{q}}(i\nu_n+i\omega_m).\end{aligned} \tag{4.21}$$

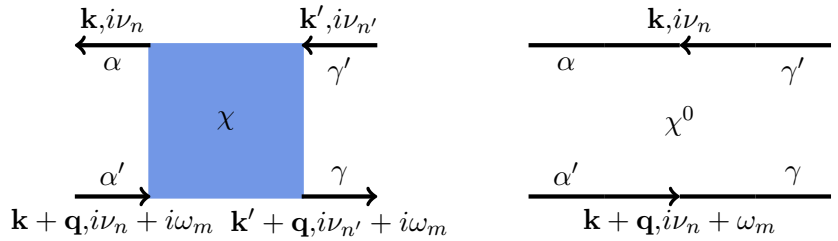

Figure 4.2: Diagrammatic representation of the generalized susceptibility χ and the bare susceptibility χ^0.

At this point we make the connection between the generalized and the physical susceptibility

$$\begin{aligned}\chi_{P_\nu O_{\nu'}}(\mathbf{q},i\omega_m) &= \frac{1}{N_\mathbf{k}^2}\sum_{\mathbf{k}\mathbf{k}'}\frac{1}{\beta^2}\sum_{nn'}\sum_{\substack{\alpha\alpha'\\\gamma\gamma'}}[P_\nu]_{\alpha\alpha'}\,[O_{\nu'}]_{\gamma\gamma'}\,\chi^{\alpha\alpha'\gamma\gamma'}_{\mathbf{k}n\mathbf{k}'n'}(\mathbf{q},i\omega_m)\\ &= \sum_{\substack{\alpha\alpha'\\\gamma\gamma'}}[P_\nu]_{\alpha\alpha'}\,[O_{\nu'}]_{\gamma\gamma'}\,\chi^{\alpha\alpha'\gamma\gamma'}(\mathbf{q},i\omega_m),\end{aligned}$$

where α, α', γ and γ' are combined indices (σ,s,m). The full susceptibility χ can be written in terms of the bare susceptibility χ^0 and the vertex function Γ using the Bethe-Salpeter equation (BSEQ). To present it in a compact form, we introduce the new indices $\bar{q} = (\mathbf{q},i\omega_m)$, $\bar{k} = (\mathbf{k},i\nu_n,\alpha,\alpha')$ and $\bar{k}' = (\mathbf{k}',i\nu_{n'},\gamma,\gamma')$, as well as the intermediate summation indices $\bar{\kappa}$ and $\bar{\kappa}'$ similar to $\bar{k}$ and $\bar{k}'$. With these abbreviations, we write the Bethe-Salpeter equation as

$$\chi_{\bar{k}\bar{k}'}(\bar{q}) = \chi^0_{\bar{k}\bar{k}'}(\bar{q}) + \frac{1}{(\beta N_\mathbf{k})^2}\sum_{\bar{\kappa}\bar{\kappa}'}\chi^0_{\bar{k}\bar{\kappa}'}(\bar{q})\Gamma_{\bar{\kappa}\bar{\kappa}'}(\bar{q})\chi_{\bar{\kappa}\bar{k}'}(\bar{q}).$$

The BSEQ is the two-particle function equivalent to the Dyson equation (2.16) for single-particle functions. The vertex function Γ in the BSEQ plays the role of the self-energy in the Dyson equation.

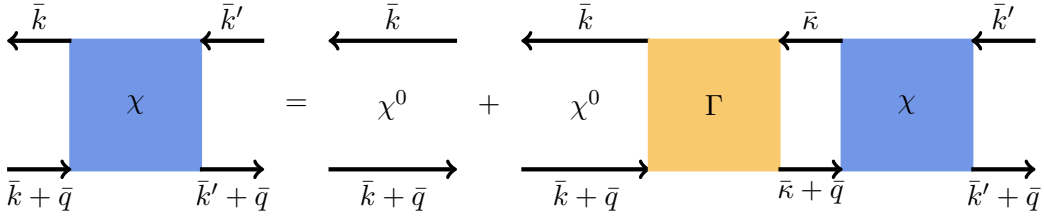

Figure 4.3: Diagrammatic representation of the Bethe-Salpeter equation. Note that $\bar{\kappa}'$ does not show up, because $\chi^0(\bar{q},\bar{k},\bar{\kappa}') \sim \delta_{\bar{k},\bar{\kappa}'}$.

We write the BSEQ in its compact matrix form

$$[\chi(\mathbf{q},i\omega_m)] = \left[\chi^0(\mathbf{q},i\omega_m)\right] + \left[\chi^0(\mathbf{q},i\omega_m)\right]\left[\Gamma(\mathbf{q},i\omega_m)\right]\left[\chi(\mathbf{q},i\omega_m)\right], \tag{4.22}$$

where the matrix entries of the susceptibility are for example $[\chi(\mathbf{q},i\omega_m)]_{\bar{k}\bar{k}'} = \chi_{\bar{k}\bar{k}'}(\bar{q})$, and similar for χ^0 and Γ. Because the BSEQ (4.22) is a self-consistent equation, we can insert it repeatedly to itself to get higher orders of expansion

$$\begin{aligned}[\chi(\mathbf{q},i\omega_m)] = &\left[\chi^0(\mathbf{q},i\omega_m)\right] + \left[\chi^0(\mathbf{q},i\omega_m)\right][\Gamma(\mathbf{q},i\omega_m)]\left[\chi^0(\mathbf{q},i\omega_m)\right] \\ &+ \left[\chi^0(\mathbf{q},i\omega_m)\right][\Gamma(\mathbf{q},i\omega_m)]\left[\chi^0(\mathbf{q},i\omega_m)\right][\Gamma(\mathbf{q},i\omega_m)]\left[\chi^0(\mathbf{q},i\omega_m)\right] \\ &+ \cdots .\end{aligned}$$

Via DMFT we obtain the lattice Green function $G^{\alpha\alpha'}_{\mathbf{k}}(i\nu_n)$, and therefore the bare lattice susceptibility defined in (4.21). The remaining challenge is to calculate the vertex $\Gamma(\bar{q},\bar{\kappa},\bar{\kappa}')$. The idea within the DMFT framework is to approximate it with its local version

$$\begin{aligned}\Gamma_{\bar{\kappa}\bar{\kappa}'}(\bar{q}) &= \Gamma^{\alpha\alpha'\gamma\gamma'}_{\mathbf{k}n\mathbf{k}n'}(\mathbf{q},i\omega_m) \\ &\approx \frac{1}{N^3_{\mathbf{k}}}\sum_{\mathbf{qkk}'}\Gamma^{\alpha\alpha'\gamma\gamma'}_{\mathbf{k}n\mathbf{k}n'}(\mathbf{q},i\omega_m) \\ &= \Gamma^{\alpha\alpha'\gamma\gamma'}_{nn'}(i\omega_m) \\ &= \Gamma_{\bar{n}\bar{n}'}(i\omega_m).\end{aligned} \tag{4.23}$$

In the last step we introduced new indices $\bar{n} = (i\nu_n,\alpha,\alpha')$ and $\bar{n}' = (i\nu_{n'},\gamma,\gamma')$, which enable us to write the vertex as a matrix with elements $[\Gamma(i\omega_m)]_{\bar{n}\bar{n}'} = \Gamma_{\bar{n}\bar{n}'}(i\omega_m)$. This local vertex approximation is exact in the limit of infinite dimensions [10, 11, 34]. With a local vertex $\Gamma_{\bar{n}\bar{n}'}(i\omega_m)$ in (4.22), the summation over all momenta $\mathbf{k}$ and $\mathbf{k}'$ is performed. This leads to the matrix equation

$$[\chi(\mathbf{q},i\omega_m)] = \left[\chi^0(\mathbf{q},i\omega_m)\right] + \left[\chi^0(\mathbf{q},i\omega_m)\right][\Gamma(i\omega_m)][\chi(\mathbf{q},i\omega_m)], \tag{4.24}$$

with indices $\bar{n}$ and $\bar{n}'$. Similarly, we can obtain the local BSEQ

$$[\chi(i\omega_m)] = \left[\chi^0(i\omega_m)\right] + \left[\chi^0(i\omega_m)\right][\Gamma(i\omega_m)][\chi(i\omega_m)]. \tag{4.25}$$

Both local susceptibility matrices $\left[\chi^0(i\omega_m)\right]$ and $[\chi(i\omega_m)]$ are calculated in DMFT. The local vertex is obtained from these matrices by inversion of (4.25)

$$[\Gamma(i\omega_m)] = \left[\chi^0(i\omega_m)\right]^{-1} - [\chi(i\omega_m)]^{-1} \tag{4.26}$$

with matrix indices $\bar{n}$ and $\bar{n}'$ and matrix inversion $[\cdots]^{-1}$. By inserting (4.26) into (4.24) the lattice susceptibility is finally given by inversion of

$$\begin{aligned}[\chi(\mathbf{q},i\omega_m)]^{-1} &= \left[\chi^0(\mathbf{q},i\omega_m)\right]^{-1} - [\Gamma(i\omega_m)] \\ &= \left[\chi^0(\mathbf{q},i\omega_m)\right]^{-1} - \left[\chi^0(i\omega_m)\right]^{-1} + [\chi(i\omega_m)]^{-1}\end{aligned} \tag{4.27}$$

with indices $\bar{n}$ and $\bar{n}'$.
To study real materials, we often need to work with supercells, which contain more than one equivalent correlated sites. The bare lattice susceptibility is then still given by equation (4.21) using a matrix Green function (2.18) in the sites.

To give an example, we consider a system with two sites per supercell. With the shortcut notation $\chi_{s_1s_2s_3s_4} = \chi^{\sigma_1 s_1 m_1,\sigma_2 s_2 m_2,\sigma_3 s_3 m_3,\sigma_4 s_4 m_4}(\mathbf{q},i\omega_m)$, and similar for $\chi^0(\mathbf{q},i\omega_m)$ and $\Gamma(i\omega_m)$, the inverse BSEQ is given by

$$\begin{pmatrix} \chi_{1111} & \chi_{1112} & \chi_{1121} & \chi_{1122} \\ \chi_{1211} & \chi_{1212} & \chi_{1221} & \chi_{1222} \\ \chi_{2111} & \chi_{2112} & \chi_{2121} & \chi_{2122} \\ \chi_{2211} & \chi_{2212} & \chi_{2221} & \chi_{2222} \end{pmatrix}^{-1} = \begin{pmatrix} \chi^0_{1111} & \chi^0_{1112} & \chi^0_{1121} & \chi^0_{1122} \\ \chi^0_{1211} & \chi^0_{1212} & \chi^0_{1221} & \chi^0_{1222} \\ \chi^0_{2111} & \chi^0_{2112} & \chi^0_{2121} & \chi^0_{2122} \\ \chi^0_{2211} & \chi^0_{2212} & \chi^0_{2221} & \chi^0_{2222} \end{pmatrix}^{-1} - \begin{pmatrix} \Gamma_{1111} & 0 & 0 & 0 \\ 0 & 0 & 0 & 0 \\ 0 & 0 & 0 & 0 \\ 0 & 0 & 0 & \Gamma_{2222} \end{pmatrix}$$

where each entry of the matrix is a matrix itself in the remaining indices.
In order to upfold to the small unit cell we use

$$\chi^{\sigma_1\sigma_2\sigma_3\sigma_4}_{m_1m_2m_3m_4}(\mathbf{q},i\omega_m) = \frac{1}{N_s}\sum_{ss'} e^{i\phi_{ss'}}\chi^{\sigma_1 s m_1,\sigma_2 s m_2,\sigma_3 s' m_3,\sigma_4 s' m_4}(\mathbf{q},i\omega_m)$$

with N_s being the number of sites and the phase factor $e^{i\phi_{ss'}}$, which is related to the site off-diagonal terms of the Hamiltonian.
The remaining summation of the spin σ and orbital m

$$\chi_{P_\nu O_{\nu'}}(\mathbf{q},i\omega_m) = \sum_{\substack{m_1m_2\\m_3m_4}}\sum_{\substack{\sigma_1\sigma_2\\\sigma_3\sigma_4}} [P_\nu]_{\sigma_1 m_1\sigma_2 m_2}\,[O_{\nu'}]_{\sigma_3 m_3\sigma_4 m_4}\,\chi^{\sigma_1\sigma_2\sigma_3\sigma_4}_{m_1m_2m_3m_4}(\mathbf{q},i\omega_m), \tag{4.28}$$

is explained in the next two sections.

4.4.2 Magnetic susceptibility

The magnetic susceptibility describes the response of the magnetic moments of a system to an external magnetic field. The associated magnetization operator is given as $\mathbf{M} = -g\mu_B\mathbf{S}$ in terms of the spin operator $\mathbf{S}$. In atomic units the Bohr magneton is $\mu_B = \frac{1}{2}$ and the electron spin g-factor is $g \approx 2$, so that $\mathbf{M} \approx -\mathbf{S}$. The three components $S_\nu = \frac{1}{2}\sigma_\nu$, with $\nu \in \{x,y,z\}$, are given in terms of the Pauli matrices, which are defined as

$$\sigma_x = \begin{pmatrix} 0 & 1 \\ 1 & 0 \end{pmatrix} \quad , \quad \sigma_y = \begin{pmatrix} 0 & -i \\ i & 0 \end{pmatrix} \quad \text{and} \quad \sigma_z = \begin{pmatrix} 1 & 0 \\ 0 & -1 \end{pmatrix}$$

in the basis $|\uparrow\rangle = (1,0)^T$ and $|\downarrow\rangle = (0,1)^T$. In second quantization the total spin operators for all orbitals are

$$S_\nu = \frac{1}{2}\sum_{\sigma\sigma'}\sum_m c^\dagger_{\sigma m}\,[\sigma_\nu]_{\sigma\sigma'}\,c_{\sigma' m}.$$

The indices σ and σ' of the spin sum take the values $\uparrow = 1$ and $\downarrow = 2$. Using the spin operators in (4.28) the spin susceptibility is the correlation function of spin operators

$$\begin{aligned}\chi^{\nu\nu'}(\mathbf{q},i\omega_m) &= \frac{1}{4}\sum_{\substack{\sigma_1\sigma_2\\\sigma_3\sigma_4}} [\sigma_\nu]_{\sigma_2\sigma_1}\,[\sigma_{\nu'}]_{\sigma_4\sigma_3}\sum_{mm'}\chi^{\sigma_1\sigma_2\sigma_3\sigma_4}_{mmm'm'}(\mathbf{q},i\omega_m) \\ &= \frac{1}{4}\sum_{\substack{\sigma_1\sigma_2\\\sigma_3\sigma_4}} [\sigma_\nu]_{\sigma_2\sigma_1}\,[\sigma_{\nu'}]_{\sigma_4\sigma_3}\,\chi^{\sigma_1\sigma_2\sigma_3\sigma_4}(\mathbf{q},i\omega_m).\end{aligned}$$

For simplicity, we do not explicitly write the remaining indices like orbital, site, frequency or momentum and focus on the spin only in the following. By using the abbreviations

$$\chi^{\sigma\sigma'} = \chi^{\sigma\sigma\sigma'\sigma'} \quad \text{and} \quad \chi^{\bar{\sigma}\bar{\sigma}'} = \chi^{\sigma-\sigma\sigma'-\sigma'}$$

the susceptibilities proportional to $\langle S_\alpha S_\alpha \rangle$ with $\alpha \in \{x,y,z\}$ are

$$\chi^{xx} = \frac{1}{4}\sum_{\sigma\sigma'} \chi^{\bar{\sigma}\bar{\sigma}'} \tag{4.29}$$

$$\chi^{yy} = \frac{1}{4}\sum_{\sigma\sigma'} (-1)^{\sigma+\sigma'} \chi^{\bar{\sigma}\bar{\sigma}'} \tag{4.30}$$

$$\chi^{zz} = \frac{1}{4}\sum_{\sigma\sigma'} (-1)^{\sigma+\sigma'} \chi^{\sigma\sigma'}. \tag{4.31}$$

In the paramagnetic phase, where the system has SU(2) symmetry, the Green function is spin diagonal $G_{\sigma\sigma'} = \delta_{\sigma,\sigma'} G_\sigma$ and the susceptibility can be reduced to six entries [35, 36]

$$\begin{pmatrix} \chi^{\uparrow\uparrow\uparrow\uparrow} & \chi^{\uparrow\uparrow\uparrow\downarrow} & \chi^{\uparrow\uparrow\downarrow\uparrow} & \chi^{\uparrow\uparrow\downarrow\downarrow} \\ \chi^{\uparrow\downarrow\uparrow\uparrow} & \chi^{\uparrow\downarrow\uparrow\downarrow} & \chi^{\uparrow\downarrow\downarrow\uparrow} & \chi^{\uparrow\downarrow\downarrow\downarrow} \\ \chi^{\downarrow\uparrow\uparrow\uparrow} & \chi^{\downarrow\uparrow\uparrow\downarrow} & \chi^{\downarrow\uparrow\downarrow\uparrow} & \chi^{\downarrow\uparrow\downarrow\downarrow} \\ \chi^{\downarrow\downarrow\uparrow\uparrow} & \chi^{\downarrow\downarrow\uparrow\downarrow} & \chi^{\downarrow\downarrow\downarrow\uparrow} & \chi^{\downarrow\downarrow\downarrow\downarrow} \end{pmatrix} = \begin{pmatrix} \chi^{\uparrow\uparrow} & 0 & 0 & \chi^{\uparrow\downarrow} \\ 0 & 0 & \chi^{\bar{\uparrow}\bar{\downarrow}} & 0 \\ 0 & \chi^{\bar{\downarrow}\bar{\uparrow}} & 0 & 0 \\ \chi^{\downarrow\uparrow} & 0 & 0 & \chi^{\downarrow\downarrow} \end{pmatrix}$$

of which only three are distinct, because

$$\chi^{\uparrow\uparrow} = \chi^{\downarrow\downarrow} \quad , \quad \chi^{\uparrow\downarrow} = \chi^{\downarrow\uparrow} \quad \text{and} \quad \chi^{\bar{\uparrow}\bar{\downarrow}} = \chi^{\bar{\downarrow}\bar{\uparrow}}.$$

Here, $\chi^{\sigma\sigma'} = \chi^{\sigma\sigma\sigma'\sigma'}$ are the spin longitudinal and $\chi^{\bar{\sigma}\bar{\sigma}'} = \chi^{\bar{\sigma}\bar{\sigma}'\bar{\sigma}'\bar{\sigma}}$ the transverse parts. Since the system is invariant under spin rotations we have

$$\chi^{xx} = \chi^{yy} = \chi^{zz}.$$

This relates the spin longitudinal and transverse parts

$$\chi^{\uparrow\uparrow} - \chi^{\uparrow\downarrow} = \chi^{\bar{\uparrow}\bar{\downarrow}}.$$

In the actual implementation we speed up calculations by either calculating the longitudinal terms $\chi^{\uparrow\uparrow}$ and $\chi^{\uparrow\downarrow}$ or the transverse term $\chi^{\bar{\uparrow}\bar{\downarrow}}$ only.
Furthermore, the mean-field contribution is zero in the paramagnetic case.
The Bethe-Salpeter equation (BSEQ) is also simpler in this limit. For the longitudinal terms [37]

$$[\chi^{zz}(\mathbf{q},i\omega_m)]^{-1} = \left[\chi^{0,zz}(\mathbf{q},i\omega_m)\right]^{-1} - \left[\chi^{0,zz}(i\omega_m)\right]^{-1} + [\chi^{zz}(i\omega_m)]^{-1},$$

where $\chi^{zz}(\mathbf{q},i\omega_m)$ is obtained by (4.31). For the transverse terms instead

$$\left[\chi^{\bar{\sigma}\bar{\sigma}'}(\mathbf{q},i\omega_m)\right]^{-1} = \left[\chi^{0,\bar{\sigma}\bar{\sigma}'}(\mathbf{q},i\omega_m)\right]^{-1} - \left[\chi^{0,\bar{\sigma}\bar{\sigma}'}(i\omega_m)\right]^{-1} + \left[\chi^{\bar{\sigma}\bar{\sigma}'}(i\omega_m)\right]^{-1}.$$

From $\chi^{\bar{\sigma}\bar{\sigma}'}(\mathbf{q},i\omega_m)$ we then obtain $\chi^{xx}(\mathbf{q},i\omega_m)$ by (4.29) and $\chi^{yy}(\mathbf{q},i\omega_m)$ by (4.30).
In a magnetically ordered phase the spin symmetry of the susceptibility is lower. With spins aligned in z-direction the susceptibility can be split into spin longitudinal $\chi^{\sigma\sigma'}$ and transverse $\chi^{\bar{\sigma}\bar{\sigma}'}$ parts. However, $G_\uparrow \neq G_\downarrow$, $\chi^{xx} = \chi^{yy} \neq \chi^{zz}$ and $\chi^{\uparrow\uparrow} \neq \chi^{\downarrow\downarrow}$, the spin summation must be done after the BSEQ and the mean-field term does not vanish.

4.4.3 Orbital susceptibility

The orbital susceptibility is defined in analogy to the spin susceptibility. More specifically, for two orbitals we introduce operators $\mathbf{O}$, whose components are $O_\nu = \frac{1}{2}\tau_\nu$ and

$$\tau_x = \begin{pmatrix} 0 & 1 \\ 1 & 0 \end{pmatrix} \quad , \quad \tau_y = \begin{pmatrix} 0 & -i \\ i & 0 \end{pmatrix} \quad \text{and} \quad \tau_z = \begin{pmatrix} 1 & 0 \\ 0 & -1 \end{pmatrix}.$$

Although these matrices are the same as the Pauli matrices, τ_i are defined in the basis $|1\rangle = (1,0)^T$ and $|2\rangle = (0,1)^T$, where 1 and 2 are orbital indices. With the orbital operators

$$O_\nu = \frac{1}{2} \sum_{mm'} \sum_{\sigma} c^\dagger_{\sigma m} \left[\tau_\nu\right]_{mm'} c_{\sigma m'}$$

the compounds of the orbital susceptibility are

$$\begin{aligned} \chi^{\nu\nu'}_{oo}(\mathbf{q},i\omega_m) &= \frac{1}{4} \sum_{\substack{m_1 m_2 \\ m_3 m_4}} \left[\tau_\nu\right]_{m_2 m_1} \left[\tau_{\nu'}\right]_{m_4 m_3} \sum_{\sigma\sigma'} \chi^{\sigma\sigma\sigma'\sigma'}_{m_1 m_2 m_3 m_4}(\mathbf{q},i\omega_m) \\ &= \frac{1}{4} \sum_{\substack{m_1 m_2 \\ m_3 m_4}} \left[\tau_\nu\right]_{m_2 m_1} \left[\tau_{\nu'}\right]_{m_4 m_3} \chi_{m_1 m_2 m_3 m_4}(\mathbf{q},i\omega_m). \end{aligned}$$

In the case of the orbital susceptibility, typically, we have to calculate all 16 entries of the susceptibility matrix.
However, using the spin symmetries can help also in the efficient calculation of the orbital susceptibility. The orbital susceptibility is calculated only from the longitudinal spin parts of the susceptibility $\chi^{\sigma\sigma'}_{m_1 m_2 m_3 m_4}$. Furthermore, in the calculation of the orbital susceptibility for a spin SU(2) symmetric system the spin summation can be done before using the Bethe-Salpeter equation. This is shown in the appendix A.3.

4.5 Basis choice for the susceptibility

4.5.1 Imaginary time formalism

In this section we describe the properties of imaginary time single- and two-particle Green functions and susceptibilities [22,37,38]. The properties of the two-particle Green function and the susceptibility are the same, except for some cases, which we will mention explicitly. The time-ordering operator $\mathcal{T}$ sorts the times in ascending order from right to left. Each permutation of two fermionic operators c or $c^\dagger$, due to time-ordering, leads to a minus sign prefactor. Explicitly the effect of $\mathcal{T}$ is shown here for the single-particle Green function in terms of θ step functions:

$$G_{\alpha\alpha'}(\tau_1,\tau_2) = -\theta(\tau_1 - \tau_2)\langle c_\alpha(\tau_1) c^\dagger_{\alpha'}(\tau_2)\rangle + \theta(\tau_2 - \tau_1)\langle c^\dagger_{\alpha'}(\tau_2) c_\alpha(\tau_1)\rangle$$

For a time translational invariant Hamiltonian, as the one considered in this thesis, a shift in all times leaves the Green function and susceptibility invariant. Using the invariance of

the trace under cyclic permutation of operators, we show then

$$\begin{aligned} G_{\alpha\alpha'}(\tau_1,\tau_2) &= -\frac{1}{\mathcal{Z}}\mathrm{Tr}\left[e^{-\beta H}c_\alpha(\tau_1)c^\dagger_{\alpha'}(\tau_2)\right] \\ &= -\frac{1}{\mathcal{Z}}\mathrm{Tr}\left[e^{-\beta H}e^{\tau_1 H}c_\alpha e^{(\tau_2-\tau_1)H}c^\dagger_{\alpha'}e^{-\tau_2 H}\right] \\ &= -\frac{1}{\mathcal{Z}}\mathrm{Tr}\left[e^{-\beta H}e^{(\tau_1-\tau_2)H}c_\alpha e^{-(\tau_1-\tau_2)H}c^\dagger_{\alpha'}\right] \\ &= G_{\alpha\alpha'}(\tau_{12}) \end{aligned} \tag{4.32}$$

for the single-particle Green function in the sector $\tau_1 > \tau_2$, and where $\tau_{ij} = \tau_i - \tau_j$. The same holds also in the sector $\tau_2 > \tau_1$. Due to the time-ordering operator $\mathcal{T}$, the Green function $G_{\alpha\alpha'}(\tau_1,\tau_2)$ has a discontinuity at $\tau_1 = \tau_2$, which translates into a discontinuity at $\tau_{12} = 0$ in $G_{\alpha\alpha'}(\tau_{12})$. For the two-particle Green function we can shift all times by subtracting τ_4 and, using the same steps as for the single-particle Green function, reduce the four time arguments to three

$$\begin{aligned} \chi_{\alpha\alpha'\gamma\gamma'}(\tau_1,\tau_2,\tau_3,\tau_4) &= \chi_{\alpha\alpha'\gamma\gamma'}(\tau_{14},\tau_{24},\tau_{34},0) \\ &= \chi_{\alpha\alpha'\gamma\gamma'}(\tau_{12}+\tau_{23}+\tau_{34},\tau_{23}+\tau_{34},\tau_{34},0) \\ &:= \chi_{\alpha\alpha'\gamma\gamma'}(\tau_{12},\tau_{34};\tau_{23}). \end{aligned} \tag{4.33}$$

The latter can be expressed in terms of the two-particle Green function

$$\mathcal{C}_{\alpha\alpha'\gamma\gamma'}(\tau_{12},\tau_{34};\tau_{23}) = \langle \mathcal{T} e^{-H\tau_{41}}c_\alpha e^{-H\tau_{12}}c^\dagger_{\alpha'}e^{-H\tau_{23}}c_\gamma e^{-H\tau_{34}}c^\dagger_{\gamma'}\rangle, \tag{4.34}$$

where $-\tau_{41} = \tau_{14} = \tau_{12} + \tau_{23} + \tau_{34}$, and the single-particle Green functions as

$$\chi_{\alpha\alpha'\gamma\gamma'}(\tau_{12},\tau_{34};\tau_{23}) = \mathcal{C}_{\alpha\alpha'\gamma\gamma'}(\tau_{12},\tau_{34};\tau_{23}) - G_{\alpha\alpha'}(\tau_{12})G_{\gamma\gamma'}(\tau_{34}). \tag{4.35}$$

With the same choice of times, the bare susceptibility can be written in terms of Green functions

$$\begin{aligned} \chi^0_{\alpha\alpha'\gamma\gamma'}(\tau_{12},\tau_{34};\tau_{23}) &= -G_{\alpha\gamma'}(\tau_{14})G_{\gamma\alpha'}(\tau_{32}) \\ &= -G_{\alpha\gamma'}(\tau_{12}+\tau_{23}+\tau_{34})G_{\gamma\alpha'}(-\tau_{23}). \end{aligned} \tag{4.36}$$

Here we used the Wick's theorem to expand the susceptibility in single-particle Green functions, and we subtracted the mean-field term $G_{\alpha\alpha'}(\tau_{12})G_{\gamma\gamma'}(\tau_{34})$. The susceptibility $\chi_{\alpha\alpha'\gamma\gamma'}(\tau_1,\tau_2,\tau_3,\tau_4)$ has discontinuities for $\tau_i = \tau_j$, which leads to discontinuities in $\chi_{\alpha\alpha'\gamma\gamma'}(\tau_{12},\tau_{34};\tau_{23})$. This is easy to see for $\chi^0_{\alpha\alpha'\gamma\gamma'}(\tau_{12},\tau_{34};\tau_{23})$, when considering the discontinuities of the single-particle Green functions.
The single-particle Green function is defined only on the interval $\tau_{12} \in]-\beta,\beta[$. Outside the convergence is not guaranteed. To show this we first consider the Lehmann representation in imaginary time

$$G_{\alpha\alpha'}(\tau_{12}) = -\frac{1}{\mathcal{Z}}\sum_{n_1 n_2}\langle n_1|c_\alpha|n_2\rangle\langle n_2|c^\dagger_{\alpha'}|n_1\rangle e^{-(\beta-\tau_{12})E_{n_1}-\tau_{12}E_{n_2}} \tag{4.37}$$

in the domain $\tau_{12} > 0$ with eigenenergies E_n and eigenstates $|n\rangle$. For arbitrarily large E_n the exponential $\exp(-(\beta-\tau_{12})E_n)$ vanishes only for $\tau_{12} < \beta$; only under this condition

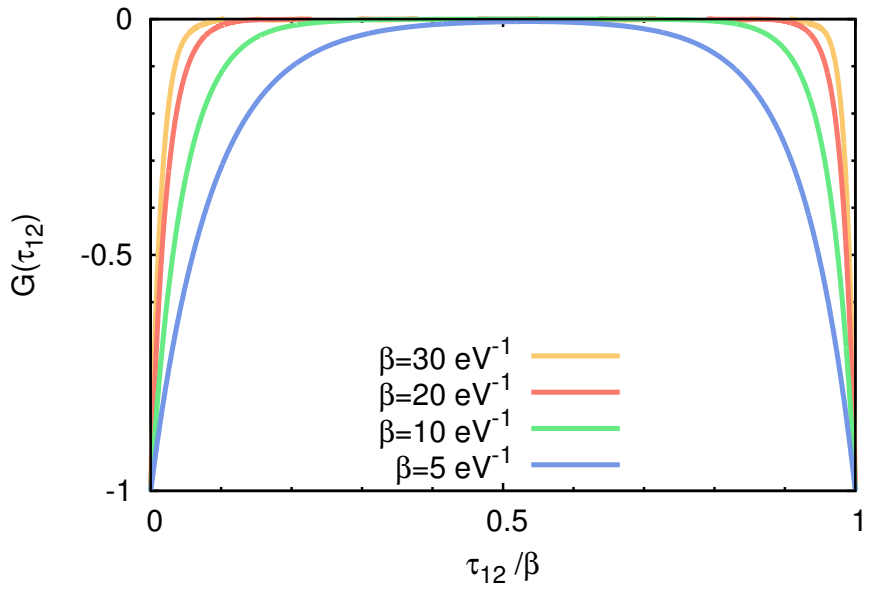

Figure 4.4: Green function $G(\tau_{12})$ for the one-band material $VOMoO_4$ at different inverse temperatures β and a Coulomb interaction $U = 5\,\mathrm{eV}$.

$G_{\alpha\alpha'}(\tau_{12})$ converges to a finite value. Correspondingly, for $\tau_{12} < 0$ the sum converges only if $\tau_{12} > -\beta$. However, we can restrict all the time τ_{12} to $\tau_{12} \in [0,\beta[$ by using the cyclic invariance of the trace. For $-\beta < \tau_{12} < 0$

$$\begin{aligned} G_{\alpha\alpha'}(\tau_{12}+\beta) &= -\frac{1}{\mathcal{Z}}\mathrm{Tr}\left[e^{-\beta H}e^{(\tau_{12}+\beta)H}c_\alpha e^{-(\tau_{12}+\beta)H}c^\dagger_{\alpha'}\right] \\ &= -\frac{1}{\mathcal{Z}}\mathrm{Tr}\left[e^{-\beta H}c^\dagger_{\alpha'}e^{\tau_{12}H}c_\alpha e^{-\tau_{12}H}\right] \\ &= -G_{\alpha\alpha'}(\tau_{12}). \end{aligned}$$

Additionally, we extend $G_{\alpha\alpha'}(\tau_{12})$ periodically to $\tau_{12} \in \mathbb{R}$, which will be advantageous when expanding the Green functions in Fourier series. We thus have

$$\begin{aligned} G_{\alpha\alpha'}(\tau_1 + n_1\beta,\tau_2 + n_2\beta) &= (-1)^{n_1+n_2}G_{\alpha\alpha'}(\tau_1,\tau_2) \\ G_{\alpha\alpha'}(\tau_{12} + n_1\beta) &= (-1)^{n_1}G_{\alpha\alpha'}(\tau_{12}) \end{aligned} \tag{4.38}$$

for $n_i \in \mathbb{Z}$, which is β-antiperiodic in τ_i or τ_{ij}.
Similar periodicity relations can be derived for the two-particle Green function. Let $\tau_1 < 0$ and $\beta > \tau_1 + \beta > \tau_2 > \tau_3 > \tau_4 > 0$ then the operators are time ordered

$$\begin{aligned} \mathcal{C}_{\alpha\alpha'\gamma\gamma'}(\tau_1+\beta,\tau_2,\tau_3,\tau_4) &= \frac{1}{\mathcal{Z}}\mathrm{Tr}\left[\mathcal{T}e^{-\beta H}c_\alpha(\tau_1+\beta)c^\dagger_{\alpha'}(\tau_2)c_\gamma(\tau_3)c^\dagger_{\gamma'}(\tau_4)\right] \\ &= \frac{1}{\mathcal{Z}}\mathrm{Tr}\left[e^{-\beta H}c_\alpha(\tau_1+\beta)c^\dagger_{\alpha'}(\tau_2)c_\gamma(\tau_3)c^\dagger_{\gamma'}(\tau_4)\right] \end{aligned}$$

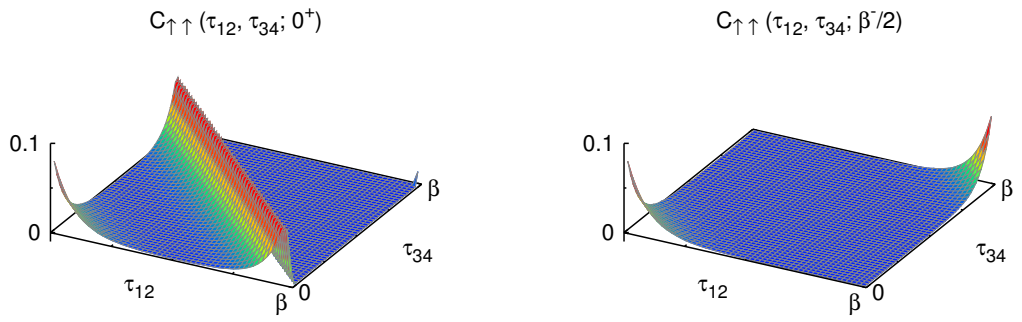

Figure 4.5: Two-particle Green function $\mathcal{C}^{\uparrow\uparrow}(\tau_{12},\tau_{34};\tau_{23})$ for the same case as in figure 4.4.

and by cyclic permutation of the operators inside the trace we eliminate β

$$\begin{aligned}\mathcal{C}_{\alpha\alpha'\gamma\gamma'}(\tau_1+\beta,\tau_2,\tau_3,\tau_4) &= \frac{1}{\mathcal{Z}}\mathrm{Tr}\left[e^{-\beta H}e^{-(\tau_{41}-\beta)H}c_\alpha e^{-(\tau_{12}+\beta)H}c^\dagger_{\alpha'}e^{-\tau_{23}H}c_\gamma e^{-\tau_{34}H}c^\dagger_{\gamma'}\right]\\ &= \frac{1}{\mathcal{Z}}\mathrm{Tr}\left[e^{-\beta H}e^{-\tau_{12}H}c^\dagger_{\alpha'}e^{-\tau_{23}H}c_\gamma e^{-\tau_{34}H}c^\dagger_{\gamma'}e^{-\tau_{41}H}c_\alpha\right]\\ &= \frac{1}{\mathcal{Z}}\mathrm{Tr}\left[e^{-\beta H}c^\dagger_{\alpha'}(\tau_2)c_\gamma(\tau_3)c^\dagger_{\gamma'}(\tau_4)c_\alpha(\tau_1)\right].\end{aligned}$$

This is the negative time-ordered form of the original

$$-\mathcal{C}_{\alpha\alpha'\gamma\gamma'}(\tau_1,\tau_2,\tau_3,\tau_4) = -\frac{1}{\mathcal{Z}}\mathrm{Tr}\left[\mathcal{T}e^{-\beta H}c_\alpha(\tau_1)c^\dagger_{\alpha'}(\tau_2)c_\gamma(\tau_3)c^\dagger_{\gamma'}(\tau_4)\right],$$

where the minus sign is due to time-ordering. With analogous derivations the β-antiperiodicity of $\mathcal{C}_{\alpha\alpha'\gamma\gamma'}(\tau_1,\tau_2,\tau_3,\tau_4)$ for all τ_i, $i \in \{1,2,3,4\}$, can be shown. Like for the single-particle Green function we also periodically extend the domain $\tau_i \in]-\beta,\beta[$ of $\mathcal{C}_{\alpha\alpha'\gamma\gamma'}(\tau_1,\tau_2,\tau_3,\tau_4)$ to all times. This results in β-antiperiodicity in each time

$$\mathcal{C}_{\alpha\alpha'\gamma\gamma'}(\tau_1+n_1\beta,\tau_2+n_2\beta,\tau_3+n_3\beta,\tau_4+n_4\beta) = (-1)^{n_1+n_2+n_3+n_4}\mathcal{C}_{\alpha\alpha'\gamma\gamma'}(\tau_1,\tau_2,\tau_3,\tau_4).$$

Using this we also find β-antiperiodicity in τ_{12} for the two-particle Green function

$$\begin{aligned}\mathcal{C}_{\alpha\alpha'\gamma\gamma'}(\tau_{12}+\beta,\tau_{34};\tau_{23}) &= \mathcal{C}_{\alpha\alpha'\gamma\gamma'}(\tau_{12}+\beta+\tau_{23}+\tau_{34},\tau_{23}+\tau_{34},\tau_{34},0)\\ &= \mathcal{C}_{\alpha\alpha'\gamma\gamma'}(\tau_1+\beta,\tau_2,\tau_3,\tau_4)\\ &= -\mathcal{C}_{\alpha\alpha'\gamma\gamma'}(\tau_{12}+\tau_{23}+\tau_{34},\tau_{23}+\tau_{34},\tau_{34},0)\\ &= -\mathcal{C}_{\alpha\alpha'\gamma\gamma'}(\tau_{12},\tau_{34};\tau_{23})\end{aligned}$$

and β-antiperiodicity in τ_{34}

$$\begin{aligned}\mathcal{C}_{\alpha\alpha'\gamma\gamma'}(\tau_{12},\tau_{34}+\beta;\tau_{23}) &= \mathcal{C}_{\alpha\alpha'\gamma\gamma'}(\tau_{12}+\tau_{23}+\tau_{34}+\beta,\tau_{23}+\tau_{34}+\beta,\tau_{34}+\beta,0)\\ &= \mathcal{C}_{\alpha\alpha'\gamma\gamma'}(\tau_1+\beta,\tau_2+\beta,\tau_3+\beta,\tau_4)\\ &= -\mathcal{C}_{\alpha\alpha'\gamma\gamma'}(\tau_{12}+\tau_{23}+\tau_{34},\tau_{23}+\tau_{34},\tau_{34},0)\\ &= -\mathcal{C}_{\alpha\alpha'\gamma\gamma'}(\tau_{12},\tau_{34};\tau_{23}).\end{aligned}$$

In τ_{23}, however, $\mathcal{C}_{\alpha\alpha'\gamma\gamma'}(\tau_{12},\tau_{34};\tau_{23})$ is β-periodic

$$\begin{aligned}\mathcal{C}_{\alpha\alpha'\gamma\gamma'}(\tau_{12},\tau_{34};\tau_{23}+\beta) &= \mathcal{C}_{\alpha\alpha'\gamma\gamma'}(\tau_{12}+\tau_{23}+\beta+\tau_{34},\tau_{23}+\beta+\tau_{34},\tau_{34},0)\\ &= \mathcal{C}_{\alpha\alpha'\gamma\gamma'}(\tau_1+\beta,\tau_2+\beta,\tau_3,\tau_4)\\ &= \mathcal{C}_{\alpha\alpha'\gamma\gamma'}(\tau_{12}+\tau_{23}+\tau_{34},\tau_{23}+\tau_{34},\tau_{34},0)\\ &= \mathcal{C}_{\alpha\alpha'\gamma\gamma'}(\tau_{12},\tau_{34};\tau_{23}).\end{aligned}$$

So the (anti)periodicity in the combined times τ_{ij} is

$$\mathcal{C}_{\alpha\alpha'\gamma\gamma'}(\tau_{12}+n_1\beta,\tau_{34}+n_2\beta;\tau_{23}+n_3\beta) = (-1)^{n_1+n_2}\mathcal{C}_{\alpha\alpha'\gamma\gamma'}(\tau_{12},\tau_{34};\tau_{23}). \tag{4.39}$$

We call times τ bosonic (fermionic) if Green functions are (anti)periodic in τ, i.e., $\mathcal{C}_{\alpha\alpha'\gamma\gamma'}(\tau_{12},\tau_{34};\tau_{23})$ has two fermionic times τ_{12} and τ_{34} and one bosonic time τ_{23}.
Finally, we make sure that $\mathcal{C}_{\alpha\alpha'\gamma\gamma'}(\tau_{12},\tau_{34};\tau_{23})$ is well defined. For $\tau_4<\tau_3<\tau_2<\tau_1$ we obtain the Lehmann representation

$$\begin{aligned}\mathcal{C}_{\alpha\alpha'\gamma\gamma'}(\tau_{12},\tau_{34};\tau_{23}) = \frac{1}{\mathcal{Z}}\sum_{n_1n_2n_3n_4}&\langle n_1|c_\alpha|n_2\rangle\langle n_2|c^\dagger_{\alpha'}|n_3\rangle\langle n_3|c_\gamma|n_4\rangle\langle n_4|c^\dagger_{\gamma'}|n_1\rangle\times\\ &\times e^{-(\beta-\tau_{14})E_{n_1}-\tau_{12}E_{n_2}-\tau_{23}E_{n_3}-\tau_{34}E_{n_4}}.\end{aligned} \tag{4.40}$$

In this case $0<\tau_{12}$, $0<\tau_{34}$ and $0<\tau_{23}$, which ensures that $0<e^{-\tau_{12}E_{n_2}-\tau_{23}E_{n_3}-\tau_{34}E_{n_4}}<1$. The condition for $\mathcal{C}_{\alpha\alpha'\gamma\gamma'}(\tau_{12},\tau_{34};\tau_{23})$ to be finite is $\tau_{14}=\tau_{12}+\tau_{23}+\tau_{34}<\beta$, because then $0<e^{-(\beta-\tau_{14})E_{n_1}}<1$ [35]. This condition can always be fulfilled for times $\tau_{ij}\in[0,\beta[$ by making use of (4.39).
At the borders $\tau=0^+=\lim_{\delta\to0}\delta$ and $\tau=\beta^-=\lim_{\delta\to0}\beta-\delta$ the Green function takes the special values

$$G_{\alpha\alpha'}(0^+) = -\delta_{\alpha,\alpha'}+n_{\alpha\alpha'} \tag{4.41}$$

$$G_{\alpha\alpha'}(\beta^-) = -n_{\alpha\alpha'} \tag{4.42}$$

with the expectation values

$$n_{\alpha\alpha'} = \langle c^\dagger_\alpha c_{\alpha'}\rangle.$$

For $\alpha=\alpha'$ this is the number of particles of flavor α. To make the connection to experiments, we introduced the physical susceptibility $\chi_{P_\nu O_{\nu'}}(\mathbf{r},\mathbf{r}',\tau,\tau')$ (4.5), which, due to the invariance of the trace under cyclic permutation, can be expressed with one time τ. It is obtained from the generalized susceptibility $\chi_{\alpha\alpha'\gamma\gamma'}(\tau_{12}=0^+,\tau_{34}=0^+;\tau_{23}=\tau)$

$$\begin{aligned}\chi_{P_\nu O_{\nu'}}(\mathbf{r},\mathbf{r}',\tau) &= \chi_{P_\nu O_{\nu'}}(\mathbf{r},\mathbf{r}',\tau,0)\\ &= -\sum_{\substack{\alpha\alpha'\\ \gamma\gamma'}}[P_\nu]_{\alpha\alpha'}[O_{\nu'}]_{\gamma\gamma'}\left(\langle\mathcal{T}c_\alpha(\tau)c^\dagger_{\alpha'}(\tau)c_\gamma c^\dagger_{\gamma'}\rangle-\langle c_\alpha c^\dagger_{\alpha'}\rangle\langle c_\gamma c^\dagger_{\gamma'}\rangle\right)\\ &= -\sum_{\substack{\alpha\alpha'\\ \gamma\gamma'}}[P_\nu]_{\alpha\alpha'}[O_{\nu'}]_{\gamma\gamma'}\chi_{\alpha\alpha'\gamma\gamma'}(0^+,0^+;\tau).\end{aligned} \tag{4.43}$$

In the following we employ the definition of $\mathcal{C}(\tau_{12},\tau_{34};\tau_{23})$ (4.34) to show some properties and symmetries of $\mathcal{C}(\tau_{12},\tau_{34};\tau_{23})$ and $\chi(\tau_{12},\tau_{34};\tau_{23})$ [22, 35, 37]).

1. Complex conjugation inverts the order of indices in the Green function

$$G_{\alpha\alpha'}(\tau_{12}) = [G_{\alpha'\alpha}(\tau_{12})]^* \tag{4.44}$$

and in two-particle Green function also the two fermionic times

$$\begin{aligned}\mathcal{C}_{\alpha\alpha'\gamma\gamma'}(\tau_{12},\tau_{34};\tau_{23}) &= \langle \mathcal{T} e^{-H\tau_{41}} c_{\gamma'} e^{-H\tau_{34}} c_{\gamma}^\dagger e^{-H\tau_{23}} c_{\alpha'} e^{-H\tau_{12}} c_{\alpha}^\dagger \rangle^* \\ &= \left[\mathcal{C}_{\gamma'\gamma\alpha'\alpha}(\tau_{34},\tau_{12};\tau_{23})\right]^*. \end{aligned} \tag{4.45}$$

2. For a Hamiltonian[4] invariant under time reversal, the local Green functions in imaginary time are real for a real basis [35]

$$\begin{aligned}[G_{\alpha\alpha'}(\tau_{12})]^* &= G_{\alpha\alpha'}(\tau_{12}) \\ \left[\mathcal{C}_{\alpha\alpha'\gamma\gamma'}(\tau_{12},\tau_{34};\tau_{23})\right]^* &= \mathcal{C}_{\alpha\alpha'\gamma\gamma'}(\tau_{12},\tau_{34};\tau_{23}).\end{aligned}$$

3. Due to the time-ordering operator $\mathcal{T}$, the α pair can be exchanged with the γ pair.

$$\begin{aligned}\mathcal{C}_{\alpha\alpha'\gamma\gamma'}(\tau_{12},\tau_{34};\tau_{23}) &= \langle \mathcal{T} e^{-H\tau_{23}} c_{\gamma} e^{-H\tau_{34}} c_{\gamma'}^\dagger e^{-H\tau_{41}} c_{\alpha} e^{-H\tau_{12}} c_{\alpha'}^\dagger \rangle \\ &= \mathcal{C}_{\gamma\gamma'\alpha\alpha'}(\tau_{34},\tau_{12};\tau_{41}). \end{aligned} \tag{4.46}$$

4. In the presence of particle-hole symmetry, it is possible to exchange operators $c_\alpha^\dagger$ with c_α. We use this and the (anti)periodicity of the Green functions ($G(\tau_{12}-\beta) = -G(\tau_{12})$ and similar for $\mathcal{C}(\tau_{12},\tau_{34};\tau_{23})$) to get

$$\begin{aligned}G_{\alpha\alpha'}(\tau_{12}) &= G_{\alpha'\alpha}(\beta-\tau_{12}) \\ &= [G_{\alpha\alpha'}(\beta-\tau_{12})]^* \\ \mathcal{C}_{\alpha\alpha'\gamma\gamma'}(\tau_{12},\tau_{34};\tau_{23}) &= \langle \mathcal{T} e^{H\tau_{23}} c_{\alpha'} e^{H\tau_{12}} c_{\alpha}^\dagger e^{H\tau_{41}} c_{\gamma'} e^{H\tau_{34}} c_{\gamma}^\dagger \rangle \\ &= \mathcal{C}_{\alpha'\alpha\gamma'\gamma}(\beta-\tau_{12},\beta-\tau_{34};\beta-\tau_{41}) \\ &= \left[\mathcal{C}_{\alpha\alpha'\gamma\gamma'}(\beta-\tau_{12},\beta-\tau_{34};\beta-\tau_{23})\right]^*. \end{aligned}$$

In the last step we used the complex conjugation relation (4.44) for the Green function $G(\tau_{12})$, and for the two-particle Green function $\mathcal{C}_{\alpha\alpha'\gamma\gamma'}(\tau_{12},\tau_{34};\tau_{23})$ we used the complex conjugation relation (4.45) as well as the pair exchange (4.46).

5. Because of the Pauli principle, we can exchange the annihilation operator c_α with c_γ. This defines the crossing symmetry

$$\begin{aligned}\mathcal{C}_{\alpha\alpha'\gamma\gamma'}(\tau_{12},\tau_{34};\tau_{23}) &= -\langle \mathcal{T} e^{-H\tau_{43}} c_{\gamma} e^{-H\tau_{32}} c_{\alpha'}^\dagger e^{-H\tau_{21}} c_{\alpha} e^{-H\tau_{14}} c_{\gamma'}^\dagger \rangle \\ &= -\mathcal{C}_{\gamma\alpha'\alpha\gamma'}(-\tau_{23},\tau_{12}+\tau_{23}+\tau_{34};-\tau_{12}) \\ &= \mathcal{C}_{\gamma\alpha'\alpha\gamma'}(\beta-\tau_{23},\tau_{12}+\tau_{23}+\tau_{34};\beta-\tau_{12}).\end{aligned}$$

[4] Hamiltonians used in this thesis all have time-reversal symmetry.

4.5.2 Matsubara frequency representation

Because the imaginary time Green functions are periodic for bosonic times and antiperiodic for fermionic times, it is natural to expand them in Fourier series. The Fourier transformation for bosonic times was given in equation (4.13) and its inverse in (4.14). Correspondingly, the transformation of fermionic times is

$$f(i\nu_n) = \int_0^\beta \mathrm{d}\tau\, f(\tau) e^{i\nu_n \tau} \tag{4.47}$$

$$f(\tau) = \frac{1}{\beta} \sum_{n=-\infty}^{\infty} f(i\nu_n) e^{-i\nu_n \tau} \tag{4.48}$$

with the fermionic Matsubara frequencies $\nu_n = (2n+1)\pi/\beta$. Fermionic and bosonic frequencies are a consequence of fermionic and bosonic times. This is explained in appendix A.4.1. Using (4.47) on $G_{\alpha\alpha'}(\tau) = G_{\alpha\alpha'}(\tau_{12})$, we get the Matsubara Green function as

$$G_{\alpha\alpha'}(i\nu_n) = \int_0^\beta \mathrm{d}\tau\, e^{i\nu_n \tau} G_{\alpha\alpha'}(\tau). \tag{4.49}$$

According to (4.48) the expansion of the imaginary time Green function in this coefficients is given by

$$G_{\alpha\alpha'}(\tau) = \frac{1}{\beta} \sum_{n=-\infty}^{\infty} e^{-i\nu_n \tau} G_{\alpha\alpha'}(i\nu_n).$$

For the two-particle Green function and susceptibility we transform all four fermionic times τ_i to fermionic frequencies ν_{n_i}

$$\begin{aligned}\chi_{\alpha\alpha'\gamma\gamma'}(i\nu_{n_1}, i\nu_{n_2}, i\nu_{n_3}, i\nu_{n_4}) = \int_0^\beta \mathrm{d}\tau_1 \int_0^\beta \mathrm{d}\tau_2 \int_0^\beta \mathrm{d}\tau_3 \int_0^\beta \mathrm{d}\tau_4\, e^{i\nu_{n_1}\tau_1 - i\nu_{n_2}\tau_2 + i\nu_{n_3}\tau_3 - i\nu_{n_4}\tau_4} \times \\ \times\, \chi_{\alpha\alpha'\gamma\gamma'}(\tau_1, \tau_2, \tau_3, \tau_4).\end{aligned}$$

In section 4.5.1 we reduced the four time arguments of $\chi_{\alpha\alpha'\gamma\gamma'}(\tau_1, \tau_2, \tau_3, \tau_4)$ to three times τ_{12}, τ_{34} and τ_{23}. Thus, we can reduce the four frequencies ν_{n_i} to three frequencies by

$$(\nu_{n_1}, \nu_{n_2}, \nu_{n_3}, \nu_{n_4}) = (\nu_n, \nu_n + \omega_m, \nu_{n'} + \omega_m, \nu_{n'})$$

and obtain the susceptibility

$$\begin{aligned}\chi_{nn'}^{\alpha\alpha'\gamma\gamma'}(i\omega_m) &:= \chi_{\alpha\alpha'\gamma\gamma'}(i\nu_n, i\nu_{n'}; i\omega_m) \\ &= \int_0^\beta \mathrm{d}\tau_{12} \int_0^\beta \mathrm{d}\tau_{34} \int_0^\beta \mathrm{d}\tau_{23}\, e^{i\nu_n\tau_{12} + i\nu_{n'}\tau_{34} - i\omega_m\tau_{23}} \chi_{\alpha\alpha'\gamma\gamma'}(\tau_{12}, \tau_{34}; \tau_{23})\end{aligned} \tag{4.50}$$

with two fermionic frequencies ν_n and $\nu_{n'}$, and one bosonic frequency ω_m. The inverse transformation is given by

$$\chi_{\alpha\alpha'\gamma\gamma'}(\tau_{12}, \tau_{34}; \tau_{23}) = \frac{1}{\beta^3} \sum_{n=-\infty}^{\infty} \sum_{n'=-\infty}^{\infty} \sum_{m=-\infty}^{\infty} e^{-i\nu_n\tau_{12} - i\nu_{n'}\tau_{34} + i\omega_m\tau_{23}} \chi_{nn'}^{\alpha\alpha'\gamma\gamma'}(i\omega_m).$$

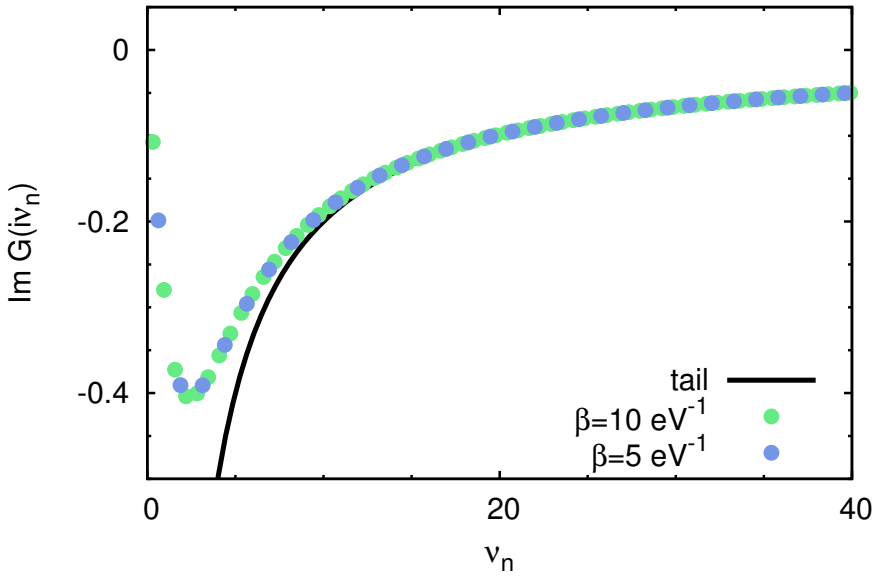

Figure 4.6: Imaginary part of Green function $G(i\nu_n)$ for the same case as in figure 4.4. For large ν_n the Green function converges against the tail $G(i\nu_n) \sim \frac{2}{i\nu_n}$.

Using the transformation (4.50) the susceptibility can be expressed in terms of Green functions, which results in eq. (4.20) and eq. (4.21) for the lattice susceptibility. The local Matsubara frequency representation can be written as

$$\chi^{\alpha\alpha'\gamma\gamma'}_{nn'}(i\omega_m) = \mathcal{C}^{\alpha\alpha'\gamma\gamma'}_{nn'}(i\omega_m) - \beta\delta_{0,m}G_{\alpha\alpha'}(i\nu_n)G_{\gamma\gamma'}(i\nu_{n'})$$

and the bare local one as

$$\chi^{0,\alpha\alpha'\gamma\gamma'}_{nn'}(i\omega_m) = -\beta\delta_{n,n'}G_{\alpha\gamma'}(i\nu_n)G_{\gamma\alpha'}(i\nu_n + i\omega_m). \tag{4.51}$$

The susceptibility for $m = 0$, which means frequency $\omega_0 = 0$, is the static susceptibility $\chi_{\alpha\alpha'\gamma\gamma'}(0)$.
Formally, we can expand the operators

$$c_\alpha(\tau) = \frac{1}{\beta}\sum_{n=-\infty}^{\infty} c_\alpha(i\nu_n)e^{-i\nu_n\tau} \quad , \quad c^\dagger_\alpha(\tau) = \frac{1}{\beta}\sum_{n=-\infty}^{\infty} c^\dagger_\alpha(i\nu_n)e^{i\nu_n\tau}$$

in Matsubara frequencies, and express for example the two-particle Green function in these operators

$$\mathcal{C}^{\alpha\alpha'\gamma\gamma'}_{nn'}(i\omega_m) = \langle c_\alpha(i\nu_n)c^\dagger_{\alpha'}(i\nu_n + i\omega_m)c_\gamma(i\nu_{n'} + i\omega_m)c^\dagger_{\gamma'}(i\nu_{n'})\rangle. \tag{4.52}$$

Physical interesting properties, like the expectation value $n_{\alpha\alpha'}$, are extracted from the borders $\tau = 0^+,\beta^-$ of the imaginary time Green functions. These translate to summation

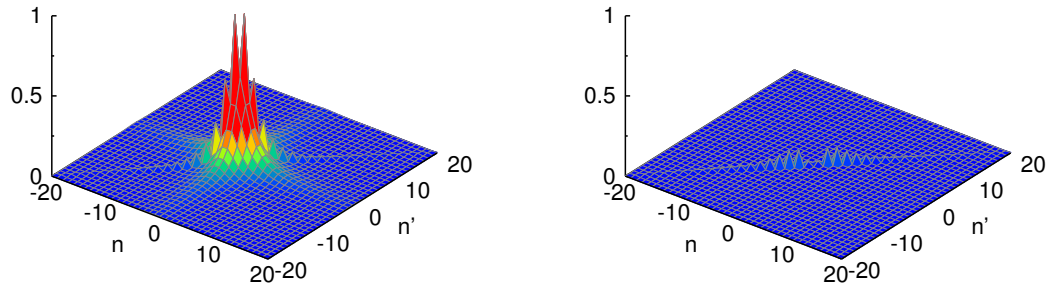

Figure 4.7: Real part of magnetic static susceptibility $\chi^{zz}_{nn'}(0)$ and bare part $\chi^{0,zz}_{nn'}(0)$ for the same case as in figure 4.4.

formulas of the Matsubara functions. From the single-particle Green function, we get the particle numbers by

$$\frac{1}{\beta}\sum_{n=-\infty}^{\infty} e^{-i\nu_n 0^+} G_{\alpha\alpha'}(i\nu_n) = \frac{1}{\beta}\sum_{n=-\infty}^{\infty} G_{\alpha\alpha'}(i\nu_n) = -\delta_{\alpha,\alpha'} + n_{\alpha\alpha'}$$
$$\frac{1}{\beta}\sum_{n=-\infty}^{\infty} e^{-i\nu_n \beta^-} G_{\alpha\alpha'}(i\nu_n) = \frac{1}{\beta}\sum_{n=-\infty}^{\infty} e^{i\nu_n 0^+} G_{\alpha\alpha'}(i\nu_n) = -n_{\alpha\alpha'}.$$

For the susceptibility the summation over the fermionic frequencies is used to get the physical susceptibility

$$\chi_{\alpha\alpha'\gamma\gamma'}(i\omega_m) = \frac{1}{\beta^2}\sum_{nn'} e^{-i(\nu_n+\nu_{n'})0^+}\chi^{\alpha\alpha'\gamma\gamma'}_{nn'}(i\omega_m) = \frac{1}{\beta^2}\sum_{nn'}\chi^{\alpha\alpha'\gamma\gamma'}_{nn'}(i\omega_m).$$

Numerically the sum over n and n' has to be restricted $\sum_{n,n'} \sim \sum_{n,n'=n_{\min}}^{n_{\max}}$. Taking symmetries into account we choose $n_{\min} = -n_{\max} - m - 1$.[5]

The high-frequency $|\nu_n| \to \infty$ behavior of the Matsubara Green function is shown in figure 4.6 to be $G_{\alpha\alpha'}(i\nu_n) \sim \frac{a}{i\nu_n}$, which is also clear from its expansion (A.25). Because the bare susceptibility (4.51) is given by the product of two Green functions, it decays like $\frac{b}{(i\nu_n)^2}$. It can be shown that the high frequency behavior of the susceptibility $\chi^{\alpha\alpha'\gamma\gamma'}_{nn'}(i\omega_m)$ is the same [37].
Let us focus here on the behavior of the physical susceptibility $\chi_{P_\nu O_{\nu'}}(\mathbf{q},i\omega_m)$ and how it depends on the bosonic frequency ω_m. For this we consider its Lehmann spectral representation

$$\chi_{P_\nu O_{\nu'}}(\mathbf{q},i\omega_m) = \frac{1}{\mathcal{Z}}\sum_{n_1 n_2}\frac{e^{-\beta E_{n_1}} - e^{-\beta E_{n_2}}}{E_{n_2} - E_{n_1} - i\omega_m} P^{n_1 n_2}_{\nu}(\mathbf{q}) O^{n_2 n_1}_{\nu'}(-\mathbf{q}). \tag{4.53}$$

[5]The central point, where the lines of high symmetry cross, is at $n,n' = -(m+1)/2$.

Here $P_\nu^{n_1 n_2}(\mathbf{q}) = \langle n_1|\Delta P_\nu(\mathbf{q})|n_2\rangle$ and $O_\nu^{n_1 n_2}(\mathbf{q}) = \langle n_1|\Delta O_\nu(\mathbf{q})|n_2\rangle$ are the matrix elements of the operators $\mathbf{P}(\mathbf{q})$ and $\mathbf{O}(\mathbf{q})$ in the eigenbasis $|n\rangle$ with eigenenergies E_n. Because all observables are hermitian $P_i^{nm}(\mathbf{q}) = [P_i^{mn}(-\mathbf{q})]^*$ and $O_i^{nm}(\mathbf{q}) = [O_i^{mn}(-\mathbf{q})]^*$, the symmetry

$$\chi_{P_\nu O_{\nu'}}(\mathbf{q},i\omega_m) = \left[\chi_{P_\nu O_{\nu'}}(-\mathbf{q},i\omega_m)\right]^*$$

holds. From this it is clear that the local susceptibility is real

$$\chi_{P_\nu O_{\nu'}}(i\omega_m) = \frac{1}{N_\mathbf{q}} \sum_\mathbf{q} \chi_{P_\nu O_{\nu'}}(\mathbf{q},i\omega_m) = \mathrm{Re}[\chi_{P_\nu O_{\nu'}}(i\omega_m)].$$

Let us rewrite the Lehmann representation

$$\chi_{P_\nu O_{\nu'}}(\mathbf{q},i\omega_m) = \frac{1}{2\mathcal{Z}} \sum_{n_1 n_2} \frac{e^{-\beta E_{n_1}} - e^{-\beta E_{n_2}}}{(E_{n_1} - E_{n_2})^2 + \omega_m^2} \left[\Delta(\mathbf{q}) + \Delta^*(-\mathbf{q})\right]$$

with

$$\Delta(\mathbf{q}) = (E_{n_1} - E_{n_2} + i\omega_m) P_\nu^{n_1 n_2}(\mathbf{q}) O_{\nu'}^{n_2 n_1}(-\mathbf{q}).$$

In this thesis we consider only combination of observables, for which the product $P_\nu O_{\nu'}$ is real, i.e., $P_\nu = O_{\nu'} = S_z$. Thus, the real part of the susceptibility decays like

$$\mathrm{Re}\,\chi_{P_\nu O_{\nu'}}(\mathbf{q},i\omega_m) \overset{|\omega_m|\to\infty}{\sim} \frac{1}{\omega_m^2}$$

We already showed that the imaginary part of the local susceptibility vanishes. The imaginary part of the lattice susceptibility $\mathrm{Im}[\chi_{P_\nu O_{\nu'}}(\mathbf{q},i\omega_m)]$ vanishes, for example, because of inversion symmetry $\chi_{P_\nu O_{\nu'}}(-\mathbf{q},i\omega_m) = \chi_{P_\nu O_{\nu'}}(\mathbf{q},i\omega_m)$, which holds throughout this thesis.

The symmetries and properties of the local imaginary time susceptibility $\chi_{\alpha\alpha'\gamma\gamma'}(\tau_{12},\tau_{34};\tau_{23})$ can be used to derive equivalent relations in the Matsubara frequency representation $\chi_{nn'}^{\alpha\alpha'\gamma\gamma'}(i\omega_m)$ [22, 35].

1. For the single-particle Green function, complex conjugation leads to

$$\begin{aligned}
[G_{\alpha\alpha'}(i\nu_n)]^* &= \left[\int_0^\beta \mathrm{d}\tau\, e^{i\nu_n\tau} G_{\alpha\alpha'}(\tau)\right]^* \\
&= \int_0^\beta \mathrm{d}\tau\, e^{-i\nu_n\tau} G_{\alpha'\alpha}(\tau) \\
&= G_{\alpha'\alpha}(-i\nu_n)
\end{aligned}$$

   For the susceptibility we use complex conjugation on the definition (4.50) and replace the complex conjugated $\chi_{\alpha\alpha'\gamma\gamma'}(\tau_{12},\tau_{34};\tau_{23})$ according to (4.45).

$$\begin{aligned}
\left[\chi_{nn'}^{\alpha\alpha'\gamma\gamma'}(i\omega_m)\right]^* &= \int_0^\beta \mathrm{d}\tau_{12} \int_0^\beta \mathrm{d}\tau_{34} \int_0^\beta \mathrm{d}\tau_{23}\, e^{-i\nu_n\tau_{12} - i\nu_{n'}\tau_{34} + i\omega_m\tau_{23}} \times \\
&\quad \times \chi_{\gamma'\gamma\alpha'\alpha}(\tau_{34},\tau_{12};\tau_{23}) \\
&= \chi_{-n'-1,-n-1}^{\gamma'\gamma\alpha'\alpha}(-i\omega_m)
\end{aligned} \tag{4.54}$$

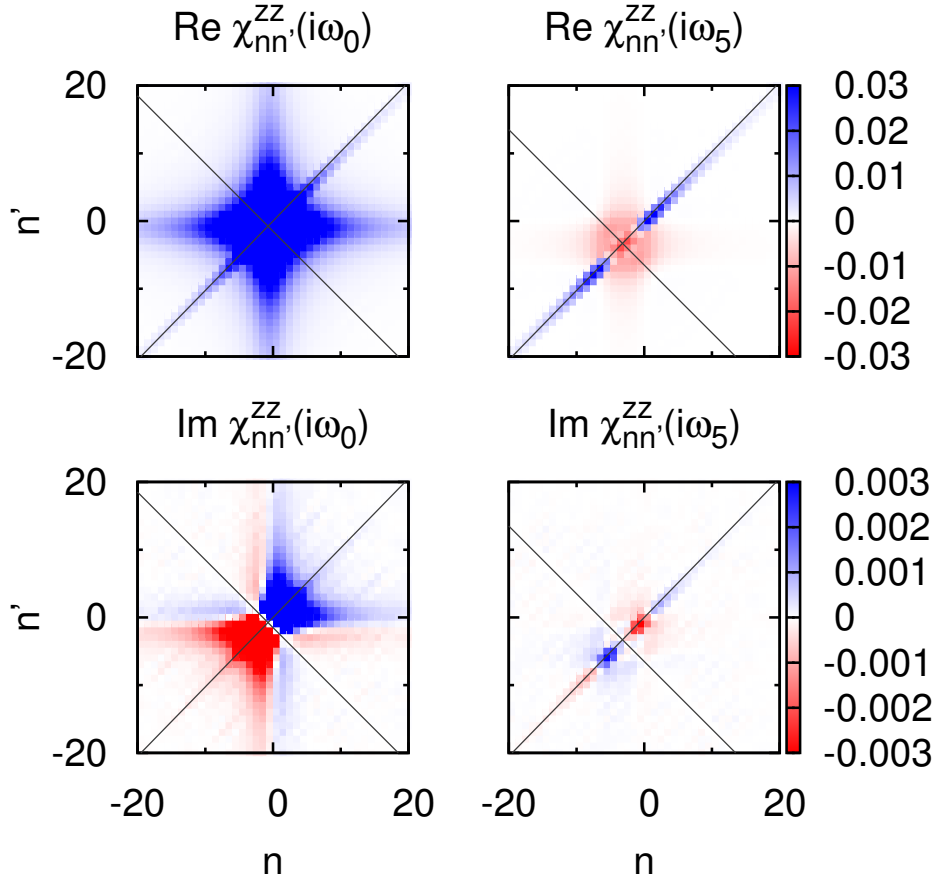

Figure 4.8: Real (top) and imaginary (bottom) part of magnetic susceptibility $\chi^{zz}_{nn'}(i\omega_m)$ for the same case as in figure 4.4. The left shows the static $\omega_m = 0$ susceptibility; on the right side $\chi^{zz}_{nn'}(i\omega_5)$ is shown. Symmetry axis are indicated by lines.

2. In the time reversal symmetric case for a real basis the complex conjugated $G_{\alpha\alpha'}(\tau)$ and $\chi_{\alpha\alpha'\gamma\gamma'}(\tau_{12},\tau_{34};\tau_{23})$ do not change, which leads to the symmetries

$$\begin{aligned}[G_{\alpha\alpha'}(i\nu_n)]^* &= \int_0^\beta \mathrm{d}\tau\, e^{-i\nu_n\tau} G_{\alpha\alpha'}(\tau) \\ &= G_{\alpha\alpha'}(-i\nu_n)\end{aligned}$$

$$\begin{aligned}\left[\chi^{\alpha\alpha'\gamma\gamma'}_{nn'}(i\omega_m)\right]^* &= \int_0^\beta \mathrm{d}\tau_{12} \int_0^\beta \mathrm{d}\tau_{34} \int_0^\beta \mathrm{d}\tau_{23}\, e^{-i\nu_n\tau_{12} - i\nu_{n'}\tau_{34} + i\omega_m\tau_{23}} \times \\ &\quad \times \chi_{\alpha\alpha'\gamma\gamma'}(\tau_{12},\tau_{34};\tau_{23}) \\ &= \chi^{\alpha\alpha'\gamma\gamma'}_{-n-1,-n'-1}(-i\omega_m) \end{aligned} \tag{4.55}$$

3. By replacing the imaginary time susceptibility with its exchanged α and γ representation (4.46) and reordering the times in the exponential, we get a representation

with the bosonic frequency added to the fermionic ones

$$\begin{aligned}\chi^{\alpha\alpha'\gamma\gamma'}_{nn'}(i\omega_m) &= \int_0^\beta \mathrm{d}\tau_{12}\int_0^\beta \mathrm{d}\tau_{34}\int_0^\beta \mathrm{d}\tau_{23}\, e^{(i\nu_n+i\omega_m)\tau_{12}+(i\nu_{n'}+i\omega_m)\tau_{34}+i\omega_m\tau_{41}}\times \\ &\quad\times \chi_{\gamma\gamma'\alpha\alpha'}(\tau_{34},\tau_{12};\tau_{41}) \\ &= \int_0^\beta \mathrm{d}\tau_{12}\int_0^\beta \mathrm{d}\tau_{34}\int_0^\beta \mathrm{d}\tau_{41}\, e^{(i\nu_n+i\omega_m)\tau_{12}+(i\nu_{n'}+i\omega_m)\tau_{34}+i\omega_m\tau_{41}}\times \\ &\quad\times \chi_{\gamma\gamma'\alpha\alpha'}(\tau_{34},\tau_{12};\tau_{41}) \\ &= \chi^{\gamma\gamma'\alpha\alpha'}_{n'+m,n+m}(-i\omega_m). \end{aligned} \tag{4.56}$$

4. For particle-hole symmetric Hamiltonians the following holds

$$\begin{aligned}G_{\alpha\alpha'}(i\nu_n) &= -G_{\alpha'\alpha}(-i\nu_n) \\ &= -\left[G_{\alpha\alpha'}(i\nu_n)\right]^*,\end{aligned}$$

which requires the Green function $G_{\alpha\alpha'}(i\nu_n)$ to be purely imaginary. The susceptibility is purely real, as can be seen from

$$\begin{aligned}\chi^{\alpha\alpha'\gamma\gamma'}_{nn'}(i\omega_m) &= \int_0^\beta \mathrm{d}\tau_{12}\int_0^\beta \mathrm{d}\tau_{34}\int_0^\beta \mathrm{d}\tau_{41}\, e^{-(i\nu_n+i\omega_m)\tau_{12}-(i\nu_{n'}+i\omega_m)\tau_{34}-i\omega_m\tau_{41}}\times \\ &\quad\times \chi_{\alpha'\alpha\gamma'\gamma}(\tau_{12},\tau_{34};\tau_{41}) \\ &= \chi^{\alpha'\alpha\gamma'\gamma}_{-n-m-1,-n'-m-1}(i\omega_m) \\ &= \left[\chi^{\alpha\alpha'\gamma\gamma'}_{nn'}(i\omega_m)\right]^*.\end{aligned}$$

5. The crossing symmetry for the two-particle Matsubara Green function is defined as

$$\begin{aligned}\mathcal{C}^{\alpha\alpha'\gamma\gamma'}_{nn'}(i\omega_m) &= -\int_0^\beta \mathrm{d}\tau_{12}\int_0^\beta \mathrm{d}\tau_{34}\int_0^\beta \mathrm{d}\tau_{23}\, e^{i\nu_n\tau_{12}+i\nu_{n'}\tau_{34}-i\omega_m\tau_{23}}\times \\ &\quad\times \mathcal{C}_{\gamma\alpha'\alpha\gamma'}(\tau_{32},\tau_{14};\tau_{21}) \\ &= -\int_0^\beta \mathrm{d}\tau_{32}\int_0^\beta \mathrm{d}\tau_{14}\int_0^\beta \mathrm{d}\tau_{21}\, e^{i(\nu_{n'}+\omega_m)\tau_{32}+i\nu_{n'}\tau_{14}-i(\nu_n-\nu_{n'})\tau_{21}}\times \\ &\quad\times \mathcal{C}_{\gamma\alpha'\alpha\gamma'}(\tau_{32},\tau_{14};\tau_{21}) \\ &= -\mathcal{C}^{\gamma\alpha'\alpha\gamma'}_{n'+m,n'}(i\nu_n-i\nu_{n'}).\end{aligned}$$

To derive it, we exchanged α and γ and consequently ν_n and $\nu_{n'}+\omega_m$.

4.5.3 Compact basis function representation

Although the Matsubara frequencies are a natural choice, they are not the best choice in every aspect. In the following we introduce two more compact alternatives: the Legendre and intermediate representation. We will first discuss Legendre polynomials, whose usage for DMFT was introduced in Ref. [39], and then the intermediate representation, which was introduced in Ref. [40].

The expansion of Green functions and susceptibilities in Legendre polynomials $P_l(x)$ (appendix A.4.2) leads to compact representations of those functions and can act as a noise filter of Monte Carlo data. The Legendre representation of the single-particle Green function is given by

$$G_l^{\alpha\alpha'} = \int_0^\beta \mathrm{d}\tau \, f_l^0(\tau) G_{\alpha\alpha'}(\tau) \tag{4.57}$$

and the inverse transformation is

$$G_{\alpha\alpha'}(\tau) = \frac{1}{\beta} \sum_{l=0}^{\infty} f_l^0(\tau) G_l^{\alpha\alpha'}.$$

Here, we introduced the abbreviation

$$f_l^m(\tau) = \sqrt{2l+1} P_l(x(\tau)) e^{-i\frac{\omega_m}{2}\tau}$$

with $x(\tau) = 2\tau/\beta - 1$. For the susceptibility, we transform the fermionic times to Legendre polynomials and the bosonic time to Matsubara frequencies, which gives us the mixed Legendre-Matsubara representation

$$\begin{aligned}\chi_{ll'}^{\alpha\alpha'\gamma\gamma'}(i\omega_m) = (-1)^{l'+m+1} \int_0^\beta \mathrm{d}\tau_{12} \int_0^\beta \mathrm{d}\tau_{34} \int_0^\beta \mathrm{d}\tau_{23} \, f_l^m(\tau_{12}) f_{l'}^m(\tau_{34}) e^{-i\omega_m \tau_{23}} \times \\ \times \chi_{\alpha\alpha'\gamma\gamma'}(\tau_{12}, \tau_{34}; \tau_{23}).\end{aligned} \tag{4.58}$$

The imaginary time susceptibility is then reconstructed by

$$\begin{aligned}\chi_{\alpha\alpha'\gamma\gamma'}(\tau_{12}, \tau_{34}; \tau_{23}) = \frac{1}{\beta^3} \sum_{l=0}^{\infty} \sum_{l'=0}^{\infty} \sum_{m=-\infty}^{\infty} (-1)^{l'+m+1} f_l^{-m}(\tau_{12}) f_{l'}^{-m}(\tau_{34}) e^{i\omega_m \tau_{23}} \times \\ \times \chi_{ll'}^{\alpha\alpha'\gamma\gamma'}(i\omega_m).\end{aligned} \tag{4.59}$$

For finite frequencies $|\omega_m| > 0$ the basis functions $f_l^m(\tau)$ contain a phase factor given by $e^{-i\frac{\omega_m}{2}\tau}$. This choice gives the most compact $\chi_{ll'}^{\alpha\alpha'\gamma\gamma'}(i\omega_m)$ in l and l'.
The transformation between Legendre and Matsubara frequency representation of the single-particle Green function

$$G_{\alpha\alpha'}(i\nu_n) = \sum_{l=0}^{\infty} U_{nl}^0 G_l^{\alpha\alpha'} \tag{4.60}$$

and the susceptibility

$$\chi_{nn'}^{\alpha\alpha'\gamma\gamma'}(i\omega_m) = \sum_{l=0}^{\infty} \sum_{l'=0}^{\infty} U_{nl}^m \chi_{ll'}^{\alpha\alpha'\gamma\gamma'}(i\omega_m) \, [U_{n'l'}^m]^*$$

is done by the unitary matrix

$$U_{nl}^m = \frac{1}{\beta} \int_0^\beta \mathrm{d}\tau \, e^{i\nu_n \tau} f_l^m(x(\tau)). \tag{4.61}$$

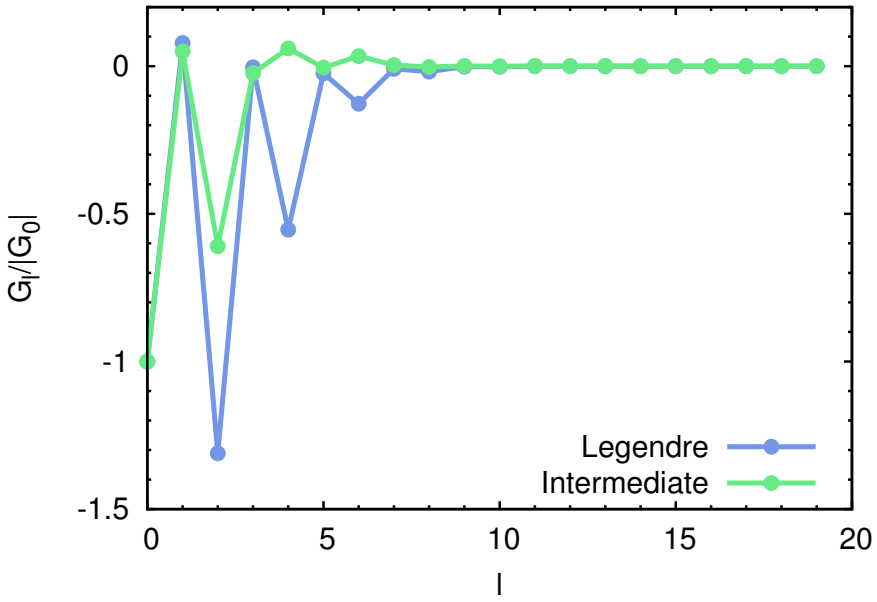

Figure 4.9: Legendre and intermediate representation G_l of Green function for the same case as in figure 4.4.

The complex conjugation of U_{nl}^m (A.24) is

$$[U_{nl}^m]^* = (-1)^{l'+m+1} U_{nl}^m. \tag{4.62}$$

In our choice the resulting prefactor $(-1)^{l'+m+1}$ is in (4.58) and (4.59).
One advantage of the Legendre polynomial representation is that

$$U_{nl}^m = \begin{cases} \delta_{0,l} & \text{if} \quad 2n+m+1=0 \\ \sqrt{2l+1} i^{l+2n+m+1} j_l\left(\frac{\pi}{2}(2n+m+1)\right) & \text{else} \end{cases}$$

can be calculated analytically (A.22) from the spherical Bessel functions $j_l(z)$. This makes it possible to increase the numerical accuracy of the tail of the Green function $G_{\alpha\alpha'}(i\nu_n)$ by use of (A.28)

$$\bar{G}_l^{\alpha\alpha'} = G_l^{\alpha\alpha'} + \left(\delta_{\alpha,\alpha'} - \sum_{l'=0}^{\infty} U_{l'}^{(1)} G_{l'}^{\alpha\alpha'}\right) \frac{U_l^{(1)}}{\sum_{l'=0}^{\infty} |U_{l'}^{(1)}|^2},$$

with the coefficients

$$U_l^{(1)} = \frac{2}{\beta}\sqrt{2l+1}\delta_{l,\text{even}}.$$

A $\bar{G}_{\alpha\alpha'}(i\nu_n)$ obtained from $\bar{G}_l^{\alpha\alpha'}$ using (4.60) will have the correct tail for $i\nu_n \to \infty$.
Because in the QMC we calculate $\mathcal{C}_{ll'}^{\alpha\alpha'\gamma\gamma'}(i\omega_m)$ and $G_l^{\alpha\alpha'}$, we give the formula to get the susceptibility $\chi_{ll'}^{\alpha\alpha'\gamma\gamma'}(i\omega_m)$ directly from the Green functions

$$\chi_{ll'}^{\alpha\alpha'\gamma\gamma'}(i\omega_m) = \mathcal{C}_{ll'}^{\alpha\alpha'\gamma\gamma'}(i\omega_m) + (-1)^{l'}\beta\delta_{m,0} G_l^{\alpha\alpha'} G_{l'}^{\gamma\gamma'}, \tag{4.63}$$

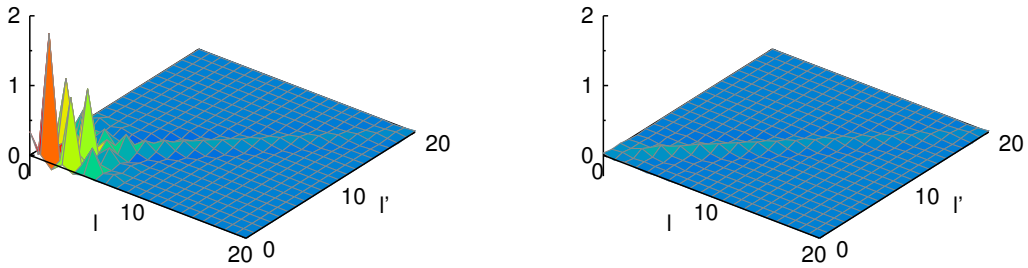

Figure 4.10: Legendre representation of magnetic static susceptibility $\chi^{zz}_{ll'}(0)$ and bare part $\chi^{0,zz}_{ll'}(0)$ for the same case as in figure 4.4.

which is obtained by transforming (4.35) from imaginary time to Legendre polynomials. The bare susceptibility can be calculated from the single-particle Matsubara Green functions

$$\begin{aligned}\chi^{0,\alpha\alpha'\gamma\gamma'}_{ll'}(i\omega_m) &= \sum_{n=-\infty}^{\infty} [U^m_{nl}]^* \, \chi^{0,\alpha\alpha'\gamma\gamma'}_{nn}(i\omega_m) U^m_{nl'} \\ &= -\beta \sum_{n=-\infty}^{\infty} [U^m_{nl}]^* \, G_{\alpha\gamma'}(i\nu_n) G_{\gamma\alpha'}(i\nu_n + i\omega_m) U^m_{nl'}. \end{aligned} \tag{4.64}$$

Finally, we sum over l to get the particle number $n_{\alpha\alpha'}$ by

$$\begin{aligned}\frac{1}{\beta}\sum_{l=0}^{\infty} f^0_l(x(0)) G^{\alpha\alpha'}_l &= \frac{1}{\beta}\sum_{l=0}^{\infty} \sqrt{2l+1}(-1)^l G^{\alpha\alpha'}_l = -\delta_{\alpha\alpha'} + n_{\alpha\alpha'} \\ \frac{1}{\beta}\sum_{l=0}^{\infty} f^0_l(x(\beta)) G^{\alpha\alpha'}_l &= \frac{1}{\beta}\sum_{l=0}^{\infty} \sqrt{2l+1} G^{\alpha\alpha'}_l = -n_{\alpha\alpha'} \end{aligned}$$

and the susceptibility $\chi_{\alpha\alpha'\gamma\gamma'}(i\omega_m)$ by

$$\begin{aligned}\chi_{\alpha\alpha'\gamma\gamma'}(i\omega_m) &= \frac{1}{\beta^2}\sum_{ll'=0}^{\infty} (-1)^{l'+m+1} f^{-m}_l(x(0)) f^{-m}_{l'}(x(0)) \chi^{\alpha\alpha'\gamma\gamma'}_{ll'}(i\omega_m) \\ &= \frac{1}{\beta^2}\sum_{ll'=0}^{\infty} (-1)^{l+m+1} \sqrt{2l+1}\sqrt{2l'+1} \chi^{\alpha\alpha'\gamma\gamma'}_{ll'}(i\omega_m). \end{aligned} \tag{4.65}$$

In practice we must choose a cutoff $l_{\max}$ to approximate the summation. To decrease the necessary $l_{\max}$ we subtract the bare susceptibility $\chi^{0,\alpha\alpha'\gamma\gamma'}_{ll'}(i\omega_m)$ before summation and

add the converged value $\chi^{0,\alpha\alpha'\gamma\gamma'}(i\omega_m)$ afterwards

$$\begin{aligned}\chi_{\alpha\alpha'\gamma\gamma'}(i\omega_m) \approx \frac{1}{\beta^2}\sum_{ll'=0}^{l_{\max}}(-1)^{l'+m+1} f_l^{-m}(x(0)) f_{l'}^{-m}(x(0))\times \\ \times\left(\chi_{ll'}^{\alpha\alpha'\gamma\gamma'}(i\omega_m) - \chi_{ll'}^{0,\alpha\alpha'\gamma\gamma'}(i\omega_m)\right) \\ + \chi^{0,\alpha\alpha'\gamma\gamma'}(i\omega_m).\end{aligned} \tag{4.66}$$

The term $\chi^{0,\alpha\alpha'\gamma\gamma'}(i\omega_m)$ is the result of a Matsubara summation of $\chi_{nn'}^{0,\alpha\alpha'\gamma\gamma'}(i\omega_m)$ with a high number of frequencies ν_n. To get the lattice susceptibility $\chi^{\alpha\alpha'\gamma\gamma'}(\mathbf{q},i\omega_m)$ we use the Bethe-Salpeter equation (BSEQ) (4.27). The procedure was explained in section 4.4.1 for the susceptibility with Matsubara frequencies $\chi_{nn'}^{\alpha\alpha'\gamma\gamma'}(\mathbf{q},i\omega_m)$. Because the transformation from Matsubara frequencies to Legendre polynomials is unitary (4.61), the matrix form of the inverse BSEQ in local vertex approximation

$$[\chi(\mathbf{q},i\omega_m)]^{-1} = \left[\chi^0(\mathbf{q},i\omega_m)\right]^{-1} - \left[\chi^0(i\omega_m)\right]^{-1} + [\chi(i\omega_m)]^{-1}$$

is the same, except that the matrix indices are now given by (l,α,α') and (l',γ,γ'). The bare local susceptibility $\chi_{ll'}^{0,\alpha\alpha'\gamma\gamma'}(i\omega_m)$ is given by (4.64). For the bare lattice susceptibility $\chi_{ll'}^{0,\alpha\alpha'\gamma\gamma'}(\mathbf{q},i\omega_m)$ we use a similar formula, extended to lattice susceptibilities

$$\chi_{ll'}^{0,\alpha\alpha'\gamma\gamma'}(\mathbf{q},i\omega_m) = -\frac{\beta}{N_{\mathbf{k}}}\sum_{\mathbf{k}}\sum_{n=-\infty}^{\infty}[U_{nl}^m]^* G_{\mathbf{k}}^{\alpha\gamma'}(i\nu_n) G_{\mathbf{k}+\mathbf{q}}^{\gamma\alpha'}(i\nu_n + i\omega_m) U_{nl'}^m.$$

The local susceptibility $\chi_{ll'}^{\alpha\alpha'\gamma\gamma'}(i\omega_m)$ results from DMFT using (4.63).

Related to the properties of the imaginary time susceptibility, we derive some properties of the local Legendre representation $\chi_{ll'}^{\alpha\alpha'\gamma\gamma'}(i\omega_m)$.

1. For complex conjugation of the Green function we get the Legendre coefficients by inverting the order of the indices.

$$\begin{aligned}\left[G_l^{\alpha\alpha'}\right]^* &= \left[\sqrt{2l+1}\int_0^\beta \mathrm{d}\tau\, P_l(x(\tau)) G_{\alpha\alpha'}(\tau)\right]^* \\ &= \sqrt{2l+1}\int_0^\beta \mathrm{d}\tau\, P_l(x(\tau)) G_{\alpha'\alpha}(\tau) \\ &= G_l^{\alpha'\alpha}\end{aligned}$$

   Using the complex conjugated $\chi_{\alpha\alpha'\gamma\gamma'}(\tau_{12},\tau_{34};\tau_{23})$ from (4.45) we get the equation

$$\left[\chi_{ll'}^{\alpha\alpha'\gamma\gamma'}(i\omega_m)\right]^* = (-1)^{l+l'}\chi_{l'l}^{\gamma'\gamma\alpha'\alpha}(-i\omega_m). \tag{4.67}$$

   Because left and right hand side are calculated independently in the CT-QMC, this relation can be used to get an error estimation, as well as an error reduction by averaging over equivalent entries.

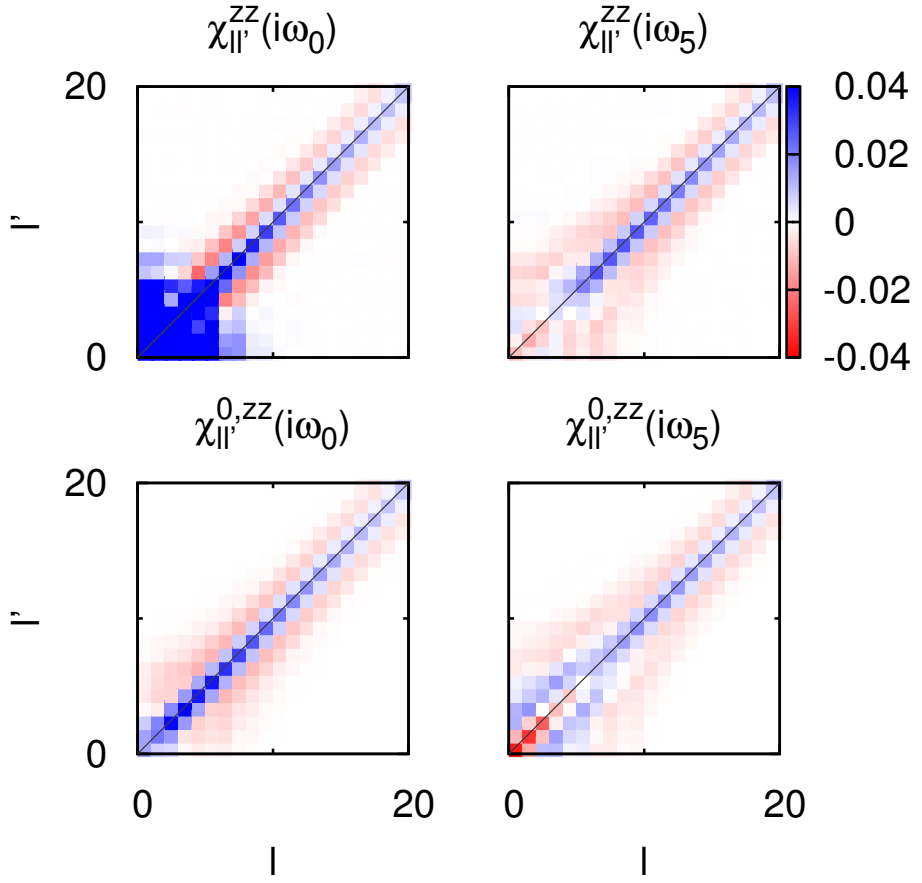

Figure 4.11: Legendre representation of magnetic susceptibility $\chi^{zz}_{ll'}(i\omega_m)$ (top) and bare susceptibility $\chi^{0,zz}_{ll'}(i\omega_m)$ (bottom) for the same case as in figure 4.4. The left shows the static $\omega_m = 0$ susceptibility; on the right side $\chi^{zz}_{ll'}(i\omega_5)$ is shown. The symmetry axis is indicated by a line.

2. For a time reversal symmetric system in a real basis we use that $G_{\alpha\alpha'}(\tau)$ and $\chi_{\alpha\alpha'\gamma\gamma'}(\tau_{12},\tau_{34};\tau_{23})$ are real. For the single-particle Green function it follows

$$\left[G_l^{\alpha\alpha'}\right]^* = G_l^{\alpha\alpha'},$$

which means $G_l^{\alpha\alpha'}$ is also real. For the susceptibility we find the relation

$$\left[\chi^{\alpha\alpha'\gamma\gamma'}_{ll'}(i\omega_m)\right]^* = \chi^{\alpha\alpha'\gamma\gamma'}_{ll'}(-i\omega_m). \tag{4.68}$$

Due to this relation it is sufficient to calculate the susceptibility for $\omega_m \geq 0$.

3. Exchange of the operator pairs α and γ (4.46) can be used to derive

$$\begin{aligned}\chi_{ll'}^{\alpha\alpha'\gamma\gamma'}(i\omega_m) &= (-1)^{l'+m+1}\sqrt{2l+1}\sqrt{2l'+1}\int_0^\beta \mathrm{d}\tau_{12}\int_0^\beta \mathrm{d}\tau_{34}\int_0^\beta \mathrm{d}\tau_{23}\times \\ &\quad\times P_l(x(\tau_{12}))P_{l'}(x(\tau_{34}))e^{i\omega_m\left(\tau_{41}+\frac{\tau_{12}+\tau_{34}}{2}\right)}\chi_{\gamma\gamma'\alpha\alpha'}(\tau_{34},\tau_{12};\tau_{41}) \\ &= (-1)^{l+l'}\chi_{l'l}^{\gamma\gamma'\alpha\alpha'}(-i\omega_m). \end{aligned} \tag{4.69}$$

This relation holds in every step of the CT-QMC sampling, which means numerical all symmetric values are the same. Therefore, it is sufficient to measure only half of the entries.

4. The particle-hole symmetry lets us derive the following relation

$$\begin{aligned}G_l^{\alpha\alpha'} &= (-1)^l G_l^{\alpha'\alpha} \\ &= (-1)^l \left[G_l^{\alpha\alpha'}\right]^*.\end{aligned}$$

This means that the Green function $G_l^{\alpha\alpha'}$ is real for even l and imaginary for odd l. If additionally time reversal symmetry holds, the Green function $G_l^{\alpha\alpha'}$ is real and for odd l the coefficients must vanish: $G_{2l+1}^{\alpha\alpha'} = 0$. Apart from time reversal symmetry the coefficients also vanish if $G_l^{\alpha\alpha'} = G_l^{\alpha'\alpha}$. One example of this is a one-band model with SU(2) spin symmetry. Because of particle-hole symmetry, the susceptibility defined below is purely real if the sum $l + l'$ is even, and imaginary if $l + l'$ is odd.

$$\begin{aligned}\chi_{ll'}^{\alpha\alpha'\gamma\gamma'}(i\omega_m) &= (-1)^{l'+m+1}\sqrt{2l+1}\sqrt{2l'+1}\int_0^\beta \mathrm{d}\tau_{12}\int_0^\beta \mathrm{d}\tau_{34}\int_0^\beta \mathrm{d}\tau_{23}\times \\ &\quad\times P_l(x(\tau_{12}))P_{l'}(x(\tau_{34}))e^{i\omega_m\left(\tau_{41}+\frac{\tau_{12}+\tau_{34}}{2}\right)}\times \\ &\quad\times \chi_{\alpha'\alpha\gamma'\gamma}(\beta-\tau_{12},\beta-\tau_{34};\beta-\tau_{41}) \\ &= (-1)^{l+m+1}\sqrt{2l+1}\sqrt{2l'+1}\int_0^\beta \mathrm{d}\tau_{12}\int_0^\beta \mathrm{d}\tau_{34}\int_0^\beta \mathrm{d}\tau_{41}\times \\ &\quad\times P_l(x(\tau_{12}))P_{l'}(x(\tau_{34}))e^{-i\omega_m\left(\tau_{41}+\frac{\tau_{12}+\tau_{34}}{2}\right)}\chi_{\alpha'\alpha\gamma'\gamma}(\tau_{12},\tau_{34};\tau_{41}) \\ &= (-1)^{l+l'}\chi_{ll'}^{\alpha'\alpha\gamma'\gamma}(i\omega_m) \\ &= (-1)^{l+l'}\left[\chi_{ll'}^{\alpha\alpha'\gamma\gamma'}(i\omega_m)\right]^*\end{aligned}$$

For certain relations between the indices α, α', γ and γ', like in a one-band model with SU(2) symmetry, the odd $l + l'$ entries vanish and the susceptibility is real.

As a benchmark, in figure 4.12 we compare our method to independent DMFT calculations with the Hirsch-Fye quantum Monte Carlo solver (HF-QMC) [37]. In the HF-QMC the $\chi^{zz}(\tau)$ was calculated directly in τ. An advantage of the CT-QMC is its continues time, opposed to the HF-QMC, which uses a discretized imaginary time grid with time slices of size $\Delta\tau$. For small $\Delta\tau$ the HF-QMC results converge to the CT-QMC results as shown in figure 4.12. The CT-QMC results were achieved by calculation of the total tensor $\chi_{ll'}^{\alpha\alpha'\gamma\gamma'}(i\omega_m)$, summation over l and l', and finally an inverse Fourier

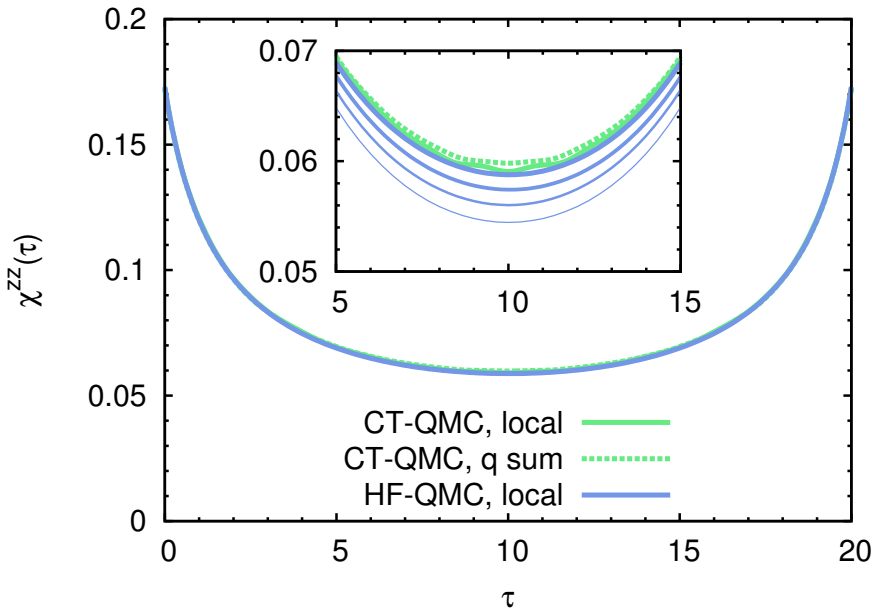

Figure 4.12: Magnetic local imaginary time susceptibility for the compound $La_{1.7}Sr_{0.3}CuO_4$ at $\beta = 20\,\mathrm{eV}^{-1}$. We compare the local CT-QMC (green) result with the summed lattice result (green dashed) and the HF-QMC results (blue). The HF-QMC calculations were done with decreasing discretization intervals $\Delta\tau$ from bottom (thin) to top (thick).

transformation to τ.[6] In the same figure 4.12 we show the local susceptibility $\chi^{zz}(\tau)$ calculated by momentum summation $\chi^{zz}(i\omega_m) = \frac{1}{N_\mathbf{q}} \sum_\mathbf{q} \chi^{zz}(\mathbf{q},i\omega_m)$ and inverse Fourier transformation. All methods yield the same result, as expected.

Having successfully decreased the number of expansion coefficients by using the Legendre representation instead of the Matsubara one, the question arises if there is an even more compact alternative. Recently, a numerical recipe [40] was introduced to construct a more compact representation, called the intermediate representation.[7] The idea is to do a singular value decomposition (SVD) of the kernel $K_F(\tau,\omega) = \frac{e^{-\tau\omega}}{1+e^{-\beta\omega}}$, which results in basis functions $u_l(x(\tau))$ and $v_l(y(\omega))$, with $y = \beta\omega$. The method has its name from the kernel $K_F(\tau,\omega)$ being between imaginary time τ and real frequency ω axis. In order to apply a standard SVD to the kernel, we must discretize its time and frequencies, and write it as a matrix. While the time $\tau \in [0,\beta]$ is bounded, we need to introduce a cutoff frequency $y_\mathrm{max} \geq \beta|\omega|$ to discretize the frequency axis. Once the basis $u_l(x(\tau))$ is obtained, we use it to express the Green functions and susceptibility in the basis functions

$$f_l^m(x(\tau)) = \sqrt{2} u_l(x(\tau)) e^{-i\frac{\omega_m}{2}\tau}. \tag{4.70}$$

All formulas for the intermediate representation follow from the Legendre formulas by

[6] In this calculation we fit the $\frac{1}{\omega_m^2}$ tail to $\chi^{zz}(i\omega_m)$ and transform to $\chi^{zz}(\tau)$ using 10^4 frequencies.

[7] See section A.4.5 for details on the construction.

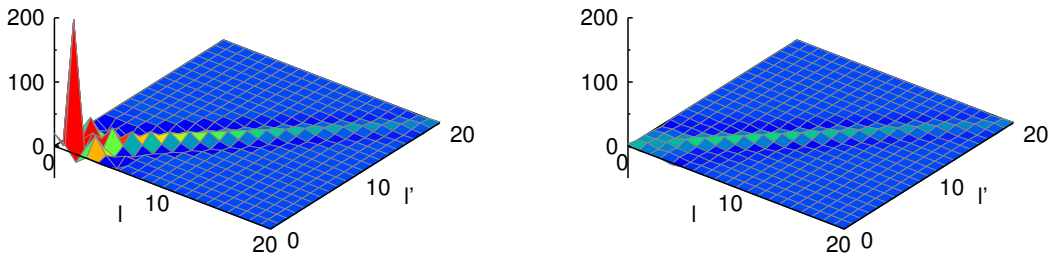

Figure 4.13: Intermediate representation of magnetic static susceptibility $\chi^{zz}_{ll'}(0)$ and bare part $\chi^{0,zz}_{ll'}(0)$ for the same case as in figure 4.4.

replacing $f^m_l(x(\tau))$ according to formula (4.70). The symmetries apply, because $u_l(x)$ have by construction the same symmetry properties as $P_l(x)$. However, the formulas (4.61) and (4.65) cannot be evaluated analytically.
In the construction of the intermediate representation we introduced the parameter $y_{\max}$. In figure 4.14 we show the convergence of the summation (4.66) for different $y_{\max}$. The optimal value turns out to be $y_{\max} \approx \beta U$, which is approximately the width of the density of states. For $y_{\max} \to 0$ the intermediate representation converges to the Legendre representation.[8]

We conclude by comparing the four representations: imaginary time, Matsubara frequency, Legendre and intermediate. The time representation is smooth, except for its discontinuities, and the time is a continuous variable. It needs more memory to store it on a computer than the other three basis. The Matsubara frequency representation is discrete, and its high frequency behavior is known analytically.
The continuous-time quantum Monte Carlo (CT-QMC) is naturally formulated in imaginary time, however the measurement formulas can be easily transformed to all basis. The Bethe-Salpeter equation (BSEQ) can be formulated in all basis, but is more complicated in imaginary time.
Computation time and memory, for the CT-QMC as well as the BSEQ, is decreased by a compact representation. The most compact, and therefore computational favorable, representation is the intermediate, followed by the Legendre. However, for the bare susceptibility the Matsubara representation has the advantage of being diagonal in the frequencies.
In contrast to the intermediate basis, the Legendre basis polynomials are known analytically, and can be calculated up to arbitrarily high order, but the order of the intermediate representation is given by the number of singular values. For higher bosonic frequencies ω_m the sum in (4.66) converges also for higher $l_{\max}$. Because in the intermediate representation $l_{\max}$ is fixed by the number of singular values, the sum in (4.66) is cut off before

[8] A proof was given in the appendix of Ref. [40].

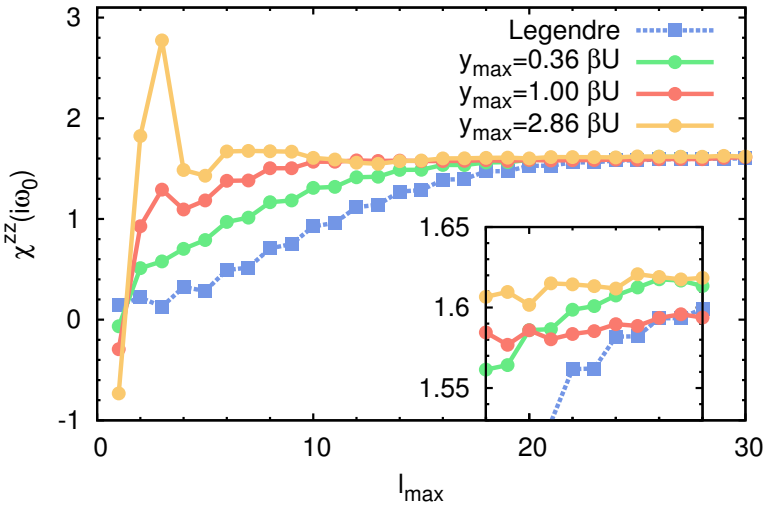

Figure 4.14: Convergence plots (4.66) for static susceptibility $\chi^{zz}(0)$ of the same material as in figure 4.12. We compare the intermediate representation for different cutoffs $y_{\max}$ with the stable Legendre result. The inset shows that they match best for $y_{\max} \approx \beta U$.

it converges for large ω_m. A method to obtain polynomials for arbitrarily large $l_{\max}$ in the intermediate representation was presented in Ref. [41], but was only shown to work for single-particle Green functions.
As a result of this discussion, we use the Legendre representation to measure the single-particle Green function and dynamical susceptibilities. The intermediate representation is used for static susceptibility measurements, especially at low temperatures. The DMFT loop, particularly the Dyson equation, is calculated in Matsubara frequencies. The BSEQ is either solved in Legendre or intermediate representation.

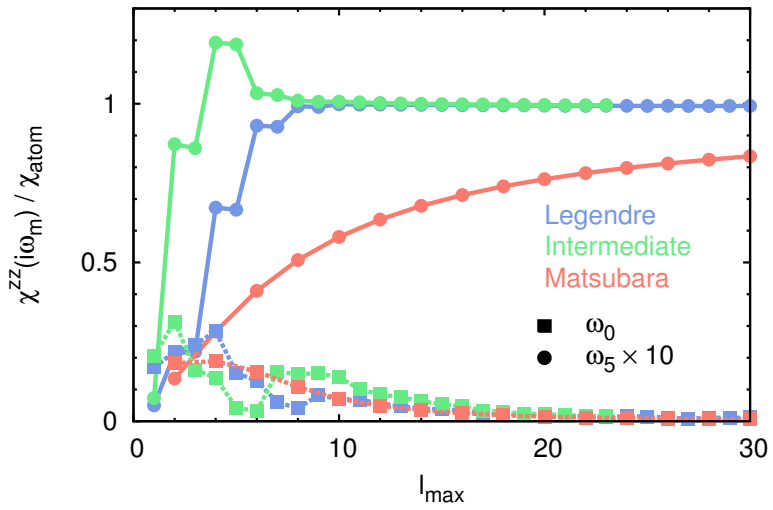

Figure 4.15: Convergence plots (4.66) for $\chi^{zz}(i\omega_m)$ in Legendre, intermediate and Matsubara frequency representation, normalized to the atomic value $\chi_{\text{atom}} \sim \beta/4$. We show results for the static susceptibility ω_0 and one finite frequency ω_5, enhanced by a factor of 10, for the same case as in figure 4.4.

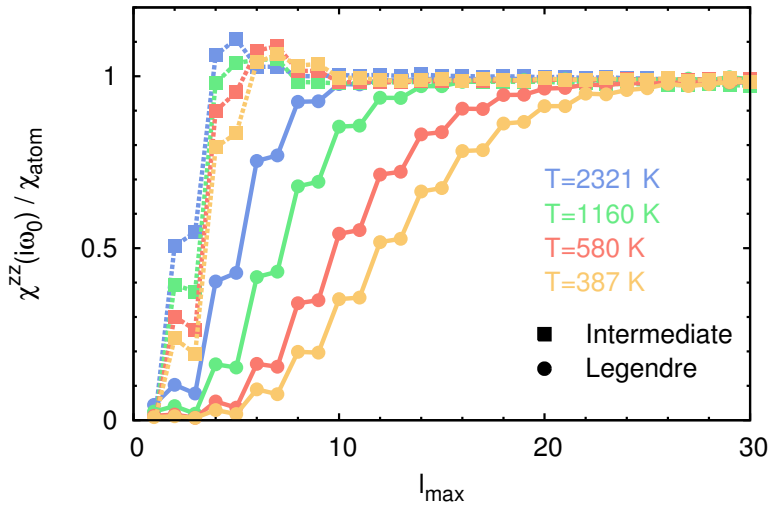

Figure 4.16: Convergence plots (4.66) for $\chi^{zz}(0)$ in Legendre (circles) and intermediate (squares) representation with $y_{\max} \approx \beta U$, normalized to the atomic value $\chi_{\text{atom}} \sim \beta/4$. For lower temperatures the intermediate representation converges faster than the Legendre. The calculations were done for the ambient pressure structure of K_2CuF_4 with reduced distortions.

4.5.4 Real frequency representation

In the previous chapters we calculated the Green function $G(i\nu_n)$ using DMFT and the susceptibility $\chi_{P_\nu O_{\nu'}}(\mathbf{q},i\omega_m)$ using DMFT and the BSEQ. To make the connection to the experiment, we have to transform $G(i\nu_n)$ and $\chi_{P_\nu O_{\nu'}}(\mathbf{q},i\omega_m)$ to the real frequency ω axis [22,38]. More specifically, we will achieve the spectral function $A(\mathbf{k},\omega)$ (4.15) and the correlation function $S^{\nu\nu'}(\mathbf{q},\omega)$ (4.17).
We start with the Lehmann spectral representation of the susceptibility (4.53). By replacing $i\omega_m$ in the Lehmann representation with a general complex variable z plus an infinitesimal shift δ

$$i\omega_m \to z + i\delta$$

we get $\chi_{P_\nu O_{\nu'}}(\mathbf{q},z)$, which is analytic in the upper complex plane $\operatorname{Im} z \geq 0$. This includes the real axis ω, where the Lehmann representation is

$$\chi_{P_\nu O_{\nu'}}(\mathbf{q},\omega) = \frac{1}{\mathcal{Z}} \sum_{n_1 n_2} \frac{e^{-\beta E_{n_1}} - e^{-\beta E_{n_2}}}{E_{n_2} - E_{n_1} - \omega - i\delta} P_\nu^{n_1 n_2}(\mathbf{q}) O_{\nu'}^{n_2 n_1}(-\mathbf{q}). \tag{4.71}$$

These extension of the domain of a function is called analytic continuation. Similar to section 4.5.2 for $\chi_{P_\nu O_{\nu'}}(\mathbf{q},i\omega_m)$, the assumption of $P_\nu^{n_1 n_2}(\mathbf{q})$ and $O_\nu^{n_1 n_2}(\mathbf{q})$ being hermitian leads to

$$\chi_{P_\nu O_{\nu'}}(\mathbf{q},\omega) = \left[\chi_{P_\nu O_{\nu'}}(-\mathbf{q},-\omega)\right]^*, \tag{4.72}$$

which means that the real part is even and the imaginary part odd

$$\begin{aligned} \operatorname{Re}\left[\chi_{P_\nu O_{\nu'}}(\mathbf{q},\omega)\right] &= \operatorname{Re}\left[\chi_{P_\nu O_{\nu'}}(-\mathbf{q},-\omega)\right] \\ \operatorname{Im}\left[\chi_{P_\nu O_{\nu'}}(\mathbf{q},\omega)\right] &= -\operatorname{Im}\left[\chi_{P_\nu O_{\nu'}}(-\mathbf{q},-\omega)\right]. \end{aligned}$$

If we compare the Lehmann representation of $\chi_{P_\nu O_{\nu'}}(\mathbf{q},\omega)$ in (4.71) with the one of the correlation function

$$S_{P_\nu O_{\nu'}}(\mathbf{q},\omega) = \frac{2\pi}{\mathcal{Z}} \sum_{nm} e^{-\beta E_n} P_\nu^{nm}(\mathbf{q}) O_{\nu'}^{mn}(-\mathbf{q}) \delta(\omega - E_m + E_n)$$

introduced in (4.17), it is clear that

$$\chi_{P_\nu O_{\nu'}}(\mathbf{q},\omega) = -\int_{-\infty}^{\infty} \frac{\mathrm{d}\omega'}{2\pi} \frac{\mathcal{S}_{P_\nu O_{\nu'}}(\mathbf{q},\omega') - \mathcal{S}_{O_{\nu'} P_\nu}(-\mathbf{q},-\omega')}{\omega - \omega' + i\delta}.$$

Simplifying this by use of the principle of detailed balance [22]

$$\mathcal{S}_{O_{\nu'} P_\nu}(-\mathbf{q},-\omega) = e^{-\beta\omega} \mathcal{S}_{P_\nu O_{\nu'}}(\mathbf{q},\omega),$$

which can be derived from (4.17), we get the relation

$$\chi_{P_\nu O_{\nu'}}(\mathbf{q},\omega) = -\int_{-\infty}^{\infty} \frac{\mathrm{d}\omega'}{2\pi} \mathcal{S}_{P_\nu O_{\nu'}}(\mathbf{q},\omega') \frac{1 - e^{-\beta\omega'}}{\omega - \omega' + i\delta}.$$

The correctness of this equation is shown by replacing $\mathcal{S}_{P_\nu O_{\nu'}}(\mathbf{q},\omega')$ by its definition (4.17). To get the inverse transform, we need the Sokhotski-Plemelj formula

$$\frac{1}{\omega + i\delta} = \mathcal{P}\frac{1}{\omega} - i\pi\delta(\omega) \tag{4.73}$$

with the Cauchy principal value $\mathcal{P}$.[9] Using the formula (4.73) for the integrand[10] we get the general equation

$$\begin{aligned}\chi_{P_\nu O_{\nu'}}(\mathbf{q},\omega) = -\mathcal{P}\int_{-\infty}^{\infty}\frac{\mathrm{d}\omega'}{2\pi}\mathcal{S}_{P_\nu O_{\nu'}}(\mathbf{q},\omega')\frac{1-e^{-\beta\omega'}}{\omega-\omega'} \\ + \frac{i}{2}\mathcal{S}_{P_\nu O_{\nu'}}(\mathbf{q},\omega)(1-e^{-\beta\omega}).\end{aligned}$$

If the product $P_\nu O_{\nu'}$ is real as in the cases considered in this thesis (section 4.5.2), and likewise $S_{P_\nu O_{\nu'}}(\mathbf{q},\omega)$ is real, the correlation function follows from the imaginary part of the susceptibility

$$\mathcal{S}_{P_\nu O_{\nu'}}(\mathbf{q},\omega) = \frac{2\,\mathrm{Im}\,\chi_{P_\nu O_{\nu'}}(\mathbf{q},\omega)}{1-e^{-\beta\omega}}. \tag{4.74}$$

This is the fluctuation-dissipation theorem, saying that fluctuations described by $S_{P_\nu O_{\nu'}}(\mathbf{q},\omega)$ are proportional to energy dissipation given by $\mathrm{Im}\,\chi_{P_\nu O_{\nu'}}(\mathbf{q},\omega)$.
We started this section with the analytic continuation from $\chi_{P_\nu O_{\nu'}}(\mathbf{q},i\omega_m)$ to $\chi_{P_\nu O_{\nu'}}(\mathbf{q},\omega)$. This is simple if we know $\chi_{P_\nu O_{\nu'}}(\mathbf{q},i\omega_m)$ analytically. If we calculate it numerically, however, this is very difficult, because it is an ill posed problem. A general relation between real and imaginary frequency axis is

$$\begin{aligned}&\frac{1}{\pi}\int_{-\infty}^{\infty}\mathrm{d}\omega\,\frac{\mathrm{Im}\,\chi_{P_\nu O_{\nu'}}(\mathbf{q},\omega)}{\omega - i\omega_m} \\ &= \frac{1}{2\pi}\int_{-\infty}^{\infty}\mathrm{d}\omega\,\left(1-e^{-\beta\omega}\right)\frac{\mathcal{S}_{P_\nu O_{\nu'}}(\mathbf{q},\omega)}{\omega - i\omega_m} \\ &= \frac{1}{\mathcal{Z}}\sum_{n_1 n_2}\frac{e^{-\beta E_{n_1}} - e^{-\beta E_{n_2}}}{E_{n_2} - E_{n_1} - i\omega_m}P_\nu^{n_1 n_2}(\mathbf{q})O_{\nu'}^{n_2 n_1}(-\mathbf{q}) \\ &= \chi_{P_\nu O_{\nu'}}(\mathbf{q},i\omega_m)\end{aligned} \tag{4.75}$$

Here, we used the definitions of $\mathcal{S}_{P_\nu O_{\nu'}}(\mathbf{q},\omega) \sim \delta(\omega - E_{n_2} + E_{n_1})$ (4.17) and $\chi_{P_\nu O_{\nu'}}(\mathbf{q},i\omega_m)$ (4.53). A similar equation

$$G_{\alpha\alpha'}(\mathbf{k},i\nu_n) = \frac{1}{2\pi}\int_{-\infty}^{\infty}\mathrm{d}\omega\,\frac{A_{\alpha\alpha'}(\mathbf{k},\omega)}{i\nu_n - \omega} \tag{4.76}$$

connects the single-particle Green function, whose other form of Lehmann representation is

$$G_{\alpha\alpha'}(\mathbf{k},i\nu_n) = \frac{1}{\mathcal{Z}}\sum_{n_1 n_2}\frac{e^{-\beta E_{n_1}} + e^{-\beta E_{n_2}}}{E_{n_1} - E_{n_2} + i\nu_n}\langle n_2|c_{\mathbf{k}\alpha'}^\dagger|n_1\rangle\langle n_1|c_{\mathbf{k}\alpha}|n_2\rangle,$$

[9] Cauchy principal value: $\mathcal{P}\int_{-\infty}^{\infty}\mathrm{d}\omega\,\frac{1}{\omega} = \lim_{\epsilon\to 0}\left(\int_{-\infty}^{-\epsilon}\mathrm{d}\omega + \int_{\epsilon}^{\infty}\mathrm{d}\omega\right)\frac{1}{\omega}$.
[10] The Sokhotski-Plemelj formula is only defined for integrals.

with the spectral function $A_{\alpha\alpha'}(\mathbf{k},\omega) \sim \delta(\omega - E_{n_2} + E_{n_1})$ (4.15). When we do the analytic continuation of $G_{\alpha\alpha'}(\mathbf{k},i\nu_n)$ by replacing $i\nu_n \to \omega + i\delta$, we get the retarded Green function $G^R_{\alpha\alpha'}(\mathbf{k},\omega)$. By use of (4.76) and formula (4.73) the imaginary part of the retarded Green function is

$$\begin{aligned}\operatorname{Im} G^R_{\alpha\alpha'}(\mathbf{k},\omega) &= \operatorname{Im} \frac{1}{2\pi} \int_{-\infty}^{\infty} \mathrm{d}\omega' \, \frac{A_{\alpha\alpha'}(\mathbf{k},\omega')}{\omega - \omega' + i\delta} \\ &= -\frac{1}{2} A_{\alpha\alpha'}(\mathbf{k},\omega).\end{aligned}$$

Equations (4.75) and (4.76) are Fredholm integral equations of first kind

$$f(x) = \int \mathrm{d}y \, K(x,y) g(y), \tag{4.77}$$

where $K(x,y)$ is the kernel, $f(x)$ is on the imaginary frequency axis x and $g(y)$ on the real axis y. Formally, analytic continuation is the inversion this equation to get $g(y)$ for a known $f(x)$. The question remains, how to invert the equation (4.77) numerically. An idea would be to invert a discretized version of the equation (4.77) directly. The problems are the noisy nature of the data points $f(x)$, and that a matrix inversion of K is ill defined. This becomes clear by looking at the Fourier transform of (4.76)

$$G_{\alpha\alpha'}(\mathbf{k},\tau) = -\int_{-\infty}^{\infty} \frac{\mathrm{d}\omega}{2\pi} \frac{e^{-\tau\omega}}{1 + e^{-\beta\omega}} A_{\alpha\alpha'}(\mathbf{k},\omega) \tag{4.78}$$

and at the Fourier transform of (4.75)

$$\chi_{P_\nu O_{\nu'}}(\mathbf{q},\tau) = \int_0^{\infty} \frac{\mathrm{d}\omega}{\pi} \frac{\omega \left(e^{-\tau\omega} + e^{-(\beta-\tau)\omega}\right)}{1 - e^{-\beta\omega}} \frac{\operatorname{Im} \chi_{P_\nu O_{\nu'}}(\mathbf{q},\omega)}{\omega}. \tag{4.79}$$

Both kernels decay exponentially to zero for large frequencies, making them numerically hard to invert. Put another way, many functions $A_{\alpha\alpha'}(\mathbf{k},\omega)$ ($\operatorname{Im} \chi_{P_\nu O_{\nu'}}(\mathbf{q},\omega)$) on the right will give numerically the same $G_{\alpha\alpha'}(\mathbf{k},\tau)$ ($\chi_{P_\nu O_{\nu'}}(\mathbf{q},\tau)$).
Before going on, we point out that we put an additional ω in the kernel of (4.79) and divided $\operatorname{Im} \chi_{P_\nu O_{\nu'}}(\mathbf{q},\omega)$ by the same. This removes the singularity at $\omega = 0$ from the kernel. So we also do this for the Matsubara frequency representation, and additionally use the symmetry (4.72) and the inversion symmetry $\chi_{P_\nu O_{\nu'}}(\mathbf{q},\omega) = \chi_{P_\nu O_{\nu'}}(-\mathbf{q},\omega)$ to get

$$\begin{aligned}\chi_{P_\nu O_{\nu'}}(\mathbf{q},i\omega_m) &= \int_{-\infty}^{\infty} \frac{\mathrm{d}\omega}{\pi} \frac{\omega(\omega + i\omega_m)}{(\omega - i\omega_m)(\omega + i\omega_m)} \frac{\operatorname{Im} \chi_{P_\nu O_{\nu'}}(\mathbf{q},\omega)}{\omega} \\ &= \int_0^{\infty} \frac{\mathrm{d}\omega}{\pi} \frac{2\omega^2}{\omega^2 + \omega_m^2} \frac{\operatorname{Im} \chi_{P_\nu O_{\nu'}}(\mathbf{q},\omega)}{\omega}.\end{aligned}$$

We are using the nowadays standard maximum entropy method (MEM) for the analytic continuation.[11] The idea of the MEM is to find $g(y)$ by maximizing its probability given $f(x)$

$$p(g|f) \sim e^{\alpha S(g) - \chi^2(g)/2},$$

[11] Details on the MEM are given in appendix A.5.

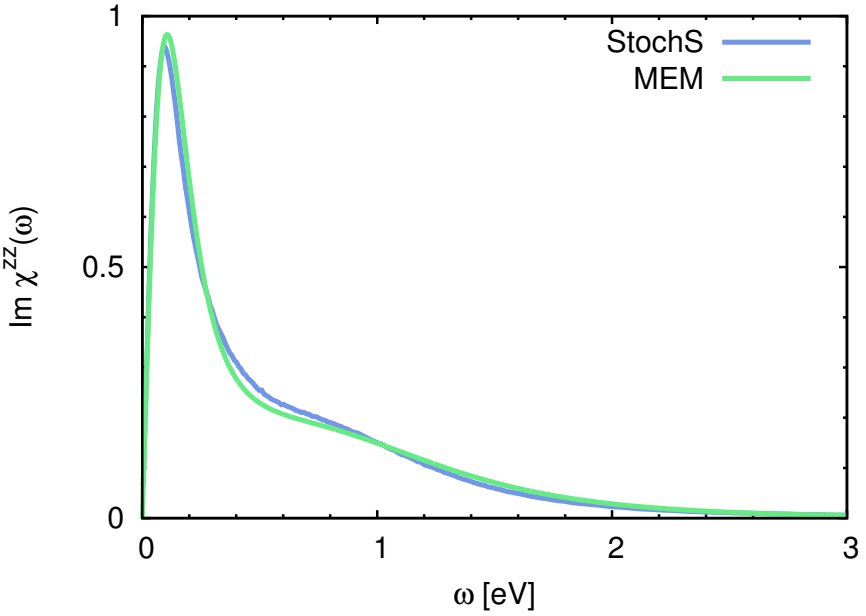

Figure 4.17: Comparison of imaginary part of magnetic dynamical susceptibility $\chi^{zz}(\omega)$ from imaginary time data $\chi^{zz}(\tau)$ presented in figure 4.12.

where $\chi(g)$ is a measure for the distance of the data f and a $\tilde{f}(g)$ resulting from g by (4.77), and $\alpha S(g)$ the similarity of g to some default model. Thus, the solution of this is

$$g = \arg\max_{g} \alpha S(g) - \chi^2(g)/2.$$

A different approach is the stochastic sampling (StochS) approach [42] and its extensions [43]. The idea of StochS is not to rely on the entropy term $S(g)$, but instead to average over all g such that

$$g = \int \mathrm{d}g'\, g'\, e^{-\chi^2(g')/2}.$$

In a case study we compared the results of the MEM and StochS for a representative material in figure 4.17, and found good agreement of the peak position and the occurrence of a shoulder.

5 Orbital ordering in the layered perovskite K_2CuF_4

This chapter has been partially published in J. Musshoff, G. Zhang, E. Koch and E. Pavarini, Phys. Rev. B **100***, 045116 (2019).*

The origin of orbital and magnetic ordering is an old problem. Orbital ordering can be explained by electron-phonon interaction [44] as well as by superexchange [45], a pure electronic mechanism. It was debated for a long time which of the two mechanisms dominates. This has been recently clarified for the cubic perovskites $KCuF_3$ [46] and $LaMnO_3$ [47]. For layered systems the problem remains open, however. In this chapter we study the origin of orbital ordering for a representative layered perovskite, K_2CuF_4. We show that, as in the case of the cubic perovskites $KCuF_3$ and $LaMnO_3$, the superexchange interaction cannot drive orbital ordering alone. Furthermore, we show that in K_2CuF_4, in addition to the normal superexchange interaction active in cubic perovskites, a Zeeman orbital term is present. We study its role.

5.1 Model

The building block of a perovskite is made by a central ion A surrounded by an octahedron of ions B and a cubic cage of ions C. In $KCuF_3$ and K_2CuF_4, a Cu^{2+} ion is surrounded by six F^- ions and both are enclosed by a cage of eight K^+ ions. In $KCuF_3$ the K^+ cages repeat in all directions. In K_2CuF_4 the K^+ cages repeat in the same way in a layer spanned by the lattice vectors $\mathbf{a}$ and $\mathbf{b}$. In direction of the lattice vector $\mathbf{c}$ the K^+ cages repeat with a shift parallel to the $\mathbf{a}$-$\mathbf{b}$-plane. This makes K_2CuF_4 a layered material. K_2CuF_4 has two possible structures, Bbcm, found in experiments at ambient pressure, and Ammm, found at high pressure. Both structures are depicted in figure 5.1 together with the directions of the lattice vectors $\mathbf{a}$, $\mathbf{b}$ and $\mathbf{c}$. The difference is that consecutive layers in the Ammm structure are shifted by $(\mathbf{b}+\mathbf{c})/2$, while in the Bbcm structure they are shifted by $(\mathbf{a}+\mathbf{b}+\mathbf{c})/2$. Also, in terms of the lattice vectors the K^+ cages of the Bbcm structure are rotated by 45° compared to the Ammm structure. We define the pseudotetragonal axis as follows, $z \sim \mathbf{c}$ for both structures, $x \sim \mathbf{a}$ and $y \sim \mathbf{b}$ in the Ammm case, and in the Bbcm case $x \sim (\mathbf{a}+\mathbf{b})/2$ and $y \sim (\mathbf{b}-\mathbf{a})/2$
The nominal electron configurations of the ions in $KCuF_3$ and K_2CuF_4 are K^+=[Ar] $4s^0$, Cu^{2+}=[Ar] $4s^0$ $3d^9$ and F^-=[He] $2s^2$ $2p^6$. Thus, while K^+ and F^- have closed shells, Cu^{2+} has one unpaired hole in the 3d orbitals. Due to the cubic symmetry of the K^+ cage and

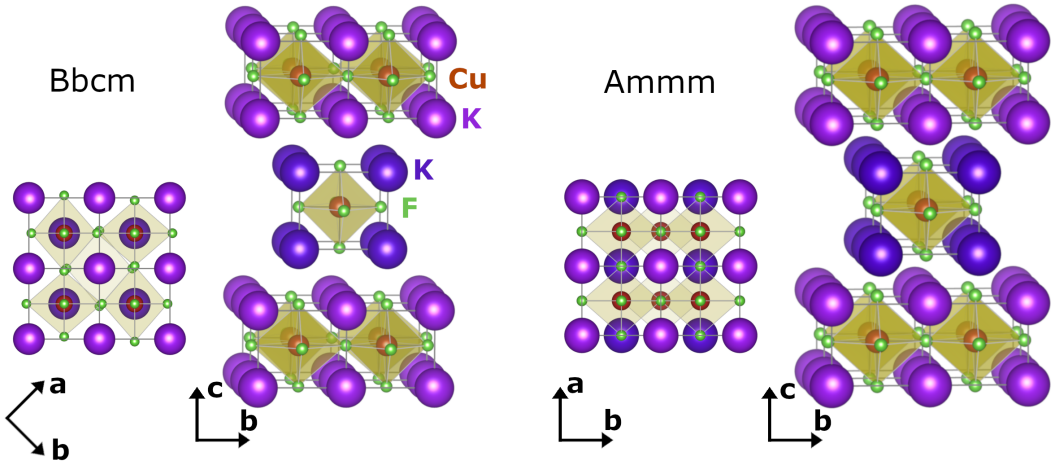

Figure 5.1: Structure of layered perovskite K_2CuF_4 at ambient pressure (Bbcm) [48] and at high pressure (Ammm) [49]. The different colors of the K ions represent the different layers.

F^- octahedron, the 3d orbitals of Cu^{2+} split into a lower energy t_{2g} triplet and a high energy e_g doublet, which contains the hole. In LDA the e_g bands cross the Fermi-level, while the t_{2g} bands are filled.
We thus model these systems with a Hubbard model (2.11) for the two e_g orbitals with quarter hole filling [50]

$$\begin{aligned} H_{\text{Hub}} = &- \sum_{ii'} \sum_{\sigma} \sum_{mm'} t_{mm'}^{ii'} c_{i,\sigma m}^{\dagger} c_{i',\sigma m'} + U \sum_{i} \sum_{m} \hat{n}_{i,\uparrow m} \hat{n}_{i,\downarrow m} \\ &+ \frac{1}{2} \sum_{i} \sum_{\sigma\sigma'} \sum_{m \neq m'} \left(U - 2J - J\delta_{\sigma,\sigma'} \right) \hat{n}_{i,\sigma m} \hat{n}_{i,\sigma' m'} \\ &- J \sum_{i} \sum_{m \neq m'} \left(c_{i,\uparrow m}^{\dagger} c_{i,\downarrow m}^{\dagger} c_{i,\uparrow m'} c_{i,\downarrow m'} + c_{i,\uparrow m}^{\dagger} c_{i,\downarrow m} c_{i,\downarrow m'}^{\dagger} c_{i,\uparrow m'} \right) \\ &- H_{\text{loc}}^{\text{DC}} - \mu \sum_{i} \sum_{\sigma} \sum_{m} \hat{n}_{i\sigma m}. \end{aligned} \tag{5.1}$$

Here, i is the site, $\sigma \in \{\uparrow, \downarrow\}$ is the spin and $m \in \{3z^2 - r^2, x^2 - y^2\}$ the orbital index. The one-particle part $t_{mm'}^{ii'}$ contains the hopping integrals $t_{mm'}^{i \neq i'}$ and the on-site crystal-field matrix $\epsilon_{mm'}^{\text{CF}} = t_{mm'}^{ii}$. With the shortcut notation $|0\rangle = |3z^2 - r^2\rangle$ and $|\pi\rangle = |x^2 - y^2\rangle$ the difference of the diagonal elements is the tetragonal term $\epsilon_{\text{T}} = \epsilon_{3z^2-r^2} - \epsilon_{x^2-y^2} = t_{00}^{ii} - t_{\pi\pi}^{ii}$ and the Jahn-Teller term is given by the off-diagonal elements $\epsilon_{\text{JT}} = 2|t_{0\pi}^{ii}|$.
The two-particle interaction for the e_g doublet depends only on the direct screened Coulomb term U and the exchange screened Coulomb term J [50]. The two-particle term consists of density-density interactions, with $\hat{n}_{i,m\sigma} = c_{i,m\sigma}^{\dagger} c_{i,m\sigma}$, as well as spin-flip and pair-hopping terms. We use the values $U = 7\,\text{eV}$ and $J = 0.9\,\text{eV}$, which have been established for the similar compound $KCuF_3$ [46].

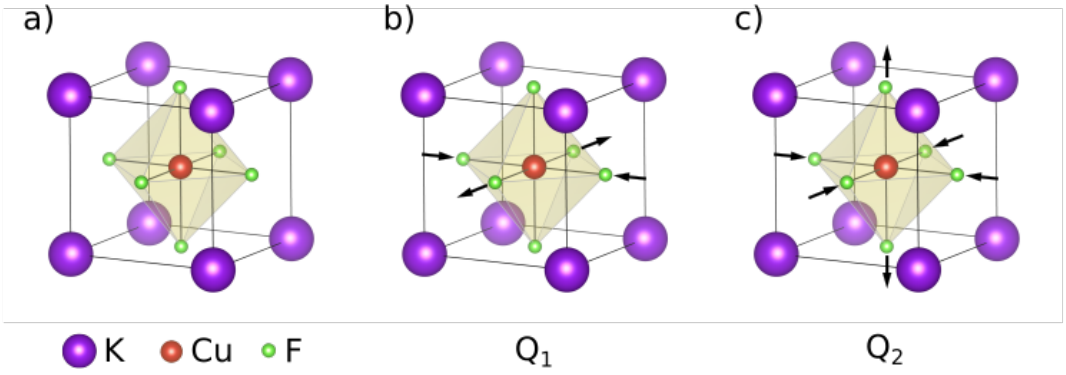

Figure 5.2: Unit cell of a cubic perovskite a), Jahn-Teller vibrational mode b) and tetragonal mode c).

5.2 Orbital and magnetic ordering mechanism

5.2.1 Electron-phonon mechanism

Orbital ordering can occur because of electron-phonon interaction leading to a Jahn-Teller distortion [44, 51]. The reason is the Jahn-Teller theorem [52], that states that, in any non-linear molecule with a degenerated electronic ground-state, the degeneracy is lifted by distortions, resulting in a ground-state with lower energy. The only exception are Kramer degeneracies.
Let us first focus on one Cu^{2+} ion in the center of the octahedron formed by six F^- ions (figure 5.2 a)). For the regular cubic structure the two e_g orbitals of the hole are degenerated. The Hamiltonian of the ions $H_n = T_n + U_n$ consists of the kinetic part $T_n = -\sum_j \nabla^2_{\mathbf{R}_j}/M_j$ and the potential U_n. Let $\{\mathbf{R}^0_j\}$ be the lattice positions of the ions in the undistorted structure and $\epsilon(\{\mathbf{R}^0_j\})$ their potential energy. We expand U_n in powers of $\mathbf{u}_j = \mathbf{R}_j - \mathbf{R}^0_j$, the deviation of the jth ion position from $\mathbf{R}^0_j$,

$$U_n = \epsilon(\{\mathbf{R}^0_j\}) + \sum_{j\alpha}\left[\frac{\partial U_n}{\partial u_{\alpha j}}\right]_{\{\mathbf{R}^0_j\}} u_{\alpha j} + \frac{1}{2}\sum_{\substack{j\alpha\\ j'\alpha'}}\left[\frac{\partial^2 U_n}{\partial u_{\alpha j}\partial u_{\alpha' j'}}\right]_{\{\mathbf{R}^0_j\}} u_{\alpha j}u_{\alpha' j'} + \cdots \tag{5.2}$$

with $\alpha \in \{x,y,z\}$. We set $\epsilon(\{\mathbf{R}^0_j\}) = 0$ for convenience. The gradient (first order term) must be zero if $\{\mathbf{R}^0_j\}$ are the equilibrium positions. Thus, the lowest order of U_n is the quadratic harmonic term $U_n^{\mathrm{PH}}(\{\mathbf{R}^0_j\})$. By diagonalizing

$$\begin{aligned} H_n &\sim T_n + U_n^{\mathrm{PH}}(\{\mathbf{R}^0_j\}) \\ &\sim \frac{1}{2}\sum_{j\alpha}\left(P^2_{\alpha j} + \omega^2_j Q^2_{\alpha j}\right) \end{aligned}$$

we obtain the eigenvectors, or normal modes, $\{Q_{\alpha j}\}$ and canonically-conjugated momenta $\{P_{\alpha j}\}$. For a single octahedron of a perovskite only two relevant modes Q_1 (figure 5.2 b))

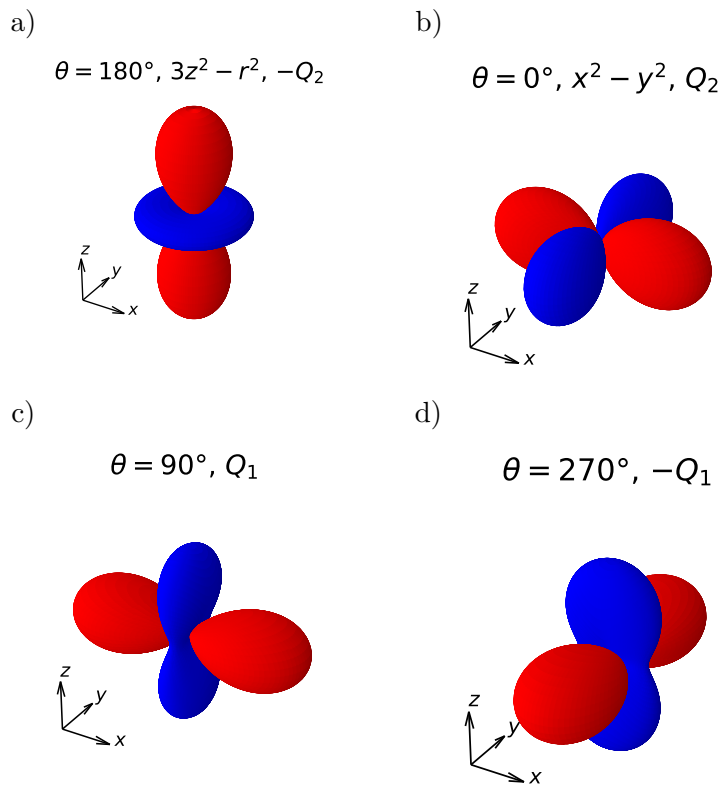

Figure 5.3: Hole state $|\theta\rangle = -\sin\frac{\theta}{2}|3z^2 - r^2\rangle + \cos\frac{\theta}{2}|x^2 - y^2\rangle$ for different θ. Positive (negative) values are red (blue).

and Q_2 (figure 5.2 c)) couple to the e_g states $|3z^2 - r^2\rangle$ and $|x^2 - y^2\rangle$. In terms of these modes the harmonic potential is given by

$$U^{\mathrm{PH}} = \frac{1}{2}C\left(Q_1^2 + Q_2^2\right). \tag{5.3}$$

A distortion of type Q_1 (Jahn-Teller mode) results in a short Cu-F bond in x- and a long bond in y-direction. A distortion of type Q_2 (tetragonal mode) is given by a shortening of bonds in x-y-direction, while the bond in z-direction is stretched.
Let us now assume that the system energy can be lowered by deviating from the $\{\mathbf{R}_j^0\}$ ion positions. The gradient in (5.2) then is not zero. Instead it leads to an electron-lattice coupling linear in the modes Q_1 and Q_2, which gives the interaction [51]

$$U^{\mathrm{JT}} = -\lambda \begin{pmatrix} Q_2 & Q_1 \\ Q_1 & -Q_2 \end{pmatrix} = -\lambda\left(Q_1\tau_x + Q_2\tau_z\right) \tag{5.4}$$

with matrices in the basis $|3z^2 - r^2\rangle$ and $|x^2 - y^2\rangle$

$$\tau_x = \begin{pmatrix} 0 & 1 \\ 1 & 0 \end{pmatrix} \quad \text{and} \quad \tau_z = \begin{pmatrix} 1 & 0 \\ 0 & -1 \end{pmatrix}.$$

Let us parametrize $Q_1 = q\sin\theta$ and $Q_2 = q\cos\theta$. In the limit $M_j \to \infty$ the kinetic lattice energy $T_n \sim 1/M_j$ can be neglected and we solve the potential Hamiltonian

$$U^{\mathrm{PH}} + U^{\mathrm{JT}} = \begin{pmatrix} \frac{1}{2}Cq^2 - \lambda q\cos\theta & -\lambda q\sin\theta \\ -\lambda q\sin\theta & \frac{1}{2}Cq^2 + \lambda q\cos\theta \end{pmatrix}. \tag{5.5}$$

The ground-state energy is $\bar{E} = \frac{1}{2}q^2 - \lambda q$. The minimum of this at $q = \frac{\lambda}{c}$ is the Jahn-Teller energy $E_{\mathrm{JT}} = -\frac{\lambda^2}{2C}$. The second solution is the energy $E = \frac{1}{2}q^2 + \lambda q > \bar{E}$. The lower-energy state is $|\bar{\theta}\rangle = \cos\frac{\theta}{2}|3z^2 - r^2\rangle + \sin\frac{\theta}{2}|x^2 - y^2\rangle$ and the higher-energy state

$$|\theta\rangle = -\sin\frac{\theta}{2}|3z^2 - r^2\rangle + \cos\frac{\theta}{2}|x^2 - y^2\rangle. \tag{5.6}$$

Because $|\bar{\theta}\rangle$ is the electronic ground-state, a hole will be in the hole state $|\theta\rangle$. For the Hamiltonian (5.5) the energies E and $\bar{E}$ are independent of θ. The harmonic Hamiltonian (5.3), however, is only the lowest order of U_n (5.2). The first anharmonic term is [51]

$$\begin{aligned} U^{\mathrm{anh}} &= -\beta\left(Q_2^3 - 3Q_2Q_1^2\right) \\ &= -\beta q^3\cos 3\theta \end{aligned} \tag{5.7}$$

Because of cubic symmetry, a degeneracy remains for $\{\theta, \theta + 120°, \theta - 120°\}$.
For $\beta > 0$ the anharmonic term is minimal for $\theta \in \{0°, 120°, 240°\}$. For these θ the octahedron is tetragonally stretched. For example, for $\theta = 0°$ it is $Q_2 = q$ and $Q_1 = 0$, and the hole is in the state $|0°\rangle = |x^2 - y^2\rangle$ figure 5.3 b).
For $\beta < 0$ the angles compatible with the anharmonic term are $\theta \in \{60°, 180°, 300°\}$. This is a tetragonal compression of the octahedron. For example, for $\theta = 180°$ the modes are $Q_2 = -q$ and $Q_1 = 0$. The hole state in this case is $|180°\rangle = -|3z^2 - r^2\rangle$ in figure 5.3 a).
The first anharmonic term U^{anh} (5.7) was dominated by the tetragonal mode Q_2. Higher orders can result in dominant off-diagonal Jahn-Teller terms (mode Q_1). For $\theta = 90°$ and $\theta = 270°$, for example, the tetragonal mode $Q_2 = 0$ and the Jahn-Teller mode is $Q_1 = \pm q$. The corresponding hole states $|90°\rangle$ and $|270°\rangle$ are depicted in figure 5.3 c) and d). Because the F^- ions attract the positive charged hole, the orbitals extent more in the direction of the short Cu-F bonds.
In a perovskite crystal occupied orbitals are periodically arranged. In the presence of lattice distortions due to electron-phonon coupling, the e_g orbitals split. If only the lowest orbitals are occupied, the system is orbitally ordered. In the presence of Coulomb repulsion, this can happen even if the crystal-field is much smaller then the bandwidth [46].
For K_2CuF_4, the tetragonal distortion Q_2 repeats at all lattice sites. The Jahn-Teller type Q_1 distortion, with a long l and a short bond s in the octahedron, alternates in the x-y-plane.

5.2.2 Superexchange mechanism

An alternative mechanism to explain orbital ordering is superexchange [45,53,54], a purely electronic mechanism. In K_2CuF_4 electrons can hop between Cu^{2+} ions via the intermediate F^- ions. Additionally, electrons on the Cu^{2+} sites repel each other by Coulomb repulsion. The result of this is the superexchange coupling. Let us consider first the case

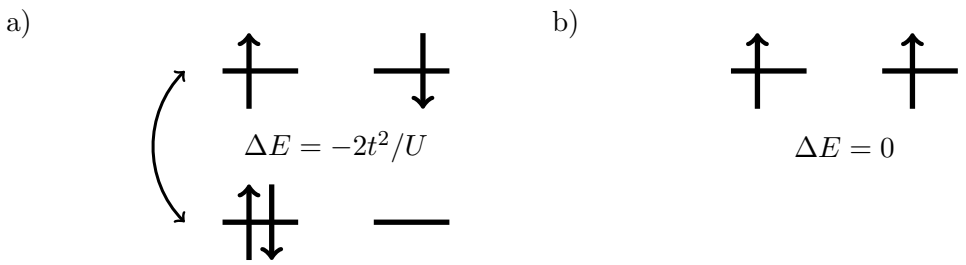

Figure 5.4: Superexchange mechanism leading to antiferromagnetism. Hopping is only possible for antiparallel spins a); the Pauli principle does not allow double occupation for parallel spins b).

with no orbital degeneracy. Superexchange for one orbital is the mechanism that leads to magnetic ordering in correlated Mott insulators. To explain it, let us consider a model made by two sites with one electron per site [54]

$$\begin{aligned} H_2 &= H_T + H_U \\ &= -t \sum_{\sigma} \left(c^{\dagger}_{1,\sigma} c_{2,\sigma} + c^{\dagger}_{2,\sigma} c_{1,\sigma} \right) + U \sum_{i=1,2} \hat{n}_{i,\uparrow} \hat{n}_{i,\downarrow}. \end{aligned}$$

The Coulomb on-site interaction U between electrons on the same site favors single occupation of sites. However, by hopping between sites the system can gain kinetic energy $-t$. Because of the Pauli principle, this hopping is only possible for electrons with opposite spin. When U is large compared to t, we can treat H_T as a perturbation of H_U [53]. In this limit, the ground-state $|G\rangle$ of the simple model is the singlet $|G\rangle \sim (|\uparrow,\downarrow\rangle - |\downarrow,\uparrow\rangle)/\sqrt{2}$ with energy $E_G \sim -4t^2/U$. In a lattice this can lead to antiferromagnetism.

Now, we consider two degenerated orbitals in the two site model. If we neglect pair hopping and spin-flip terms, for simplicity, we obtain

$$\begin{aligned} H_2 &= H_T + H_U \\ &= -t \sum_{\sigma} \sum_{m} \left(c^{\dagger}_{1,\sigma m} c_{2,\sigma m} + c^{\dagger}_{2,\sigma m} c_{1,\sigma m} \right) \\ &\quad + U \sum_{i=1,2} \sum_{m} \hat{n}_{i,\uparrow m} \hat{n}_{i,\downarrow m} + \frac{1}{2} \sum_{i=1,2} \sum_{\sigma\sigma'} \sum_{m \neq m'} \left(U - 2J - J\delta_{\sigma,\sigma'} \right) \hat{n}_{i,\sigma m} \hat{n}_{i\sigma' m'} \end{aligned}$$

from the general Hamiltonian (5.1). Here, $\sigma \in \{\uparrow, \downarrow\}$ is the spin index, m is the orbital index, i.e., $m \in \{x^2 - y^2,\ 3z^2 - r^2\}$, $i \in \{1,2\}$ the site index, U the direct and J the exchange screened Coulomb term. When U is large compared to t, we can again treat H_T as a perturbation of H_U [53]. If we consider the case of one electron, or one hole like in K_2CuF_4, in the two degenerated e_g orbitals, four interesting configurations exist (figure 5.5). Because of U the low energy states are the ones with single occupied sites $|1,1\rangle$ (top rows in figure 5.5 a)-d)). The perturbation H_T connects $|1,1\rangle$ to all states with one double occupied site $|2,0\rangle_{\alpha}$ (bottom rows in figure 5.5 a)-d)). The energy gain in second order

perturbation theory is

$$\Delta E = -\sum_{\alpha} \frac{|\langle 1,1|H_T|2,0\rangle_\alpha|^2}{E_\alpha(2,0) - E(1,1)} = -\sum_{\alpha} \frac{t^2}{E_\alpha(2,0)}$$

with $E(1,1) = \langle 1,1|H_U|1,1\rangle = 0$ and $E_\alpha(2,0) = {}_\alpha\langle 2,0|H_U|2,0\rangle_\alpha$. The results for the different processes are given in figure 5.5, which shows that the energy gain is largest ($\Delta E = -2t^2/(U-3J)$) for ferromagnetic and antiferro-orbital order.

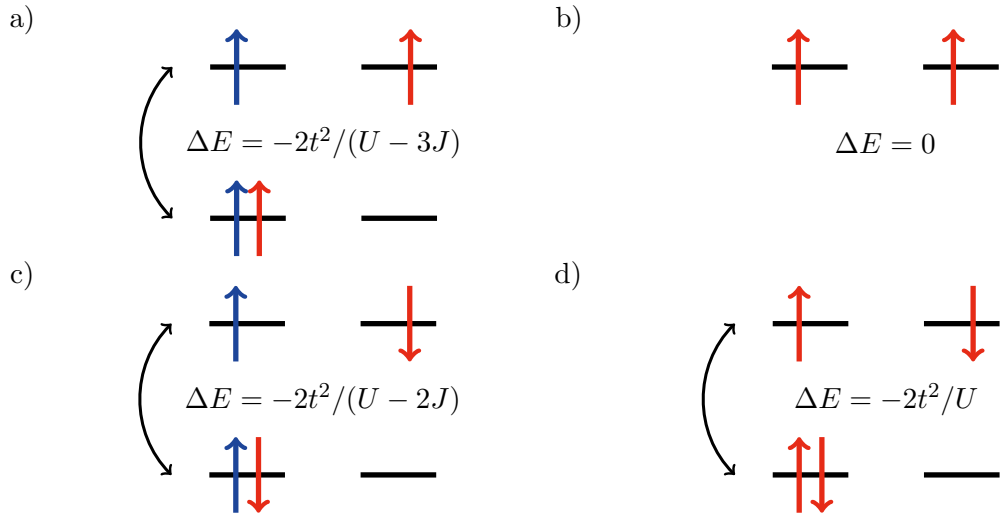

Figure 5.5: The energy gain ΔE in the superexchange mechanism for two sites and two orbitals (blue and red) is largest for ferromagnetic and antiferro-orbital order a).

We now generalize from the two site model to the lattice. Second order perturbation theory can be used to obtain an effective Hamiltonian [45,53]. We start with the Hubbard model (5.1), which has quarter filling of holes (one hole per site). The terms of (5.1) containing $t^{ii'}_{mm'}$, for which $|t^{ii'}_{mm'}| < U$, is the perturbation. For simplicity, we set $J = 0$ and consider the hopping in the z-direction with the approximated effective hopping matrix[1]

$$t^{i,i+z}_{mm'} \sim t \begin{pmatrix} 1 & 0 \\ 0 & 0 \end{pmatrix}$$

in the basis $|3z^2 - r^2\rangle$ and $|x^2 - y^2\rangle$. Then, the effective Hamiltonian in second order perturbation theory is

$$H^z_{\mathrm{SE}} = \frac{\Gamma}{2} \sum_{ii'} \left[\left(\mathbf{S}^i \cdot \mathbf{S}^{i'} - \frac{n_i n_{i'}}{4} \right) \left(O^i_z - \frac{n_i}{2} \right) \left(O^{i'}_z - \frac{n_{i'}}{2} \right) + \frac{1}{2} \left(O^i_z O^{i'}_z - \frac{n_i n_{i'}}{4} \right) \right] \tag{5.8}$$

[1] The hopping is almost only between the states $|3z^2 - r^2\rangle$ which point towards the z-direction (figure 5.3 a)).

with the effective spin and orbital coupling $\Gamma = 4t^2/U$ and

$$S^i_\nu = \frac{1}{2}\sum_{\sigma\sigma'}\sum_m c^\dagger_{i,\sigma m}\left[\sigma_\nu\right]_{\sigma\sigma'} c_{i,\sigma' m}$$
$$O^i_\nu = \frac{1}{2}\sum_{mm'}\sum_\sigma c^\dagger_{i,\sigma m}\left[\tau_\nu\right]_{mm'} c_{i,\sigma m'}.$$

Analogous relations to (5.8) can be derived for the x-direction by replacing

$$O^i_z \to -\frac{1}{2}O^i_z - \frac{\sqrt{3}}{2}O^i_x$$

and for the y-direction by replacing

$$O^i_z \to -\frac{1}{2}O^i_z + \frac{\sqrt{3}}{2}O^i_x.$$

In a layered perovskite the interlayer coupling can in first approximation be neglected and the effective Hamiltonian

$$\begin{aligned} H_{\mathrm{SE}} &= H^x_{\mathrm{SE}} + H^y_{\mathrm{SE}} \\ &= H^{(2)}_{\mathrm{SE}} + H^{(1)}_{\mathrm{SE}} + H^{(0)}_{\mathrm{SE}} \end{aligned}$$

can be split into terms, which are quadratic $H^{(2)}_{\mathrm{SE}}$, linear $H^{(1)}_{\mathrm{SE}}$ and constant $H^{(0)}_{\mathrm{SE}}$ in the operators O^i_ν. For K_2CuF_4, the term linear in the orbital operators O^i_ν is

$$H^{(1)}_{\mathrm{SE}} = -\frac{\Gamma}{2}\sum_{ii'}\left(\mathbf{S}^i\cdot\mathbf{S}^{i'} - \frac{n_i n_{i'}}{4}\right)\left(\frac{n_{i'}}{2}O^i_z + \frac{n_i}{2}O^{i'}_z\right).$$

This term is canceled out by H^z_{SE} in an infinite layer system like $KCuF_3$. It can be written as an orbital Zeeman term

$$h^z_{SE} = \sum_i B_z O^i_z. \tag{5.9}$$

Here, B_z is a field similar to a Zeeman field for spins, which is given by

$$B_z = -\frac{\Gamma}{2}\sum_{i'\neq i}\left[\mathbf{S}^i\cdot\mathbf{S}^{i'} - \frac{n_i n_{i'}}{4}\right]\frac{n_{i'}}{2}.$$

For a positive Γ this term splits the e_g states; $|3z^2 - r^2\rangle$ is the lower-energy state and $|x^2 - y^2\rangle$ the hole state. In our representation of the hole state (5.6) this corresponds to an angle $\theta = 0°$.
In K_2CuF_4 orbital ordering happens at much higher temperatures than magnetic ordering. To determine the angle θ in the paramagnetic phase, we set $\langle\mathbf{S}^i\cdot\mathbf{S}^{i'}\rangle = 0$ and $n_i = 1$. The quadratic Hamiltonian is then

$$H^{(2)}_{\mathrm{SE}} = \frac{\Gamma}{16}\sum_{ii'}\left(O^i_z O^{i'}_z + 3O^i_x O^{i'}_x\right).$$

We calculate the variational energy $E(\theta) = \langle\theta_i,\theta_{i'}|H^{(2)}_{\mathrm{SE}}|\theta_i,\theta_{i'}\rangle$ for two sites i and i', and we minimize $E(\theta)$ with respect to θ. For a ferro-orbital ordered state $|\theta_{i'}\rangle = |\theta_i\rangle = |\theta\rangle$ we obtain

$$E(\theta) = \frac{\Gamma}{64}\left(1 + 2\sin^2\theta\right).$$

This is minimal for $\theta = 0°$. For antiferro-orbital order we set $|\theta_i\rangle = |\theta\rangle$ and $|\theta_{i'}\rangle = |-\theta + 2\pi\rangle$. This means $|\theta_{i'}\rangle$ is rotated in x and y with respect to $|\theta_i\rangle$, i.e., $|x^2 - y^2\rangle \to |y^2 - x^2\rangle$ and $|3z^2 - r^2\rangle$ does not change. The minimum of the variational energy

$$E(\theta) = \frac{\Gamma}{64}\left(1 - 4\sin^2\theta\right)$$

in this case is obtained for $\theta = 90°$.

5.2.3 Susceptibility from static mean-field theory

In the last section we showed the mapping of the Hubbard model to an effective spin-orbital model (5.8) in the large U/t limit. Here, we derive the approximated susceptibility for a similar model, the spin Heisenberg model

$$H_{\mathrm{Heis}} = \frac{1}{2}\sum_{i\neq i'}\Gamma^{ii'}\mathbf{S}^i\cdot\mathbf{S}^{i'} \tag{5.10}$$

with a site dependent coupling $\Gamma^{ii'}$. Generalizations to the orbitally degenerated case are straightforward.
Although the Heisenberg model (5.10) is simpler than the Hubbard model, i.e., has a smaller state space, analytic solutions are not known in the general case. To get approximate solutions for the susceptibility, we use static mean-field theory [37, 55]. The basic idea of static mean-field theory is to write the spin operators in terms of their deviations from an average value

$$\mathbf{S}^i = \langle\mathbf{S}^i\rangle + \delta\mathbf{S}^i,$$

where $\delta\mathbf{S}^i = \mathbf{S}^i - \langle\mathbf{S}^i\rangle$, and neglect terms $\mathcal{O}\left[(\delta\mathbf{S}^i)^2\right]$ in the Hamiltonian. Applying this approximation to the Heisenberg Hamiltonian (5.10) gives

$$H'_{\mathrm{MF}} = \sum_{i\neq i'}\Gamma^{ii'}\mathbf{S}^i\cdot\langle\mathbf{S}^{i'}\rangle - \frac{1}{2}\sum_{i\neq i'}\Gamma^{ii'}\langle\mathbf{S}^i\rangle\cdot\langle\mathbf{S}^{i'}\rangle, \tag{5.11}$$

where we used $\Gamma^{ii'} = \Gamma^{i'i}$.
We add a site dependent magnetic field $\mathbf{h}^i$ and neglect the second term, which is a constant, to obtain

$$\begin{aligned} H_{\mathrm{MF}} &= \sum_{i\neq i'}\Gamma^{ii'}\mathbf{S}^i\cdot\langle\mathbf{S}^{i'}\rangle + g\mu_B\mathbf{S}^i\cdot\mathbf{h}^i \\ &= \sum_i \mathbf{S}^i\cdot\mathbf{h}^i_{\mathrm{eff}}. \end{aligned}$$

In atomic units $\mu_B \approx 1/2$, hence $g\mu_B \approx 1$ and the effective magnetic field is

$$\mathbf{h}^i_{\text{eff}} = \sum_{i'} \Gamma^{ii'} \langle \mathbf{S}^{i'} \rangle + \mathbf{h}^i.$$

In linear response theory (section 4.2) the magnetization $\mathbf{M}$ per site in terms of Matsubara frequencies is

$$\langle M^i_\nu \rangle = \sum_{\nu'} \sum_{i'} \tilde{\chi}_{M^i_\nu M^{i'}_{\nu'}} \left[h^{i'}_{\text{eff}} \right]_{\nu'} \tag{5.12}$$

with the susceptibility $\tilde{\chi}_{M^i_\nu M^{i'}_{\nu'}} = \beta \left(\langle M^i_\nu M^{i'}_{\nu'} \rangle - \langle M^i_\nu \rangle \langle M^{i'}_{\nu'} \rangle \right)$. In the paramagnetic case we can set the z-axis as quantization axis without loss of generality, thus $\nu = \nu' = z$. Within static mean-field theory we approximate the susceptibility $\tilde{\chi}_{M^i_z M^{i'}_z}(0)$ by using $\langle \mathbf{S}_i \rangle \sim \mathbf{0}$ and

$$\langle S^i_z S^{i'}_z \rangle = \begin{cases} \langle S^i_z \rangle \langle S^{i'}_z \rangle \sim 0 & \text{if} \quad i \neq i' \\ \langle S^i_z S^i_z \rangle \sim S(S+1)/3 & \text{if} \quad i = i' \end{cases}$$

with $S = 1/2$. This means the susceptibility is replaced by the local paramagnetic one of a spin

$$\begin{aligned} \tilde{\chi}_{M^i_z M^{i'}_z} &= \beta \delta_{i,i'} (g\mu_B)^2 \frac{S(S+1)}{3} \\ &\approx \delta_{i,i'} \frac{\beta}{4} = \delta_{i,i'} \tilde{\chi}. \end{aligned}$$

A long range magnetic order is related to a momentum vector $\mathbf{q}$. For a magnetic field $h^i_z = h_z e^{i\mathbf{T}_i \cdot \mathbf{q}}$ modulated with $\mathbf{q}$, where $\mathbf{T}_i$ is a lattice vector, we assume that the magnetization is $\langle M^i_z \rangle = M_z e^{i\mathbf{T}_i \cdot \mathbf{q}}$. With this (5.12) becomes a self-consistent equation in M_z

$$\begin{aligned} M_z &= \tilde{\chi} \left(-\sum_{i'} \Gamma^{ii'} M_z e^{-i(\mathbf{T}_i - \mathbf{T}_{i'}) \cdot \mathbf{q}} + h_z \right) \\ &= \tilde{\chi} \left(-\Gamma(\mathbf{q}) M_z + h_z \right) \end{aligned}$$

with the Fourier transformed coupling $\Gamma(\mathbf{q}) = \sum_i \Gamma^{0i} e^{i\mathbf{T}_i \cdot \mathbf{q}}$. This can now be brought into the form $M_z = \chi^{zz}_{MF}(\mathbf{q},0) h_z$ with the mean-field susceptibility

$$\begin{aligned} \chi^{zz}_{MF}(\mathbf{q},0) &= \frac{\tilde{\chi}}{1 + \tilde{\chi}\Gamma(\mathbf{q})} \\ &= \frac{1}{4} \frac{1}{k_B T + \Gamma(\mathbf{q})/4} \\ &= \frac{1}{4k_B} \frac{1}{T - T_{\mathbf{q}}} \end{aligned} \tag{5.13}$$

and the temperature $k_B T_{\mathbf{q}} = -\Gamma(\mathbf{q})/4$.
The phase transition happens at $T_c = T_{\mathbf{q}_c}$, where $\mathbf{q}_c$ is the vector giving the highest critical temperature. At $T = T_c$ the susceptibility diverges.

For $\Gamma^{ii'} = -\Gamma < 0$ the spins order ferromagnetically and $T_{\mathbf{q}_c} = \Gamma \sum_i e^{i\mathbf{T}\mathbf{q}}$ with $\mathbf{q}_c = \mathbf{0}$, T_c is in this case the Curie temperature and the uniform susceptibility $\chi^{zz}_{MF}(\mathbf{0},0)$ diverges at T_c.
If the parameter $\Gamma^{ii'} = \Gamma > 0$ is positive, the spins order antiferromagnetically. For example, on a two dimensional square lattice with lattice constant a the divergence is at $\mathbf{q}_c = (\pi/a, \pi/a)$. The critical temperature is the Néel temperature $T_c = T_N$. The uniform susceptibility $4k_B\chi^{zz}_{MF}(\mathbf{0},0) = 1/(T + T_N)$ does not diverge at any temperature.

5.3 Method

We start by constructing the Hamiltonian (5.1) ab-initio. The electronic structure is calculated with density-functional theory (DFT) in the local-density approximation (LDA) (section 2.1.1) using the WIEN2k code [56,57]. Then, localized Wannier functions (section 2.1.2) are calculated for the two e_g orbitals of the Cu^{2+} ions using the maximally localized Wannier function method [58, 59]. Since the Wannier functions have the same symmetry as the orbitals $|3z^2-r^2\rangle$ and $|x^2-y^2\rangle$, we use the same notation. We perform calculations for the experimental Bbcm and Ammm structure as well as idealized structures with zero crystal-field and reduced distortions of the F^- octahedron.
The Hubbard model is solved within dynamical mean-field theory (DMFT) (section 2.2) using the general Krylov solver (section 3.4). For the Ammm structure we use a one-site Hubbard model. For the Bbcm structure we use a unit cell containing two equivalent sites and thus a two site Hubbard model (figure 5.6). The two sites in that structure are equivalent due to point symmetries; the crystal-field matrix of the second site is obtained by exchanging the x- and y-axis of the first site and vice versa. To get the site dependent self-energy from the local self-energy, we use (2.19)

$$\Sigma^{\sigma}_{sm,s'm'}(i\nu_n) = \delta_{s,s'}\Sigma^{\sigma}_{m,m'}(i\nu_n),$$

because all calculations are performed in the paramagnetic phase.
From DMFT we obtain the single-particle Green function $G_l^{\sigma,mm'}$, the local static susceptibility tensor $\chi^{\sigma\sigma',m_1m_2m_3m_4}_{ll'}(0)$ and the occupation matrix $n_{\sigma,mm'} = \langle c^\dagger_{\sigma m} c_{\sigma m'}\rangle$.
By diagonalizing the occupation matrix $n_{mm'} = n_{\uparrow,mm'} + n_{\downarrow,mm'}$ we obtain the natural orbitals $|1\rangle$ and $|2\rangle$. The eigenvectors of $n_{mm'}$ can be expressed in terms of the angle θ. The lower-energy state, whose occupation is n_1, is $|\bar{\theta}\rangle = \cos\frac{\theta}{2}|3z^2-r^2\rangle + \sin\frac{\theta}{2}|x^2-y^2\rangle$ and the higher-energy state is $|\theta\rangle = -\sin\frac{\theta}{2}|3z^2-r^2\rangle + \cos\frac{\theta}{2}|x^2-y^2\rangle$ (5.6) with occupation n_2.
Let us use the abbreviations $m \in \{0,\pi\}$ in $n_{mm'}$ such that the corresponding states for the two values of m are $|\bar{\theta}=0\rangle = |3z^2-r^2\rangle$ and $|\bar{\theta}=\pi\rangle = |x^2-y^2\rangle$. The natural occupations are then the eigenvalues

$$n_{1,2} = \frac{n_{00}+n_{\pi\pi}}{2} \pm \sqrt{\frac{(n_{\pi\pi}-n_{00})^2}{4} + |n_{0\pi}|^2},$$

ordered such that $n_1 > n_2$. From the occupation of natural orbitals we calculate the orbital polarization

$$p = n_1 - n_2, \tag{5.14}$$

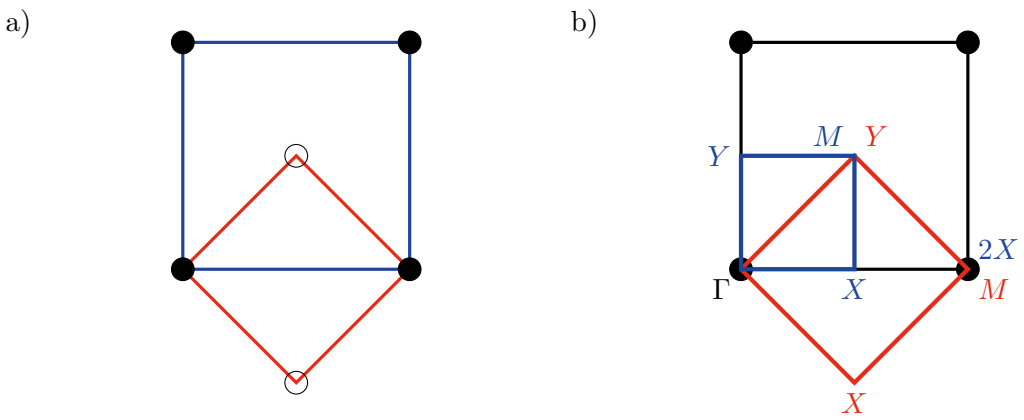

Figure 5.6: a) Unit cell (blue) for ambient pressure Bbcm structure with two formula units and unit cell (red) of high pressure Ammm structure. All lattice constants are normalized. In b) we show the related Brillouin zones.

which is maximum ($p = 1$, orbital ordered) for $n_1 = 2$ and $n_2 = 1$, and minimum ($p = 0$, para-orbital solution) for $n_1 = 1.5 = n_2$.
After the DMFT calculations, we use the susceptibility matrix $[\chi(0)]$ and the bare susceptibilities $\left[\chi^0(\mathbf{q},0)\right]$ and $\left[\chi^0(0)\right] = \sum_{\mathbf{q}} \left[\chi^0(\mathbf{q},0)\right] / N_{\mathbf{q}}$ to obtain the lattice susceptibility matrix $[\chi(\mathbf{q},0)]$. This step is done via the Bethe-Salpeter equation (BSEQ) (4.27)

$$[\chi(\mathbf{q},i\omega_m)]^{-1} = \left[\chi^0(\mathbf{q},i\omega_m)\right]^{-1} - \left[\chi^0(i\omega_m)\right]^{-1} + [\chi(i\omega_m)]^{-1}\,.$$

All matrices have the indices $(l,\sigma,s_1,m_1,s_2,m_2)$ and $(l',\sigma',s_3,m_3,s_4,m_4)$. Here, l is the index of the intermediate representation polynomial, $\sigma \in \{\uparrow\ ,\ \downarrow\}$ the spin and $m \in \{3z^2 - r^2, x^2 - y^2\}$ the orbital index. The site index is $s \in \{1,2\}$ for the Bbcm structure and $s = 1$ for the Ammm structure.
From the susceptibility tensor the magnetic susceptibility is obtained by

$$\begin{aligned}\chi^{zz}(\mathbf{q},0) = \frac{1}{4}\sum_{\sigma\sigma'}(-1)^{\sigma+\sigma'}\frac{1}{2}\sum_{ss'}e^{i\phi_{ss'}}\sum_{mm'}\frac{1}{\beta^2}\sum_{ll'}(-1)^{l'+1}\times \\ \times\, f_l^0(x(0))f_{l'}^0(x(0))\;\chi_{ll',\sigma\sigma'}^{sm,sm,s'm',s'm'}(\mathbf{q},0).\end{aligned}$$

Here, the abbreviation $\chi^{\sigma\sigma'} = \chi^{\sigma\sigma\sigma'\sigma'}$ is used, and the magnetic susceptibility is independent of the quantization axis $\chi^{zz} = \chi^{yy} = \chi^{xx}$ because we do calculations in the paramagnetic phase. The basis polynomials $f_l^0(x(\tau))$ are defined in section 4.5.3. For the upfolding of the small Brillouin zone of the Bbcm structure (figure 5.6 b)) we use the phase $\phi_{ss'}$, which for K_2CuF_4 is simply:

$$\phi_{ss'} = \left(1 - \delta_{s,s'}\right)(-1)^s(q_x + q_y)/2.$$

Here, the momenta are q_x, $q_y \in [-\pi/a, \pi/a]$.

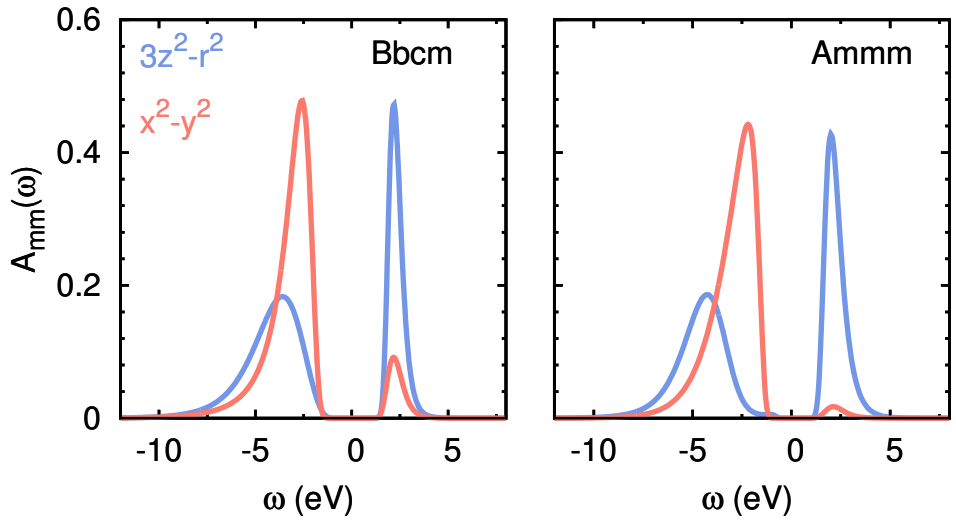

Figure 5.7: Spectral function of structure Bbcm and Ammm for the two e_g orbitals of K_2CuF_4 for $U = 7\,\text{eV}$ and $J = 0.9\,\text{eV}$ at $T \sim 290\,\text{K}$.

Finally, the orbital susceptibilities are

$$\begin{aligned}\chi^{zz}_{oo}(\mathbf{q},0) = &\sum_{\sigma\sigma'}\frac{1}{2}\sum_{ss'}e^{i\phi_{ss'}}\frac{1}{4}\sum_{mm'}(-1)^{m+m'}\frac{1}{\beta^2}\sum_{ll'}(-1)^{l'+1}\times\\ &\times f^0_l(x(0))f^0_{l'}(x(0))\;\chi^{sm,sm,s'm',s'm'}_{ll',\sigma\sigma'}(\mathbf{q},0)\\ \chi^{xx}_{oo}(\mathbf{q},0) = &\sum_{\sigma\sigma'}\frac{1}{2}\sum_{ss'}e^{i\phi_{ss'}}\frac{1}{4}\sum_{mm'}\frac{1}{\beta^2}\sum_{ll'}(-1)^{l'+1}\times\\ &\times f^0_l(x(0))f^0_{l'}(x(0))\;\chi^{sm,s(-m),s'm',s'(-m')}_{ll',\sigma\sigma'}(\mathbf{q},0)\end{aligned}$$

with $m = 3z^2 - r^2 \to -m = x^2 - y^2$ and $m = x^2 - y^2 \to -m = 3z^2 - r^2$. The l summation of the polynomials is performed up to a cutoff $l_{\max}$.[2]
From the static susceptibilities $\chi(\mathbf{q},0)$ we extract the couplings as follows

$$\Gamma(\mathbf{q}) = [\chi(\mathbf{q},0)]^{-1} - 4k_BT$$

both for the magnetic and orbital case.

5.4 Results

5.4.1 Results for the experimental structure

Let us first consider the experimental structures in figure 5.1 and figure 5.8. The orbital resolved spectral function of K_2CuF_4 for these structures, obtained with DMFT, is shown in figure 5.7. The material is a Mott insulator with a large gap.

[2]See chapter chapter 4 for the discussion of the convergence in $l_{\max}$.

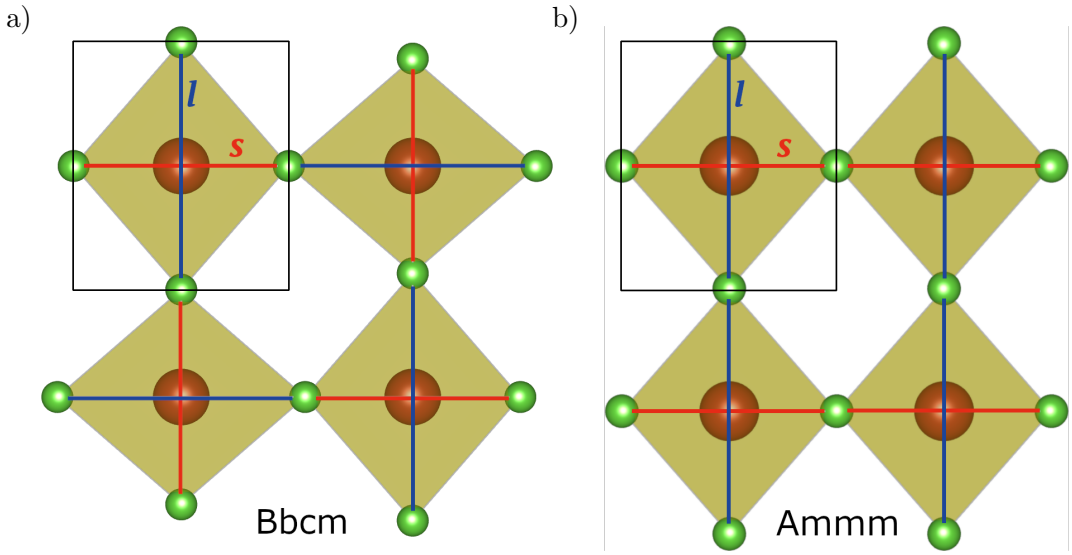

Figure 5.8: Alignment of long l and short s bonds in the x-y-plane for the Bbcm a) and Ammm structure b).

To describe the orbital ordering, we use the definition of the hole state $|\theta\rangle = -\sin\frac{\theta}{2}|3z^2 - r^2\rangle + \cos\frac{\theta}{2}|x^2 - y^2\rangle$ (5.6). At ambient pressure, in the Bbcm structure, the hole states are in an antiferro-orbital order in the x-y-plane. Under high pressure, in the Ammm structure, the orbital order is ferro-orbital in the x-y-plane. In LDA we find the following tetragonal splitting ϵ_{T}, Jahn-Teller splitting ϵ_{JT} and angle θ:

structure	Bbcm	Ammm
ϵ_{T}	460 meV	434 meV
ϵ_{JT}	500 meV	178 meV
θ	132.6°	157.6°

For the structure Ammm the tetragonal crystal-field is dominant. This explains the angle θ close to 180°, the angle for a tetragonally compressed structure in z-direction. Also, in figure 5.7 the spectral function for the hole, above the Fermi-level, is almost entirely given by $|\theta = 180°\rangle = |3z^2 - r^2\rangle$. The structure Bbcm on the other hand has a Jahn-Teller and tetragonal crystal-field of comparable size. The angle θ is therefore close to 135°, in the middle between the tetragonal angle 180° and the Jahn-Teller angle 90°.
The DMFT orbital polarization is almost maximal $p \sim 1$ up to the melting temperature. All calculations are done in the paramagnetic phase. The type of magnetic ordering at low temperatures is deduced from the magnetic lattice exchange couplings $\Gamma^{zz}(\mathbf{q})$. The exchange couplings $\Gamma^{zz}(\mathbf{q})$ are minimal, the system gains energy, at the ordering vector $\mathbf{q}_c$. In the first row of figure 5.9 we show the results for the different experimental structures. The left plot shows $\Gamma^{zz}(\mathbf{q})$ in a part of the Brillouin zone of the Bbcm structure (blue in figure 5.6), while on the right the result for a part of the Brillouin zone of the Ammm structure (red in figure 5.6) is given. For the Bbcm structure the critical vector $\mathbf{q}_c = \mathbf{0}$ indicates ferromagnetism. For the Ammm structure we find one dimensional

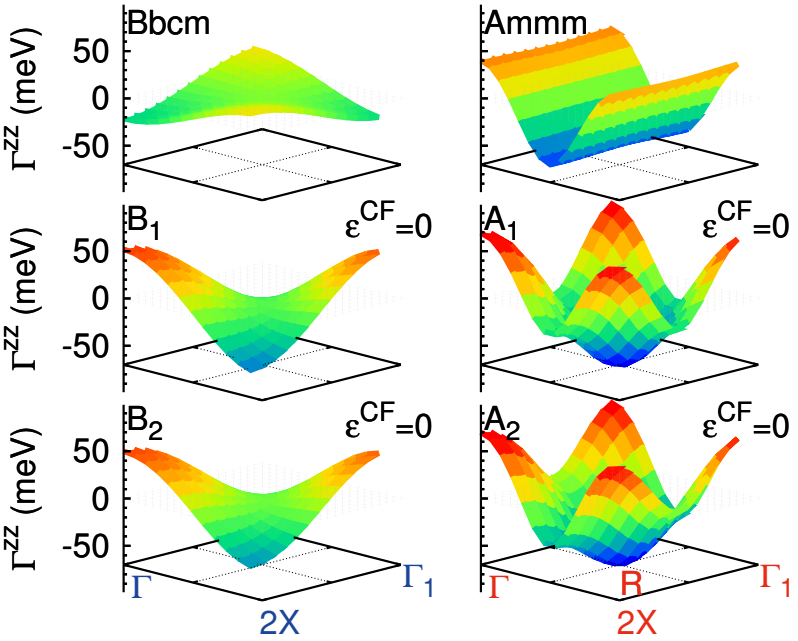

Figure 5.9: Magnetic coupling $\Gamma^{zz}(\mathbf{q})$ extracted from DMFT lattice susceptibility. The special points are $\Gamma = \mathbf{0}$, $2X = (2\pi,0,0)$, $\Gamma_1 = (2\pi,2\pi,2\pi)$ and $R = (\pi,\pi,\pi)$. The first row is for the experimental structure, all other plots are for structures with reduced disorder and removed crystal-field. All lattice constants are set to 1.

antiferromagnetism for a vector $\mathbf{q}_c = X$. These results are in agreement with experiments [60].

5.4.2 Results for the structure with removed crystal-field

To disentangle the effects of the lattice distortions from the superexchange mechanism, we perform calculations with reduced distortions and zero crystal-field ϵ^{CF}. We set $\epsilon^{\mathrm{CF}} = 0$ for all four structures A_1, A_2, B_1 and B_2 in figure 5.9. Furthermore, we remove the Jahn-Teller distortion of Q_1 type for the A_1 and B_1 structure, and we additionally remove the tetragonal Q_2 distortion in A_2 and B_2. Thus, the latter structures consist of regular octahedra of F^- ions. The cubic K^+ cage is not changed. All four structures are Mott insulators with band gaps similar to the experimental structures (figure 5.7), and they are antiferromagnets with isotropic couplings in the x-y-plane related to $\mathbf{q}_c = (\pi,\pi,0)$ in the small unit cell (red in figure 5.6).

In a similar way we study the orbital ordering in superexchange theory by calculation of the orbital exchange couplings $\Gamma^{xx}_{oo}(\mathbf{q})$ and $\Gamma^{zz}_{oo}(\mathbf{q})$. We plot the results for $\Gamma^{xx}_{oo}(\mathbf{q})$ in figure 5.10 and for $\Gamma^{zz}_{oo}(\mathbf{q})$ in figure 5.11. The structures are the same as for the magnetic calculations and we set $\epsilon^{\mathrm{CF}} = 0$ to determine the couplings for superexchange.
First of all, the order determining coupling is $\Gamma^{xx}_{oo}(\mathbf{q})$, because the energy range is much larger than for $\Gamma^{zz}_{oo}(\mathbf{q})$. For the Bbcm structure the minimum of $\Gamma^{xx}_{oo}(\mathbf{q})$ is at the Γ point. This corresponds to an antiferro-orbital ordering in the x-y-plane. More specifically, for

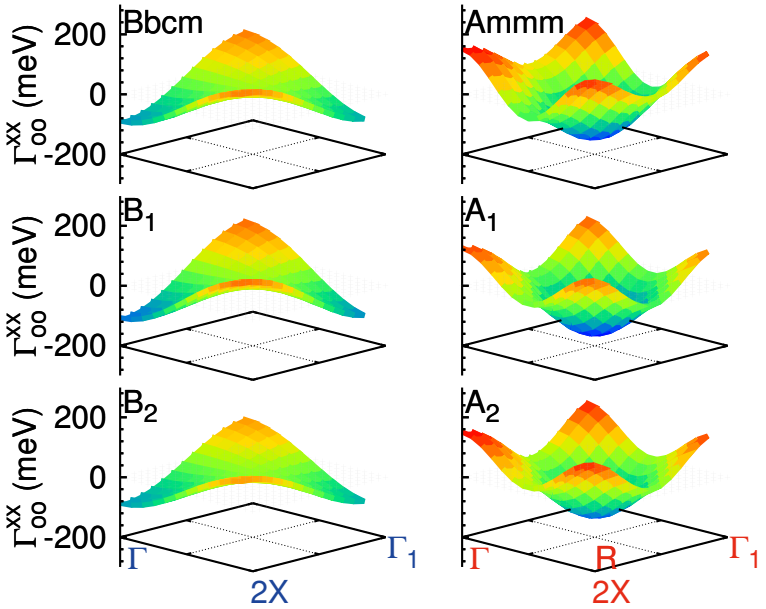

Figure 5.10: Orbital coupling $\Gamma^{xx}_{oo}(\mathbf{q})$ extracted from DMFT lattice susceptibility. The special points are $\Gamma = \mathbf{0}$, $2X = (2\pi,0,0)$, $\Gamma_1 = (2\pi,2\pi,2\pi)$ and $R = (\pi,\pi,\pi)$. For all plots the crystal-field is removed.

one site with an orbital with $\theta = 90°$, which is similar to $|x^2 - z^2\rangle$, the neighboring sites all are similar to $|y^2 - z^2\rangle$ with $\theta = 270°$ (figure 5.3). The $\Gamma^{zz}_{oo}(\mathbf{q})$ coupling is positive at the Γ point, which can lead to frustration. Because it is minimal at $\mathbf{q} = 2X$, the orbitals would order with alternating $|3z^2 - r^2\rangle$ and $|x^2 - y^2\rangle$ if we would set $\Gamma^{xx}_{oo}(\mathbf{q}) = 0$.
The right column in figure 5.10 and figure 5.11 shows the results for the high pressure structure. The predicted orderings are identical to the ambient pressure structure. For $\Gamma^{zz}_{oo}(\mathbf{q})$ the minimum at $\mathbf{q}_c = R = (\pi,\pi,\pi)$ corresponds again to an order with alternating $|3z^2 - r^2\rangle$ and $|x^2 - y^2\rangle$. The ordering vector of $\Gamma^{xx}_{oo}(\mathbf{q})$ is again $\mathbf{q}_c = R$. In this structure it indicates the same ordering as the Γ point in the Bbcm structure. Superexchange, in this case, predicts an order different from the obtained, when including the crystal-field in the experimental structure.

5.4.3 The role of the orbital Zeeman interaction

In layered materials like K_2CuF_4 the Hamiltonian linear in the orbital operator O^i_z, which is absent in cubic perovskites like $KCuF_3$, can be finite and is given by (5.9)

$$h^z_{SE} = \sum_i B_z O^i_z.$$

To further investigate orbital ordering in K_2CuF_4 and the effects of the Zeeman term, we calculate the orbital polarization p, the angle θ and the inverse of the orbital susceptibilities $\chi^{xx}_{oo}(\mathbf{q},0)$ and $\chi^{zz}_{oo}(\mathbf{q},0)$ depending on temperature. The results for the structures Bbcm and Ammm are given in figure 5.12 and figure 5.13, respectively.

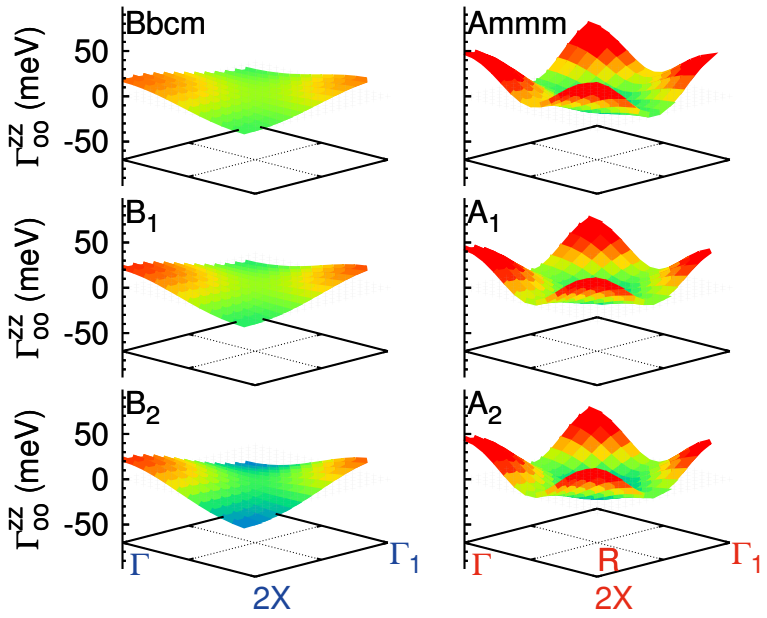

Figure 5.11: Orbital coupling $\Gamma^{zz}_{oo}(\mathbf{q})$ extracted from DMFT lattice susceptibility. The special points are $\Gamma = \mathbf{0}$, $2X = (2\pi,0,0)$, $\Gamma_1 = (2\pi,2\pi,2\pi)$ and $R = (\pi,\pi,\pi)$. For all plots the crystal-field is removed.

From the inverse susceptibility we can extract the superexchange driven orbital ordering transition temperature. At the critical momentum of the Bbcm structure $\mathbf{q}_c = \mathbf{0}$ the inverse susceptibility goes to zero at $T_{\mathrm{SE}} \sim 300K$. In the Ammm structure the transition would happen for $\mathbf{q}_c = R$ at $T_{\mathrm{SE}} \sim 400K$.
However, for the Bbcm structure the polarization is finite also above T_{SE}. This is due to the orbital Zeeman interaction, which splits the orbitals, resulting in a polarization without a phase transition. The hole state in this case is $|\theta = 0°\rangle = |x^2 - y^2\rangle$. Instead, in the ordered phase the hole state is $|\theta = 90°\rangle$ as seen above. Because of the Zeeman term, T_{SE} is reduced, and in vicinity of T_{SE} the two phases with $\theta = 0°$ and $\theta = 90°$ even coexist. This is shown in the plots for the B_1 and B_2 structure.
The role of the Zeeman term is similar for the Ammm structure. A finite orbital polarization exists above the transition temperature T_{SE}, which is again connected to the hole state $|\theta = 0°\rangle = |x^2 - y^2\rangle$, and the Zeeman field induced polarization rises until ~ 0.5. However, for this structure no transition is seen in the polarization p or angle θ below T_{SE}. The reason is that the ordering vector is $\mathbf{q}_c = R \neq \mathbf{0}$. The superexchange type of order is not compatible with the experimental structure.
Finally, the superexchange Zeeman term h^z_{SE} competes not only with the superexchange transition but also with the static crystal-field ϵ^{CF}, which favors a state with $\theta \sim 180°$. We verified that the influence of h^z_{SE} is small compared to ϵ^{CF}. This can be understood by comparing the DMFT results for the experimental structure (open black circles) with the LDA results (black line for θ), which match very well (figure 5.12 and 5.13).

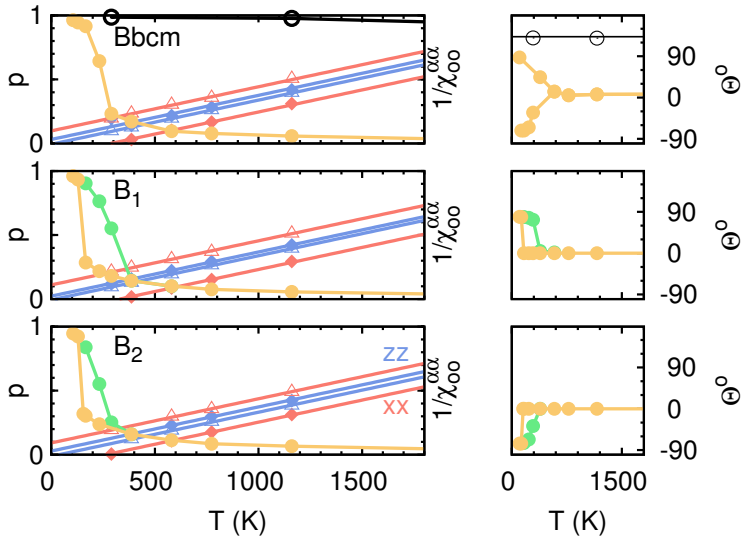

Figure 5.12: Temperature dependence of orbital polarization p, angle θ and inverse orbital susceptibility $\chi^{xx}_{oo}(\mathbf{q},0)$ in red and $\chi^{zz}_{oo}(\mathbf{q},0)$ in blue at the special points $\mathbf{q} = \mathbf{0}$ (diamonds) and $\mathbf{q} = 2X$ (triangles). The black line shows the LDA angle and the open dots the DMFT results for the experimental structure, all other structures have $\epsilon^{\mathrm{CF}} = 0$. For the B_1 and B_2 structure two solutions coexist. In the first row the two solutions with $\pm\theta$ are equivalent.

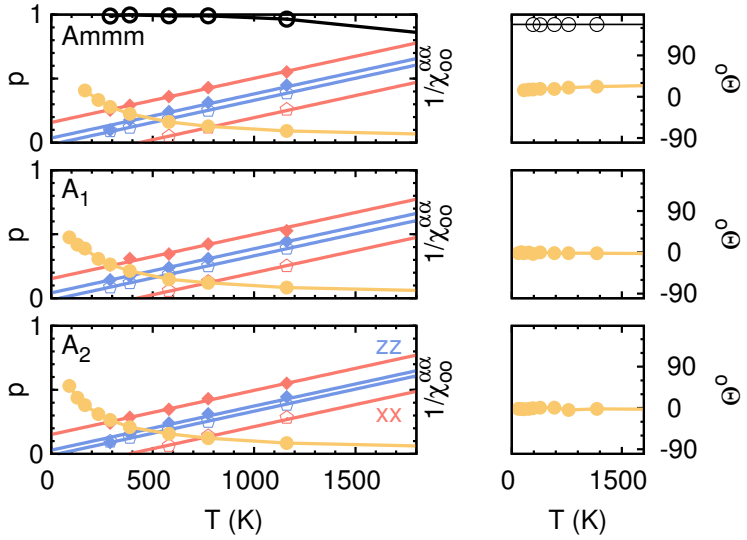

Figure 5.13: Temperature dependence of orbital polarization p, angle θ and inverse orbital susceptibility $\chi^{xx}_{oo}(\mathbf{q},0)$ in red and $\chi^{zz}_{oo}(\mathbf{q},0)$ in blue at the special points $\mathbf{q} = \mathbf{0}$ (diamonds) and $\mathbf{q} = R$ (pentagons). The black line shows the LDA angle and the open dots the DMFT results for the experimental structure, all other structures have $\epsilon^{\mathrm{CF}} = 0$.

5.5 Conclusions

By calculating the susceptibility and polarization for different structures of K_2CuF_4 with removed crystal-field we study the effects of superexchange. The orbital ordering temperature in these cases is too small compared to experiments. At high pressure superexchange even leads to a different type of ordering. We conclude that superexchange alone cannot explain orbital ordering in K_2CuF_4. The crystal-field due to the Jahn-Teller distortion via electron-phonon coupling enhanced by Coulomb effects [46] is essential for orbital ordering. The same conclusion was drawn also for the cubic perovskite $KCuF_3$. In the layered K_2CuF_4, we identified an additional Zeeman term, whose influence is small compared to the static crystal-field. This mechanism could however play a bigger role in other systems than K_2CuF_4.

6 Magnetic properties of high temperature superconducting cuprates

A publication containing this chapter is in preparation.

Since their discovery in 1986 [61], high-temperature superconducting cuprates have been studied extensively [62, 63]. Despite these ongoing efforts, questions remain open, especially on the microscopic mechanism behind the superconductivity. In some scenarios, magnetic properties are expected to play an important role for this mechanism. Within DMFT the calculation of the magnetic response functions, in particular the dynamical ones, has become feasible only in recent years. Here, we present results of magnetic response functions for a one-band Hubbard model with different parameters representing various cuprates.

6.1 Model and method

In this chapter we investigate the magnetic susceptibility for the model Hamiltonian

$$\begin{aligned} H &= H_T + H_U \\ &= -\sum_{\sigma}\sum_{ii'} t_{ii'} c^{\dagger}_{i,\sigma} c_{i',\sigma} + \sum_i U \hat{n}_{i,\uparrow}\hat{n}_{i,\downarrow} \end{aligned}$$

with $\hat{n}_{i,\sigma} = c^{\dagger}_{i,\sigma} c_{i,\sigma}$, i being the site and σ the spin. We consider hopping between nearest and next-nearest neighbors with the hopping integrals t and t', respectively. Fourier transforming H_T gives the Hamiltonian $H_T = \sum_\sigma \sum_{\mathbf{k}} \epsilon_{\mathbf{k}} \hat{n}_{\mathbf{k},\sigma}$ with

$$\epsilon_{\mathbf{k}} = -2t\left(\cos k_x + \cos k_y\right) + 4t' \cos k_x \cos k_y, \tag{6.1}$$

where we set the distance between nearest neighbors to one.
The similarity of all cuprates is that they are made of horizontal layers of CuO_2, like the one depicted in figure 6.1. Each layer is a two-dimensional square lattice formed by Cu ions. Two Cu ions are connected via one intermediate O ion, such that every Cu ion is surrounded by four O ions.
A four orbital model is sufficient to describe the low energy layer related features, which are common to all cuprates [64]. They are 4s and $3d_{x^2-y^2}$ for the Cu ions, and $2p_x$ and $2p_y$

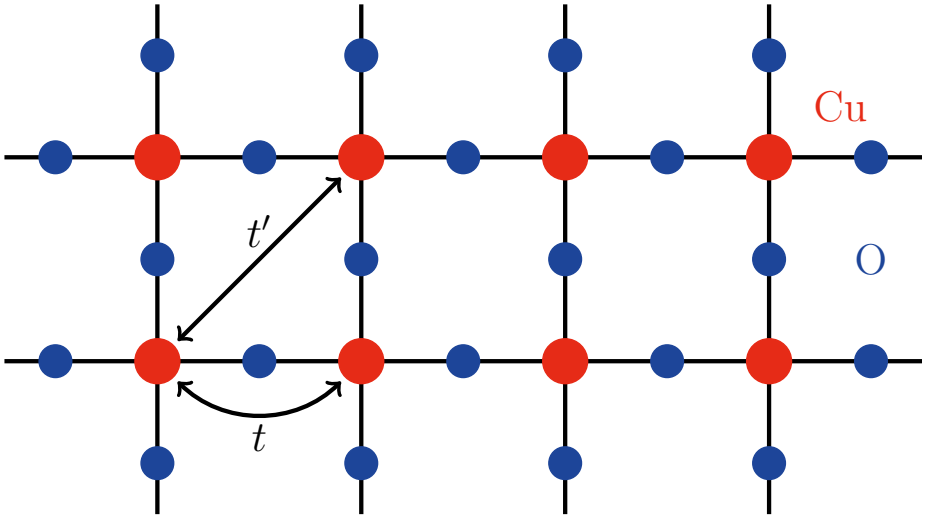

Figure 6.1: CuO_2 plane common to all superconducting cuprates. Each Cu ion is surrounded by four O ions. The nearest neighbor hopping integral is t and the next-nearest neighbor one t'.

for the O ions. We show the role of the four orbitals schematically in figure 6.2. Nearest neighbor hopping with parameter t is between Cu $d_{x^2-y^2}$ orbitals via one O p orbital. Next-nearest neighbor hopping is via two O p orbitals and one intermediate Cu s-like orbital. We set ϵ_s as the energy of the axial Cu s-like orbital, which is a combination of Cu s, Cu $3z^2 - 1$ and farther orbitals in vertical direction. In this model different cuprates have essentially a different ϵ_s, which also controls t'. Furthermore, LDA calculations showed that the relevant band structure, common to all cuprates, in vicinity of the Fermi level ϵ_F is approximately described by (6.1) [64]. We choose $t \sim 0.4\,\mathrm{eV}$ and t' in the range $0 \leq t' \leq 0.4t$ to model different cuprates. For example, for $La_{2-x}Sr_xCuO_4$ $t' \approx 0.18t$ and for $YBa_2Cu_3O_{7-\delta}$ $t' \approx 0.35t$ [64].

The choice of the screened Coulomb repulsion U is challenging. In Ref. [29] U was determined by expanding a Hubbard model at half-filling to a Heisenberg model with coupling $J \sim 4t^2/U$ and fitting the latter to an experimentally obtained spin-wave dispersion. This gives a small $U \approx 3\,\mathrm{eV}$. A small U is also supported by the constrained random-phase approximation (cRPA) [65,66]. On the other hand, results calculated with the constrained local-density approximation (cLDA) give much larger values up to $U \approx 10\,\mathrm{eV}$ [67–71]. In single-site DMFT, for our choice of hopping parameters, the critical U_c for the metal insulator transition is $U_c \sim 4.5\,\mathrm{eV}$. Only calculations with $U > U_c$ can explain an insulator with a gap comparable to the one found in experiments [63, 72–74]. To reproduce the experimentally determined gap of $\sim 2\,\mathrm{eV}$ in DMFT with a half-filled model $U \approx 7\,\mathrm{eV}$ has to be chosen. We therefore use U in the range $U \sim 4.7 - 7\,\mathrm{eV}$ and study the effects of different U.

At half-filling $n_i = 1$ and $U > U_c$ the model describes a Mott insulator, which shows

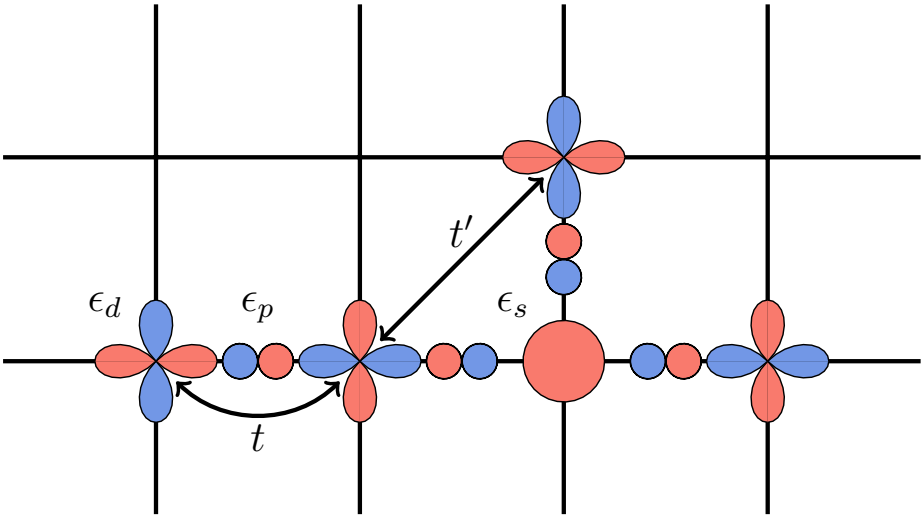

Figure 6.2: Atomic orbitals representing the relevant four orbitals for the CuO_2 layer with related energies ϵ_d, ϵ_p and ϵ_s. The nearest neighbor hopping integral is t and the next-nearest neighbor one t'. The figure is rearranged from Ref. [64].

antiferromagnetic order below the Néel temperature. In addition to the half-filled model, we consider different amounts of hole doping x, which imply smaller fillings $n_i = 1 - x$. The doped model is metallic and the magnetic order (ferro- or antiferromagnetic) of the metal depends on t' and x. Experimentally, at temperatures below the critical temperature T_c the system is superconducting. The largest T_c is found for optimal doping $x \approx 0.16$ [63]. Here, we consider the normal phase.

The DMFT and susceptibility calculations are done as explained in chapter 5. In addition, we calculate the dynamical susceptibility and, in the ordered phase of the parent compounds, magnetic susceptibilities in two orthogonal directions.
In the paramagnetic phase, $\chi^{zz}(\mathbf{q},i\omega_m)$ is calculated using the fast segment CT-QMC solver for the one-site model. For an antiferromagnetically ordered system we calculate $\chi^{zz}(\mathbf{q},i\omega_m)$ as well as $\chi^{xx}(\mathbf{q},i\omega_m)$ in a two-site supercell. The hopping Hamiltonian in the supercell is $H_T = \sum_\sigma \sum_{\mathbf{k}} \sum_{ss'} \epsilon_{\mathbf{k}}^{ss'} c^\dagger_{\mathbf{k},\sigma s} c_{\mathbf{k},\sigma s'}$ with

$$\epsilon_{\mathbf{k}}^{ss'} = \begin{pmatrix} 4t' \cos k_x \cos k_y & -2t\,(\cos k_x + \cos k_y)\, e^{-ik_x} \\ -2t\,(\cos k_x + \cos k_y)\, e^{ik_x} & 4t' \cos k_x \cos k_y \end{pmatrix}_{ss'} . \tag{6.2}$$

The self-energy of the second site is related to the first site by

$$\Sigma^2_{\sigma,\sigma'}(i\nu_n) = (-1)^{\sigma+\sigma'} \Sigma^1_{-\sigma,-\sigma'}(i\nu_n)$$

and in the Bethe-Salpeter equation we use the mapping

$$\Gamma^2_{\sigma_1,\sigma_2,\sigma_3,\sigma_4}(i\omega_m) = (-1)^{\sigma_1+\sigma_2+\sigma_3+\sigma_4} \Gamma^1_{-\sigma_1,-\sigma_2,-\sigma_3,-\sigma_4}(i\omega_m)$$

for the vertex.
In the antiferromagnetic two-site model we obtain the magnetic susceptibilities

$$\begin{aligned}\chi^{zz}(\mathbf{q},i\omega_m) &= \frac{1}{4}\sum_{\sigma\sigma'}(-1)^{\sigma+\sigma'}\frac{1}{2}\sum_{ss'}e^{i\phi_{ss'}}\frac{1}{\beta^2}\sum_{ll'}(-1)^{l'+1}\times \\ &\quad\times f_l^m(x(0))f_{l'}^m(x(0))\;\chi_{ll'}^{\sigma s,\sigma' s'}(\mathbf{q},i\omega_m) \\ \chi^{xx}(\mathbf{q},i\omega_m) &= \frac{1}{4}\sum_{\sigma\sigma'}\frac{1}{2}\sum_{ss'}e^{i\phi_{ss'}}\frac{1}{\beta^2}\sum_{ll'}(-1)^{l'+1}\times \\ &\quad\times f_l^m(x(0))f_{l'}^m(x(0))\;\chi_{ll'}^{\bar{\sigma} s,\bar{\sigma}' s'}(\mathbf{q},i\omega_m)\end{aligned}$$

with $\chi^{\sigma s,\sigma' s'} = \chi^{\sigma s,\sigma s,\sigma' s',\sigma' s'}$ and $\chi^{\bar{\sigma} s,\bar{\sigma}' s'} = \chi^{\sigma s,-\sigma s,\sigma' s',-\sigma' s'}$, $-\uparrow=\downarrow$ and $-\downarrow=\uparrow$. The compact basis functions $f_l^m(x(\tau))$ are constructed from Legendre polynomials, which give stable results even for large l and ω_m. The phase is

$$\phi_{ss'} = (-1)^s i q_x (1-\delta_{s,s'}). \tag{6.3}$$

In principle, calculations in the ordered phase could be also done using the segment solver. Then, the magnetization is $m = (n_\uparrow - n_\downarrow)/2$ and the self-energy is diagonal in the spin

$$\Sigma = \begin{pmatrix}\Sigma_\uparrow & 0\\ 0 & \Sigma_\downarrow\end{pmatrix}.$$

In practice, we use the Krylov solver, which enables us to choose the direction of the magnetization freely. CT-QMC results for $\chi^{xx}(\mathbf{q},i\omega_m)$ are less noisy if we use the rotated self-energy matrix

$$\begin{aligned}\Sigma' &= R\,\Sigma\,R^T \\ &= \frac{1}{2}\begin{pmatrix}1 & 1\\ 1 & -1\end{pmatrix}\begin{pmatrix}\Sigma_\uparrow & 0\\ 0 & \Sigma_\downarrow\end{pmatrix}\begin{pmatrix}1 & 1\\ 1 & -1\end{pmatrix} \\ &= \frac{1}{2}\begin{pmatrix}\Sigma_\uparrow+\Sigma_\downarrow & \Sigma_\uparrow-\Sigma_\downarrow\\ \Sigma_\uparrow-\Sigma_\downarrow & \Sigma_\uparrow+\Sigma_\downarrow\end{pmatrix}.\end{aligned}$$

By this rotation $\chi^{xx}(\mathbf{q},i\omega_m)$ becomes $\chi^{zz}(\mathbf{q},i\omega_m)$ and vice versa. To avoid confusion we call the susceptibility parallel to the direction of the ordered spins $\chi^{\parallel}(\mathbf{q},i\omega_m)$ and the perpendicular one $\chi^{\perp}(\mathbf{q},i\omega_m)$. In the rotated basis the magnetization is given by the off-diagonal term of the occupation matrix $m = |\langle c_\uparrow^\dagger c_\downarrow\rangle| = |\langle c_\downarrow^\dagger c_\uparrow\rangle|$.
Finally, we use the maximum entropy method to obtain the analytic continuation $\chi(\mathbf{q},\omega)$ of $\chi(\mathbf{q},i\omega_m)$.

6.2 Static and dynamical susceptibility at half-filling

In DMFT the half-filled Hubbard model on a square lattice is a Mott insulator for the here considered $U > 4.5\,\mathrm{eV}$. Above the Néel temperature T_N it is paramagnetic, while below it is antiferromagnetic.

6.2.1 Paramagnetic phase

In the paramagnetic phase, i.e., for temperatures $T > T_N$, the susceptibility is independent of the direction $\chi = \chi^{\alpha\alpha}$ with $\alpha \in \{x,y,z\}$ and the static ($\omega_m = \omega_0 = 0$) susceptibility shows Curie-Weiss behavior $\chi \sim 1/(T - T_{\mathbf{q}})$.
In the limit of large U/t the Hubbard model can be expanded to obtain a Heisenberg model (5.10)

$$H_{\text{Heis}} = \frac{1}{2} \sum_{i \neq i'} \Gamma^{ii'} \mathbf{S}^i \cdot \mathbf{S}^{i'}.$$

This expansion is in the hopping Hamiltonian H_T, which is a perturbation of H_U for large U/t (section 5.2.2). For the Hubbard model at hand, we expand the Hamiltonian up to the second order in H_T to obtain $\Gamma^{ii'}$. Fourier transformation of $\Gamma^{ii'}$ to momentum space results in

$$\Gamma(\mathbf{q}) = 2J\,(\cos q_x + \cos q_y) + 4J' \cos q_x \cos q_y + \cdots \tag{6.4}$$

with the spin coupling constants $J = 4t^2/U$ and $J' = 4t'^2/U$. For $U = 7\,\text{eV}$, deep in the Mott insulating phase, and $U = 4.5\,\text{eV}$, close to the transition to a metal, the coupling constants are:

U (eV)	J (meV)	J' (meV) for	
		$t' = 0.2t$	$t' = 0.4t$
4.5	142	6	23
7	91	5	22

Various experiments like inelastic neutron scattering [29], magnetic susceptibility measurements [75] or Raman scattering [76–79] found similar values for J corresponding to a U between 4.5 eV and 7 eV.
In DMFT the bare susceptibility (4.4) is defined by the product of two full DMFT single-particle Green functions. In contrast to the common definition of the bare susceptibility being the product of two non-interacting Green functions, in DMFT the bare susceptibility is the product of the single-particle Green functions calculated for the full Hubbard model including the Coulomb interaction term H_U. Here, we can write the bare susceptibility in terms of the renormalized $J_{r_0}(\mathbf{q}) = \Gamma(\mathbf{q})/2r_0^2$ as [80]

$$\chi^0(\mathbf{q},0) \approx \frac{1}{4r_0 U} \left[1 - \frac{1}{2U} \left(J_{r_0}(\mathbf{0}) + \frac{1}{2} J_{r_0}(\mathbf{q}) \right) \right], \tag{6.5}$$

which is the half-filling limit of (A.43). The summation over momenta $\mathbf{q}$ leads to the local bare susceptibility

$$\chi^0(0) \approx \frac{1}{4r_0 U} \left[1 - \frac{1}{2U} J_{r_0}(\mathbf{0}) \right]. \tag{6.6}$$

In addition, the local susceptibility $\chi(0)$ from DMFT is well approximated by the atomic susceptibility $\chi_{\text{atom}}(0) \approx \beta/4$. Using the latter two bare susceptibilities $\chi^0(\mathbf{q},0)$ and $\chi^0(0)$

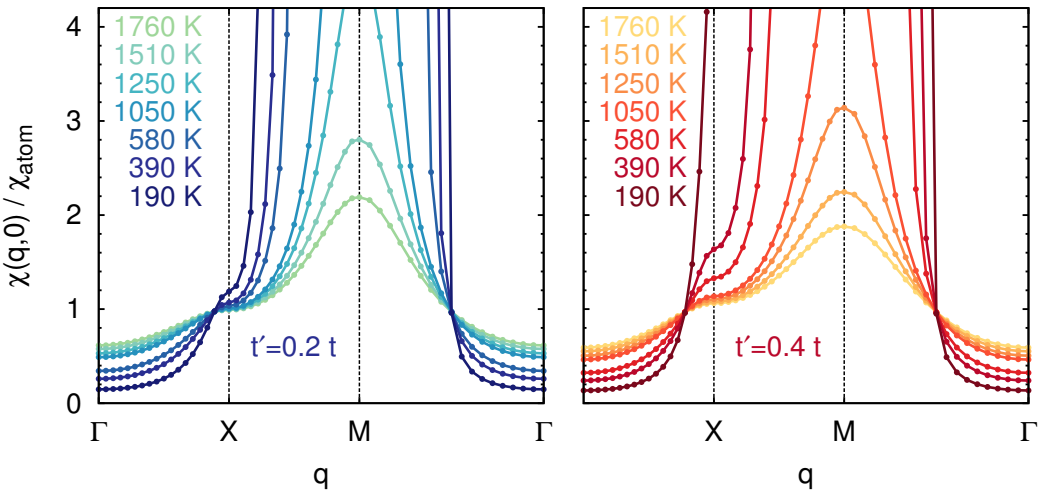

Figure 6.3: Static susceptibility $\chi(\mathbf{q},0)$ for the one-site model normalized to the atomic susceptibility $\chi_{\text{atom}}(0)$ along lines of high-symmetry in the Brillouin zone. In the left panel it is $t' = 0.2t$, in the right one $t' = 0.4t$ and for both $U = 7\,\text{eV}$. Different colors show different temperatures.

and the atomic one in the Bethe-Salpeter equation results in

$$\chi(\mathbf{q},0) \approx \frac{1}{4k_B}\frac{1}{T - T_{\mathbf{q}}}$$

with $k_B T_{\mathbf{q}} = -\frac{\Gamma(\mathbf{q})}{8r}$, where r is the renormalization of the full susceptibility. By fitting $\chi^0(\mathbf{q},0)$ and $\chi(\mathbf{q},0)$ to our DMFT results we find that the renormalization $r \approx 0.5$ is different from $r_0 \approx 1$. Similar values of r and r_0 were also found in Ref. [80].
In figure 6.4 we show that $1/\chi(\mathbf{q},0,T) \sim k_B T$ in paramagnetic DMFT by fitting straight lines to the data and the prefactor is close to the expected $1/4$. The special points of the Brillouin zone considered are $\Gamma = (0,0)$, $X = (\pi,0)$ and $M = (\pi,\pi)$. The critical point $\mathbf{q}_c$ is the M-point. This becomes clear in figure 6.3. That the M-point is $\mathbf{q}_c$ indicates the antiferromagnetic order also found in experiments [81–83].
In figure 6.3 we present the momentum dependence of $\chi(\mathbf{q},0)$ for different temperatures. The results can be understood by $\Gamma(\mathbf{q})$. At the special points $S = (\pi/2,\pi/2)$ and $\mathbf{q}_{\Gamma X}$ it is $\Gamma(\mathbf{q} = S) = 0 = \Gamma(\mathbf{q} = \mathbf{q}_{\Gamma X})$ and the susceptibility is $\chi(\mathbf{q},0) \sim \chi_{\text{atom}}(0)$. The point $\mathbf{q}_{\Gamma X}$ lies between the Γ- and X-point; if $t' = 0$ then $\mathbf{q}_{\Gamma X} = X$ and for $t' > 0$ the distance of the point $\mathbf{q}_{\Gamma X}$ to the X-point increases. The effect of t' becomes most obvious at the X-point, because $\Gamma(\mathbf{q} = X)$, obtained by perturbation theory expansion up to the second order in H_T (6.4), depends not on t but only on t'. At the M-point a larger t' decreases the value of $\chi(\mathbf{q} = M,0)$, which means a decrease of the Néel temperature. The explanation for this is that the frustration of the system increases with t'. A measure of frustration is [37, 80]

$$f = \frac{J'}{J} \approx \frac{1}{2}\frac{\chi^{-1}(\mathbf{q} = Y,0) - \chi^{-1}(\mathbf{q} = S,0)}{\chi^{-1}(\mathbf{q} = S,0) - \chi^{-1}(\mathbf{q} = X/2,0)}$$

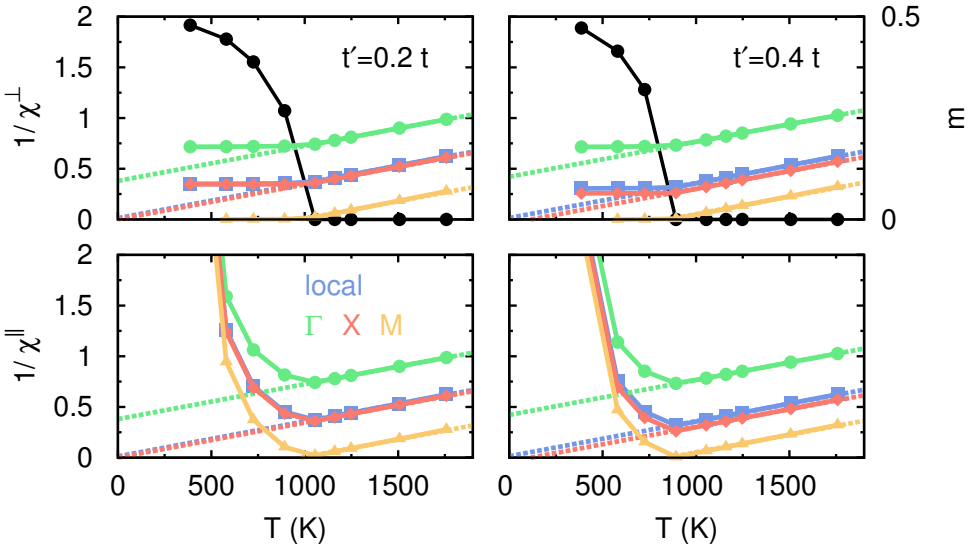

Figure 6.4: Inverse longitudinal and transverse static susceptibility for $U = 7\,\text{eV}$ and different t'. The local susceptibility $\chi^\alpha(0)$ is shown with blue squares, selected momenta $\mathbf{q}$ of the lattice susceptibility $\chi^\alpha(\mathbf{q},0)$ are the Γ- (green dots), X- (red diamonds) and M-point (yellow triangles). The dashed lines show the fit of the Curie-Weiss behavior at high temperatures. The magnetization m is shown in black with scale on the right.

with $Y = (0,\pi)$ and $X/2 = (\pi/2,0)$.[1] We extract the following f from our DMFT results:

U (eV)	f for	
	$t' = 0.2t$	$t' = 0.4t$
4.7	0.036	0.157
7	0.028	0.146

The frustration f decreases with increasing U and with decreasing t'; and it is almost temperature independent. For all considered parameters $f \ll 1$, hence, the system is weakly frustrated [37, 80].

6.2.2 Antiferromagnetic phase

In the antiferromagnetic phase $T < T_N$ the susceptibility depends on the direction. Without loss of generality, we consider a spin alignment parallel to the z-axis. For $T < T_N$ the longitudinal susceptibility $\chi^\parallel = \chi^{zz}$ then goes to zero and the transverse $\chi^\perp = \chi^{xx} = \chi^{yy}$ stays constant. This is shown in figure 6.4.
The transverse real frequency lattice susceptibility $\chi^\perp(\mathbf{q},\omega)$ shows the spin-wave spectrum expected for an antiferromagnet. For $J'/J = f < 0.2$ a good approximation is the spin-

[1] From the Hamiltonian it is clear that the X- and Y-point are equivalent and $\chi(\mathbf{q} = X,0) = \chi(\mathbf{q} = Y,0)$.

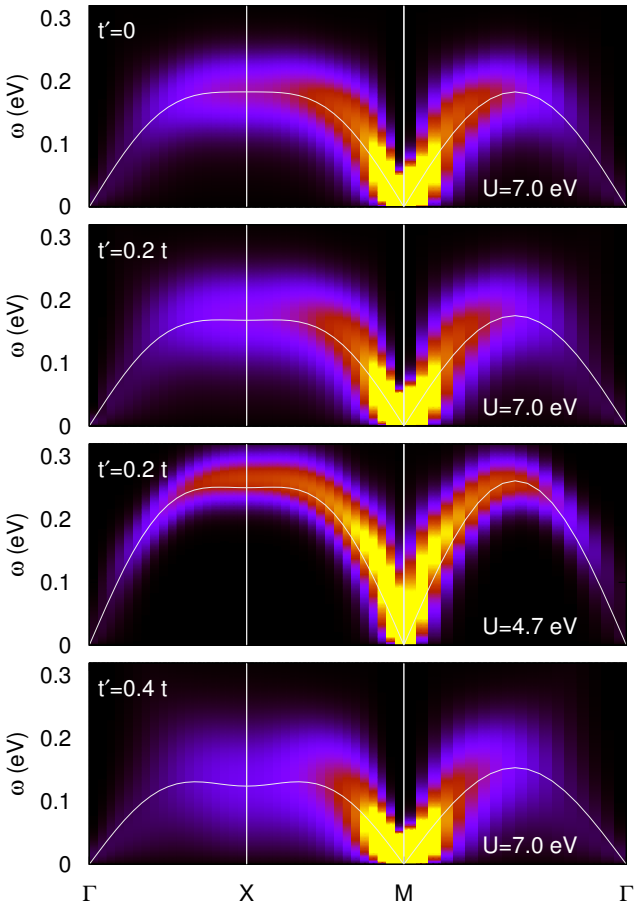

Figure 6.5: Transverse susceptibility $\chi^{\perp}(\mathbf{q},\omega)$ showing the spin-wave dispersion for different values of t' and U. The color map shows the DMFT results and the white lines the linear spin-wave theory.

wave theory for the J_1-J_2 Heisenberg model with the dispersion [84, 85]

$$\begin{aligned} \omega_{\mathbf{q}} &= J\sqrt{a_{\mathbf{q}}^2 - b_{\mathbf{q}}^2} \\ a_{\mathbf{q}} &= 2(1 - f + f\cos q_x \cos q_y) \\ b_{\mathbf{q}} &= \cos q_x + \cos q_y. \end{aligned} \tag{6.7}$$

In figure 6.5 we compare the results of DMFT for $\chi^{\perp}(\mathbf{q},\omega)$ with the spin-wave theory (6.7) and find good agreement. The bandwidth increases when going from 7 eV to 4.7 eV but the qualitative behavior does not change. Increasing t' shifts the position of the maximum of $\chi^{\perp}(\mathbf{q},\omega)$ to lower energies. This trend is strongest at the X-point.

Calculations are performed for $T \ll T_N$, so that $m \approx 1/2$. In this regime, the DMFT result can be understood in the following way. For $m \approx 1/2$ the self-energy is similar to

the Hartree-Fock one (A.36)

$$\Sigma_\sigma(i\nu_n) = \mu - p_s \sigma m U$$

with $\sigma \in \{\uparrow = 1, \downarrow = -1\}$ and $p_s \in \{1, -1\}$ for two sites s. For simplicity, we consider the case $t' = 0$. Starting from the self-energy we can construct the bare lattice (A.38) and bare local susceptibility from the full DMFT single-particle Green function. Inserting this and the approximated local susceptibility

$$\chi_{\tilde{\sigma}-\tilde{\sigma}}(i\omega_m) \approx \frac{1}{\tilde{\sigma} i\omega_m + 2J}$$

into the Bethe-Salpeter equation, we obtain the dynamical susceptibility (A.42)

$$\chi^{\perp}(\mathbf{q}, i\omega_m) \approx \frac{J(1 - \frac{b_\mathbf{q}}{2})}{\omega_m^2 + J^2(4 - b_\mathbf{q}^2)},$$

which contains approximately the spin-wave dispersion. For $t' = 0.2t$ and $U = 4.7\,\mathrm{eV}$ the spin-wave spectrum is very close to the experimentally determined spectrum of La_2CuO_4 [29]. The qualitative behavior of the spin-wave spectrum is also found for $YBa_2Cu_3O_{6.15}$ [86].

For the here considered parameters $t' = 0.2t$ and $0.4t$, and $U = 4.7\,\mathrm{eV}$ and $7\,\mathrm{eV}$ the DMFT result of the Hubbard model is close to the one of a Heisenberg model with parameters J and J' from perturbation theory. This is true both for the static susceptibility, for which we find Curie-Weiss behavior in the paramagnetic phase, and the dynamical susceptibility in the ordered phase, which yields the spin-wave spectrum of spin-wave theory. For $U = 4.7\,\mathrm{eV}$ this spectrum is in quantitative agreement with neutron scattering experiments and remains qualitative correct even for larger U.

6.3 Static and dynamical susceptibility in the hole doped regime

For finite doping x, away from half-filling $n_i = 1 - x < 1$, we distinguish the underdoped $x < 0.16$ and the overdoped $x > 0.16$ regime. Here, $x \approx 0.16$ is optimal doping, where the system has the highest critical temperature T_c. Close to half-filling the susceptibility retains features of that phase like the antiferromagnetic order. Further away, the susceptibility changes drastically showing even ferromagnetic order in the highly overdoped regime.

6.3.1 Static susceptibility

The local static susceptibility $\chi(0)$, shown on top of figure 6.6, decreases monotonically with increasing x for a fixed t' and T. For fixed x and t' it decreases with temperature. The t' dependence, however, is weak.
The behavior of the static lattice susceptibility is more complex. As shown above, the susceptibility at half-filling is well described by the one of a Heisenberg model, which is a model of localized spins. For small $x \leq 0.10$ localized spins are still important and

the susceptibility resembles the one for $x = 0$. An approximate form of the static lattice susceptibility is

$$\chi(\mathbf{q},0) \approx \frac{1}{4}\frac{1-x}{k_B T + \frac{1}{4}(1+x)\Gamma(\mathbf{q})}. \tag{6.8}$$

It shows Curie-Weiss like behavior and has an instability at the critical vector $\mathbf{q}_c = M$, indicating antiferromagnetism. The weight $(1-x)/4$, which is the local magnetic moment, decreases with x. This expression $(1-x)/4$ for the local moments is valid even for large x, in fact, for all x considered here up to $x = 0.4$, although (6.8) is not.
For larger x the system becomes more metallic and the bare uniform susceptibility $\chi^0(\mathbf{0},0)$ increases as well. The combination of the almost linear decrease of the local moment and increase of $\chi^0(\mathbf{0},0)$ results in a non-monotonic behavior of the uniform static susceptibility $\chi(\mathbf{0},0)$, in contrast to the monotonic local susceptibility.
In the bottom left panel of figure 6.6 it is shown that $\chi(\mathbf{0},0)$ for $t' = 0.2t$ increases for $x < x_c \approx 0.25$ and decreases for $x > x_c$. The bottom right panel shows that x_c, at which $\chi(\mathbf{0},0)$ reaches its maximum, is larger for $t' = 0.4t$. In fact, $\chi(\mathbf{0},0)$ diverges for small temperatures for $t' = 0.4$. The increase of x_c for increasing t' is found for all here considered $t' \leq 0.4$.
The qualitative behavior of $\chi(\mathbf{0},0)$ can be understood within the Stoner mechanism [55,84]. For small U the uniform susceptibility is approximately given by

$$\chi^{\text{Stoner}}(\mathbf{0},0) = \frac{1}{4}\frac{\rho(\epsilon_F)}{1 - \frac{1}{2}U\rho(\epsilon_F)},$$

where $\rho(\epsilon_F)$ is the density of states (DOS) at the Fermi energy. The uniform susceptibility diverges under the Stoner criterion $U_c = 2/\rho(\epsilon_F)$, which indicates ferromagnetic order.
The trend of doping and t' becomes clear from the DOS of the two-dimensional model. For $t' = 0$ and half-filling the DOS has a van-Hove singularity at the Fermi energy ϵ_F. Increasing x lowers the Fermi energy, which moves $\rho(\epsilon_F)$ away from the singularity. Thus, $\chi^{\text{Stoner}}(\mathbf{0},0)$ decreases for increasing x and $x_c = 0$. For $t' > 0$, the van-Hove singularity is below the Fermi energy at $x = 0$. The increase of x leads to an increase of $\chi^{\text{Stoner}}(\mathbf{0},0)$ up to x_c, where ϵ_F is at the singularity and $\chi^{\text{Stoner}}(\mathbf{0},0)$ is maximal. Further increasing x results in a smaller $\chi^{\text{Stoner}}(\mathbf{0},0)$. For a larger t' the value x_c becomes larger as well. The same behavior is observed here for $\mathbf{q} = \mathbf{0}$ (figure 6.6).
For $La_{2-x}Sr_xCuO_4$, the cuprate with $t' = 0.2t$, measurements of the magnetic susceptibility [87, 88] show a similar non-monotonic behavior and $x_c \approx 0.25$. The increase in the region of smaller doping $x < 0.25$ were also confirmed in NMR and nuclear quadrupole resonance (NQR) experiments [89–92]. Measurements of the Knight shift for ^{63}Cu found a similar increase also in $YBa_2Cu_3O_{6+y}$ [93] and $Tl_2Ba_2CuO_{6+y}$ [92,94,95].

The detailed momentum dependence of the static susceptibility $\chi(\mathbf{q},0)$ is shown for $U = 4.7\,\text{eV}$ in figure 6.8 and for $U = 7\,\text{eV}$ in figure 6.9. In both figures the three rows of panels at the top show results for $t' = 0.2t$ and the three rows below for $t' = 0.4t$. For the five panels in one row, the doping x increases from the left ($x = 0.1$) to the right ($x = 0.4$).
We discussed the Γ-point, where, for $t' = 0.2t$, the susceptibility first increases and then decreases with x. For $t' = 0.4t$, it only increases and even diverges at low temperatures for $x = 0.4$.

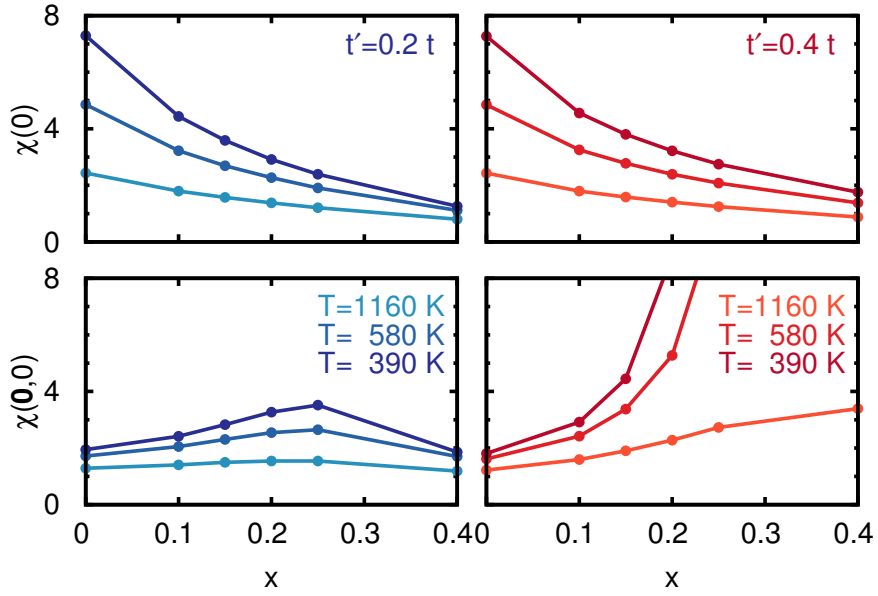

Figure 6.6: Local static susceptibility $\chi(0)$ and uniform one $\chi(\mathbf{0},0)$ for $U = 7\,\mathrm{eV}$, $t' = 0.2t$ (left) and $t' = 0.4t$ (right) in dependence of doping x for different temperatures T.

In the left column of panels, for $x = 0.1$, the susceptibilities resemble the half-filling ones shown in figure 6.3. Also for $x = 0.1$ we find Curie-Weiss behavior with a divergence at the M-point. For a larger t' we obtain a smaller $\chi(\mathbf{q} = M,0)$, and a larger U leads to a smaller $\chi(\mathbf{q} = M,0)$, as well.

For $x \geq 0.15$ the behavior of $\chi(\mathbf{q},0)$ changes significantly. Instead of one peak at the M-point, $\chi(\mathbf{q},0)$ shows two incommensurate peaks below $T \approx 500\,\mathrm{K}$: The $\mathbf{q}_{\Gamma M}$ and $\mathbf{q}_{XM}$ peak. Due to the symmetry of the Hamiltonian, each peak appears four times in the Brillouin zone by a rotation of $\pi/2$, π and $3\pi/2$.

We first consider $t' = 0.2t$. For $x = 0.15$ the two peaks have similar size and distance to the M-point. For larger x the $\mathbf{q}_{XM}$ stays almost the same but $\chi(\mathbf{q} = \mathbf{q}_{XM},0)$ decreases; on the other hand, $\mathbf{q}_{\Gamma M}$ moves closer to the Γ-point, and becomes the Γ-point for $x \geq 0.25$. $\chi(\mathbf{q} = \mathbf{q}_{\Gamma M},0)$ decreases faster than $\chi(\mathbf{q} = \mathbf{q}_{XM},0)$ for $U = 4.7\,\mathrm{eV}$ and slower for $U = 7\,\mathrm{eV}$. For this larger U and $x \geq 0.25$ the global maximum of $\chi(\mathbf{q},0)$ is at the Γ-point.

Also for $t' = 0.4t$, the $\mathbf{q}_{XM}$ is almost fixed and $\mathbf{q}_{\Gamma M}$ moves to the Γ-point. However, for all U and x $\mathbf{q}_{\Gamma M}$ is the dominant peak, and leads to a diverging $\chi(\mathbf{0},0)$ at the Γ-point for low T. At $T = 390\,\mathrm{K}$ the susceptibility $\chi(\mathbf{q},0)$ diverges for $U = 4.7\,\mathrm{eV}$ and $x = 0.4$; and for $U = 7\,\mathrm{eV}$ it diverges already for $x = 0.25$.

The effect of t' for small doping $x = 0.10$ is similar to its effect for $x = 0$. For increasing t' the peak at the M-point decreases and close to the Γ-point $\chi(\mathbf{q},0)$ increases. For larger doping the two incommensurate peaks close to the M-point change in the following way: The peak at $\mathbf{q}_{XM}$ decreases in size, for increasing t', but the position $\mathbf{q}_{XM}$ does not change significantly. The peak at $\mathbf{q}_{\Gamma M}$ moves closer to the Γ-point and increases close to it. $\chi(\mathbf{q},0)$ does not change for $\mathbf{q} = X$ and $\mathbf{q} = \mathbf{q}_i$, where $\mathbf{q}_i$ is an isobestic point between the Γ- and M-point.

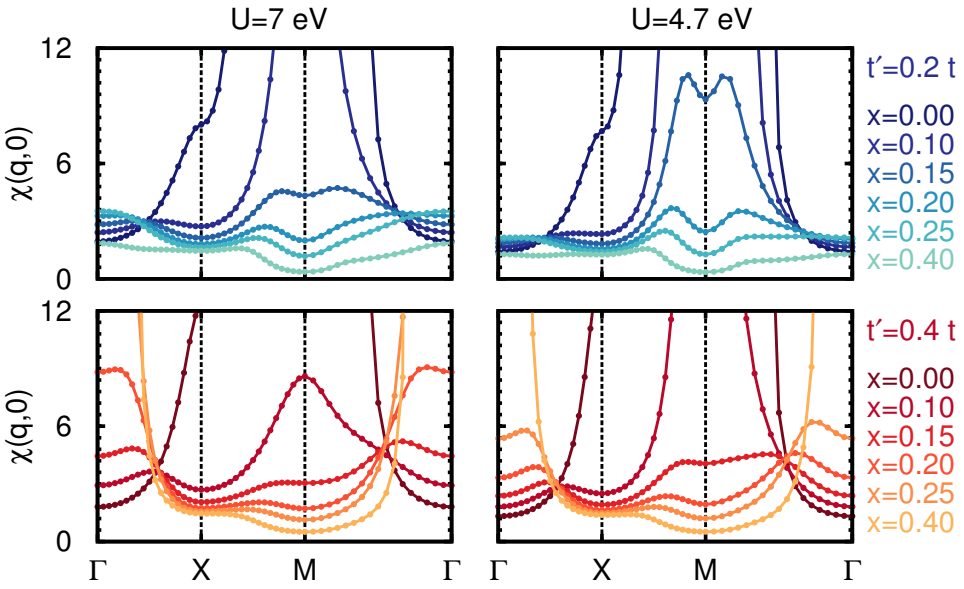

Figure 6.7: Comparison of static susceptibilities for $T = 390\,\mathrm{K}$, different x, U and t'.

For the here considered U range the static susceptibility does not change qualitatively. $\chi(\mathbf{q},0)$ decreases around the M-point for larger U and increases around the Γ-point, similar to the half-filled case. We described the change for increasing x from a $\chi(\mathbf{q},0)$ with a dominant peak at the M-point to a $\chi(\mathbf{q},0)$ with a dominant peak at the Γ-point. The x value, at which $\chi(\mathbf{q} = \Gamma,0)$ is larger than $\chi(\mathbf{q},0)$ in vicinity of the M-point, decreases with increasing U.
In summary, a larger t', x or U has similar effects. A larger value increases $\chi(\mathbf{q},0)$ close to the Γ-point and decreases $\chi(\mathbf{q},0)$ around the M-point. For $x = 0.1$ we find a peak at the M-point, which develops into to incommensurate peaks for $x \sim 0.15$. For $U = 4.7\,\mathrm{eV}$ and $t' = 0.2t$ the major peaks occur at $\mathbf{q}_{XM}$. Increasing U, t' or x makes the peak at $\mathbf{q}_{\Gamma M}$ the dominant one, and finally leading to a divergent $\chi(\mathbf{0},0)$.
The incommensurate peaks in momentum space lead to magnetic stripe formation seen in experiments. Diagonal stripes associated with $\mathbf{q}_{\Gamma M}$ were found in $La_{1.98}Sr_{0.02}CuO_4$ [96]; stripes related to $\mathbf{q}_{XM}$ in $La_{1.88}Sr_{0.12}CuO_4$ [97, 98] and La_2CuO_{4+y} [99, 100]. Spin order and stripes were also reported in $La_{2-x}Ba_xCuO_4$ [101, 102] and in $La_{1.6-x}Nd_{0.4}Sr_xCuO_4$ [103].

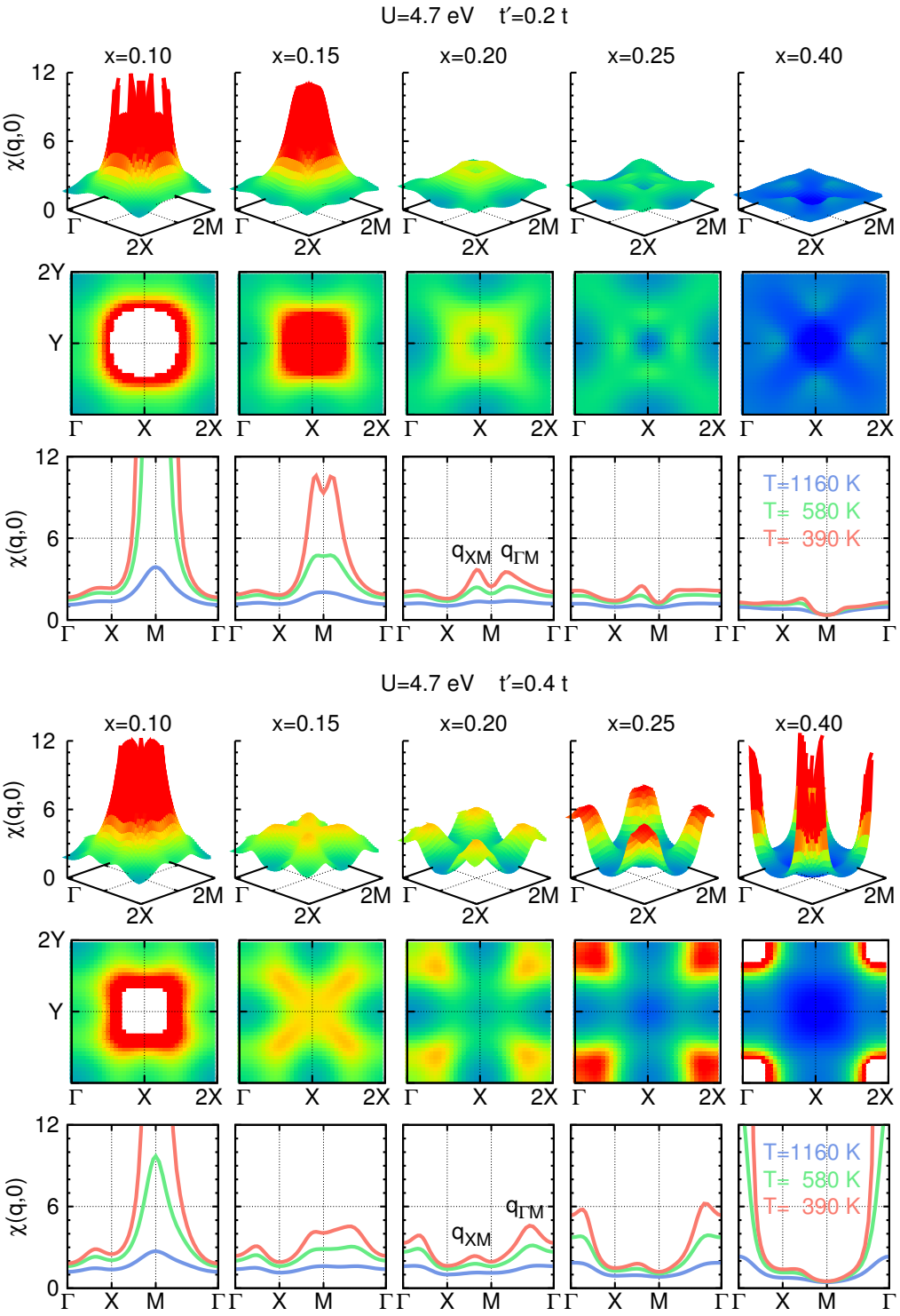

Figure 6.8: Static susceptibility $\chi(\mathbf{q},0)$ for $U = 4.7\,\mathrm{eV}$, $t' = 0.2t$ (top) and $t' = 0.4t$ (bottom). For the three dimensional and contour plots $T = 390\,\mathrm{K}$. The special points are $\Gamma = (0,0)$, $X = (\pi,0)$, $2X = (2\pi,0)$, $Y = (0,\pi)$, $2Y = (0,2\pi)$, $M = (\pi,\pi)$ and $2M = (2\pi,2\pi)$.

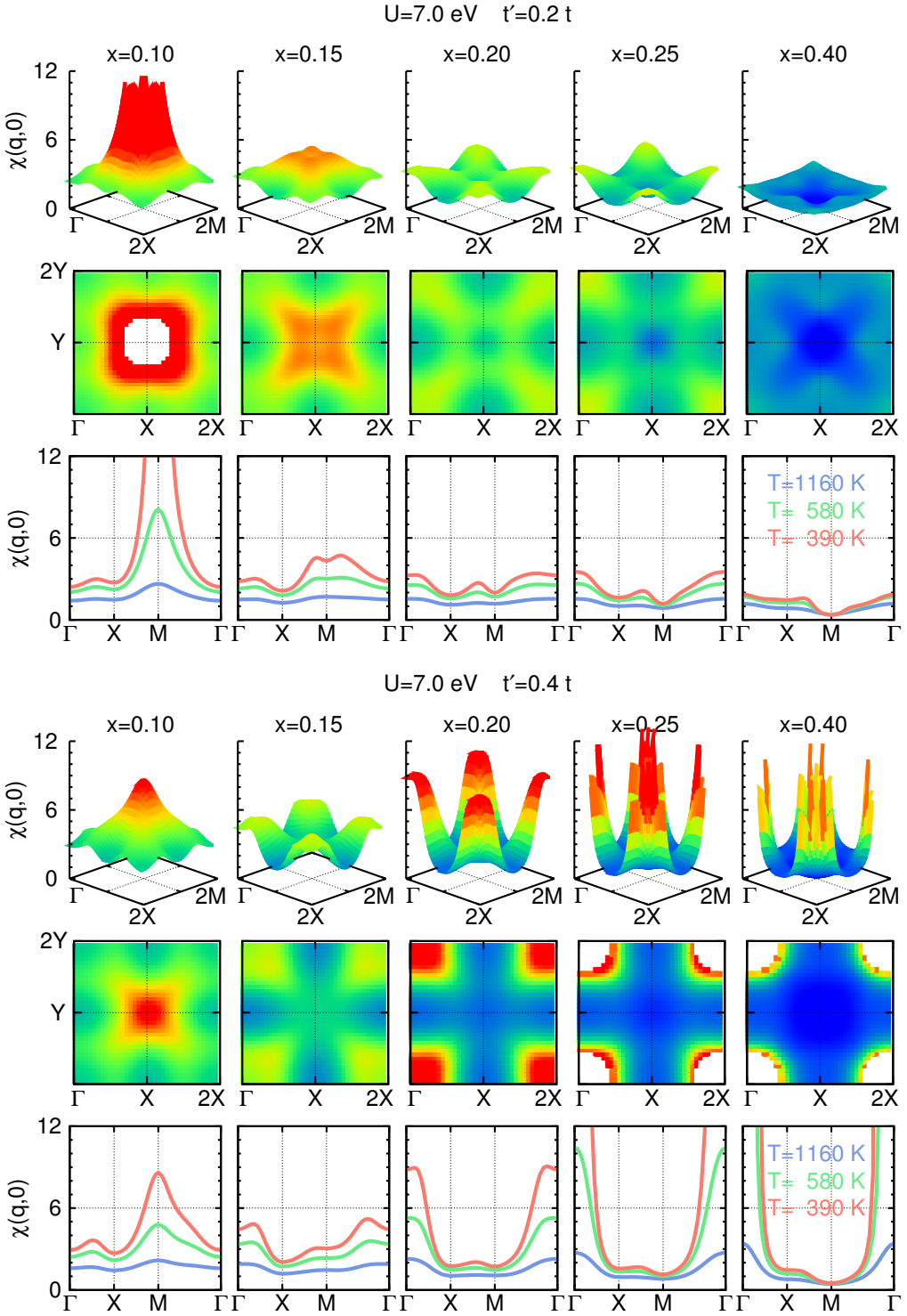

Figure 6.9: Static susceptibility $\chi(\mathbf{q},0)$ for $U = 7\,\mathrm{eV}$, $t' = 0.2t$ (top) and $t' = 0.4t$ (bottom). For the three dimensional and contour plots $T = 390\,\mathrm{K}$. The special points are $\Gamma = (0,0)$, $X = (\pi,0)$, $2X = (2\pi,0)$, $Y = (0,\pi)$, $2Y = (0,2\pi)$, $M = (\pi,\pi)$ and $2M = (2\pi,2\pi)$.

6.3.2 Dynamical susceptibility

To study bosonic excitations for hole doped cuprates we calculate the dynamical lattice susceptibility $\chi(\mathbf{q},\omega)$. The imaginary part $\mathrm{Im}\,\chi(\mathbf{q},\omega)$ is shown in figure 6.10 as a color map for $t' = 0.2t$ in the top row and $t' = 0.4t$ in the bottom panels for finite doping. This gives the dispersion of bosonic excitations. The horizontal axis shows momenta along a path through high-symmetry points of the Brillouin zone, while the vertical axis shows different frequencies. The doping x is increasing from the left to the right. The results for $U = 4.7\,\mathrm{eV}$ are similar to the ones for $U = 7\,\mathrm{eV}$ shown in figure 6.10.
First of all, for $\omega \sim 0$ the $\mathrm{Im}\,\chi(\mathbf{q},\omega)$ results resemble the static susceptibility $\chi(\mathbf{q},0)$ results. For small doping $x = 0.10$ the spectrum is very similar to the spin-wave spectrum at half-filling ($x = 0$) shown in figure 6.5. The intensity maximum is at the M-point and the intensity decreases to a minimum at the Γ-point. Furthermore, it decreases slightly with t'. Apart from this, the $t' = 0.2t$ and $t' = 0.4t$ results are very similar.
Increasing the doping to optimal ($x = 0.15$) and beyond shifts the weight away from the M- in direction of the Γ-point. Incommensurate features appear. For $t' = 0.2t$ the maximum intensity is at the Γ-point in the overdoped $x = 0.25$ case; for $t' = 0.4t$ already at $x = 0.20$ the Γ-point is the intensity maximum. Apart from this enhancement of the doping by t', the trends are the same for both t'.
For small x and t' similar theoretical results were obtained in Ref. [104] with the dual boson method. Ref. [105] finds a shift of the intensity maximum at low energies from the M- to the Γ-point for increasing doping, similar to our result, using determinant quantum Monte Carlo (DQMC). However, Ref. [105] also does not discuss the t' dependency.
Experiments studied the spin excitations, e.g., with inelastic neutron scattering (INS) and resonant inelastic x-ray scattering (RIXS). Early INS experiments [100, 106] on $La_{2-x}Sr_xCuO_4$ found dynamical incommensurate peaks close to the M-point in the underdoped regime. For increasing doping the peaks move away from the M-point and are present up to the overdoped regime $x = 0.25$. Ref. [107] found similar peaks in $YBa_2Cu_3O_{6.6}$. Later, Refs. [108, 109] reported the disappearance of the peaks for doping increased up to $x = 0.30$ in $La_{2-x}Sr_xCuO_4$.
On the other hand RIXS measurements found magnetic high energy excitations also in the overdoped regime up to $x = 0.4$ in $La_{2-x}Sr_xCuO_4$ [110]. The observed peaks broaden with doping, but do not disappear. The persistence of magnetic excitations in the overdoped regime was also reported for a variety of different cuprates [111–113].

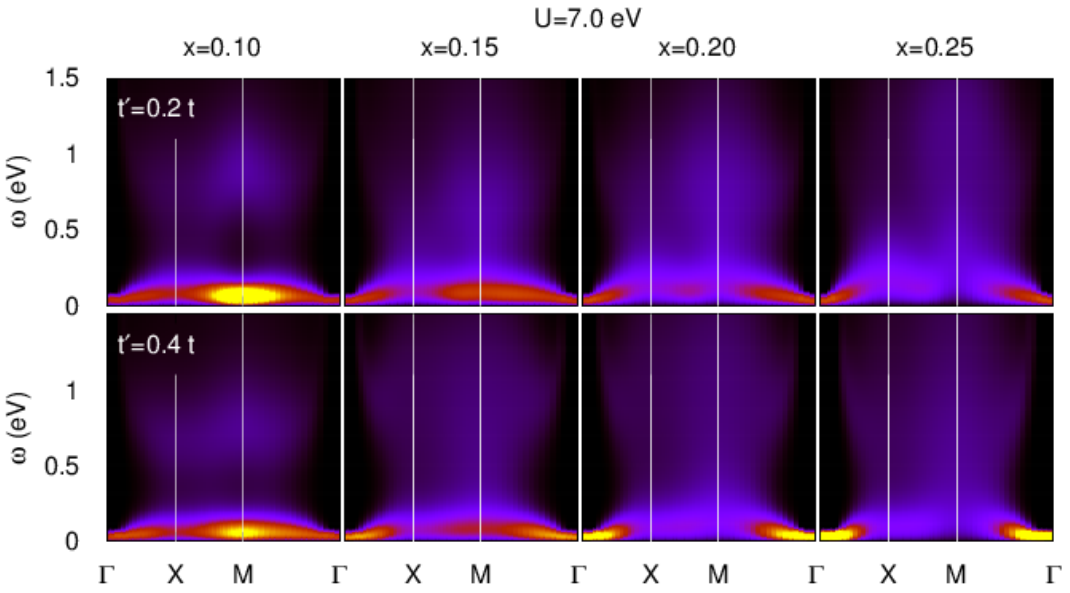

Figure 6.10: Dynamical susceptibility Im $\chi(\mathbf{q},\omega)$ for $U = 7\,\mathrm{eV}$, $t' = 0.2t$ (top) and $t' = 0.4t$ (bottom) at $T = 580\,\mathrm{K}$. The doping increases going from left to right.

6.4 Conclusions

We investigated magnetic properties of high temperature superconducting cuprates by studying the appropriate Hubbard model, and found good agreement with experiments in many parameter regimes. For half-filling, DMFT reproduces the Curie-Weiss behavior in the paramagnetic phase and shows the spin-wave dispersion in the antiferromagnetic phase. Both findings are explained with analytic expressions.
For the finite doped case we presented a systematic analysis of the dependence of the magnetic susceptibility on doping x, next-nearest neighbor hopping t' and Coulomb interaction U. We found a general trend from antiferromagnetism to ferromagnetism for increasing x, t' and U. In addition to excitations at the Γ- and M-point, we found incommensurate peaks, which indicate stripe order.

7 Summary

In this thesis we studied susceptibilities in strongly correlated systems. To this end, we extended our implementation of LDA+DMFT to calculate dynamical local susceptibilities and implemented the Bethe-Salpeter equation to obtain dynamical lattice susceptibilities. Using this implementation we studied orbital and magnetic phenomena in the layered perovskite K_2CuF_4 and magnetism in the Hubbard model, a model describing high-temperature superconducting cuprates.

For the investigation of strongly correlated materials the DFT in combination with DMFT has become the established method. In this work we started with a short overview of the DFT in the LDA, as well as DMFT for strongly correlated materials and its extension to calculate susceptibilities. This short overview was followed by a more detailed description of the central part of our implementation, the CT-QMC impurity solver and its way of calculating susceptibilities.

It is the possibility to compare susceptibilities to experiments and their ability to give new insights into materials, which made them our central topic. In chapter 4 we introduced the generalized susceptibilities, which we calculated using LDA+DMFT and the Bethe-Salpeter equation. LDA+DMFT can be computational demanding by itself, and calculations of susceptibilities are significantly more demanding, even for supercomputers. Hence, there is a need for efficient algorithms and implementations. The essential part of our implementation is the choice of an efficient basis for the susceptibilities. We compared different basis functions to represent susceptibilities and presented their symmetries. Legendre polynomials are analytic functions, which lead to a compact form of the susceptibility. The use of this form reduces the demand in memory and computational time. We showed that an even more compact basis is the intermediate representation. During the course of this work we implemented a highly parallelized and efficient implementation of susceptibility calculations in either of the two basis. Our calculations were performed successfully on multiple supercomputers at the Forschungszentrum Jülich. We showed that the scaling with the number of processors is almost ideal. The implementation was further improved by use of the presented symmetries of the susceptibilities.

In chapter 5 we investigated the role of superexchange and Jahn-Teller distortions for orbital ordering in the layered perovskite K_2CuF_4 at ambient and high pressure using susceptibility calculations. Previous studies explained the orbital ordering in infinite layered perovskites like $KCuF_3$. To explain the role of the superexchange mechanism we calculated orbital susceptibilities for structures without crystal-field and reduced distortions. From these we extracted the type of order and the superexchange orbital ordering transition temperature. Among the two ordering mechanisms, the superexchange mechanism and ordering because of a crystal-field due to Jahn-Teller distortions, superexchange alone

cannot explain orbital ordering. The determined transition temperature is too small to explain experiments, where orbital order is found at very high temperatures, and in the high pressure case the type of order is wrong. These conclusions are similar to the ones for infinite layered systems. This is remarkable, because in K_2CuF_4 the layered structure leads to an orbital Zeeman term, which is absent in cubic structures. We found that the effect of the term is small compared to the crystal-field effects. In more covalent layered materials it could be important.
In the last chapter we investigated the Hubbard model on a square lattice, a model for high temperature superconducting cuprates. We calculated magnetic susceptibilities for a large range of model parameters. Specifically, we varied the Coulomb interaction U, the doping x and the next-nearest neighbor hopping t', representing different cuprates. At half-filling we found that for $t/U \ll 1$ the Hubbard model can be described by the equivalent Heisenberg model, as expected. In the paramagnetic phase the inverse susceptibility decreases almost linearly with temperature. Below the Néel temperature the model is antiferromagnetically (AFM) ordered. The transverse susceptibility stays constant with decreasing temperature while the longitudinal one decreases. The bosonic excitation spectrum, which we obtained from dynamical lattice susceptibilities, yields the spin-wave dispersion. All of this is qualitatively in agreement with experiments. For small hole doping $x < 0.1$ we obtained results of the static and dynamical lattice susceptibility similar to the ones at half-filling with a dominant peak at the AFM ordering vector. For larger dopings incommensurate peaks, which suggest the possibility of magnetic stripe order, evolve in the susceptibilities. Stripe order is well known from experiments on the doped cuprates. With increasing doping the susceptibilities change significantly. More specifically, the peaks close to the AFM ordering vector become less pronounced or move away to the ferromagnetic (FM) ordering vector. For large dopings the susceptibility shows a maximum at the FM ordering vector. This trend from AFM to FM is further enhanced by increasing t' or U.
The applications showed that our implementation to calculate susceptibilities in LDA+DMFT allows us to study different physical phenomena of complex strongly correlated materials and draw conclusions by comparison to experiments.

A Appendix

A.1 Determinant ratios and matrix updates for hybridization function

During the Monte Carlo (MC) sampling in the CT-QMC we need to calculate the acceptance probability (3.9), which depends on the quotient of determinants of the matrices M_b^{-1}. Furthermore, we need to update the matrices M_b^{-1}. In this section we give efficient formulas to perform the calculations of the quotients and the updates of M_b^{-1} for specific changes like insertion, removal, or change of rows and columns. For this we use and store the inverse matrices M_b instead of M_b^{-1}. We follow the derivations of Ref. [1].

A.1.1 Insertion and removal of a single row and column

We first describe the insertion of a row and a column at the end of the matrix M_b^{-1}. The insertion into a matrix M_b^{-1}, which has $n_b \times n_b$ entries, leads to the matrix $\tilde{M}_b^{-1}$, which has $(n_b+1)\times(n_b+1)$ entries. With a row vector R, a column vector Q and a scalar S the new matrix follows from the old one by

$$\tilde{M}_b^{-1} = \begin{pmatrix} M_b^{-1} & Q \\ R & S \end{pmatrix}.$$

The matrix $\tilde{M}_b^{-1}$ can be decomposed to

$$\tilde{M}_b^{-1} = \begin{pmatrix} M_b^{-1} & 0 \\ R & 1 \end{pmatrix} \begin{pmatrix} 1 & M_b Q \\ 0 & S - R M_b Q \end{pmatrix},$$

which can be checked simply by performing the multiplication on the right hand side. With the help of the latter we calculate the determinant ratio

$$\frac{\det \tilde{M}_b^{-1}}{\det M_b^{-1}} = \det(S - R M_b Q), \tag{A.1}$$

which occurs during the proposal of a MC step. Since S as well as the product RM_bQ are scalars, it is not necessary to write the determinant explicitly on the right hand side. However, (A.1) applies also in more general cases where S is a matrix. If the MC move is accepted, we calculate and store $\tilde{M}_b$. The entries $\tilde{P}$, $\tilde{Q}$, $\tilde{R}$ and $\tilde{S}$ in

$$\tilde{M}_b = \begin{pmatrix} \tilde{P} & \tilde{Q} \\ \tilde{R} & \tilde{S} \end{pmatrix}$$

are calculated by inversion by partitioning [114]

$$\begin{aligned}\tilde{S} &= (S - RM_bQ)^{-1}\\ \tilde{P} &= M_b + (M_bQ)\tilde{S}(RM_b)\\ \tilde{Q} &= -(M_bQ)\tilde{S}\\ \tilde{R} &= -\tilde{S}(RM_b).\end{aligned}$$

One can show that this is correct by calculating the product $\tilde{M}_b^{-1}\tilde{M}_b = \mathbb{1}$. As mentioned before, we store M_b instead of M_b^{-1}. Therefore, the calculation of (A.1) and $\tilde{M}_b$ is of order $\mathcal{O}(n_b^2)$.
So far, we considered the insertion of a row and column at the end of M_b^{-1}. To insert the row at a position i_0 and the column at a position j_0, we perform the actions described above and permute the rows and columns. Then, the determinant might get a minus sign, which results in a determinant ratio

$$\frac{\det\tilde{M}_b^{-1}}{\det M_b^{-1}} = (-1)^{i_0+j_0}\det(S - RM_bQ) = (-1)^{i_0+j_0}\det\tilde{S}^{-1}. \tag{A.2}$$

The matrix $\tilde{M}_b^{i_0,j_0}$, which is stored, is the inverse of M_b^{-1} with the permuted rows and columns. To get the matrix $\tilde{M}_b^{i_0,j_0}$, we first calculate $\tilde{M}_b$. The entries of the needed matrix $\tilde{M}_b^{i_0,j_0}$ are then given by

$$(\tilde{M}_b^{i_0,j_0})_{ij} = (\tilde{M}_b)_{\pi(i)\pi'(j)}.$$

The sequences $\pi(i)$ and $\pi'(i)$ describe the permutations of the rows and columns and consist of the following elements

$$\begin{aligned}\pi &= 1,\cdots,j_0-1,n_b+1,j_0,\cdots,n_b\\ \pi' &= 1,\cdots,i_0-1,n_b+1,i_0,\cdots,n_b \quad .\end{aligned}$$

Note that the column and row index is interchanged with respect to $\tilde{M}_b^{-1}$. That means $\pi(i)$, where i is the index of the rows of $\tilde{M}_b^{i_0,j_0}$, is determined by the column index j_0 of M_b^{-1}.

Let us describe the removal of a row and a column at the end of a matrix $\tilde{M}_b^{-1}$ and afterwards the removal at an arbitrary position. By removing a row and a column of $\tilde{M}_b^{-1}$, which has $(n_b+1)\times(n_b+1)$ entries, we get a matrix M_b^{-1}, which has $n_b \times n_b$ entries. Then, the determinant ratio is obtained from the last element of $\tilde{M}_b$, which we named $\tilde{S}$ above

$$\frac{\det M_b^{-1}}{\det\tilde{M}_b^{-1}} = \det\tilde{S}. \tag{A.3}$$

Here $\tilde{S} = (\tilde{M}_b)_{n_b+1,n_b+1}$ is a known scalar. After the MC step is accepted, the new matrix M_b is obtained as

$$M_b = \tilde{P} - \tilde{Q}\tilde{S}^{-1}\tilde{R}, \tag{A.4}$$

which is an operation of order $\mathcal{O}(n_b^2)$. If we remove a row at position i_0 and a column at position j_0, the determinant ratio is multiplied by $(-1)^{i_0+j_0}$ and $\tilde{S} = (\tilde{M}_b)_{j_0 i_0}$. To calculate the new matrix M_b, we first permute the rows and columns to the end, without changing the order of the other rows and columns, and afterwards apply equation (A.4).

A.1.2 Insertion and removal of two rows and columns

The procedure for insertion and removal of two rows and columns relies on the equations given in the previous section. If we insert two rows and two columns, the new matrix

$$\tilde{M}_b^{-1} = \begin{pmatrix} M_b^{-1} & Q \\ R & S \end{pmatrix}$$

consists of a 2×2 matrix S a $2 \times n_b$ matrix R and a $n_b \times 2$ matrix Q. The determinant ratio is given by

$$\frac{\det \tilde{M}_b^{-1}}{\det M_b^{-1}} = (-1)^{i_0+j_0+k_0+l_0} \det(S - R M_b Q). \tag{A.5}$$

The new matrix $\tilde{M}_b^{i_0,j_0,k_0,l_0}$ is constructed by first calculating $\tilde{M}_b$ using inversion by partitioning, with the two new rows and columns at the end, and permutation of them to the correct position afterwards.

If we remove two columns and two rows from the matrix $\tilde{M}_b^{-1}$, we get the determinant ratio

$$\frac{\det M_b^{-1}}{\det \tilde{M}_b^{-1}} = (-1)^{i_0+j_0+k_0+l_0} \det \tilde{S} = (-1)^{i_0+j_0+k_0+l_0} (\tilde{M}_{j_0 i_0} \tilde{M}_{l_0 k_0} - \tilde{M}_{l_0 i_0} \tilde{M}_{j_0 k_0}). \tag{A.6}$$

The new matrix is calculated by permuting both rows and columns to the end and removing them.
To calculate the new matrix after insertion or removal of two rows and columns, it is of course also possible to apply the insertion or removal of one row and one column two times.

A.1.3 Change of a single row or column

Changing one row or column of a matrix A to get a new A' can be expressed by the rank-1 update $A' = A + \mathbf{u}\mathbf{v}^T$ with column vector $\mathbf{u}$ and row vector $\mathbf{v}^T$. For example, changing a row at the position i_0 means setting $u_i = \delta_{i,i_0}$ and $v_j^T = A'_{i_0 j} - A_{i_0 j}$. It can be shown [1] that

$$\det\left(\mathbb{1} + \mathbf{u}\mathbf{v}^T\right) = 1 + \mathbf{v}^T\mathbf{u}$$

and thus

$$\begin{aligned} \det\left(A + \mathbf{u}\mathbf{v}^T\right) &= \det\left(A(\mathbb{1} + (A^{-1}\mathbf{u})\mathbf{v}^T)\right) \\ &= \det(A)(1 + \mathbf{v}^T A^{-1}\mathbf{u}). \end{aligned}$$

Exchanging one row of the matrix M_b^{-1} at the position i_0 with a new row $(\tilde{M}_b^{-1})_{i_0 j}$ leads to a determinant ratio of

$$\frac{\det \tilde{M}_b^{-1}}{\det M_b^{-1}} = \sum_{j=1}^{n_b} (\tilde{M}_b^{-1})_{i_0 j} (M_b)_{j i_0}. \tag{A.7}$$

This calculation is of order $\mathcal{O}(n_b)$. We need to calculate the new matrix elements $(\tilde{M}_b^{-1})_{i_0 j}$ directly with the hybridization function by

$$(\tilde{M}_b^{-1})_{i_0 j} = F_{\tilde{\alpha}^b_{i_0} \alpha^b_j}(\tilde{\tau}^b_{i_0} - \tau^b_j).$$

If the exchanged row i_0 in M_b^{-1} also needs to be permuted to a different position i_0' the determinant ratio is multiplied by $(-1)^{i_0 - i_0'}$.
Similarly, exchanging one column of the matrix M_b^{-1} at the position j_0 with a new column leads to a determinant ratio of

$$\frac{\det \tilde{M}_b^{-1}}{\det M_b^{-1}} = \sum_{i=1}^{n_b} (M_b)_{j_0 i} (\tilde{M}_b^{-1})_{i j_0}. \tag{A.8}$$

Here the matrix elements $(\tilde{M}_b^{-1})_{i j_0} = F_{\tilde{\alpha}^b_i \alpha^b_{j_0}}(\tilde{\tau}^b_i - \tau^b_{j_0})$. If the exchanged column j_0 in M_b^{-1} also needs to be permuted to a different position j_0', the determinant ratio is multiplied by $(-1)^{j_0 - j_0'}$.
To calculate the new matrices, we use the Sherman-Morrison formula[1]

$$(A + \mathbf{u}\mathbf{v}^T)^{-1} = A^{-1} - \frac{A^{-1}\mathbf{u}\mathbf{v}^T A^{-1}}{1 + \mathbf{v}^T A^{-1}\mathbf{u}}, \tag{A.9}$$

which gives the inverse of a matrix A after a general rank-1 update.
After changing a single row in M_b^{-1}, the new matrix $\tilde{M}_b$ is given by

$$(\tilde{M}_b)_{ij} = \begin{cases} \frac{\det M_b^{-1}}{\det \tilde{M}_b^{-1}} (M_b)_{i i_0} & \text{if} \quad j = i_0 \\ (M_b)_{ij} - (\tilde{M}_b)_{i i_0} \sum_{k=1}^{n_b} (\tilde{M}_b^{-1})_{i_0 k} (M_b)_{kj} & \text{if} \quad j \neq i_0 \end{cases}. \tag{A.10}$$

This operation is of order $\mathcal{O}(n_b^2)$. For a row permutation, the new matrix $\tilde{M}_b^{(i_0')}$ follows from $\tilde{M}_b$ by permuting the columns with index i_0 and i_0'.
The change of one column in M_b^{-1} leads to the new matrix $\tilde{M}_b$, whose entries are calculated by

$$(\tilde{M}_b)_{ij} = \begin{cases} \frac{\det M_b^{-1}}{\det \tilde{M}_b^{-1}} (M_b)_{j_0 i} & \text{if} \quad i = j_0 \\ (M_b)_{ij} - (\tilde{M}_b)_{j_0 j} \sum_{k=1}^{n_b} (M_b)_{ik} (\tilde{M}_b^{-1})_{k j_0} & \text{if} \quad i \neq j_0 \end{cases}. \tag{A.11}$$

If we permute the column afterwards, the new matrix $\tilde{M}_b^{(j_0')}$ follows from $\tilde{M}_b$ by permuting the rows with index j_0 and j_0'.

[1] The formula is derived on page 78 of Ref. [114].

A.2 Imaginary time evolution operator

In the Schrödinger picture operators are time independent, the time-evolution of a state

$$|\psi^S(\tau)\rangle = e^{-\tau H}|\psi(0)\rangle = U^S(\tau)|\psi(0)\rangle$$

is governed by the full Hamiltonian H, and therefore the time-evolution operator is

$$U^S(\tau) = e^{-\tau H}.$$

For the interaction picture the Hamiltonian is separated into an interacting H_1 and a non-interacting part H_0:

$$H = H_0 + H_1.$$

The time-evolution of an operator O and a state $|\psi\rangle$ in the interaction picture are given by

$$O^I(\tau) = e^{H_0\tau} O e^{-H_0\tau} \quad \text{and} \quad |\psi^I(\tau)\rangle = e^{H_0\tau}|\psi^S(\tau)\rangle. \tag{A.12}$$

We define a new time-evolution operator $U^I(\tau)$ by

$$|\psi^I(\tau)\rangle = U^I(\tau)|\psi^I(0)\rangle = U^I(\tau)|\psi^S(0)\rangle. \tag{A.13}$$

This implies the following relation between the two time-evolution operators

$$U^I(\tau) = e^{H_0\tau} U^S(\tau) = e^{H_0\tau} e^{-H\tau}.$$

The state $|\psi^I(\tau)\rangle$ in (A.13) is the solution of the equation of motion

$$\frac{\partial}{\partial\tau}|\psi^I(\tau)\rangle = -H_1(\tau)|\psi^I(\tau)\rangle \tag{A.14}$$

governed by the perturbation Hamiltonian H_1. Putting (A.13) into equation (A.14) and integrating over time we get

$$U^I(\tau) = \mathbb{1} - \int_0^\tau \mathrm{d}\tau'\, H_1^I(\tau') U^I(\tau').$$

We recursively insert the self consistent determined $U^I(\tau)$ to get the row expansion

$$\begin{aligned} U^I(\tau) &= \mathbb{1} - \int_0^\tau \mathrm{d}\tau'\, H_1^I(\tau') U^I(\tau') + \int_0^\tau \mathrm{d}\tau'\, H_1^I(\tau') \int_0^{\tau'} \mathrm{d}\tau''\, H_1^I(\tau'') U^I(\tau'') - \cdots \\ &= \sum_{n=0}^{\infty} (-1)^n \int_0^\tau \mathrm{d}\tau_1 \int_0^{\tau_1} \mathrm{d}\tau_2 \cdots \int_0^{\tau_{n-1}} \mathrm{d}\tau_n\, H_1^I(\tau_1) H_1^I(\tau_2) \cdots H_1^I(\tau_n). \end{aligned}$$

Using the time-ordering operator $\mathcal{T}$ and dividing by $n!$ the integration boundaries can be made equal for the time evolution up to time β

$$\begin{aligned} U^I(\beta) &= \sum_{n=0}^{\infty} \frac{(-1)^n}{n!} \int_0^\beta \mathrm{d}\tau_1 \int_0^\beta \mathrm{d}\tau_2 \cdots \int_0^\beta \mathrm{d}\tau_n\, \mathcal{T}\left(H_1^I(\tau_1) H_1^I(\tau_2) \cdots H_1^I(\tau_n)\right) \\ &= \mathcal{T}(e^{-\int_0^\beta \mathrm{d}\tau\, H_1^I(\tau)}). \end{aligned} \tag{A.15}$$

Here, the time-ordering operator $\mathcal{T}$ orders all operators descending in time from the left to the right. Time ordering bosonic operators is equivalent to a permutation of these operators. When time ordering fermionic operators, in addition, we obtain a global minus sign if the permutation is odd. An odd permutation is equal to an odd number of pairwise permutations.

A.3 Bethe-Salpeter equation in paramagnetic systems

In order to calculate the orbital susceptibility we need to perform the spin summation

$$[\chi(\mathbf{q},i\omega_m)] = \sum_{\sigma\sigma'} \chi^{\sigma\sigma'},$$

where $\chi^{\sigma\sigma'} = \left[\chi^{\sigma\sigma\sigma'\sigma'}(\mathbf{q},i\omega_m)\right]$ is the spin longitudinal susceptibility, and the matrix indices are (n,s_1m_1,s_2m_2) and (n',s_3m_3,s_4m_4). Here we show that the summation over spins can be performed on $\chi^0(\mathbf{q},i\omega_m)$, $\chi^0(i\omega_m)$ and $\chi(i\omega_m)$ before the inverted Bethe-Salpeter equation (BSEQ) (4.27)

$$[\chi(\mathbf{q},i\omega_m)]^{-1} = \left[\chi^0(\mathbf{q},i\omega_m)\right]^{-1} - \left[\chi^0(i\omega_m)\right]^{-1} + [\chi(i\omega_m)]^{-1}$$

is used to calculate $\chi(\mathbf{q},i\omega_m)$. A very similar prove for χ^{zz} was given in appendix A.3 of Ref. [37]. We start by writing the BSEQ

$$[\chi(\mathbf{q},i\omega_m)] = \left[\chi^0(\mathbf{q},i\omega_m)\right] + \left[\chi^0(\mathbf{q},i\omega_m)\right][\Gamma(i\omega_m)][\chi(\mathbf{q},i\omega_m)] \tag{A.16}$$

in matrix form for the individual spins

$$\begin{pmatrix} \chi^{\uparrow\uparrow} & \chi^{\uparrow\downarrow} \\ \chi^{\downarrow\uparrow} & \chi^{\downarrow\downarrow} \end{pmatrix} = \begin{pmatrix} \chi^{0,\uparrow\uparrow} & 0 \\ 0 & \chi^{0,\downarrow\downarrow} \end{pmatrix} \left(\mathbb{1} + \begin{pmatrix} \Gamma^{\uparrow\uparrow} & \Gamma^{\uparrow\downarrow} \\ \Gamma^{\downarrow\uparrow} & \Gamma^{\downarrow\downarrow} \end{pmatrix} \begin{pmatrix} \chi^{\uparrow\uparrow} & \chi^{\uparrow\downarrow} \\ \chi^{\downarrow\uparrow} & \chi^{\downarrow\downarrow} \end{pmatrix} \right).$$

Performing the matrix operations on the right-hand side and using the symmetries $\chi^{\uparrow\uparrow} = \chi^{\downarrow\downarrow}$, $\chi^{\uparrow\downarrow} = \chi^{\downarrow\uparrow}$, and the same for χ^0 and Γ, this gives two independent equations

$$\begin{aligned} \chi^{\uparrow\uparrow} &= \chi^{0,\uparrow\uparrow}(\mathbb{1} + \Gamma^{\uparrow\uparrow}\chi^{\uparrow\uparrow} + \Gamma^{\uparrow\downarrow}\chi^{\uparrow\downarrow}) \\ \chi^{\uparrow\downarrow} &= \chi^{0,\uparrow\uparrow}(\Gamma^{\uparrow\uparrow}\chi^{\uparrow\downarrow} + \Gamma^{\uparrow\downarrow}\chi^{\uparrow\uparrow}). \end{aligned}$$

Using this, we express the spin summed susceptibility as

$$\begin{aligned} \chi &= \sum_{\sigma\sigma'} \chi^{\sigma\sigma'} \\ &= 2\left(\chi^{\uparrow\uparrow} + \chi^{\uparrow\downarrow}\right) \\ &= \chi^0 + \frac{1}{4}\chi^0\Gamma\chi. \end{aligned}$$

We invert this equation and write the momentum $\mathbf{q}$ explicitly to get the vertex as

$$\Gamma(\mathbf{q}) = 4\left(\left[\chi^0(\mathbf{q})\right]^{-1} - [\chi(\mathbf{q})]^{-1}\right).$$

By setting $\chi^{\sigma\sigma'} = \left[\chi^{\sigma\sigma\sigma'\sigma'}(i\omega_m)\right]$ and using the $\mathbf{q}$ summed local form of the BSEQ, we get a similar relation for the local vertex

$$\Gamma = 4\left(\left[\chi^0\right]^{-1} - [\chi]^{-1}\right).$$

Finally, we employ the local vertex approximation $\Gamma(\mathbf{q}) \approx \Gamma$ to get the result

$$[\chi(\mathbf{q})]^{-1} = \left[\chi^0(\mathbf{q})\right]^{-1} - \left[\chi^0\right]^{-1} + [\chi]^{-1},$$

which we can use instead of the spin dependent BSEQ.

A.4 Basis functions

A.4.1 Matsubara frequency representation

The Fourier expansion of a 2β periodic function is

$$g(\tau) = \frac{1}{\beta} \sum_{j=-\infty}^{\infty} g_j e^{-i\frac{\pi j}{\beta}\tau}$$

with the coefficients

$$g_j = \frac{1}{2} \int_{-\beta}^{\beta} \mathrm{d}\tau\, g(\tau) e^{i\frac{\pi j}{\beta}\tau}.$$

We can restrict the integral to $\tau \in [0,\beta[$ by using the relation (4.38) to replace $g(\tau)$ with $-g(\tau+\beta)$ for fermionic times

$$\begin{aligned} g_j &= \frac{1}{2}\left(\int_0^{\beta} \mathrm{d}\tau\, g(\tau) e^{i\frac{\pi j}{\beta}\tau} - \int_{-\beta}^{0} \mathrm{d}\tau\, g(\tau+\beta) e^{i\frac{\pi j}{\beta}\tau} \right) \\ &= \frac{1}{2}(1 - e^{i\pi j}) \int_0^{\beta} \mathrm{d}\tau\, g(\tau) e^{i\frac{\pi j}{\beta}\tau}. \end{aligned}$$

The prefactor $\frac{1}{2}(1-e^{i\pi j})$ is zero for even $j = 2m$ and one for odd $j = 2n+1$, which defines the fermionic frequencies $\nu_n = (2n+1)\pi/\beta$. For bosonic times a similar derivation using $g(\tau) = g(\tau+\beta)$ leads to a prefactor $\frac{1}{2}(1+e^{i\pi j})$. Because this prefactor is zero for odd $j = 2n+1$ and one for even $j = 2m$, it defines the bosonic Matsubara frequencies $\omega_m = 2m\pi/\beta$. The basis functions $e^{i\nu_n\tau}$ are orthogonal

$$\delta_{n,n'} = \delta_{\nu_n,\nu_{n'}} = \frac{1}{\beta} \int_0^{\beta} \mathrm{d}\tau\, e^{i(\nu_n - \nu_{n'})\tau},$$

where ν_n are either both fermionic or bosonic frequencies. This basis is also complete on the interval $[0,\beta]$, which is equivalent to

$$\delta(\tau - \tau') = \frac{1}{\beta} \sum_{n=-\infty}^{\infty} e^{-i\nu_n(\tau-\tau')}. \tag{A.17}$$

A.4.2 Legendre polynomials

The Legendre polynomials $P_l(x)$ with $l \in \mathbb{N}$ and $x \in [-1,1]$ are recursively defined as

$$(l+1)P_{l+1}(x) = (2l+1)xP_l(x) - lP_{l-1}(x)$$

with the initial values

$$P_0(x) = 1 \quad \text{and} \quad P_1(x) = x.$$

To use $P_l(x)$ on the interval $\tau \in [0,\beta]$, we substitute $x(\tau) = 2\tau/\beta - 1$. Depending on l being even or odd, the Legendre polynomials are either symmetric or antisymmetric about $x = 0$ or $\tau = \beta/2$

$$P_l(-x) = P_l(x(\beta-\tau)) = (-1)^l P_l(x). \tag{A.18}$$

They form an orthogonal

$$\int_{-1}^{1} \mathrm{d}x\, P_l(x)P_{l'}(x) = \frac{2}{\beta}\int_0^\beta \mathrm{d}\tau\, P_l(x(\tau))P_{l'}(x(\tau)) = \frac{2}{2l+1}\delta_{ll'} \tag{A.19}$$

and complete

$$\sum_{l=0}^{\infty} \frac{2l+1}{2} P_l(x)P_l(x') = \delta(x-x') = \frac{\beta}{2}\delta(\tau-\tau')$$

basis. Because of that, any function $f(x)$ defined on $x \in [-1,1]$ can be expanded in the Legendre polynomials by

$$f(x) = \sum_{l=0}^{\infty} \frac{2l+1}{2} f_l P_l(x). \tag{A.20}$$

The coefficients f_l are then given by the scalar product

$$f_l = \langle f,P_l\rangle = \int_{-1}^{1} \mathrm{d}x\, f(x)P_l(x) = \frac{2}{\beta}\int_0^\beta \mathrm{d}\tau\, f(x(\tau))P_l(x(\tau)). \tag{A.21}$$

A.4.3 Unitary transformation from Legendre to Matsubara representation

In (4.61) the unitary matrix U_{nl}^m, which connects Legendre and Matsubara frequency representation, was defined. Following Ref. [39] and [1], the matrix elements can be expressed in terms of spherical Bessel functions $j_l(z)$ by

$$\begin{aligned} U_{nl}^m &= \frac{\sqrt{2l+1}}{\beta}\int_0^\beta \mathrm{d}\tau\, e^{i\frac{\pi}{\beta}(2n+m+1)\tau} P_l(x(\tau)) \\ &= \begin{cases} \delta_{0,l} & \text{if} \quad 2n+m+1=0 \\ \sqrt{2l+1}\, i^{l+2n+m+1} j_l\left(\frac{\pi}{2}(2n+m+1)\right) & \text{else} \end{cases} \end{aligned} \tag{A.22}$$

where we used the integral 7.243.5 of Ref. [115]

$$\int_{-1}^{1} \mathrm{d}x\, e^{iax} P_l(x) = i^l\sqrt{\frac{2\pi}{a}} J_{l+\frac{1}{2}}(a) = 2i^l j_l(a)$$

with Bessel functions $J_{l+\frac{1}{2}}(a)$ for the case $2n+m+1 \neq 0$. For the case $2n+m+1=0$, we make use of (A.19) with $P_0(x)=1$ and therefore $\int_{-1}^{1}\mathrm{d}x\, P_l(x) = \delta_{l,0}$. The spherical Bessel functions [116] can be expanded as

$$\begin{aligned} j_l(z) = z^{-1}\Bigg(&\sin(z-\pi\frac{l}{2}) \sum_{k=0}^{\left|\frac{l}{2}\right|} (-1)^k \frac{(l+2k)!(2z)^{-2k}}{(2k)!(l-2k)!} + \\ &\cos(z-\pi\frac{l}{2}) \sum_{k=0}^{\left|\frac{l-1}{2}\right|} (-1)^k \frac{(l+2k+1)!(2z)^{-2k-1}}{(2k+1)!(l-2k-1)!} \Bigg). \end{aligned} \tag{A.23}$$

The complex conjugation of U_{nl}^m leads to a sign change in n and m, or simply a multiplication with $(-1)^{l+m+1}$

$$\begin{aligned}[U_{nl}^m]^* &= \frac{\sqrt{2l+1}}{\beta}\int_0^\beta \mathrm{d}\tau\, e^{-i\frac{\pi}{\beta}(2n+m+1)\tau} P_l(x(\tau)) \\ &= U_{-nl}^{-m} \\ &= (-1)^{l+m+1} U_{nl}^m. \end{aligned} \tag{A.24}$$

To obtain this result we substituted τ with $\beta-\tau$ and used (A.18). The unitarity is shown using equation (A.17) and (A.19)

$$\begin{aligned}\sum_{n=\infty}^{\infty} U_{nl}^m \,[U_{nl'}^m]^* &= \sum_{n=\infty}^{\infty} \frac{\sqrt{2l+1}\sqrt{2l'+1}}{\beta^2}\int_0^\beta \mathrm{d}\tau \int_0^\beta \mathrm{d}\tau'\, e^{i\frac{\pi}{\beta}(2n+m+1)(\tau-\tau')} P_l(x(\tau))P_{l'}(x(\tau')) \\ &= \frac{\sqrt{2l+1}\sqrt{2l'+1}}{\beta}\int_0^\beta \mathrm{d}\tau\, P_l(x(\tau))P_{l'}(x(\tau)) \\ &= \delta_{l,l'}\end{aligned}$$

A.4.4 Improvement of Green function tail

Expanding the integral in equation (4.49) recursively using integration by parts we get

$$\begin{aligned}G_{\alpha\alpha'}(i\nu_n) &= \sum_{m=0}^{\infty}(-1)^{m+1}\frac{G_{\alpha\alpha'}^{(m)}(\beta^-) + G_{\alpha\alpha'}^{(m)}(0^+)}{(i\nu_n)^{m+1}} \\ &= \sum_{p=1}^{\infty}\frac{(G_p)}{(i\nu_n)^p},\end{aligned} \tag{A.25}$$

where $G^{(m)}(\tau)$ stands for the m-th derivative of $G(\tau)$. The first coefficient is given by the anti-commutator

$$(G_1) = \langle\{c_\alpha, c_{\alpha'}^\dagger\}\rangle = \delta_{\alpha,\alpha'}. \tag{A.26}$$

This follows also from the equations (4.41) and (4.42). Higher orders can be calculated by the Heisenberg equation. However, the high frequency tail is determined by (G_1), which becomes clear for example in figure 4.6. An expansion similar to (A.25) is also possible for the transformation matrix U_{nl}^m, which is given by[2]

$$U_{nl}^0 = \sum_{p=1}^{l+1}\frac{U_l^{(p)}}{(i\nu_n)^p} \tag{A.27}$$

and the coefficients

$$U_l^{(p)} = 2\sqrt{2l+1}\frac{(-1)^p}{\beta^p}\frac{(l+p-1)!}{(p-1)!(l-p+1)!}\delta_{p+l,\mathrm{odd}}$$

[2]Because we are discussing the single-particle Green functions, we consider only $m=0$.

are known analytically from equation (A.23). By inserting (A.25) and (A.27) into (4.60) we get the relation

$$(G_p) = \sum_{l=p-1}^{\infty} U_l^{(p)} G_l.$$

To use the information of the first coefficient (G_1) (A.26) we treat the last equation as the point-normal form $a = \mathbf{n} \cdot \mathbf{x}$ of a hyperplane by setting $a = (G_1)$, $n_l = U_l^{(1)}$ and $x_l = G_l$. We can then project $\mathbf{x}$ to the hyperplane associated with a to get the improved

$$\mathbf{x}' = \mathbf{x} + (a - \mathbf{n} \cdot \mathbf{x}) \frac{\mathbf{n}}{\mathbf{n} \cdot \mathbf{n}}.$$

In practice, we restrict our calculations to a finite number of $l \leq l_{\max}$ to get the Green function

$$G_l' = G_l + \left((G_1) - \sum_{l'=0}^{l_{\max}} U_{l'}^{(1)} G_{l'} \right) \frac{U_l^{(1)}}{\sum_{l'=0}^{l_{\max}} |U_{l'}^{(1)}|^2}, \tag{A.28}$$

which now gives a numerically more accurate tail, when transformed to Matsubara frequency representation [1, 39].

A.4.5 Intermediate representation

The idea of the intermediate representation [40] starts from the analytic continuation of the Green function (4.78), where the fermionic kernel can be written as

$$K_F(x(\tau), y(\omega)) = \frac{e^{-\frac{x+1}{2} y}}{1 + e^{-y}} \tag{A.29}$$

with the usual definition $x(\tau) = \frac{2\tau}{\beta} - 1$ and $y = \beta\omega$. We restrict ourselves here to the fermionic kernel, but the results hold also for the bosonic kernel. For $x \in]-1,1[$, the kernel vanishes for $|y| \to \infty$. We can therefore introduce a cutoff frequency $y_{\max}$, which is central for the shape of the basis functions, such that $y \in [-y_{\max}, y_{\max}]$. As described in section 4.5.3 choosing $y_{\max} \approx \beta U$ is optimal. A natural choice for the discretization of $K(x,y)$ is a double logarithmic grid.
To get this, we linearly discretize $\tilde{x} \in [-3,3]$ with N_x points $\tilde{x}_n$, and $\tilde{y} \in [-4, \tilde{y}_{\max}]$ with N_y points $\tilde{y}_n$. The borders of the intervals ($|x| = 3$ and $y \geq -4$) are chosen such that the borders of the logarithmic grid are approximated with sufficient precision. The numbers of discrete time and frequency points are in practice chosen to be $N_x = N_y = 1000$. The choice $\tilde{y}_{\max} = \sinh^{-1}(2 \ln(y_{\max})/\pi)$ becomes clear, when we look at the mapping from the linear to the double exponential grid. The double exponential time grid x_n is given by

$$x_n = \tanh\left(\frac{\pi}{2} \sinh \tilde{x}_n \right).$$

For the frequency grid, we construct the positive frequencies $y_n > 0$ by

$$y_n = e^{\left(\frac{\pi}{2} \sinh \tilde{y}_n \right)}$$

and the negative frequencies $y_n < 0$ follow from the positive ones by multiplication with minus one and inversion of the order. For the linear grid, the distance of two times $\Delta\tilde{x}_n = \frac{6}{N_x - 1}$ and the distance of two frequencies $\Delta\tilde{y}_n = \frac{\tilde{y}_{\max}+4}{N_y-1}$ are constant. For the double logarithmic grid we get the distance by

$$\frac{\Delta x_n}{\Delta\tilde{x}_n} \approx \frac{\mathrm{d}x_n}{\mathrm{d}\tilde{x}_n} = \frac{\pi}{2}\frac{\cosh\tilde{x}_n}{\cosh^2\left(\frac{\pi}{2}\sinh\tilde{x}_n\right)} \tag{A.30}$$

and

$$\frac{\Delta y_n}{\Delta\tilde{y}_n} \approx \frac{\mathrm{d}y_n}{\mathrm{d}\tilde{y}_n} = \frac{\pi}{2}\cosh\tilde{y}_n e^{\left(\frac{\pi}{2}\sinh\tilde{y}_n\right)}. \tag{A.31}$$

Central for the idea of the intermediate representation is the singular value decomposition (SVD) of the kernel $K(x,y)$. We do this for $\tilde{K}_{nm} = K(\tilde{x}_n,\tilde{y}_m)$, the kernel evaluated on the linear grid. The SVD

$$\tilde{K}_{nm} = \sum_{l=0}^{N_l} \tilde{u}_{l,n} s_l \tilde{v}^*_{l,m}$$

provides us with the linear discretized basis functions $\tilde{u}_{l,n} = \tilde{u}_l(\tilde{x}_n)$ and $\tilde{v}_{l,n} = \tilde{v}_l(\tilde{y}_n)$, and the singular values s_l. All values are real. The number of singular values $N_l = \min(N_x,2N_y)$ as a result of the SVD is large (in our case $N_l = 1000$). However, because most of the s_l are small, the number N_l can be drastically decreased by taking into account only values $s_l > s_{\min}$. In the here considered cases $s_{\min} = 10^{-12}$ which results in $N_l \ll 100$. The basis functions on the double logarithmic grid are given by

$$u_{l,n} = \frac{\tilde{u}_{l,n}}{\sqrt{\Delta x_n}} \quad \text{and} \quad v_{l,n} = \frac{\tilde{v}_{l,n}}{\sqrt{\Delta y_n}}.$$

The normalization factors follow from (A.30) and (A.31), and are chosen such that

$$\int_{-1}^{1} \mathrm{d}x\, u_l(x)u_{l'}(x) \approx \sum_{n=0}^{N_x-1} \Delta x_n u_{l,n}u_{l',n} = \delta_{ll'}$$
$$\int_{-y_{\max}}^{y_{\max}} \mathrm{d}y\, v_l(y)v_{l'}(y) \approx \sum_{n=0}^{2N_y-1} \Delta y_n v_{l,n}v_{l',n} = \delta_{ll'}.$$

This is correct, because the matrices $\tilde{u}_{l,n}$ and $\tilde{v}_{l,n}$ are orthogonal as result of the SVD. Finally, we make sure that $u_l(x(0)) = (-1)^l$ by inverting its sign if necessary. Similar to the Legendre basis, we can expand any function in imaginary time in this new basis

$$f(x) = \sum_{l=0}^{\infty} f_l u_l(x). \tag{A.32}$$

The coefficients f_l are then given by

$$\begin{aligned} f_l &= \int_{-1}^{1} \mathrm{d}x\, f(x)u_l(x) = \frac{2}{\beta}\int_0^{\beta} \mathrm{d}\tau\, f(x(\tau))u_l(x(\tau)) \\ &\approx \sum_{n=0}^{N_x-1} \Delta x_n f(x_n)u_{l,n} \end{aligned} \tag{A.33}$$

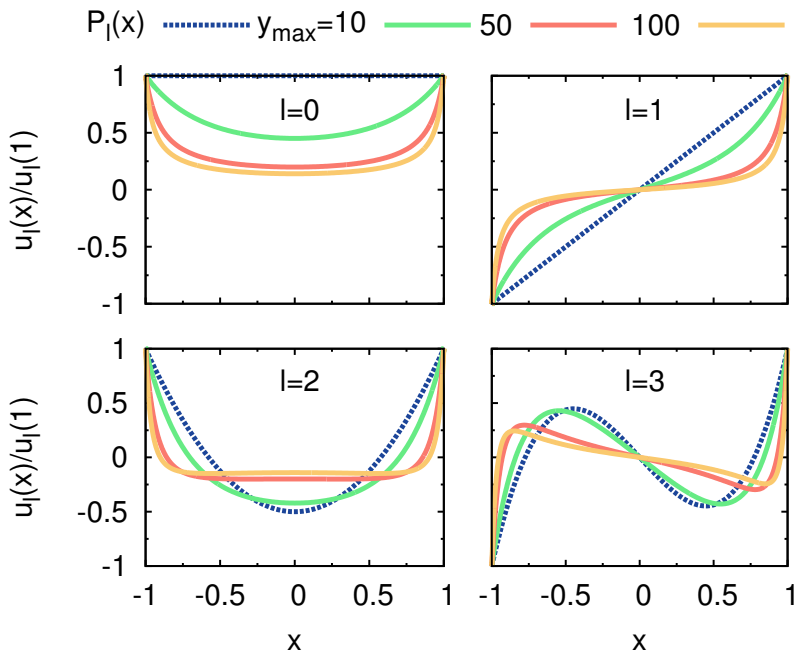

Figure A.1: Intermediate representation basis functions $u_l(x)$ in time x for different cutoffs $y_{\max}$ in comparison with Legendre polynomials $P_l(x)$.

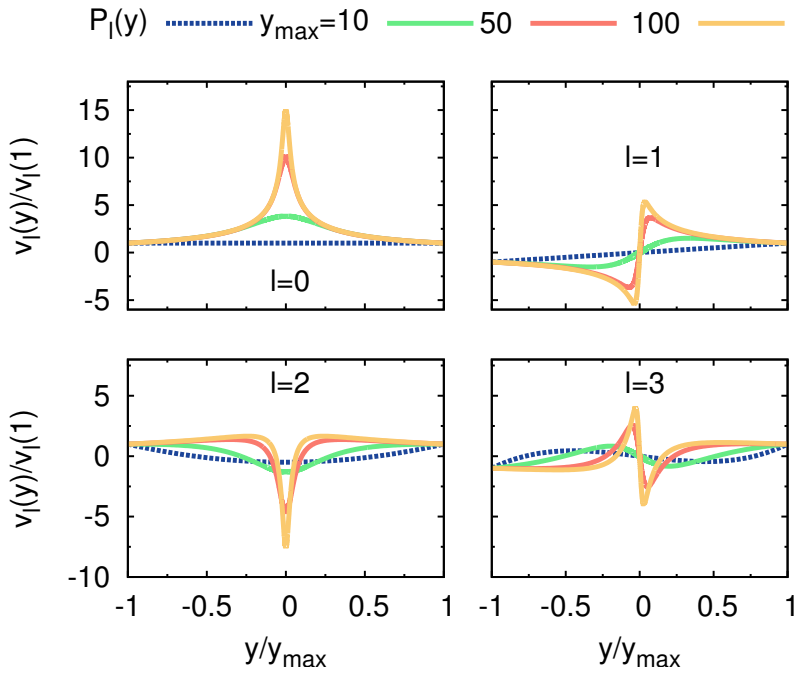

Figure A.2: Intermediate representation basis functions $v_l(y)$ in frequency y for different cutoffs $y_{\max}$ in comparison with Legendre polynomials $P_l(y/y_{\max})$.

A.5 Maximum entropy method

The maximum entropy method (MEM) [117, 118] determines the most probable solution $g(\omega)$ for a given $f(i\omega_n)$ in (4.77). Without loss of generality, we focus on equation (4.78) here, in a simplified form

$$G(\tau) = -\int_{-\infty}^{\infty} \frac{\mathrm{d}\omega}{2\pi} \frac{e^{-\tau\omega}}{1+e^{-\beta\omega}} A(\omega), \tag{A.34}$$

and determine $A(\omega)$ from $G(\tau)$. For susceptibilities one has to replace $A(\omega)$ with $\frac{\mathrm{Im}\,\chi(\omega)}{\omega}$ and use a bosonic kernel. For the most probable spectrum $A(\omega)$ the probability $p(A|G)$ for A given the data $G(\tau)$ is maximum. Bayes theorem states that

$$p(A|G)p(G) = p(G|A)p(A).$$

We do not consider $p(G)$, because there is only one data G. The two relevant remaining probabilities are the prior probability $p(A)$ and the likelihood function $p(G|A)$.
The likelihood function $p(G|A)$ is the probability of the data G following from A using (A.34). To calculate $p(G|A)$ we use (A.34) to get $\tilde{G}(\tau)$ from $A(\omega)$. In practice, the input data $G(\tau)$ is given by N points in time τ_n. The weighted distance of $\tilde{G}(\tau_n)$ to the data $G(\tau_n)$ is

$$\chi^2(A,G) = \frac{1}{N}\sum_{m=1}^{N} \frac{|G(\tau_n) - \tilde{G}(\tau_n)|^2}{\sigma_n^2},$$

where σ_n is the error of each $G(\tau_n)$. With this, the likelihood function is proportional to the normal distribution

$$p(G|A) \sim e^{-\chi^2(A,G)/2}.$$

To determine the prior probability, we use knowledge about the spectrum A. It is always positive definite and bounded. For the spectral function $A(\omega)$ it is $\int \mathrm{d}\omega\, A(\omega) = 2\pi$. Also the susceptibility is bounded, because $\int \mathrm{d}\omega \frac{\mathrm{Im}\,\chi(\omega)}{\omega} = \frac{\pi}{2}\chi(i\omega_0)$.
It is then argued [117] that for the prior probability $p(A) \sim e^{\alpha S(A,m)}$. Here α is a parameter and $S(A,m)$ the entropy

$$S(A,m) = \int \mathrm{d}\omega \left[A(\omega) - m(\omega) - A(\omega)\ln\frac{A(\omega)}{m(\omega)}\right] \tag{A.35}$$

depending itself on the default model $m(\omega)$. The default model m is positive definite and equal to A in the absence of data G. Prior probability and likelihood function together give the total probability

$$p(A|G,m,\alpha) \sim e^{\alpha S(A,m) - \chi^2(A,G)/2}.$$

The MEM chooses A such that the exponent $\alpha S - \chi^2/2$ is maximum.
This is influenced by the choice of m and α. A constant is a good choice for m, because it does not enforce a structure on A. Opposed to a constant m, a default model m containing sharp features can spoil the result A.

The parameter α controls the competition between S and χ. In the limit of a vanishing α the spectrum A resembles the result of a least square fit. In that case, the noise of the data G has a large influence on A, which is therefore noisy itself. For a large α on the other hand, the entropy term S gets pronounced and the resulting A resembles the default model. To find the optimal α, different schemes where proposed. An early choice was to adjust α such that $\chi^2 = N$.
Bryan [119] introduced the idea of averaging over different α such that

$$A = \int \mathrm{d}\alpha \, A(\alpha) P(\alpha|G,m),$$

where $P(\alpha|G,m)$ is determined by a method similar to the one for $p(A|G,m,\alpha)$ described above. Bryan's method leads in general to better results than simpler approaches.

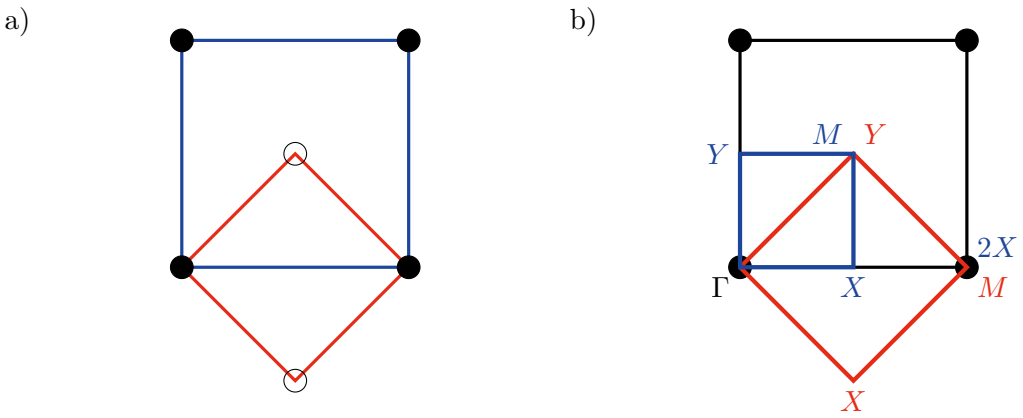

Figure A.3: a) Unit cell (red) for the one-band Hubbard model and supercell (blue) containing two sites. In b) we show the related Brillouin zones.

A.6 Analytic calculations for magnetic susceptibilities in cuprates

A.6.1 Bare dynamical lattice susceptibility for an antiferromagnetic Mott insulator

In the following we obtain the bare lattice susceptibility for the antiferromagnetic phase of a Mott insulator with the kinetic part of the Hamiltonian (6.2). In DMFT the bare susceptibility is constructed from the DMFT Green functions containing the full Coulomb interaction effects in the self-energy. With $\epsilon_{\mathbf{k}} = -2t(\cos(k_x a) + \cos(k_y a))$ and $\epsilon'_{\mathbf{k}} = 4t' \cos(k_x a)\cos(k_y a)$ the Hamiltonian becomes the site dependent matrix

$$H_{\mathbf{k}} = \begin{pmatrix} \epsilon'_{\mathbf{k}} & \epsilon_{\mathbf{k}} e^{-ik_x a} \\ \epsilon_{\mathbf{k}} e^{ik_x a} & \epsilon'_{\mathbf{k}} \end{pmatrix}.$$

To obtain this matrix we enlarge the unit cell to the supercell with two sites shown in figure A.3.
This step is necessary in the antiferromagnetic phase, because neighboring sites have opposite spin. The local self-energy is approximately the Hartree-Fock self-energy

$$\Sigma_\sigma(i\nu_n) - \mu = \begin{pmatrix} -\sigma m U & 0 \\ 0 & \sigma m U \end{pmatrix} \tag{A.36}$$

with m being the magnetization, U the screened Coulomb interaction, and $\sigma = \uparrow = 1$ and $\sigma = \downarrow = -1$. With this we can readily write down the Green function matrix as

$$\begin{aligned} G_{\sigma\mathbf{k}}(i\nu_n) &= [i\nu_n - H_{\mathbf{k}} - \Sigma_\sigma(i\nu_n) + \mu]^{-1} \\ &= \frac{1}{D_{\mathbf{k}}(i\nu_n)} \begin{pmatrix} i\nu_n - \epsilon'_{\mathbf{k}} - \sigma m U & \epsilon_{\mathbf{k}} e^{-ik_x a} \\ \epsilon_{\mathbf{k}} e^{ik_x a} & i\nu_n - \epsilon'_{\mathbf{k}} + \sigma m U \end{pmatrix} \end{aligned}$$

with the determinant

$$D_{\mathbf{k}}(i\nu_n) = (i\nu_n - \epsilon'_{\mathbf{k}})^2 - (\epsilon^{\pm}_{\mathbf{k}})^2$$

and the dispersions $\epsilon^{\pm}_{\mathbf{k}} = \pm\sqrt{\epsilon^2_{\mathbf{k}} + (mU)^2}$. These are the dispersions of two bands split by mU if $t' = 0 = \epsilon'_{\mathbf{k}}$. Let us introduce

$$\begin{aligned} E^{\pm}_{\mathbf{k}} &= \epsilon'_{\mathbf{k}} + \epsilon^{\pm}_{\mathbf{k}} \\ &= \epsilon'_{\mathbf{k}} \pm \sqrt{\epsilon^2_{\mathbf{k}} + (mU)^2}. \end{aligned}$$

Using partial fraction decomposition each element of the Green function matrix can then be written as

$$G^{ss'}_{\sigma\mathbf{k}}(i\nu_n) = \sum_{p=\pm} W^{ss'}_{\sigma\mathbf{k}p} \frac{1}{i\nu_n - E^p_{\mathbf{k}}}. \tag{A.37}$$

Here, the weights for the site diagonal entries are

$$\begin{aligned} W^{11}_{\sigma\mathbf{k}p} &= \frac{1}{2}\left(1 - \frac{\sigma mU}{\epsilon^p_{\mathbf{k}}}\right) \\ &= W^{22}_{-\sigma\mathbf{k}p} \end{aligned}$$

and for the off-diagonal entries the weights are

$$\begin{aligned} W^{12}_{\sigma\mathbf{k}p} &= \frac{1}{2} e^{-ik_x a} \frac{\epsilon_{\mathbf{k}}}{\epsilon^p_{\mathbf{k}}} \\ &= \left[W^{21}_{\sigma\mathbf{k}p}\right]^*. \end{aligned}$$

In terms of the Green functions the bare lattice susceptibility is given as

$$\chi^{0,ss'}_{\tilde{\sigma}\tilde{\sigma}'}(\mathbf{q}, i\omega_m) = -\frac{1}{N_{\mathbf{k}}} \sum_{\mathbf{k}} \frac{1}{\beta} \sum_n G^{ss'}_{\tilde{\sigma}\mathbf{k}}(i\nu_n) G^{s's}_{\tilde{\sigma}'\mathbf{k}+\mathbf{q}}(i\nu_n + i\omega_m).$$

Here, we use $\chi^{0,ss'}_{\tilde{\sigma}\tilde{\sigma}'} = \chi^{0,sss's'}_{\tilde{\sigma}\tilde{\sigma}'\tilde{\sigma}'\tilde{\sigma}}$. For the summation over the fermionic Matsubara frequencies we use [22, 38]

$$\frac{1}{\beta} \sum_n \frac{1}{i\nu_n - x} \frac{1}{i\nu_n - y} = \begin{cases} \beta n_F(x)(n_F(x) - 1) & \text{if} \quad x = y \\ \frac{n_F(x) - n_F(y)}{x - y} & \text{else} \end{cases}$$

with the Fermi-Dirac distribution $n_F(\epsilon) = (1 + e^{\beta\epsilon})^{-1}$. We perform the sum over the fermionic Matsubara frequency, which introduces the term

$$I^{pp'}_{\mathbf{k},\mathbf{q}}(i\omega_m) = \begin{cases} \beta n_F(E^p_{\mathbf{k}})(n_F(E^p_{\mathbf{k}}) - 1) & \text{if} \quad i\omega_m + E^p_{\mathbf{k}} - E^{p'}_{\mathbf{k}+\mathbf{q}} = 0 \\ \frac{n_F(E^p_{\mathbf{k}}) - n_F(E^{p'}_{\mathbf{k}+\mathbf{q}})}{i\omega_m + E^p_{\mathbf{k}} - E^{p'}_{\mathbf{k}+\mathbf{q}}} & \text{else} \end{cases},$$

and results in the bare susceptibility

$$\chi^{0,ss'}_{\tilde{\sigma}\tilde{\sigma}'}(\mathbf{q}, i\omega_m) = -\frac{1}{N_{\mathbf{k}}} \sum_{\mathbf{k}} \sum_{pp'=\pm} W^{ss'}_{\tilde{\sigma}\mathbf{k}p} W^{s's}_{\tilde{\sigma}'\mathbf{k}+\mathbf{q}p'} I^{pp'}_{\mathbf{k},\mathbf{q}}(i\omega_m). \tag{A.38}$$

With the phase factor $\phi_{ss'} = (1-\delta_{s,s'})(-1)^s i q_x$ the susceptibility is then given as

$$\begin{aligned}\chi^0_{\tilde{\sigma}\tilde{\sigma}'}(\mathbf{q},i\omega_m) &= \frac{1}{2}\sum_{ss'} e^{i\phi_{ss'}}\chi^{0,ss'}_{\tilde{\sigma}\tilde{\sigma}'}(\mathbf{q},i\omega_m) \\ &= -\frac{1}{N_\mathbf{k}}\sum_{\mathbf{k}}\sum_{pp'=\pm} W^{pp'}_{\tilde{\sigma}\tilde{\sigma}'\mathbf{k},\mathbf{q}} I^{pp'}_{\mathbf{k},\mathbf{q}}(i\omega_m).\end{aligned}$$

And the weights of that susceptibility are

$$W^{pp'}_{\sigma\sigma'\mathbf{k},\mathbf{q}} = \frac{1}{4}\left(1 - mU\left(\frac{\sigma}{\epsilon^p_\mathbf{k}} + \frac{\sigma'}{\epsilon^{p'}_{\mathbf{k}+\mathbf{q}}}\right) + \frac{(mU)^2\sigma\sigma' + \epsilon_\mathbf{k}\epsilon_{\mathbf{k}+\mathbf{q}}}{\epsilon^p_\mathbf{k}\epsilon^{p'}_{\mathbf{k}+\mathbf{q}}}\right).$$

The two magnetic susceptibilities are obtained by the spin sums

$$\begin{aligned}\chi^{0,zz}(\mathbf{q},i\omega_m) &= \frac{1}{4}\sum_{\tilde{\sigma}}\chi^0_{\tilde{\sigma}\tilde{\sigma}}(\mathbf{q},i\omega_m) \\ \chi^{0,xx}(\mathbf{q},i\omega_m) &= \frac{1}{4}\sum_{\tilde{\sigma}}\chi^0_{-\tilde{\sigma}\tilde{\sigma}}(\mathbf{q},i\omega_m).\end{aligned}$$

In a compact form they are then given as

$$\chi^{0,\alpha\alpha}(\mathbf{q},i\omega_m) = -\frac{1}{4}\frac{1}{N_\mathbf{k}}\sum_{\mathbf{k}}\sum_{pp'=\pm} W^{\alpha\alpha,pp'}_{\mathbf{k},\mathbf{q}} I^{pp'}_{\mathbf{k},\mathbf{q}}(i\omega_m) \tag{A.39}$$

with the weights

$$W^{zz,pp'}_{\mathbf{k},\mathbf{q}} = \frac{1}{2}\left(1 + \frac{\epsilon_\mathbf{k}\epsilon_{\mathbf{k}+\mathbf{q}} + (mU)^2}{\epsilon^p_\mathbf{k}\epsilon^{p'}_{\mathbf{k}+\mathbf{q}}}\right) \tag{A.40}$$

$$W^{xx,pp'}_{\mathbf{k},\mathbf{q}} = \frac{1}{2}\left(1 + \frac{\epsilon_\mathbf{k}\epsilon_{\mathbf{k}+\mathbf{q}} - (mU)^2}{\epsilon^p_\mathbf{k}\epsilon^{p'}_{\mathbf{k}+\mathbf{q}}}\right). \tag{A.41}$$

Here, the difference between $\chi^{0,zz}(\mathbf{q},i\omega_m)$ and $\chi^{0,xx}(\mathbf{q},i\omega_m)$ is only the minus sign in front of the term $(mU)^2$ in the weights. At low temperatures $I^{pp'}_{\mathbf{k},\mathbf{q}}(i\omega_m)$ is finite only for $p' = -p$, while $I^{pp}_{\mathbf{k},\mathbf{q}}(i\omega_m)$ goes to zero.

A.6.2 Dynamical lattice susceptibility for an antiferromagnetic Mott insulator

The bare lattice susceptibility $\chi^{0,ss'}_{\tilde{\sigma}\tilde{\sigma}'}(\mathbf{q},i\omega_m)$ in the antiferromagnetic phase was given in the last section as (A.38). From this, we derive an approximate expression for the transverse dynamical lattice susceptibility $\chi^{xx}(\mathbf{q},i\omega_m)$. Let us set $t' = 0$ for simplicity and consider the low temperature limit with $m = \frac{1}{2}$ and a small t/U. The term $I^{pp'}_{\mathbf{k},\mathbf{q}}(i\omega_m)$ is different from zero only for $p' = -p$ and can then be approximated as

$$\begin{aligned}I^{p-p}_{\mathbf{k},\mathbf{q}}(i\omega_m) &\approx -p\frac{1}{i\omega_m + E^p_\mathbf{k} - E^{-p}_{\mathbf{k}+\mathbf{q}}} \\ &\approx -p\frac{1}{i\omega_m + pU}.\end{aligned}$$

To calculate the weights we use the approximation

$$\begin{aligned}\frac{1}{\epsilon_{\mathbf{k}}^{\pm}} &= \pm\frac{2}{U}\frac{1}{\sqrt{1+\frac{4\epsilon_{\mathbf{k}}^2}{U^2}}} \\ &\approx \pm\frac{2}{U}\left(1-\frac{2\epsilon_{\mathbf{k}}^2}{U^2}\right)\end{aligned}$$

and the summations

$$\begin{aligned}\frac{1}{N_{\mathbf{k}}}\sum_{\mathbf{k}}\epsilon_{\mathbf{k}}^2 &\approx \frac{1}{(2\pi)^2}\int_{-\pi}^{\pi}\mathrm{d}k_x\int_{-\pi}^{\pi}\mathrm{d}k_y\,\epsilon_{\mathbf{k}}^2 \\ &= 4t^2 = UJ \\ &\approx \frac{1}{N_{\mathbf{k}}}\sum_{\mathbf{k}}\epsilon_{\mathbf{k}+\mathbf{q}}^2 \\ \frac{1}{N_{\mathbf{k}}}\sum_{\mathbf{k}}\epsilon_{\mathbf{k}}\epsilon_{\mathbf{k}+\mathbf{q}} &\approx 2t^2(\cos q_x+\cos q_y) \\ &= UJf_{\mathbf{q}}\end{aligned}$$

with $f_{\mathbf{q}} = \frac{1}{2}(\cos q_x + \cos q_y)$ and $J = 4t^2/U$. We introduce new weights

$$\begin{aligned}W_{\tilde{\sigma}\mathbf{q}}^{11} &= \frac{1}{N_{\mathbf{k}}}\sum_{\mathbf{k}}W_{\tilde{\sigma}\mathbf{k}+}^{11}W_{-\tilde{\sigma}\mathbf{k}+\mathbf{q}-}^{11} \\ &\approx \frac{1}{4}\left[1-\tilde{\sigma}\left(1-\frac{2J}{U}\right)\right]^2 \\ &\approx W_{-\tilde{\sigma}\mathbf{q}}^{22} \\ W_{\tilde{\sigma}\mathbf{q}}^{12} &= \frac{1}{N_{\mathbf{k}}}\sum_{\mathbf{k}}W_{\tilde{\sigma}\mathbf{k}+}^{12}W_{-\tilde{\sigma}\mathbf{k}+\mathbf{q}-}^{21}e^{-iq_x} \\ &\approx -\frac{J}{U}f_{\mathbf{q}} \\ &\approx W_{-\tilde{\sigma}\mathbf{q}}^{21}\end{aligned}$$

with the help of which we write down the bare susceptibility as

$$\chi_{\tilde{\sigma}-\tilde{\sigma}}^{0,ss'}(\mathbf{q},i\omega_m) \approx \left[-\frac{W_{\tilde{\sigma}\mathbf{q}}^{ss'}}{i\omega_m-U}+\frac{W_{-\tilde{\sigma}\mathbf{q}}^{ss'}}{i\omega_m+U}\right]e^{-i\phi_{ss'}}.$$

We sum this over the momentum $\mathbf{q}$ to get the local bare susceptibility matrix

$$\chi_{\tilde{\sigma}-\tilde{\sigma}}^{0,ss'}(i\omega_m) \approx \left[-\frac{W_{\tilde{\sigma}}^{ss'}}{i\omega_m-U}+\frac{W_{-\tilde{\sigma}}^{ss'}}{i\omega_m+U}\right]$$

with $W_{\tilde{\sigma}}^{ss'} = W_{\tilde{\sigma}\mathbf{q}}^{ss'}\delta_{s,s'}$. The bare lattice $\chi_{\tilde{\sigma}-\tilde{\sigma}}^{0,ss'}(\mathbf{q},i\omega_m)$ and the bare local $\chi_{\tilde{\sigma}-\tilde{\sigma}}^{0,ss'}(i\omega_m)$ differ where $s \neq s'$.

The full local susceptibility is approximately given by

$$\chi_{\tilde{\sigma}-\tilde{\sigma}}(i\omega_m) \approx \frac{1}{\tilde{\sigma} i\omega_m + 2J}.$$

Because of the antiferromagnetic order, the susceptibility of neighboring sites is obtained by inverting the spins, i.e., $\chi^{22}_{\tilde{\sigma}-\tilde{\sigma}} = \chi^{11}_{-\tilde{\sigma}\tilde{\sigma}}$. At this point, we can calculate the Bethe-Salpeter equation in the matrix representation of the sites

$$\begin{aligned}\left[\chi_{\tilde{\sigma}-\tilde{\sigma}}(\mathbf{q},i\omega_m)\right]^{-1} &= \left[\chi_{\tilde{\sigma}-\tilde{\sigma}}(i\omega_m)\right]^{-1} - \left[\chi^0_{\tilde{\sigma}-\tilde{\sigma}}(i\omega_m)\right]^{-1} + \left[\chi^0_{\tilde{\sigma}-\tilde{\sigma}}(\mathbf{q},i\omega_m)\right]^{-1} \\ &= \begin{pmatrix} i\omega_m + 2J & 2Jf_{\mathbf{q}} \\ 2Jf_{\mathbf{q}} & -i\omega_m + 2J \end{pmatrix}^{-1} e^{i\phi_{ss'}}.\end{aligned}$$

Finally, the sum over spin and sites gives the transverse susceptibility

$$\begin{aligned}\chi^{xx}(\mathbf{q},i\omega_m) &= \frac{1}{4}\sum_{\tilde{\sigma}} \frac{1}{2}\sum_{ss'} e^{i\phi_{ss'}} \chi^{ss'}_{\tilde{\sigma}-\tilde{\sigma}}(\mathbf{q},i\omega_m) \\ &= \frac{J(1-f_{\mathbf{q}})}{\omega_m^2 + 4J^2(1-f_{\mathbf{q}}^2)},\end{aligned} \tag{A.42}$$

which is the susceptibility of spin-wave theory.

A.6.3 Static lattice susceptibility close to half-filling

Following the derivations for the Hubbard model at half-filling in Ref. [22], we derive the bare and full static susceptibility close to half-filling $n_\sigma = (1-x)/2$ with a small x. The self-energy in this case is [120, 121]

$$\begin{aligned}\Sigma_\sigma(i\nu_n) - \mu &= \frac{n_{-\sigma}(1-n_{-\sigma})U^2 r_0^2}{i\nu_n + \mu - B_\sigma - U(1-n_{-\sigma})} - \tilde{\mu} \\ &= \frac{A}{i\nu_n - B} - \tilde{\mu}\end{aligned}$$

with the chemical potentials μ and $\tilde{\mu} = \mu - Un_{-\sigma}$, the renormalization factor r_0, which is obtained by fitting to the exact self-energy, and $B_\sigma = \sum_{ij} t_{ij}\langle c^\dagger_{i,\sigma} c_{j,\sigma}(2n_{i,-\sigma}-1)\rangle$. Since the system is paramagnetic $n_{-\sigma} = n_\sigma$. At half-filling and for $B_\sigma = 0$ we get the self-energy of an atom $\Sigma_\sigma(i\nu_n) = U^2 r_0^2/4i\nu_n$. With the help of the abbreviations $A = n_\sigma(1-n_\sigma)U^2 r_0^2$ and $B = B_\sigma + U(1-n_\sigma) - \mu$ we write the lattice single-particle Green function as

$$\begin{aligned}G^\sigma_{\mathbf{k}}(i\nu_n) &= \frac{1}{i\nu_n - \epsilon_{\mathbf{k}} + \tilde{\mu} - \frac{A}{i\nu_n - B}} \\ &= \frac{1}{E^+_{\mathbf{k}} - E^-_{\mathbf{k}}}\left(\frac{E^+_{\mathbf{k}} - B}{i\nu_n - E^+_{\mathbf{k}}} - \frac{E^-_{\mathbf{k}} - B}{i\nu_n - E^-_{\mathbf{k}}}\right).\end{aligned}$$

Here, the energies are given in terms of $\epsilon_{\mathbf{k}} = -2t(\cos k_x + \cos k_y) + 4t' \cos k_x \cos k_y$ as

$$E^\pm_{\mathbf{k}} = \frac{1}{2}(\epsilon_{\mathbf{k}} + U - 2\mu + B_\sigma) \pm \frac{1}{2}\left\{\left[\epsilon_{\mathbf{k}} - B_\sigma + (2n_\sigma - 1)U\right]^2 + 4n_\sigma(1-n_\sigma)U^2 r_0^2\right\}^{1/2}.$$

The bare lattice susceptibility is defined as

$$\chi^{0,zz}(\mathbf{q},i\omega_m) = -\frac{1}{\beta}\frac{1}{N_\mathbf{k}}\frac{1}{4}\sum_\sigma\sum_\mathbf{k}\sum_n G^\sigma_\mathbf{k}(i\nu_n)G^\sigma_{\mathbf{k}+\mathbf{q}}(i\nu_n+i\omega_m).$$

By summing over the fermionic Matsubara frequencies we obtain

$$I^{pp'}_{\mathbf{k},\mathbf{q}} = \frac{(E^p_\mathbf{k}-B)(E^{p'}_{\mathbf{k}+\mathbf{q}}-B)}{(E^+_\mathbf{k}-E^-_\mathbf{k})(E^+_{\mathbf{k}+\mathbf{q}}-E^-_{\mathbf{k}+\mathbf{q}})}\begin{cases}\beta n_F(E^p_\mathbf{k})(n_F(E^p_\mathbf{k})-1) & \text{if} \quad i\omega_m+E^p_\mathbf{k}-E^{p'}_{\mathbf{k}+\mathbf{q}}=0\\ \frac{n_F(E^p_\mathbf{k})-n_F(E^{p'}_{\mathbf{k}+\mathbf{q}})}{i\omega_m+E^p_\mathbf{k}-E^{p'}_{\mathbf{k}+\mathbf{q}}} & \text{else}\end{cases}.$$

This can be combined to the even parts $A_{\mathbf{k},\mathbf{q}}(i\omega_m)$ and odd parts $B_{\mathbf{k},\mathbf{q}}(i\omega_m)$

$$\begin{aligned}A_{\mathbf{k},\mathbf{q}}(i\omega_m) &= -I^{++}_{\mathbf{k},\mathbf{q}}(i\omega_m) - I^{--}_{\mathbf{k},\mathbf{q}}(i\omega_m)\\ B_{\mathbf{k},\mathbf{q}}(i\omega_m) &= I^{+-}_{\mathbf{k},\mathbf{q}}(i\omega_m) + I^{-+}_{\mathbf{k},\mathbf{q}}(i\omega_m),\end{aligned}$$

with the help of which the bare susceptibility is given as

$$\chi^{0,zz}(\mathbf{q},i\omega_m) = \frac{1}{2}\frac{1}{N_\mathbf{k}}\sum_\mathbf{k}\left[A_{\mathbf{k},\mathbf{q}}(i\omega_m)+B_{\mathbf{k},\mathbf{q}}(i\omega_m)\right].$$

We consider that away from half-filling the system becomes metallic and take the large βU limit. In this limit it is $n_F(E^+_\mathbf{k}) \approx 1-2n_\sigma$ and $n_F(E^-_\mathbf{k}) \approx 2n_\sigma$. The difference of $n(E^\pm_\mathbf{k})$ and $n(E^\pm_{\mathbf{k}+\mathbf{q}})$ in the even part $A_{\mathbf{k},\mathbf{q}}(i\omega_m)$ than vanishes and $A_{\mathbf{k},\mathbf{q}}(i\omega_m) \approx 0$. The expansion of $B_{\mathbf{k},\mathbf{q}}(i\omega_m)$ in powers of U and summation over $\mathbf{k}$ leads to the approximation

$$\chi^{0,zz}(\mathbf{q},0) \approx \frac{1}{4r_0U}\left\{C_1 - \frac{C_2}{2U}\left[J_{r_0}(\mathbf{0})+\frac{1}{2}J_{r_0}(\mathbf{q})\right]\right\} \tag{A.43}$$

with the constants

$$\begin{aligned}C_1 &= \frac{(4n_\sigma-1)4n_\sigma(1-n_\sigma)}{\left[\frac{(2n_\sigma-1)^2}{r_0^2}+4n_\sigma(1-n_\sigma)\right]^{3/2}}\\ C_2 &= \frac{-16(4n_\sigma-1)n_\sigma(1-n_\sigma)\left[\frac{(2n_\sigma-1)^2}{r_0^2}-n_\sigma(1-n_\sigma)\right]}{\left[\frac{(2n_\sigma-1)^2}{r_0^2}+4n_\sigma(1-n_\sigma)\right]^{7/2}},\end{aligned}$$

which for half-filling both become one, and the renormalized spin dispersion

$$J_{r_0}(\mathbf{q}) = \frac{J}{r_0^2}(\cos q_x+\cos q_y)+\frac{2J'}{r_0^2}\cos q_x\cos q_y.$$

The spin coupling constants are $J=4t^2/U$ and $J'=4(t')^2/U$. The bare local susceptibility follows from (A.43) by summation over $\mathbf{q}$ and is given by

$$\begin{aligned}\chi^{0,zz}(0) &= \frac{1}{N_\mathbf{q}}\sum_\mathbf{q}\chi^{0,zz}(\mathbf{q},i\omega_m)\\ &\approx \frac{1}{4r_0U}\left\{C_1-\frac{C_2}{2U}J_{r_0}(\mathbf{0})\right\},\end{aligned} \tag{A.44}$$

because $\sum_{\mathbf{q}} J_{r_0}(\mathbf{q}) = 0$. To calculate the lattice susceptibility $\chi^{zz}(\mathbf{q},0)$ via the Bethe-Salpeter equation we need the local susceptibility $\chi^{zz}(0)$. Here, we approximate $\chi^{zz}(0)$ by the local susceptibility of a single atom

$$\begin{aligned}\chi_{\text{atom}}(0) &= \frac{\beta}{4}\left(n_\uparrow + n_\downarrow - \frac{2e^{-\beta(U-2\mu)}}{1+2e^{\beta\mu}+e^{-\beta(U-2\mu)}}\right)\\ &\approx \frac{\beta}{4}(n_\uparrow + n_\downarrow) = \frac{\beta}{2}n_\sigma,\end{aligned}$$

where the last approximation is again valid in the large βU limit. The lattice susceptibility is then obtained using the Bethe-Salpeter equation in the local vertex approximation (4.24)

$$\begin{aligned}\chi^{zz}(\mathbf{q},0) &= \left(\left[\chi^{0,zz}(\mathbf{q},0)\right]^{-1} - \left[\chi^{0,zz}(0)\right]^{-1} + \left[\chi^{zz}(0)\right]^{-1}\right)^{-1}\\ &\approx \frac{1}{4}\frac{2n_\sigma}{k_BT + n_\sigma\frac{C_2}{2C_1^2}r_0 J_{r_0}(\mathbf{q})}.\end{aligned}$$

For small doping x we can further approximate $C_1 \approx C_2 \approx 1-2x$ and, using that $2n_\sigma = 1-x$, we obtain

$$\chi^{zz}(\mathbf{q},0) \approx \frac{1}{4}\frac{1-x}{k_BT + \frac{1}{4}\frac{1-x}{1-2x}r_0 J_{r_0}(\mathbf{q})}. \tag{A.45}$$

In the case of half-filling we get

$$\chi^{zz}(\mathbf{q},0) = \frac{1}{4k_B}\frac{1}{T-T_{\mathbf{q}}} \tag{A.46}$$

with $k_BT_{\mathbf{q}} = -r_0 J_{r_0}(\mathbf{q})/4$.

A.6.4 Stoner susceptibility

The Stoner mechanism [55, 84] can explain magnetism in weakly correlated metals, where the U can be treated as a perturbation.
For the non-interacting Hubbard model the Hamiltonian is given by

$$H_0 = \sum_\sigma \sum_{\mathbf{k}} \epsilon_{\mathbf{k}} \hat{n}_{\mathbf{k},\sigma}.$$

In an external magnetic field h_z the energy dispersion $\epsilon_{\mathbf{k}}$ becomes

$$\epsilon_{\mathbf{k},\sigma} = \epsilon_{\mathbf{k}} + \frac{1}{2}\sigma h_z,$$

now depending on the spin. The magnetization is proportional to the difference of $\uparrow$- and $\downarrow$-spins, which at zero temperature is

$$\begin{aligned}M_z &= -\frac{1}{2}\frac{1}{N_{\mathbf{k}}}\sum_{\mathbf{k}}\left[n_{\mathbf{k},\uparrow} - n_{\mathbf{k},\downarrow}\right]\\ &\approx \frac{1}{4}\rho(\epsilon_F)h_z.\end{aligned} \tag{A.47}$$

Because $M_z = \chi(0)h_z$, we find the Pauli susceptibility for metals

$$\chi^{\mathrm{P}}(0) = \frac{1}{4}\rho(\epsilon_F)$$

with the density of states $\rho(\epsilon)$ at the Fermi energy ϵ_F.
Let us describe the influence of U by approximating the Coulomb Hamiltonian $H_U = U\sum_i n_{i,\uparrow}n_{i,\downarrow}$ by the Hartree-Fock Hamiltonian

$$H_U^{\mathrm{HF}} = U\sum_i \left[n_{i,\uparrow}\langle n_{i,\downarrow}\rangle + \langle n_{i,\uparrow}\rangle n_{i,\downarrow} - \langle n_{i,\uparrow}\rangle\langle n_{i,\downarrow}\rangle\right]$$

and the total Hamiltonian is $H_0 + H_U$. Effectively, this leads to a modification of the energy dispersion

$$\begin{aligned}\epsilon^U_{\mathbf{k},\sigma} &= \epsilon_{\mathbf{k},\sigma} + n_{-\sigma}U \\ &= \epsilon_{\mathbf{k}} + \frac{1}{2}(n_\uparrow + n_\downarrow)U - \sigma m U + \frac{1}{2}h_z\sigma\end{aligned}$$

with $m = (n_\uparrow - n_\downarrow)/2$. So the $-\sigma m U$ term is formally like an additional magnetic field. Finally, using that $M_z = -g\mu_B m$, and setting $g\mu_B \approx 1$, we obtain the self-consistent equation

$$M_z \approx \chi^{\mathrm{P}}(0)\left[h_z + 2UM_z\right]. \tag{A.48}$$

From its solution for M_z we obtain the susceptibility like in (A.47). This is the Stoner susceptibility

$$\begin{aligned}\chi^{\mathrm{S}}(\mathbf{0},0) &= \frac{\chi^{\mathrm{P}}(0)}{1 - 2U\chi^{\mathrm{P}}(0)} \\ &= \frac{1}{4}\frac{\rho(\epsilon_F)}{1 - \frac{1}{2}U\rho(\epsilon_F)}.\end{aligned} \tag{A.49}$$

A phase transition to a ferromagnetically ordered phase occurs for $U > U_c$, where the critical value for U is

$$U_c = \frac{2}{\rho(\epsilon_F)}. \tag{A.50}$$

Let us now investigate the effects of the next-nearest neighbor hopping t' and doping x in the cuprate dispersion (6.1) on the non-interacting density of states $\rho(\epsilon)$ and the Stoner susceptibility χ^{S}. In figure A.4 we show two numerical approximated density of states for $t' = 0$ (left) and $t' = 0.2t$ (right), and the chemical potential $\mu = \epsilon_F$ for different dopings. Without next-nearest neighbor hopping ($t' = 0$) a van-Hove singularity is at the Fermi energy for half-filling $x = 0$. Increasing x lowers ϵ_F and consequently the value $\rho(\epsilon_F)$. As a result, the Stoner susceptibility decreases with x as well, which is shown in figure A.5.

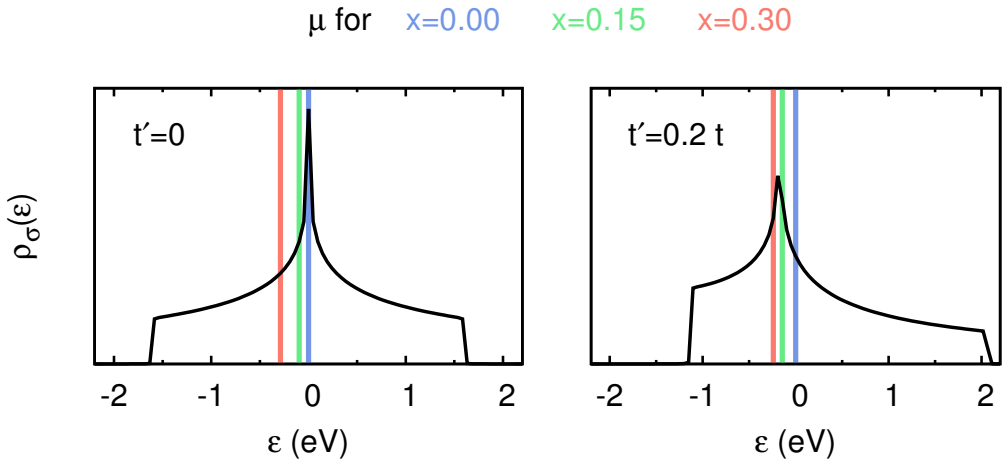

Figure A.4: Density of states for the non-interacting cuprate dispersion (6.1). The left side shows $t' = 0$, while the right shows $t' = 0.2t$. The chemical potential for three dopings is depicted as colored vertical lines.

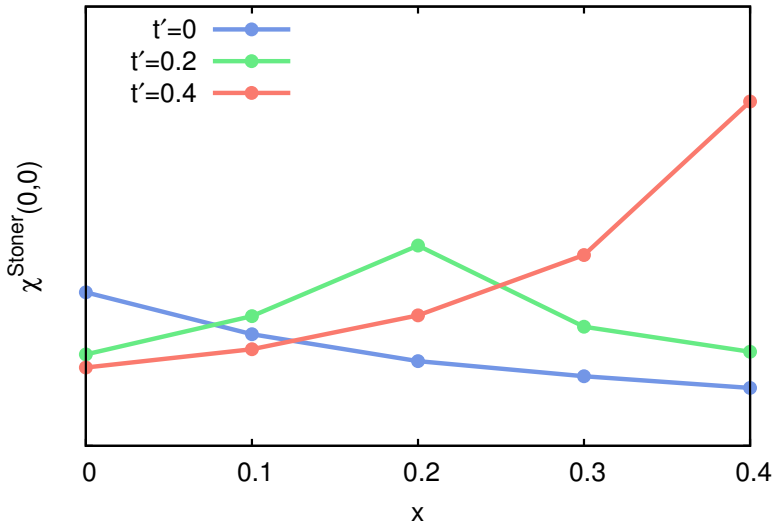

Figure A.5: Dependence of the Stoner susceptibility $\chi^{\mathrm{S}}(\mathbf{0},0)$ on the doping x for different t'. The perturbation $U = 1\,\mathrm{eV}$ is chosen small enough that all calculations are paramagnetic.

For $t' > 0$, shown on the right of figure A.4, the van-Hove singularity is shifted to negative energies. Increasing x shifts the chemical potential again to the left, but here the $\rho(\epsilon)$ is increasing until a x_c and decreasing only for $x > x_c$. This effect translates to the Stoner susceptibility depicted in figure A.5. For $t' = 0.2t$ it has a non monotonic behavior with $x_c \approx 0.2$. Finally, for $t' = 0.4t$ the chemical potential is always above the van-Hove singularity for the here considered $x < 0.4$. Therefore, the Stoner susceptibility is only increasing with x.

A.7 Notes on the implementation of DMFT with a CT-QMC solver and the Bethe-Salpeter equation

In this thesis we extended the implementation of the DMFT code with the CT-QMC solver described in Refs. [1, 2]. We added the possibility to measure two-particle Green functions during the QMC sampling as described in chapter 3. The measurement is possible for generalized two-particle Green functions in the segment and Krylov solver. The Green functions can be measured in the imaginary time, the Legendre or the intermediate representation. Furthermore, we implemented a code to calculate lattice susceptibilities from the CT-QMC results using the Bethe-Salpeter equation. Details on this procedure are given in chapter 4. The Bethe-Salpeter equation is solved either in Legendre or intermediate representation.
Both codes are written in standard C++. No additional external libraries are used compared to the existing code, which uses "getopt.h" from the GNU C Library[3], the Boost library[4], BLAS[5] and LAPACK[6]. The codes can be compiled and executed on Linux compatible operation systems. They are parallelized using MPI, but a serial execution is possible as well. A debug mode with additional checks during execution is implemented. The codes have been successfully used on supercomputers of the Forschungszentrum Jülich including JUQUEEN, JURECA, JURECA Booster and JUWELS. We provide Makefiles for these supercomputers as well. We extended the existing documentation using Doxygen[7] and added the implemented formulas in an additional documentation. Finally, we provide example input files, job scripts for the supercomputers and results for representative test cases.

[3] www.gnu.org/s/libc/
[4] https://www.boost.org/
[5] http://www.netlib.org/blas
[6] http://www.netlib.org/lapack
[7] http://www.doxygen.nl/

Bibliography

[1] A. R. Flesch. *Electronic Structure of Strongly Correlated Materials*. PhD thesis, RWTH Aachen, 2013.

[2] A. Flesch, E. Gorelov, E. Koch, and E. Pavarini. Multiplet effects in orbital and spin ordering phenomena: A hybridization-expansion quantum impurity solver study. *Phys. Rev. B*, 87:195141, May 2013.

[3] P. Hohenberg and W. Kohn. Inhomogeneous electron gas. *Phys. Rev.*, 136:B864–B871, Nov 1964.

[4] W. Kohn and L. J. Sham. Self-consistent equations including exchange and correlation effects. *Phys. Rev.*, 140:A1133–A1138, Nov 1965.

[5] O. Andersen. Chapter 3 - NMTOs and their Wannier functions. In E. Pavarini, E. Koch, F. Anders, and M. Jarrell, editors, *Correlated Electrons: From Models to Materials*. Forschungszentrum Jülich GmbH, 2012.

[6] J. Kuneš. Chapter 4 - Wannier functions and construction of model Hamiltonians. In E. Pavarini, E. Koch, D. Vollhardt, and A. Lichtenstein, editors, *The LDA+DMFT approach to strongly correlated materials*. Forschungszentrum Jülich GmbH, 2011.

[7] W. Metzner and D. Vollhardt. Correlated lattice fermions in $d = \infty$ dimensions. *Phys. Rev. Lett.*, 62:324–327, Jan 1989.

[8] E. Müller-Hartmann. Correlated fermions on a lattice in high dimensions. *Zeitschrift für Physik B Condensed Matter*, 74(4):507–512, 1989.

[9] A. Georges and G. Kotliar. Hubbard model in infinite dimensions. *Phys. Rev. B*, 45:6479–6483, Mar 1992.

[10] A. Georges, G. Kotliar, W. Krauth, and M. J. Rozenberg. Dynamical mean-field theory of strongly correlated fermion systems and the limit of infinite dimensions. *Rev. Mod. Phys.*, 68:13–125, Jan 1996.

[11] M. Jarrell. Hubbard model in infinite dimensions: A quantum Monte Carlo study. *Phys. Rev. Lett.*, 69:168–171, Jul 1992.

[12] T. Pruschke, M. Jarrell, and J. K. Freericks. Anomalous normal-state properties of high-T_c superconductors: intrinsic properties of strongly correlated electron systems? *Advances in Physics*, 44(2):187–210, 1995.

[13] F. Aryasetiawan, T. Miyake, and R. Sakuma. Chapter 7 - The constrained RPA method for calculating the Hubbard U from first-principles. In E. Pavarini, E. Koch, D. Vollhardt, and A. Lichtenstein, editors, *The LDA+DMFT approach to strongly correlated materials*. Forschungszentrum Jülich GmbH, 2011.

[14] P. Werner, A. Comanac, L. de' Medici, M. Troyer, and A. J. Millis. Continuous-time solver for quantum impurity models. *Phys. Rev. Lett.*, 97:076405, Aug 2006.

[15] E. Gull, A. J. Millis, A. I. Lichtenstein, A. N. Rubtsov, M. Troyer, and P. Werner. Continuous-time Monte Carlo methods for quantum impurity models. *Rev. Mod. Phys.*, 83:349–404, May 2011.

[16] F. F. Assaad. Chapter 7 - Continuous-time QMC solvers for electronic systems in fermionic and bosonic baths. In E. Pavarini, E. Koch, D. Vollhardt, and A. Lichtenstein, editors, *DMFT at 25: Infinite Dimensions*. Forschungszentrum Jülich GmbH, 2014.

[17] N. Metropolis, A. W. Rosenbluth, M. N. Rosenbluth, A. H. Teller, and E. Teller. Equation of state calculations by fast computing machines. *The Journal of Chemical Physics*, 21(6):1087–1092, 1953.

[18] W. K. Hastings. Monte Carlo sampling methods using Markov chains and their applications. *Biometrika*, 57(1):97–109, 04 1970.

[19] A. M. Läuchli and P. Werner. Krylov implementation of the hybridization expansion impurity solver and application to 5-orbital models. *Phys. Rev. B*, 80:235117, Dec 2009.

[20] C. Lanczos. An iteration method for the solution of the eigenvalue problem of linear differential and integral operators. *Journal of Research of the National Bureau of Standards*, 1950.

[21] E. Koch. Chapter 7 - Exact diagonalization and Lanczos method. In E. Pavarini, E. Koch, and S. Zhang, editors, *Many-Body Methods for Real Materials*. Forschungszentrum Jülich GmbH, 2019.

[22] E. Pavarini. Chapter 6 - Linear response functions. In E. Pavarini, E. Koch, D. Vollhardt, and A. Lichtenstein, editors, *DMFT at 25: Infinite Dimensions*. Forschungszentrum Jülich GmbH, 2014.

[23] H. Ibach and H. Lüth. *Solid-State Physics: An Introduction to Principles of Materials Science*. Springer, 2009.

[24] M. Sing. Chapter 14 - Introduction to photoemission spectroscopy. In E. Pavarini, E. Koch, D. Vollhardt, and A. Lichtenstein, editors, *DMFT at 25: Infinite Dimensions*. Forschungszentrum Jülich GmbH, 2014.

[25] C. Hess. Chapter 14 - Introduction to scanning tunneling spectroscopy of correlated materials. In E. Pavarini, E. Koch, J. van den Brink, and G. Sawatzky, editors, *Quantum Materials: Experiments and Theory*. Forschungszentrum Jülich GmbH, 2016.

[26] T. Chatterji. Chapter 1 - Magnetic neutron scattering. In T. Chatterji, editor, *Neutron Scattering from Magnetic Materials*, pages 1–24. Elsevier Science, Amsterdam, 2006.

[27] J. van den Brink. Chapter 12 - Resonant inelastic x-ray scattering on elementary excitations. In E. Pavarini, E. Koch, J. van den Brink, and G. Sawatzky, editors, *Quantum Materials: Experiments and Theory*. Forschungszentrum Jülich GmbH, 2016.

[28] L. L. Braicovich, J. van den Brink, V. Bisogni, M. Moretti Sala, L. J. P. Ament, N. B. Brookes, G. M. De Luca, M. Salluzzo, T. Schmitt, V. N. Strocov, and G. Ghiringhelli. Magnetic excitations and phase separation in the underdoped $La_{2-x}Sr_xCuO_4$ superconductor measured by resonant inelastic x-ray scattering. *Phys. Rev. Lett.*, 104:077002, Feb 2010.

[29] R. Coldea, S. M. Hayden, G. Aeppli, T. G. Perring, C. D. Frost, T. E. Mason, S.-W. Cheong, and Z. Fisk. Spin waves and electronic interactions in La_2CuO_4. *Phys. Rev. Lett.*, 86:5377–5380, Jun 2001.

[30] D. van der Marel. Chapter 11 - Optical properties of correlated electrons. In E. Pavarini, E. Koch, J. van den Brink, and G. Sawatzky, editors, *Quantum Materials: Experiments and Theory*. Forschungszentrum Jülich GmbH, 2016.

[31] H. Alloul. Chapter 13 - NMR in correlated electron systems: Illustration on the cuprates. In E. Pavarini, E. Koch, J. van den Brink, and G. Sawatzky, editors, *Quantum Materials: Experiments and Theory*. Forschungszentrum Jülich GmbH, 2016.

[32] L. Boehnke and F. Lechermann. Competing orders in Na_xCoO_2 from strong correlations on a two-particle level. *Phys. Rev. B*, 85:115128, Mar 2012.

[33] T. Moriya. Nuclear Magnetic Relaxation near the Curie Temperature. *Progress of Theoretical Physics*, 28(2):371–400, 08 1962.

[34] V. Zlatic and B. Horvatic. The local approximation for correlated systems on high dimensional lattices. *Solid State Communications*, 75(3):263–267, 1990.

[35] G. Rohringer, A. Valli, and A. Toschi. Local electronic correlation at the two-particle level. *Phys. Rev. B*, 86:125114, Sep 2012.

[36] L. Boehnke. *Susceptibilities in materials with multiple strongly correlated orbitals*. PhD thesis, Universität Hamburg, 2015.

[37] A. Kiani Sheikhabadi. *Linear response functions of Strongly Correlated Materials: LDA+DMFT approach*. PhD thesis, RWTH Aachen University, 2015.

[38] H. Bruss and K. Flensberg. *Many-Body Quantum Theory in Condensed Matter Physics*. Oxford University Press, 2004.

[39] L. Boehnke, H. Hafermann, M. Ferrero, F. Lechermann, and O. Parcollet. Orthogonal polynomial representation of imaginary-time Green's functions. *Phys. Rev. B*, 84:075145, Aug 2011.

[40] H. Shinaoka, J. Otsuki, M. Ohzeki, and K. Yoshimi. Compressing Green's function using intermediate representation between imaginary-time and real-frequency domains. *Phys. Rev. B*, 96:035147, Jul 2017.

[41] N. Chikano, J. Otsuki, and H. Shinaoka. Performance analysis of a physically constructed orthogonal representation of imaginary-time Green's function. *Phys. Rev. B*, 98:035104, Jul 2018.

[42] A. W. Sandvik. Stochastic method for analytic continuation of quantum Monte Carlo data. *Phys. Rev. B*, 57:10287–10290, May 1998.

[43] K. Ghanem. *Stochastic Analytic Continuation: A Bayesian Approach*. PhD thesis, RWTH Aachen University, 2017.

[44] J. Kanamori. Crystal distortion in magnetic compounds. *Journal of Applied Physics*, 31(5):S14–S23, 1960.

[45] K. I. Kugel and D. I. Khomskii. Crystal structure and magnetic properties of substances with orbital degeneracy. *Sov. Phys. JETP*, 37(4):725–730, 1973.

[46] E. Pavarini, E. Koch, and A. I. Lichtenstein. Mechanism for orbital ordering in $KCuF_3$. *Phys. Rev. Lett.*, 101:266405, Dec 2008.

[47] E. Pavarini and E. Koch. Origin of Jahn-Teller distortion and orbital order in $LaMnO_3$. *Phys. Rev. Lett.*, 104:086402, Feb 2010.

[48] M. Hidaka, K. Inoue, I. Yamada, and P. J. Walker. X-ray diffraction study of the crystal structures of K_2CuF_4 and $K_2Cu_xZn_{1-x}F_4$. *Physica B+C*, 121(3):343 – 350, 1983.

[49] M. Ishizuka, M. Terai, M. Hidaka, S. Endo, I. Yamada, and O. Shimomura. Pressure-induced structural phase transition in the two-dimensional Heisenberg ferromagnet K_2CuF_4. *Phys. Rev. B*, 57:64–67, Jan 1998.

[50] E. Pavarini. Chapter 6 - The LDA+DMFT approach. In E. Pavarini, E. Koch, D. Vollhardt, and A. Lichtenstein, editors, *The LDA+DMFT approach to strongly correlated materials*. Forschungszentrum Jülich GmbH, 2011.

[51] E. Pavarini. Chapter 6 - Crystal-field theory, tight-binding method and Jahn-Teller effect. In E. Pavarini, E. Koch, F. Anders, and M. Jarrell, editors, *Correlated Electrons: From Models to Materials*. Forschungszentrum Jülich GmbH, 2012.

[52] H. A. Jahn, E. Teller, and F. G. Donnan. Stability of polyatomic molecules in degenerate electronic states - I–orbital degeneracy. *Proceedings of the Royal Society of London. Series A - Mathematical and Physical Sciences*, 161(905):220–235, 1937.

[53] E. Pavarini. Chapter 7 - Orbital ordering. In E. Pavarini, E. Koch, J. van den Brink, and G. Sawatzky, editors, *Quantum Materials: Experiments and Theory*. Forschungszentrum Jülich GmbH, 2016.

[54] E. Koch. Chapter 7 - Exchange mechanisms. In E. Pavarini, E. Koch, D. Vollhardt, and A. Lichtenstein, editors, *Correlated Electrons: From Models to Materials*. Forschungszentrum Jülich GmbH, 2012.

[55] E. Pavarini. Chapter 3 - Magnetism: Models and mechanisms. In E. Pavarini, E. Koch, and U. Schollwöck, editors, *Emergent Phenomena in Correlated Matter*. Forschungszentrum Jülich GmbH, 2013.

[56] P. Blaha, K. Schwarz, G. K. H. Madsen, D. Kvasnicka, and J. Luitz. *WIEN2k: An Augmented Plane Wave Plus Local Orbitals Program for Calculating Crystal Properties*. Technische Universitat Wien, 2001.

[57] P. Blaha, K. Schwarz, P. Sorantin, and S. B. Trickey. Full-potential, linearized augmented plane wave programs for crystalline systems. *Computer Physics Communications*, 59(2):399 – 415, 1990.

[58] N. Marzari and D. Vanderbilt. Maximally localized generalized Wannier functions for composite energy bands. *Phys. Rev. B*, 56:12847–12865, Nov 1997.

[59] A. A. Mostofi, J. R. Yates, Y. Lee, I. Souza, D. Vanderbilt, and N. Marzari. wannier90: A tool for obtaining maximally-localised Wannier functions. *Computer Physics Communications*, 178(9):685 – 699, 2008.

[60] M. Ishizuka, M. Terai, S. Endo, M. Hidaka, I. Yamada, and O. Shimomura. Pressure-induced magnetic phase transition in the two-dimensional Heisenberg ferromagnet K_2CuF_4. *Journal of Magnetism and Magnetic Materials*, 177-181:725 – 726, 1998. International Conference on Magnetism.

[61] J. G. Bednorz and K. A. Müller. Possible high T_c superconductivity in the Ba-La-Cu-O system. *Z. Physik B*, 64:189–193, June 1986.

[62] J. R. Schrieffer and J. S. Brooks, editors. *Handbook of High-Temperature Superconductivity. Theory and Experiments*. Springer Science + Business Media, New York, 2007.

[63] N. Plakida. *High-Temperature Cuprate Superconductors*. Series in Solid-State Sciences. Springer, Heidelberg Dordrecht London New York, 2010.

[64] E. Pavarini, I. Dasgupta, T. Saha-Dasgupta, O. Jepsen, and O. K. Andersen. Band-structure trend in hole-doped cuprates and correlation with $T_{c\max}$. *Phys. Rev. Lett.*, 87:047003, Jul 2001.

[65] P. Werner, R. Sakuma, F. Nilsson, and F. Aryasetiawan. Dynamical screening in La_2CuO_4. *Phys. Rev. B*, 91:125142, Mar 2015.

[66] S. Jang, H. Sakakibara, H. Kino, T. Kotani, K Kuroki, and M. J. Han. Direct theoretical evidence for weaker correlations in electron-doped and Hg-based hole-doped cuprates. *Scientific Reports*, page 33397, 2016.

[67] F. Aryasetiawan, K. Karlsson, O. Jepsen, and U. Schönberger. Calculations of Hubbard U from first-principles. *Phys. Rev. B*, 74:125106, Sep 2006.

[68] A. K. McMahan, Richard M. Martin, and S. Satpathy. Calculated effective Hamiltonian for La_2CuO_4 and solution in the impurity Anderson approximation. *Phys. Rev. B*, 38:6650–6666, Oct 1988.

[69] M. S. Hybertsen, M. Schlüter, and N. E. Christensen. Calculation of Coulomb-interaction parameters for La_2CuO_4 using a constrained-density-functional approach. *Phys. Rev. B*, 39:9028–9041, May 1989.

[70] V. I. Anisimov, M. A. Korotin, I. A. Nekrasov, Z. V. Pchelkina, and S. Sorella. First principles electronic model for high-temperature superconductivity. *Phys. Rev. B*, 66:100502, Sep 2002.

[71] A. K. McMahan, James F. Annett, and Richard M. Martin. Cuprate parameters from numerical Wannier functions. *Phys. Rev. B*, 42:6268–6282, Oct 1990.

[72] N. Nücker, J. Fink, B. Renker, D. Ewert, C. Politis, P. J. W. Weijs, and J. C. Fuggle. Experimental electronic structure studies of $La_{2-x}Sr_xCuO_4$. *Z. Phys. B Condensed Matter*, 67:9–14, Mar 1987.

[73] J. M. Ginder, M. G. Roe, Y. Song, R. P. McCall, J. R. Gaines, E. Ehrenfreund, and A. J. Epstein. Photoexcitations in La_2CuO_4: 2-eV energy gap and long-lived defect states. *Phys. Rev. B*, 37:7506–7509, May 1988.

[74] S. Uchida, T. Ido, H. Takagi, T. Arima, Y. Tokura, and S. Tajima. Optical spectra of $La_{2-x}Sr_xCuO_4$: Effect of carrier doping on the electronic structure of the CuO_2 plane. *Phys. Rev. B*, 43:7942–7954, Apr 1991.

[75] T. Thio and A. Aharony. Weak ferromagnetism and tricriticality in pure La_2CuO_4. *Phys. Rev. Lett.*, 73:894–897, Aug 1994.

[76] P. E. Sulewski, P. A. Fleury, K. B. Lyons, S-W. Cheong, and Z. Fisk. Light scattering from quantum spin fluctuations in R_2CuO_4 (R=La, Nd, Sm). *Phys. Rev. B*, 41:225–230, Jan 1990.

[77] K. B. Lyons, P. A. Fleury, L. F. Schneemeyer, and J. V. Waszczak. Spin fluctuations and superconductivity in $Ba_2YCu_3O_{6+\delta}$. *Phys. Rev. Lett.*, 60:732–735, Feb 1988.

[78] M. Ogata and H. Fukuyama. The t–J model for the oxide high-T_c superconductors. *Reports on Progress in Physics*, 71, Feb 2008.

[79] K. B. Lyons, P. A. Fleury, J. P. Remeika, A. S. Cooper, and T. J. Negran. Dynamics of spin fluctuations in lanthanum cuprate. *Phys. Rev. B*, 37:2353–2356, Feb 1988.

[80] A. Kiani and E. Pavarini. Electronic correlation and magnetic frustration in Li_2VOSiO_4 and $VOMoO_4$. *Phys. Rev. B*, 94:075112, Aug 2016.

[81] G. Shirane, Y. Endoh, R. J. Birgeneau, M. A. Kastner, Y. Hidaka, M. Oda, M. Suzuki, and T. Murakami. Two-dimensional antiferromagnetic quantum spin-fluid state in La_2CuO_4. *Phys. Rev. Lett.*, 59:1613–1616, Oct 1987.

[82] H. A. Mook, M. Yethiraj, G. Aeppli, T. E. Mason, and T. Armstrong. Polarized neutron determination of the magnetic excitations in $YBa_2Cu_3O_7$. *Phys. Rev. Lett.*, 70:3490–3493, May 1993.

[83] B. Keimer, N. Belk, R. J. Birgeneau, A. Cassanho, C. Y. Chen, M. Greven, M. A. Kastner, A. Aharony, Y. Endoh, R. W. Erwin, and G. Shirane. Magnetic excitations in pure, lightly doped, and weakly metallic La_2CuO_4. *Phys. Rev. B*, 46:14034–14053, Dec 1992.

[84] W. Nolting and A. Ramakanth. *Quantum Theory of Magnetism*. Springer, Heidelberg Dordrecht London New York, 2009.

[85] Q. F. Zhong and S. Sorella. Spin-wave theory on finite lattices: Application to the J_1-J_2 Heisenberg model. *Europhysics Letters (EPL)*, 21(5):629–635, Feb 1993.

[86] S. M. Hayden, G. Aeppli, T. G. Perring, H. A. Mook, and F. Doğan. High-frequency spin waves in $YBa_2Cu_3O_{6.15}$. *Phys. Rev. B*, 54:R6905–R6908, Sep 1996.

[87] J. B. Torrance, A. Bezinge, A. I. Nazzal, T. C. Huang, S. S. P. Parkin, D. T. Keane, S. J. LaPlaca, P. M. Horn, and G. A. Held. Properties that change as superconductivity disappears at high-doping concentrations in $La_{2-x}Sr_xCuO_4$. *Phys. Rev. B*, 40:8872–8877, Nov 1989.

[88] T. Nakano, M. Oda, C. Manabe, N. Momono, Y. Miura, and M. Ido. Magnetic properties and electronic conduction of superconducting $La_{2-x}Sr_xCuO_4$. *Phys. Rev. B*, 49:16000–16008, Jun 1994.

[89] G.-Q. Zheng, T. Kuse, Y. Kitaoka, K. Ishida, S. Ohsugi, K. Asayama, and Y. Yamada. ^{17}O NMR study of $La_{2-x}Sr_xCuO_4$ in the lightly- and heavily-doped regions. *Physica C: Superconductivity*, 208(3):339–346, 1993.

[90] S. Ohsugi, Y. Kitaoka, K. Ishida, G.-Q. Zheng, and K. Asayama. Cu NMR and NQR studies of high-T_c superconductor $La_{2-x}Sr_xCuO_4$. *Journal of the Physical Society of Japan*, 63(2):700–715, 1994.

[91] K. Asayama, Y. Kitaoka, G.-Q. Zheng, K. Ishida, and S. Ohsugi. NMR in highly correlated superconductors. *Hyperfine Interactions*, 79(1):835–849, Mar 1993.

[92] K. Asayama, Y. Kitaoka, G.-Q. Zheng, and K. Ishida. NMR studies of high T_c superconductors. *Progress in Nuclear Magnetic Resonance Spectroscopy*, 28(3):221 – 253, 1996.

[93] A. Rigamonti, F. Borsa, and P. Carretta. Basic aspects and main results of NMR-NQR spectroscopies in high-temperature superconductors. *Reports on Progress in Physics*, 61(10):1367, 1998.

[94] K. Fujiwara, Y. Kitaoka, K. Asayama, Y. Shimakawa, T. Manako, and Y. Kubo. ^{63}Cu Knight shift study in high-T_c superconductor $Tl_2Ba_2CuO_{6+y}$ with a single CuO_2 layer. *Journal of the Physical Society of Japan*, 59(10):3459–3462, 1990.

[95] K. Fujiwara, Y. Kitaoka, K. Ishida, K. Asayama, Y. Shimakawa, T. Manako, and Y. Kubo. NMR and NQR studies of superconductivity in heavily doped $Tl_2Ba_2CuO_{6+y}$ with a single plane CuO_2. *Physica C: Superconductivity*, 184(4-6):207–219, 1991.

[96] M. Matsuda, M. Fujita, K. Yamada, R. J. Birgeneau, Y. Endoh, and G. Shirane. Electronic phase separation in lightly doped $La_{2-x}Sr_xCuO_4$. *Phys. Rev. B*, 65(13):134515, 2002.

[97] T. Suzuki, T. Goto, K. Chiba, T. Shinoda, T. Fukase, H. Kimura, K. Yamada, M. Ohashi, and Y. Yamaguchi. Observation of modulated magnetic long-range order in $La_{1.88}Sr_{0.12}CuO_4$. *Phys. Rev. B*, 57(6):R3229, 1998.

[98] H. Kimura, K. Hirota, H. Matsushita, K. Yamada, Y. Endoh, S.-H. Lee, C. F. Majkrzak, R. Erwin, G. Shirane, M. Greven, et al. Neutron-scattering study of static antiferromagnetic correlations in $La_{2-x}Sr_xCu_{1-y}Zn_yO_4$. *Phys. Rev. B*, 59(9):6517, 1999.

[99] B. O. Wells, Y. S. Lee, M. A. Kastner, R. J. Christianson, R. J. Birgeneau, K. Yamada, Y. Endoh, and G. Shirane. Incommensurate spin fluctuations in high-transition temperature superconductors. *Science*, 277(5329):1067–1071, 1997.

[100] K. Yamada, C. H. Lee, K. Kurahashi, J. Wada, S. Wakimoto, S. Ueki, H. Kimura, Y. Endoh, S. Hosoya, G. Shirane, et al. Doping dependence of the spatially modulated dynamical spin correlations and the superconducting-transition temperature in $La_{2-x}Sr_xCuO_4$. *Phys. Rev. B*, 57(10):6165, 1998.

[101] M. Fujita, H. Goka, K. Yamada, J. M. Tranquada, and L. P. Regnault. Stripe order, depinning, and fluctuations in $La_{1.875}Ba_{0.125}CuO_4$ and $La_{1.875}Ba_{0.075}Sr_{0.050}CuO_4$. *Phys. Rev. B*, 70(10):104517, 2004.

[102] M. Fujita, H. Goka, T. Adachi, Y. Koike, and K. Yamada. Neutron scattering study on stripe correlations in $La_{2-x}Ba_xCuO_4$. *Physica C: Superconductivity*, 426:257–261, 2005.

[103] J. M. Tranquada, B. J. Sternlieb, J. D. Axe, Y. Nakamura, and S. Uchida. Evidence for stripe correlations of spins and holes in copper oxide superconductors. *nature*, 375(6532):561–563, 1995.

[104] E. A. Stepanov, L. Peters, I. S. Krivenko, A. I. Lichtenstein, M. I. Katsnelson, and A. N. Rubtsov. Quantum spin fluctuations and evolution of electronic structure in cuprates. *npj Quantum Materials*, 3(54), Oct 2018.

[105] C. J. Jia, E. A. Nowadnick, K. Wohlfeld, Y. F. Kung, C.-C. Chen, S. Johnston, T. Tohyama, B. Moritz, and T. P. Devereaux. Persistent spin excitations in doped antiferromagnets revealed by resonant inelastic light scattering. *Nature communications*, 5(3314):1–7, 2014.

[106] S.-W. Cheong, G. Aeppli, T. E. Mason, H. Mook, S. M. Hayden, P. C. Canfield, Z. Fisk, K. N. Clausen, and J. L. Martinez. Incommensurate magnetic fluctuations in $La_{2-x}Sr_xCuO_4$. *Phys. Rev. Lett.*, 67(13):1791, 1991.

[107] H. A. Mook, P. Dai, S. M. Hayden, G. Aeppli, T. G. Perring, and F. Doğan. Spin fluctuations in $YBa_2Cu_3O_{6.6}$. *Nature*, 395:580–582, Oct 1998.

[108] S. Wakimoto, H. Zhang, K. Yamada, I. Swainson, Hyunkyung Kim, and R. J. Birgeneau. Direct relation between the low-energy spin excitations and superconductivity of overdoped high-T_c superconductors. *Phys. Rev. Lett.*, 92:217004, May 2004.

[109] S. Wakimoto, K. Yamada, J. M. Tranquada, C. D. Frost, R. J. Birgeneau, and H. Zhang. Disappearance of antiferromagnetic spin excitations in overdoped $La_{2-x}Sr_xCuO_4$. *Phys. Rev. Lett.*, 98:247003, Jun 2007.

[110] M. P. M. Dean, G. Dellea, R. S. Springell, F. Yakhou-Harris, K. Kummer, N. B. Brookes, X. Liu, Y. J. Sun, J. Strle, T. Schmitt, et al. Persistence of magnetic excitations in $La_{2-x}Sr_xCuO_4$ from the undoped insulator to the heavily overdoped non-superconducting metal. *Nature Materials*, 12(11):1019–1023, 2013.

[111] D. Meyers, H. Miao, A. C. Walters, V. Bisogni, R. S. Springell, M. d'Astuto, M. Dantz, J. Pelliciari, H. Y. Huang, J. Okamoto, D. J. Huang, J. P. Hill, X. He, I. Božović, T. Schmitt, and M. P. M. Dean. Doping dependence of the magnetic excitations in $La_{2-x}Sr_xCuO_4$. *Phys. Rev. B*, 95:075139, Feb 2017.

[112] M. Le Tacon, G. Ghiringhelli, J. Chaloupka, M. Moretti Sala, V. Hinkov, M. W. Haverkort, M. Minola, M. Bakr, K. J. Zhou, S. Blanco-Canosa, et al. Intense paramagnon excitations in a large family of high-temperature superconductors. *Nature Physics*, 7(9):725–730, 2011.

[113] M. Le Tacon, M. Minola, D. C. Peets, M. Moretti Sala, S. Blanco-Canosa, V. Hinkov, R. Liang, D. A. Bonn, W. N. Hardy, C. T. Lin, T. Schmitt, L. Braicovich, G. Ghiringhelli, and B. Keimer. Dispersive spin excitations in highly overdoped cuprates revealed by resonant inelastic x-ray scattering. *Phys. Rev. B*, 88:020501, Jul 2013.

[114] W. H. Press, S. A. Teukolsky, W. T. Vetterling, and B. P. Flannery. *Numerical Recipes - The Art of Scientific Computing*. Cambridge University Press, 3rd edition, 2007.

[115] I. S. Gradshteyn and I. M. Ryzhik. *Table of Integrals, Series, and Products*. Academic Press, 2000.

[116] M. Abramowitz and I. A. Stegun, editors. *Handbook of mathematical functions with formulas, graphs and mathematical tables*. National Bureau of Standards, 1964.

[117] M. Jarrell. Chapter 13 - The maximum entropy method: Analytic continuation of QMC data. In E. Pavarini, E. Koch, D. Vollhardt, and A. Lichtenstein, editors, *Correlated Electrons: From Models to Materials*. Forschungszentrum Jülich GmbH, 2012.

[118] M. Jarrell and J. E. Gubernatis. Bayesian inference and the analytic continuation of imaginary-time quantum Monte Carlo data. *Physics Reports*, 269(3):133 – 195, 1996.

[119] R. K. Bryan. Maximum entropy analysis of oversampled data problems. *European Biophysics Journal*, 18(3):165–174, 1990.

[120] M. Maśka. Self-energy approach to the t-J model. *Phys. Rev. B*, 48:1160–1166, Jul 1993.

[121] M. Potthoff, T. Herrmann, T. Wegner, and W. Nolting. The moment sum rule and its consequences for ferromagnetism in the Hubbard model. *physica status solidi (b)*, 210(1):199–228, 1998.

Acknowledgements

This work was only possible because of the support of several people, who I like to express my gratitude to.
First and foremost, I thank Prof. Eva Pavarini for letting me be part of her group, for her guidance and comments, sharing her experience in physics and in strongly correlated materials. I am especially grateful for her support during my entire time as a Ph.D. student.
I am thankful to Prof. Stefan Wessel for being my second supervisor in the Research Training Group (RTG1995) and for reviewing this thesis.
I always appreciated the discussions with Prof. Erik Koch, not only on Physics, and thank him for his advise.
I am thankful to my former and current colleagues in our Institute of Advanced simulation (IAS-3) group in Jülich Dr. Amin Kiani, Dr. Esmaeel Sarvestani, Dr. Guoren Zhang, Dr. Xuejing Zhang and Neda Samani, from whom I learned a lot and who provided a great atmosphere for work. My special thanks go to Dr. Amin Kiani for introducing me to susceptibilities and DMFT and helping me with Hirsch-Fye QMC results, and to Dr. Guoren Zhang for answering my physics and group theory questions and for his LDA calculations on K_2CuF_4.
I thank the GRS students and members, especially Dr. Qian Zhang for our time together including our bus trips and Dr. Khaldoon Ghanem for his help with analytic continuation using StochS.
I express my thank to all RTG students who I met, foremost my office mates at RWTH Aachen Dr. Jovan Odavic, Dr. Andishe Khedri and Dr. Niklas Dittmann. The RTG provided an inspiring environment with fruitful discussions.
My gratitude goes to the RTG and the IAS-3 for financing my Ph.D. and inspiring conferences, and also to the Jülich Supercomputing Center (JSC), without which these work would have been impossible.
I am very grateful to Luise Snyders and Gillian Hewitt for their support especially with administrative issues.
In place of all the people who had a positive influence on me during my education I thank my former supervisor Prof. Frithjof Anders and remember Prof. Mark Jarrell.
Last but not least, I am grateful to my parents and sister for their encouragement, support and interest in my work.
Most of all, I thank my wife for her assistance, patience and love while preparing this work. And I am thankful to my son for cheering me up, being patient, and going over this thesis multiple times.

Eidesstattliche Erklärung

Julian Mußhoff

erklärt hiermit, dass diese Dissertation und die darin dargelegten Inhalte die eigenen sind und selbstständig, als Ergebnis der eigenen originären Forschung, generiert wurden.

Hiermit erkläre ich an Eides statt

1. Diese Arbeit wurde vollständig oder größtenteils in der Phase als Doktorand dieser Fakultät und Universität angefertigt;
2. Sofern irgendein Bestandteil dieser Dissertation zuvor für einen akademischen Abschluss oder eine andere Qualifikation an dieser oder einer anderen Institution verwendet wurde, wurde dies klar angezeigt;
3. Wenn immer andere eigene- oder Veröffentlichungen Dritter herangezogen wurden, wurden diese klar benannt;
4. Wenn aus anderen eigenen- oder Veröffentlichungen Dritter zitiert wurde, wurde stets die Quelle hierfür angegeben. Diese Dissertation ist vollständig meine eigene Arbeit, mit der Ausnahme solcher Zitate;
5. Alle wesentlichen Quellen von Unterstützung wurden benannt;
6. Wenn immer ein Teil dieser Dissertation auf der Zusammenarbeit mit anderen basiert, wurde von mir klar gekennzeichnet, was von anderen und was von mir selbst erarbeitet wurde;
7. Teile dieser Arbeit wurden zuvor veröffentlicht und zwar in:
   Phys. Rev. B 100, 045116 (2019)